Lyman Continuum and Lyman α Emission from Galaxies at High Redshift

Thesis by

Milan Bogosavljević

In Partial Fulfillment of the Requirements

for the Degree of

Doctor of Philosophy

California Institute of Technology

Pasadena, California

2010

(Defended January 14, 2010)

To my wife Radica, a true teacher of compassion.

Acknowledgements

"As an adolescent I aspired to lasting fame,
I craved factual certainty,
and I thirsted for a meaningful vision of human life -
so I became a scientist.
This is like becoming an archbishop so you can meet girls."

- Matt Cartmill, anthropologist

The production of this thesis took a number of years, as beside the daily chores of research the author had spent a lot of mental time trying to understand and direct his life in a scientist environment. As the quote above accurately describes (thanks to PT and his friend), there were important surprises to be encountered, and some life lessons were not at all easy to accept. I owe great many thanks to a lot of people who were picking me up as I stumbled along the way.

First and foremost, my gratitude goes to my advisor, Chuck Steidel. Without his determination to see me through to the end none of this would ever get finished. Many conversations I had with Gwen Rudie, Alice Shapley and Brian Siana were also very helpful in gathering the strength to climb the last few steps. Thanks to Ashish Mahabal for guiding my first steps, many years ago.

I would also like to thank the staff at Mt. Palomar and W. M. Keck Observatories for keeping them such great places to be and work in. Thanks to Caltech Astronomy Department staff, Judy, Judith, Gina, Gita, Anu, Patrick and others, for being nice people at work and saving the day countless times.

I'm especially grateful to Ciro & Simona, Samir, Dušan and Irena, for their friendship and support. Finally, I would like to thank everybody at Caltech Shorinji Kempo club for the lasting inspiration.

Abstract

In this thesis we present two studies of star-forming galaxies at $z \approx 2$–3 based on deep spectroscopic and narrow band imaging observations. The first study addresses pressing questions regarding the nature of galaxies with significant escaping Lyman continuum radiation. Our second study investigates the nature of spatially extended Lyman α emission first observed in the form of luminous Lyman α "blobs."

In part I of this thesis we present the results of a deep spectroscopic survey to detect Lyman continuum radiation from individual galaxies at $z \approx 3$. Our measurements suggest that the escape fraction is strongly variable among galaxies at all luminosities, but that there is a significant preference for higher escape fraction in objects with luminosity lower than L_*. The integrated escaping radiation from galaxies is sufficient to complement the contribution of AGN in keeping the hydrogen in the Universe ionized. Using supporting near-IR and mid-IR photometry we derive model stellar population parameters and discover that Lyman continuum is preferentially detected among objects with lowest values for dust extinction and star-formation rate. This finding may indicate a connection between Lyman continuum escape and the evolutionary stage of a galaxy.

In part II we present deep imaging observations in a narrow band centered on Lyman α and H α at the redshift of a known protocluster of star-forming galaxies ($z = 2.3$). We discover 6 new giant and bright Lyman α "blobs" and identify a large number of Lyman α and H α emitters at the protocluster redshift. We find an anticorrelation between Lyman α and H α selection, which is explained by the observation that H α emitters show Lyman α line in absorption in their spectra. However, the composite Lyman α narrow-band image of H α emitters uncovers extended emission resembling Lyman α blobs in miniature. We conclude that faint Lyman α emission from gas within a radius of 40 kpc (or more) is likely a feature common to most galaxies at these redshifts. If ionizing photons produced in star-forming regions are responsible for this faint Lyman α "glow", then this extended flux represents a significant fraction of total predicted Lyman α equivalent width.

Contents

List of Figures

List of Tables

Foreword

For the duration of the PhD program, graduate students are expected to acquire a substantial factual knowledge and hands-on experience. Perhaps more importantly, through such work the students should also develop their own intuition about research in general. The author of this thesis is grateful that he had ample opportunity to work on many different projects over the years spent at Caltech. In this foreword I present an overview of some of these projects that, for various reasons, were not a part of the final thesis as presented here. Even though they span a broader range of scientific topics, they were an important component of the learning process which was necessary for the completion of this thesis.

Under the guidance of my first advisor, George S. Djorgovski, I got acquainted with observational techniques on large telescopes. In the very first year at Caltech I learned a great deal about imaging and spectroscopic instruments used on the 200-inch Hale telescope at Mt. Palomar and Keck telescopes at the W.M. Keck Observatory (Mauna Kea, Hawaii). In our first project, we have searched for "Barkana-Loeb" effect (Barkana & Loeb 2003), the signature of infall of the neutral IGM into host galaxies of luminous quasars at high redshift. The findings were presented at the annual AAS conference (Bogosavljevic et al. 2002). I had my first experience with near-infrared instruments in the course of a study of rest frame UV/optical continuum emission for a sample of quasars at redshifts $z \approx 4$ (Bogosavljevic et al. 2005). The Palomar-Quest Synoptic Sky Survey (Mahabal et al. 2003; Djorgovski et al. 2004a,b), a large collaboration between Caltech and Yale University, has taught me a great deal about mosaic CCD camera instrument design (Rabinowitz et al. 2003), drift-scan survey observations and the related technical challenges in processing of a large volume of survey data (Bauer et al. 2003; Mahabal et al. 2005b). During the Palomar-Quest High-Redshift Quasar Survey project (Djorgovski et al. 2003), a joint effort with the group led by C. Baltay at Yale University, we made an attempt to identify new quasars at $z \approx 6$ and investigate the end of the reionization era (Djorgovski et al. 2006). This work has provided me with sufficient experience and skills to undertake a survey of faint quasars at $z \approx 4$, using public NOAO Deep Wide Field Survey (Jannuzi & Dey 1999) and Deep Lens Survey (Wittman et al. 2002) imaging data. After spectroscopic followup of quasar candidates at Keck Observatory, we were successful in discovering 23 QSOs in the redshift range $z = 3.8-5.2$ and with luminosity $-26.0 < M_{1450} < -22.0$.

The results of this survey and the derived luminosity function of faint quasars at $z \approx 4$ are presented in Glikman et al. 2009. A surprising side result of this project was the discovery of two QSOs with a very interesting and rare N IV] 1486 Å emission line (Glikman et al. 2007).

I also wish to extend my gratitude for the experience, knowledge and skills I obtained in the first half of my graduate education to the many collaborators at Yale University and Caltech Center for Advanced Computing Research (CACR).

Chapter 1

Introduction

The evolution of baryonic matter distribution on the largest scales ($> 100\,\mathrm{Mpc}$) in the Universe is for the most part determined by nonbaryonic cold dark matter (CDM) and gravity. The picture becomes much more complex as we look down to a scale of few Mpc after the appearance of the first galaxies. Mechanical shocks and radiation induced by star formation, radiative cooling of gas, galaxy mergers and AGN activity influence the physical condition of baryons in galaxies as well as the surrounding intergalactic matter (IGM). Understanding the IGM at high redshift is crucial for a complete picture of the growth of structure, as at these early times it contains 90% of all the baryons. Studies of IGM absorption lines in the spectra of luminous quasars tell us that the hydrogen in the IGM is completely ionized throughout the redshift range $0 < z < 6$ (Fan et al. 2006; Djorgovski et al. 2006; Mesinger & Haiman 2007; though see Mesinger 2009 for caveats at $z \approx 6$). This would imply that the physical state of the IGM is defined by the metagalactic UV radiation. On the other hand, the presence of metals has been observed in the intracluster medium (ICM) as well as in many of the Lyman α forest systems. This demonstrates that significant "mixing" of the material processed in galaxies and the primordial IGM has taken place, presumably through a combination of supernova driven galactic winds, ram pressure stripping and outflows from Active Galactic Nuclei (AGN).

Owing to the advantage of 10-meter class telescopes coupled with large area CCD cameras, optical surveys have now been able to uncover galaxies as early as 1 Gyr after the Big Bang (Ouchi et al. 2009; Overzier et al. 2009; Shimasaku et al. 2003). Various techniques for selecting galaxies by means of their observed colors have been employed for this purpose. One of the most successful has been the Lyman break technique (Steidel & Hamilton 1993), first used to identify thousands of galaxies at redshifts $z \approx 3$. These Lyman Break Galaxies (LBGs, Steidel et al. 2003) have been studied extensively over the past years, at all wavelengths from X-ray to radio (Laird et al. 2006; Carilli et al. 2008). A great abundance of information about stellar populations and the state of the interstellar medium (ISM) in LBGs has been obtained (for an early review, see Giavalisco 2002). One of the most important findings related to the influence of galaxies on the IGM was the prevailing presence of galactic outflows of gas. The velocities observed are often greater than the

escape velocity from the galaxy, and so these outflows are one of the channels for the input of metal enriched material into the IGM. Additionally, by disturbing the local ISM, the outflows might also facilitate the escape of ionizing radiation into the IGM. It is becoming apparent that an investigation into the details of all of these mechanisms is necessary in order to untangle the joint evolution of the IGM and galaxies.

As mentioned earlier, the key ingredient of the IGM physics is the metagalactic UV background. Many attempts have been made to identify the sources contributing to it. It has been demonstrated long ago that UV radiation from AGN is not sufficient (Bechtold et al. 1987; Miralda-Escude & Ostriker 1990) to keep the IGM ionized beyond z =2–3 where the number density of AGN is seen to decrease (Hunt et al. 2004; Siana et al. 2008; Cowie et al. 2009). A significant contribution from galaxies to the ionizing photon budget is needed. Unfortunately, UV radiation originating in starforming regions of galaxies has a great probability of being absorbed by the neutral hydrogen in the ISM. As the ISM has a clumpy, multi-phase structure, it is very hard to predict precisely what fraction of ionizing photons will suffer this fate. Direct observations are necessary, and hence the great hunt for ionizing photons from galaxies has started.

Space-based observations of galaxies below $z = 2$ have been able to bring only upper limits on the amount of escaping ionizing radiation (Leitherer et al. 1995; Deharveng et al. 2001; Malkan et al. 2003; Siana et al. 2007). It became apparent that at these redshifts the escape fraction is likely below 10% for most galaxies, but the core of the issue lies beyond $z = 2$ where the contribution of AGN to the UV background is falling below the requirements. A number of ground-based attempts ensued to investigate the situation at redshift $z \approx 3$, where the onset of the Lyman continuum (LyC) is redshifted enough for these photons to pass safely through the Earth's atmosphere. The studies of Giallongo et al. 2002; Inoue et al. 2005; Fernández-Soto et al. 2003 have also only been able to place upper limits, with no direct detections found. The first measurement of the average escape fraction was presented in Steidel et al. 2001, using an average spectrum of a sample of galaxies at $z \approx 3.4$. Cases of direct detection of ionizing radiation were reported by Shapley et al. 2006 and Iwata et al. 2009. However, no clues that would illuminate the nature of galaxies with significant escaping LyC flux have been found. In Part I of this thesis, we describe a large spectroscopic survey where we successfully detect LyC photons from a number individual galaxies at $z \approx 3$. We were also able to address this question of which galaxies allow significant LyC flux to escape absorption by the ISM.

The interplay between galaxies and the IGM is likely going to be more noticeable in overdense regions ("proto-clusters") where future clusters of galaxies will form. It is now well established that clusters observed when the Universe was at only half of its present age ($z \approx 1$) appear to be very similar to local clusters in terms of the total mass, gas fraction and metallicity of ICM (Hashimoto et al. 2004; Maughan et al. 2004). However, a completely new phenomenon was discovered during one of the first studies of a protocluster at higher redshift : giant regions ($> 100\,\mathrm{kpc}$) of gas glowing in

Lyman α emission (Lyman α "blobs", Steidel et al. 2000). Since then, a number of other examples of giant blobs have been discovered and studied beyond $z = 2$ (Dey et al. 2005; Smith et al. 2008; Prescott 2009). As no obvious source of UV radiation responsible for the strong Lyman α emission has been found in many of the cases, the nature of the blobs continues to be a source of debate. Follow-up observations in the near-infrared and far-infrared suggest that blobs are sites of massive galaxy formation (Chapman et al. 2004). However, recent numerical simulations predict the existence of cold gas streams that feed galaxies at high redshifts (Kereš et al. 2005). Using this prediction, Goerdt et al. 2009 have proposed that the conversion of gravitational potential energy through collisional excitation of the in-falling cold gas can explain the apparent size and luminosity of Lyman α blobs. Whatever the truth may be, it is clear that the mystery of Lyman α blobs takes us right to the frontier where the IGM and star-formation meet. Part II of this thesis is devoted to further investigaton of this frontier in a survey for new cases of giant Lyman α blobs.

Throughout this work we assume a cosmology with $\Omega_m = 0.3, \Omega_\Lambda = 0.7, h_{100} = 0.7$. All optical magnitudes are given in the AB magnitude system, whereas near-IR photometry is given in Vega magnitudes.

Part I

Lyman Continuum Emission From Galaxies at $z \approx 3$

Abstract

We present a deep spectroscopic survey for detection of Lyman Continuum (LyC) in a sample of 121 star-forming galaxies at $z \approx 3$. LyC is detected in 11 galaxies, and the inferred escape fractions (f_{esc}) range between 14% and 150% under standard assumptions about shape of the stellar continuum below 912 Å and mean IGM opacity. The relative number of galaxies with LyC detection ($\approx 13\%$) in our sample is independent of UV continuum luminosity. However, we find that f_{esc} is roughly inversely proportional to UV continuum luminosity. The integrated escaping radiation from galaxies appears sufficient to complement AGN in ionizing hydrogen in the Universe.

The composite spectrum of galaxies with LyC detection reveals stronger Lyman α emission and weaker ISM absorption lines when compared to spectra of nondetections.

Using supporting near-IR and mid-IR observations we derive model SED parameters describing stellar populations for half of the galaxies in the sample, including 5 with LyC detections. Galaxies with escaping LyC are found among objects with the lowest amount of dust extinction ($E(B-V) \leq 0.1$) and star-formation rate ($\Psi_o < 58$ h^{-2} M$_\odot$/ yr) .

The average two-dimensional composite spectrogram of detected LyC shows that it is either spatially extended or otherwise not aligned with the bulk of UV continuum radiation. We also report on the first detection of molecular hydrogen absorption lines (H_2) in the UV spectra of star-forming galaxies at high redshift.

Chapter 2

Deep Lyman Continuum Survey (DLCS)

2.1 Introduction

Identifying sources of UV radiation responsible for the ionization of hydrogen in the IGM is one of the crucial steps required for further understanding of galaxy formation and evolution. In the past two decades, many attempts were made at directly observing Lyman Continuum (LyC, $h\nu > 13.6\,\mathrm{eV}$, $\lambda < 912\,\text{Å}$) radiation in galaxies, both locally and at high redshifts. Table 2.1 summarizes these attempts, focusing on the number of objects studied and the chosen observational approach, in order of increasing targeted redshift. The largest survey to date, in terms of the number of sources observed, is the imaging survey of Iwata et al. 2009. These authors presented narrow-band imaging observations (tuned to LyC in the rest frame) of 198 galaxies, members of a known proto-cluster in the field SSA22 ($z \approx 3.09$, Steidel et al. 1998). Successful detection of LyC radiation was reported for a total of 17 objects, 7 Lyman-break galaxies (LBG) and 10 Lyman α emitters. Unfortunately, imaging studies such as these provided little insight into the properties of the objects found with significant escaping LyC radiation. To investigate the nature of these LyC "leaking" galaxies, we initiated a large, high-sensitivity spectroscopic survey (the Deep Lyman Continuum Survey, DLCS), which targets star-forming galaxies at high redshift.

The Low Resolution Imaging Spectrometer (LRIS) for the Cassegrain focus of the Keck 10-meter telescope on Mauna Kea (Oke et al. 1995; Steidel et al. 2004) has played an important role in numerous studies of distant galaxies. As the very successful surveys of Lyman-break galaxies have demonstrated (Steidel et al. 1999, 2003, 2004), multislit LRIS data can be used to identify many hundreds of galaxies from a broad range in redshift ($1.4 < z < 4$), while keeping the telescope time investment moderate (less than 2 hours of integration per multiobject slit mask).

The brightest[1] LBGs at $z \approx 3.0$ have an apparent magnitude in the range $\mathcal{R} \approx 22$–23. More

[1] Not counting the rare cases of strongly lensed galaxies, for examples see Pettini et al. 2002; Dessauges-Zavadsky

Table 2.1. Review of previous surveys aimed at detecting Lyman continuum

Reference	N[a]	Redshift z	Comment
Bland-Hawthorn and Maloney 1999	1	0	Milky Way[b]
Bergvall et al. 2006	1	0.02	spectrum
Leitherer et al. 1995	4	0.02–0.03	spectrum
Deharveng et al. 2001	1	0.045	spectrum
Siana et al. 2007	21	1.1–1.5	imaging
Malkan et al. 2003	11	≈ 1.2	imaging
Fernández-Soto et al. 2003	27	1.9–3.5	imaging
Shapley et al. 2006	14	2.8–3.3	spectrum
Giallongo et al. 2002	2	2.96–3.32	spectrum
Inoue et al. 2005	2	3.10–3.27	imaging
Iwata et al. 2009	198	3.09	imaging
Steidel et al. 2001	29	≈ 3.4	spectrum
DLCS	140[c]	2.7–3.4	spectrum

[a]Number of galaxies targeted

[b]Indirect measurement based on Hα emission of high-velocity clouds (HVC); see also Putman et al. 2003.

[c]Including 4 AGN objects

representative members of LBG population have a brightness close to or below the "break" in the LBG luminosity function (L_*), which at $z \approx 3.0$ is found to correspond to $\mathcal{R} \approx 24.5$ (Reddy et al. 2008). Because of their low apparent flux, even with the benefit of a 10-meter telescope, spectra of LBGs by and large have a signal to noise (S/N) of just a few per resolution element. Taken individually, such spectra are mainly used for object classification, redshift determination, and identification of a few of the strongest spectral features.

With the addition of the blue channel LRIS spectrograph (LRIS-B, Steidel et al. 2003) in September 2000, projects demanding a spectrograph with high efficiency in near-UV and blue wavelengths (3300–4500 Å) became feasible. One of these studies, to which we will be referring to often in this thesis, has presented the first direct detection of Lyman Continuum emission in the spectrum of an individual star-forming galaxy at $z \approx 3$ (Shapley et al. 2006, S06). These authors observed a sample of 14 LBGs with LRIS in multislit mode for a total of 22 hrs, reaching an unprecedented depth in individual galaxy spectra of $3 \times 10^{-31}\,\mathrm{ergs\,s^{-1}\,cm^{-2}\,Hz^{-1}}$ at 3600 Å (3σ detection limit). This corresponds to $m_{AB} = 27.6$, which is about 15 times lower than the continuum brightness of L_* galaxies.

The DLCS survey expands on the study of S06 in several respects. First, the DLCS sample is larger by an order of magnitude, collecting observations for 121 star-forming galaxies at redshifts in

et al. 2009; Quider et al. 2009.

the interval $2.7 < z < 3.6$. Second, our sample covers a broad range in galaxy luminosity, reaching as faint as $0.2\,L_*$. Lastly, owing to existing near-IR and mid-IR photometry for more than half of the objects in DLCS sample, we were able to derive stellar population parameters and characterize the galaxies in terms of their star-formation rate, age and dust extinction. The DLCS observations result in individual galaxy spectra of unprecedented quality, and the composite spectrum of the full DLCS sample provides the most in-depth look into the high-redshift galaxies to date.

In the attempt to secure such a difficult measurement for a large sample of objects, a number of challenges in the data reduction process were encountered. Much of the discussion in this chapter will be devoted to the technical details of the data reduction process. Some of the issues addressed are specific for LRIS instrument, but the lessons learned are also of value for the design of the next generation of spectroscopic instruments.

Our investigation into the detailed nature of LyC "leakers" is presented in chapter 3. However, as we demonstrate later, the sensitivity of DLCS observations and the breath of the sample allows for many other future studies of the detailed structure of Lyman-break galaxies. For example, a cursory analysis of the deep spectra already resulted in several unexpected findings. Not only did we successfully detect LyC radiation in the spectra of a number of individual galaxies, the improved data-reduction process allowed for an observation of the spatially resolved extent of the radiation (section 3.7.2). Another interesting unexpected result is the first detection of molecular hydrogen (H_2) absorption bands in the rest-UV spectrum of high-redshift galaxies. These findings demonstrate the abundance of new information made available by our survey, which will initiate separate in-depth studies.

2.2 DLCS Sample Selection

The Earth's atmosphere efficiently blocks ultraviolet (UV) radiation with a sharp transparency cutoff preventing photons with $\lambda \leq 3200$ Å from reaching the surface. Therefore ground-based observations of LyC photons are not possible for objects with a redshift below $z \approx 2.7$.

On the other end, there is a practical upper limit in redshift for LyC detection, considering the sensitivity that can be reached by currently available instruments and 10m class telescopes. LyC measurements at redshifts higher than $z \approx 3$ become increasingly more difficult for two reasons. First, the average optical depth for absorption of LyC photons in the IGM quickly increases with redshift. Second, the night sky brightness is also progressively higher at longer wavelengths. These circumstances make measurement of LyC radiation from sources at $z > 3.6$ currently unfeasible.

Figure 2.1 shows an example spectrum of a relatively bright LBG at $z = 3.0$ ($\mathcal{R} = 24.0$), compared to the night sky brightness in the observed blue end of the optical spectrum. The night sky is more than 20 times brighter than the continuum flux at 1500 Å in the rest frame. Flux below

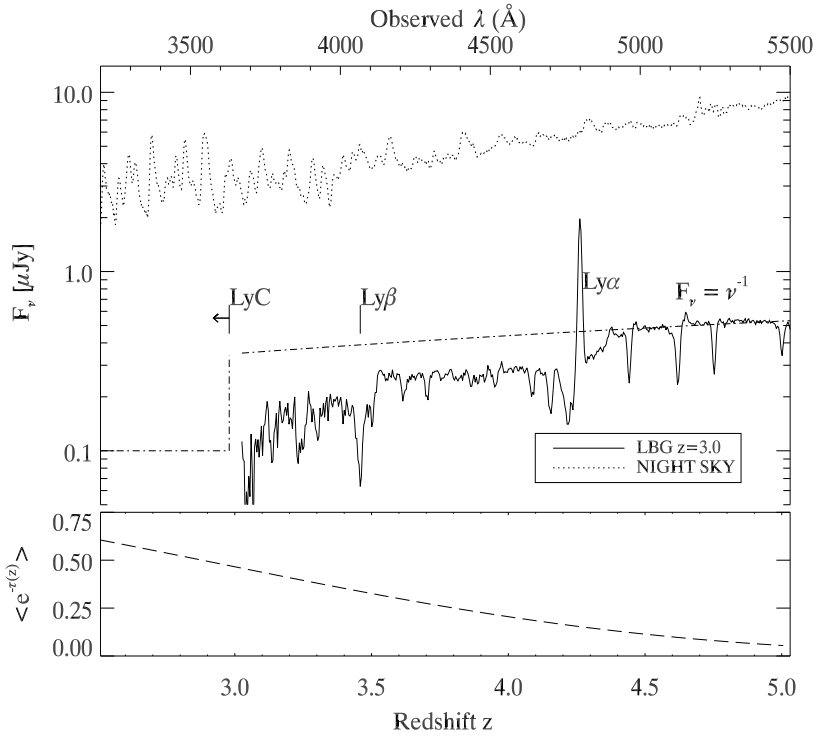

Figure 2.1 *Upper panel:* Typical night sky brightness in the wavelength range $\lambda = (3200, 5500)$ Å (dotted) compared to an example spectrum of a Lyman-break galaxy with brightness $\mathcal{R} = 24.0$ and redshift $z = 3.0$. *Lower panel:* The average IGM transparency ($e^{-\tau(z)}$) at redshifts corresponding to Lyman continuum in the observed frame.

1216 Å will suffer some attenuation by the dense clouds of neutral hydrogen in the IGM. Theoretical estimates and numerical simulations predict that the average IGM transparency (Figure 2.1, lower panel) for LyC photons decreases from about 38% at $z = 3.0$ to less than 20% at $z = 4.0$ (Madau 1995; Bershady et al. 1999; Inoue & Iwata 2008). Assuming LBGs have an intrinsic spectral slope $F_\nu \sim \nu^{-1}$ and a break in the spectrum near 912 Å ("Lyman-break") by a factor of 3 (Steidel et al. 2001; Inoue et al. 2005), the expected LyC flux coming from a LBG with $\mathcal{R} = 24.0$, will be at least 30 times fainter than the night sky flux at 3500 Å. Note that we have not included any dust extinction from the ISM in the galaxy itself, and that we assumed that all of LyC photons escape the ISM for this rough estimate. It is clear that accurate sky subtraction is a crucial data reduction step for LyC measurements. Section 2.3 will be devoted to numerous technical problems that had to be solved in order to ensure that background subtraction in the spectra is performed with minimal systematic error.

Targets for the DLCS were chosen from nine separate fields on the sky (Table 2.2). For six of the nine DLCS fields, selection of star-forming galaxy candidates using rest-UV continuum photometry was performed during the course of $z \approx 3$ Lyman-break galaxy (LBG) and $1.4 \leq z \leq 2.5$ "Redshift Desert" surveys (Steidel et al. 2003, 2004). Three additional fields (Q0100+1300, Q1009+2956 and

Table 2.2. Target fields of the Deep Lyman Continuum Sample

Field	RA (J2000)[a]	Dec (J2000)[a]	N_{obs}[b]	N[c]	N_{det}[d]	Obs. runs	ADC	t_{exp}[e](hrs)
Q0100+1300[g,i]	01:03:11.27	+13:16:18.0	15	12	0	dec06, sep07	no, yes	10.3
Q0256−000[f]	02:59:05.13	+00:11:06.8	15 (1)	11	0 (1)	nov07	yes	8.5
B20902+34[f]	09:05:31.23	+34:08:01.7	14 (1)	13	0 (0)	nov07, apr08	yes	8.4
Q0933+2854[f]	09:33:36.09	+28:45:34.8	26	21	2	mar07, apr08	no, yes	9.2, 8.2[h]
Q1009+2956[g]	10:11:54.49	+29:41:33.5	12	11	0	dec06	no	7.0
Westphal[f]	14:17:43.21	+52:28:48.5	15	15	3	june08	yes	8.5
Q1422+2309[f]	14:24:36.98	+22:53:49.6	13 (1)	12	3 (0)	apr08	yes	8.2
Q1549+1919[g]	15:51:54.75	+19:10:48.0	12 (1)	12	2 (1)	apr08, jun08	yes	8.5
DSF2237b[f]	22:39:34.10	+11:51:38.8	14	14	1	sep07, nov07	yes	12.8
TOTAL			136 (4)	121	11 (2)			

[a]Positions of the field centers.

[b]Number of $z > 2.7$ galaxies observed. Number of $z > 2.7$ AGN observed is given in parenthesis.

[c]Number of galaxies included in DLCS sample

[d]Number of galaxies (AGN, in parenthesis) with detected Lyman Continuum flux.

[e]Total exposure time

[f]Fields from $z \sim 3.0$ LBG survey Steidel et al. 2003

[g]Fields from $1.4 < z < 2.5$ "Redshift Desert" survey Steidel et al. 2004

[h]Two separate sets of DLCS targets observed in this field

[i]Also known as PHL957

Q1549+1919) were surveyed in an identical manner during the period 2004 to 2006. Photometry and catalogs of rest-UV color-selected Lyman-break galaxy candidates in these new fields were obtained using LRIS imaging data. Spectroscopic follow-up observations aimed at redshift identifications were executed during a number of LRIS multislit observing runs in the same period. We refer the reader to Steidel et al. 2003, 2004 where standard LBG color selection criteria, methods used for spectroscopic follow-up and redshift determination are described in detail.

Owing to extensive spectroscopic follow-up of LBG candidates in these fields, we were in a position to compile an initial list of several hundred star-forming galaxies within $2.7 < z < 3.6$ and $\mathcal{R} \leq 25.5$. We obtained deep spectra for a total of 136 galaxies and 4 AGN objects. However, 15 galaxies were later excluded from DLCS analysis owing to instrumental defects, object crowding or other sources of error that made Lyman continuum flux measurements less secure (see detailed description in §2.8).

We used a survey strategy that assigned highest priority to comparatively brighter ($\mathcal{R} \leq 24.5$) LBGs in a redshift interval $2.9 \leq z \leq 3.3$. Other star-forming galaxies in a broader redshift range $2.7 < z < 3.6$ were assigned lower priority. Finally, "filler" rest-UV selected targets without any previous spectroscopic followup were added if slit space was still available on a mask.

Three panels of Figure 2.2 present a comparison of apparent magnitude $\mathcal{R}$, redshift z and color $G - \mathcal{R}$ distributions between DLCS galaxies (shaded histogram) and all galaxies with redshifts $2.7 < z < 3.6$ located in these DLCS fields (solid background histogram, scaled to equal total area for clarity). The top panel of Figure 2.2 shows that the DLCS sample has a moderate excess of sources with $\mathcal{R} < 24.5$ and a related deficiency of galaxies with $25.0 \leq \mathcal{R} \leq 25.5$, which is an expected consequence of our observing strategy. The redshift distribution of DLCS galaxies also demonstrates our slight preference for targets in $2.9 \leq z \leq 3.3$ redshift "window." We find no difference in distribution of $G-\mathcal{R}$ color between DLCS and all known galaxies in these fields (Figure 2.2, bottom panel). We therefore conclude that the DLCS sample is fully representative of the LBG population at these redshifts.

2.3 Spectroscopic Observations

Deep spectroscopic observations have been collected during six separate observing runs in the period from 2006 December to 2008 June. Total on-source integration times per slit mask were between 8 and 12 hrs (Table 2.2). Observations were carried out on Keck I using LRIS in its double-beamed mode (Steidel et al. 2004). The "d500" dichroic was used to split the focused beam between two arms of the LRIS spectrograph, below and above $\lambda \sim 5000$ Å. Blue side spectrograph (LRIS-B) was configured with the 400 lines/mm grism blazed at 3400 Å. LRIS-B camera CCD detector pixels were binned by a factor of 2 along the dispersion direction at readout. This setting provided a dispersion of ~ 2.18 Å in observed frame per output pixel and $0''.135$ per pixel in the slit direction. Red side of the LRIS spectrograph (LRIS-R) was configured with a 600 lines/mm grating blazed at 5000 Å, for a dispersion of 1.28 Å per pixel (observed frame) in the dispersion direction.

Taking as a representative angular size of $0''.9$ for Lyman-break galaxies at $z \sim 3$ (Law et al. 2007), these settings would provide an observed frame spectroscopic resolution of $\Delta\lambda \simeq 7$ Å and $\Delta\lambda \simeq 5$ Å for LRIS-B and LRIS-R spectra respectively.

Data were collected under mostly photometric observing conditions and the seeing was below $1''.0$ throughout. Prior to installment of the Atmospheric Dispersion Corrector (ADC, commissioned on Keck I in summer of 2007) all observations were taken at elevations within 30° of zenith and position angle close to the paralactic in order to minimize effects of differential refraction. Commission of the ADC on Keck has greatly enhanced the efficiency of the survey, allowing us to freely choose a mask's position angle that maximizes the number of high-priority targets. Furthermore, by removing differential refraction the ADC has improved the data quality in the blue side spectrograph and enabled us to apply more robust data reduction and extraction techniques (see §2.5.4).

Individual exposure time was set to 1800 seconds, and a survey field was observed throughout the night for as long as the elevation remained relatively high and the atmospheric conditions stable.

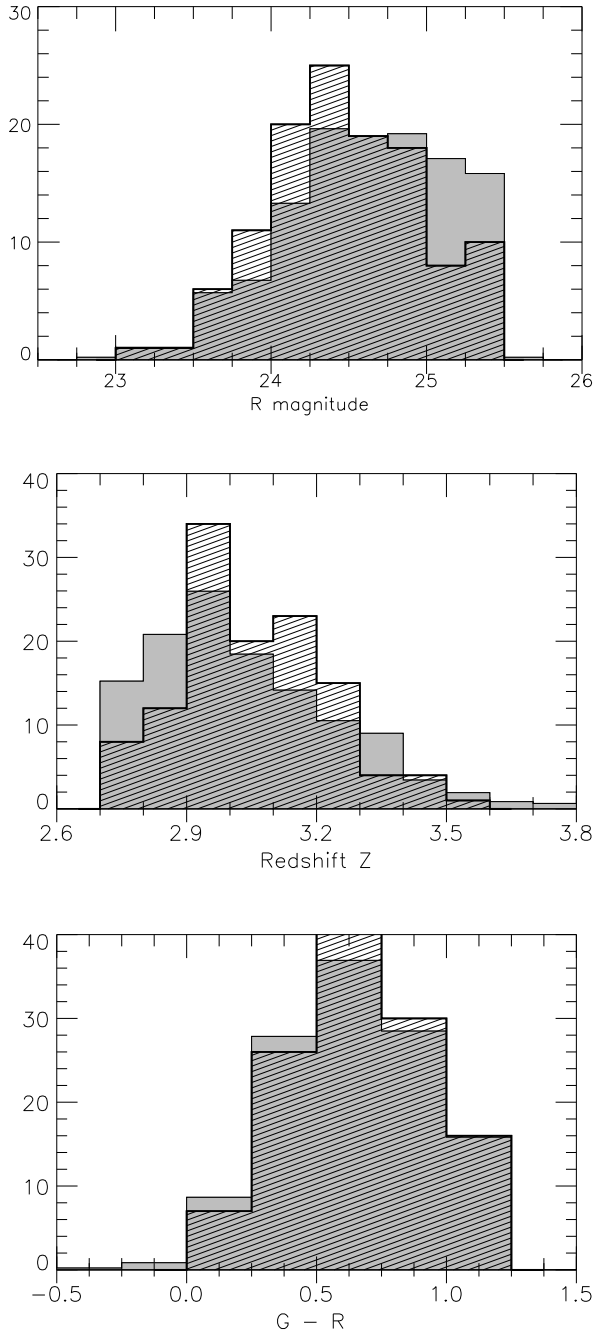

Figure 2.2 Distributions of $\mathcal{R}$ magnitude, redshift (z) and $G-\mathcal{R}$ color for the DLCS sample (shaded) and the sample of all confirmed LBGs in nine DLCS fields (gray, background). The latter histogram has been scaled to equal total area for clarity. Apart from the slight preference for brighter objects ($\mathcal{R} \leq 25$) and for objects at redshift $z \approx 3.0$, the DLCS sample is not significantly biased with respect to LBG population.

About a half of our masks were completed (with at least 8 hrs total integration) during a single multi-night observing run, with the other half having observations split between two separate observing runs (Table 2.2).

All masks were designed with $1\farcs2$ wide slits. Individual slits lengths varied between $10''$and $30''$, with a median of $20''$. We commonly observed one DLCS slit mask per survey field, containing between 8 and 15 galaxies at redshifts $2.7 < z < 3.6$. An exception is the field Q0933+2854 where two masks were observed. The first mask in Q0933+2854 contained 15 DLCS sources and was observed in March 2007 with total exposure time of 9.2 hrs. The second mask in this field was observed in April 2008, with 13 DLCS sources accumulating a total exposure time of 8.2 hrs. Two sources (D20 and MD75) were placed on both the 2007 March and 2008 April masks, accumulating a total exposure time of 17.4 hrs.

Combined LRIS-B and LRIS-R spectra for all but a few sources cover the range 3200–7600 Å in observed frame. The start of the wavelength range covered by LRIS-R is for most sources close to the rest frame Lyman α (1215.6 Å). At longer wavelengths our primary interest was in accurate measurement of equivalent width (EW) of absorption or emission features, and in estimating average continuum flux. The higher spectral resolution setup of LRIS-R (600 lines/mm grating) was chosen as better spectral sampling is advantageous for more accurate measurements of line equivalent width. On the other hand, LRIS-B setup was geared toward high sensitivity and robust estimation of flux in the Lyman continuum, so a configuration providing maximum spectrograph efficiency at shortest wavelengths was applied.

We have obtained spectroscopic flat field calibration images for LRIS-R and LRIS-B separately. Internal halogen lamp spectrum provides ample signal for flat fields at all wavelengths recorded by LRIS-R. Twilight sky observations were necessary for flat fields of the very blue LRIS-B coverage (§2.5.1). Internal arc lamp spectra (Hg, Ne, Ar, Zn, Cd) were used for wavelength calibration of both sides of the spectrograph. Spectrophotometric standard stars were observed once each night through a long slit of $1\farcs0$ width and configuration settings identical to mask observations.

We caution the reader that absolute flux calibration uncertainties in multislit spectroscopy are often of the order of $\sim 20\%$. Varying photometric conditions during long exposure sequences, slit losses resulting from differing source angular sizes and mask alignment errors are all hard to properly account for. Standard star observations used for flux calibration are typically performed once per night, and with a different slit mode ("long slit"), incurring an absolute flux error that is also difficult to estimate. However, errors in absolute flux calibration do not influence our goal of estimating LyC escape fraction, since in its derivation we use a normalization with respect to rest-UV continuum flux.

2.4 Data Reduction

In this section we present an overview of the standard data reduction approach which has been used, up to the present, to process data from both the red and blue side of LRIS spectrograph. The design of the standard data processing pipeline used in the LBG and $z \sim 2$ surveys (Steidel et al. 2003, 2004) was geared more toward streamlining the multislit spectroscopy data reduction than toward high-sensitivity measurements. We will use this overview to point out segments of the data reduction process where we identified sources of statistical or systematic error. The focus will be on data obtained with the blue side (LRIS-B) spectrograph as it plays a crucial role in the DLCS.

The red side spectrograph (LRIS-R) has a completely separate set of light-dispersing elements and CCD detectors and therefore requires a separate evaluation of sources of error. Additionally, the longer wavelength range observed with LRIS-R presents a different set of challenges in data reduction which are not a concern for the blue side data. Nevertheless, this thorough reevaluation of the performance of the standard LBG spectroscopy pipeline for LRIS-B data may serve as a good guideline for future improvements of data reduction process designed for LRIS-R as well.

After bias subtraction and CCD gain correction, raw multislit science and calibration frames are cut along rectangular sections that contain the trace of each slit in the mask. Further processing is then performed on individual two-dimensional spectrograms rather than the full multislit frame.

In the standard data reduction pipeline, no image rectification (or resampling) is applied to correct for the curvature of the single slit trace on the CCD, so cutting up the full frame along rectangular regions incurs an small but notable decrease of available slit length. Section 2.5.2 describes a practical partial image rectification method we implemented for cutting of multislit frames that will greatly simplify subsequent data reduction and extraction tasks while preserving original pixel values.

Following the cut up, all science observations are corrected for the pixel-to-pixel variation in response to photons of a given wavelength ("flat fielding"). This step is crucial for high sensitivity measurements, as one can observe a sharp increase in pixel response variation below 4000 Å for LRIS-B detector. We will discuss the improvements to the flat fielding task that we implemented in Section 2.5.1. We also discuss adverse effects of stray scattered light in the spectrograph, as it is closely related to problems encountered in the flat fielding process.

Owing to limitations in the slit-milling technology, slits can have small but sharp, sudden changes in their width. These can create variation in illumination along the slit direction on the order of $\sim 1\% - 2\%$. From our experience about 10% of the slits milled will have these defects, but sometimes this fraction can be much higher. In §2.5.3 we present a way of implementing a slit-illumination correction which was not performed in the standard data reduction.

Cosmic rays are identified using IRAF's *szap* procedure. Pixels contaminated with cosmic ray

flux are recorded and excluded from further processing using pixel masks.

In the standard pipeline, night sky flux is modeled and subtracted by an iterative polynomial fit in the spatial direction at each dispersion point. The order of the fit used is determined based on slit length, varying from order 3 to order 5 for slit size range $\sim 10''$ to $\sim 20''$. Following background subtraction, individual science exposures are registered, both spatially and in wavelength, and averaged. IRAF task *apall* is used to determine the object trace in the two-dimensional spectrogram and extract a one-dimensional spectrum.

The new data pipeline works with rectified slit images as mentioned above. This improvement also enabled a background subtraction step that includes source masking (§2.5.5). Additionally, we made one dimensional spectrum extraction more robust by eliminating the need for object self-tracing (§2.5.4).

Wavelength solutions are determined from arc spectra extracted along an identical trace curve in the corresponding arc observations. Extinction correction and flux calibration are determined from long-slit observations of a spectrophotometric standard.

2.5 Improvements in LRIS-B Data Reduction

2.5.1 Scattered Light and Flat Fielding

At wavelengths above the atmospheric transparency cutoff ($\geq$ 3200 Å), the efficiency of LRIS-B triples in value from $\sim 17\%$ at $\lambda = 3300$ Å to $\sim 50\%$ at $\lambda = 4000$ Å. Because of this, a bright source of UV light is required to create a good flat field image, and an observation of the twilight sky is commonly used for the purpose. In practice however, to get sufficient counts in near-UV one must set the twilight sky exposure time long enough that the counts observed at optical wavelength rise close to (or above) pixel saturation. This approach inadvertently increases the number of potential stray photons, in the wavelength range where the efficiency of detection is higher. The wavelength range from 3200 to 4000 Åis especially sensitive to accurate flat fielding correction and crucial for measurements of LyC flux.

Extensive tests were performed during several LRIS observing runs established that stray light in the spectrograph can be present at a level detectable by the LRIS-B CCD. Further in this text we will refer to image artifacts caused by scattered light as "ghosts." Unfortunately, stray light "ghosts" are especially apparent in twilight sky observations, when the sky is much brighter than in the science exposures taken during the night. If they remain hidden in twilight images used for flat field correction, ghosts can adversely affect the data in science frames as well. An example of a two-dimensional spectrogram used as a flat field by the standard pipeline is given in Figure 2.3. Scattered light is clearly seen below 3400 Å. As the detected sky counts even in half-hour long exposures are comparatively low, no significant scattered light in science exposures could be observed.

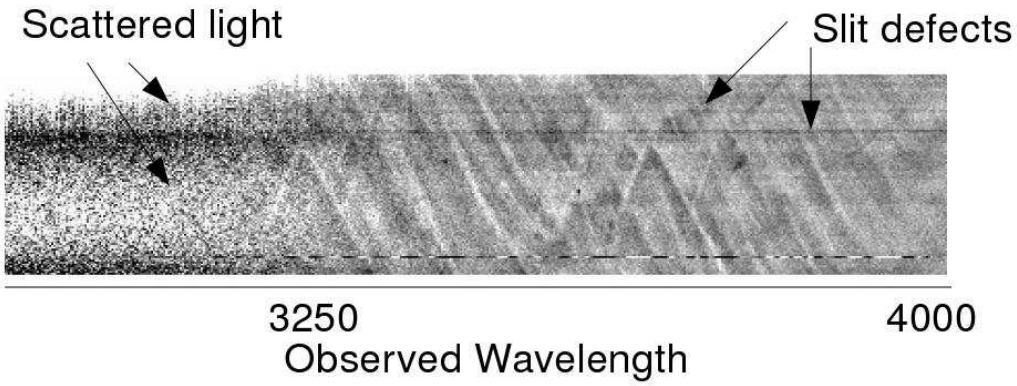

Figure 2.3 An example of a two-dimensional spectrogram created from a twilight sky observation and used as a flat field in the standard data reduction. Strong variation in pixel sensitivity is apparent in the range 3250–4000 Å. Note that the scattered light can be seen affecting the flat field longward of 3250 Å. Darker "streaks" caused by slit milling defects are also noticeable.

We adopted an improved observing strategy for twilight sky flat field. Composite twilight sky observations were created from exposures taken with and without the inclusion of the U_n filter in the multislit setup. The U_n filter has a transmission cutoff above $\sim$ 3900 Å and efficiently blocks the appearance of "ghosts" coming from stray light at longer wavelengths. With the addition of U_n filter in LRIS-B beam we are able to safely obtain longer twilight sky exposures that achieve a high signal to noise below 3900 Å. These images are then combined with shorter exposures taken without the U_n filter in the beam to create a composite twilight spectrum that has high signal to noise throughout the range 3200–5000 Å detected by LRIS-B. After continuum normalization, this composite twilight sky observation can be used to flat field the science data without introducing scattered light artifacts.

2.5.2 Image Rectification

We have included a simple image rectification scheme during cut up of individual slits in our improved LRIS-B data reduction approach. By instrument design the slit direction and pixel rows on the CCD are approximately aligned, for slits with the position angle equal to the position angle of the multislit mask. We have used a modification of the XIDL task *long_slitmask* (Prochaska & Hennawi, private communication[2]) to delineate the individual spectrograms in the multislit image. This task determines the position of slit edges in regular intervals in the dispersion direction, and then fits a third-order polynomial curve. This fit can be used to shift the CCD image rows and spatially align pixels at every dispersion point. Constraining the shift to be an integer amount of pixels, the spatial position of pixels along a given column will be equal to within $0\farcs135$ (1 pixel in LRIS-B). The two-dimensional spectrogram obtained will still be rectangular, but with the benefit that the

[2]A version of the XIDL package is available at http://www.ucolick.org/~xavier/IDL/index.html

wavelength and spatial direction are crudely aligned with columns and rows.

After the installation of the ADC, another benefit of the single slit spectrograms rectified in this way is that the spectrum trace of an object can be well approximated by a simple straight line in the dispersion direction.

Compared to proper image rectification, which demands two dimensional wavelength solutions and pixel resampling, this approach is favored since it preserves original flux counts in the data.

2.5.3 Variations in Slit Illumination

Imperfect milling of slitlets in the multislit mask can create an appearance of uneven slit illumination in the spatial direction ("slit function"). This slit function will also incorporate any intrinsic illumination gradients from vignetting present in the spectrograph field of view. During the course of several observing runs, we found that slit milling defects frequently cause irregular spatial variations in the background intensity at $\sim 1\% - 2\%$ level. Typical examples of the appearance of slit-milling defects are shown in Figure 2.3. This can cause problems for background fitting task, which attempts to model the background with a smooth polynomial curve. As a result, small systematic deviation from zero mean can remain in the background-subtracted images. In short exposures this problem can easily go unnoticed, as other sources of random error are dominant. However, its systematic influence becomes clear in the average of many hours of LRIS-B exposures.

Custom procedures in IDL were developed to correct for variation in slit function that is affecting science and calibration exposures equally. The slit function can simply be obtained from rectified two-dimensional spectrograms (§2.5.2) as a vector of values equal to a clipped average of pixels in the dispersion direction, normalized to a unit median. We determine the slit function in this manner using the same observations of twilight sky used in deriving the flat field correction. The illumination correction is performed on all science and calibration exposures.

2.5.4 Atmospheric Dispersion Correction and Object Tracing

Prior to deployment of the ADC the trace of an object spectrum would differ from the trace of its slit edge by an amount determined by atmospheric dispersion. Exact value of this apparent spatial shift in source position is dependent on wavelength, effective airmass and atmospheric conditions (temperature, pressure, water vapor pressure) at the time of observation. In the course of DLCS survey, both prior and after installation of the ADC, it was necessary to work with a single multislit mask at wide range of air masses. As a consequence, individual exposures of the same source could not be spatially registered at all wavelengths simultaneously. The difference in the apparent spatial position of the object can be of the order of $1''$ ($\approx$ 7–8 LRIS-B pixels).

We developed an approach that deals with this problem in data reduction of DLCS data taken

prior to 2007 September. Using the atmospheric dispersion model of Filippenko 1982 we predict the value of the apparent offset between the object trace and slit edge as a function of wavelength. We would then implement this additional shift during the slit rectification step, and again obtain two-dimensional spectrogram in which objects have a straight line trace as a result. Tests performed on observations of bright sources demonstrated that using values of average atmospheric conditions for a given night at Keck Observatory provided sufficient precision in predicting the shift caused by atmospheric dispersion. After September 2007, the ADC removes the atmospheric dispersion shift.

Another benefit of using rectified images is in eliminating the need for object self-tracing during extraction of the one-dimensional spectrum. This provides additional accuracy for spectrum extraction at wavelengths where the object has very low detected signal.

2.5.5 LRIS-B Background Subtraction

Once careful slit illumination and flat field correction are applied (§2.5.3 and §2.5.1), a low-order polynomial becomes a much more adequate approximation of night-sky brightness in the slit direction. The accuracy of the background fit will depend to a large extent on the particular number of "clean" sky pixels that receive no light contribution from objects detected. However, our experience show that the number of clean pixels has a principle limitation determined by source crowding, an important consideration consideration in observations reaching sensitivities close to $\mathcal{R} \sim 28.0$.

During DLCS mask design we would assign slit lengths $\geq 15''$ to our high priority targets, and $\geq 10''$ for lower priority targets. A majority of the slits included serendipitous sources detected in the vicinity of the primary target. In fact, after combining ≥ 8 hrs of LRIS spectroscopic observations the sensitivity is high enough to clearly detect spectra of all sources seen in our deepest ground-based broadband G or Rs images within the slit footprint. Imaging observations of these fields typically have 1σ limits of $G \sim 28.5$ and $\mathcal{R} \sim 28.0$ (for a $2''$ diameter photometric aperture, see Steidel et al. 2003, 2004). Using faint object positions from deep imaging, we were in a position to exclude all pixels that could be registering photons other than night sky emission from the background fit.

Background subtraction is performed in two stages. First-pass background subtraction uses object masks created from sources with significant detections in single short LRIS-B exposures. In the second stage we would compare the stack of resulting two-dimensional spectrograms with broadband imaging and mask additional slit regions containing any source visible in the images. An iterative fit with a polynomial function of order 2 to 4 is used to determine the final background which is subtracted from observations.

2.6 A Test of Systematic Errors

In this section we present an example of the performance of the improved data reduction process. Most importantly, we test for the presence of residual systematic errors in background subtraction. We investigate this by creating an average two-dimensional spectrum for a set of very deep LRIS-B observations.

Fully processed, background-subtracted two-dimensional rectified spectrograms for a sample of 10 Lyman-break galaxies from DLCS were wavelength calibrated and resampled onto a common wavelength grid. Before the spectrograms are averaged, all pixels detecting flux other than the night sky are masked. The effective exposure time for this composite is ~ 100 hrs, so the sensitivity is several times higher than in the deepest single object exposures we obtained.

The resulting average spectrogram is shown in Figure 2.4, and histograms of counts per pixel in two wavelength regions are presented in Figure 2.5. The noise increases towards shorter wavelengths, as expected due to lower LRIS-B sensitivity, but we could not find any residual systematics that would be related to spatial or wavelength direction. The observed noise in the composite can be accounted for with photon-counting statistics and read-out noise.

As a second test, we recreate the composite spectrum but this time we do not mask the flux of the target galaxy, and spectrograms are registered according to slit position of the target. The resulting two-dimensional composite is presented in Figure 2.6. This composite spectrum is used to test for systematic error related to the position of the target object on the slit.

Contrary to random error, any systematic error should become more prominent as we average more of high sensitivity spectrograms. We find that the noise distribution in this composite is less regular, indicating that night sky counts were not perfectly removed during background subtraction. We conclude that some residual systematic error correlated with the position of the brightest object in the slit remains. However, when we look at the magnitude of residual deviation from zero, given in Figure 2.7, we see that it is comparable to the statistical error.

2.7 Data Reduction: Concluding Remarks

We presented an overview of the improvements made to the data reduction procedure used in surveys of Steidel et al. 1999, 2003, 2004. A number of sources of statistical and systematical error were examined.

Scattered light in the instrument was observed to be present at a significant level in twilight sky exposures, which were previously used for creating a flat field correction. A new observing strategy is developed that provides flat field calibration free of scattered light artifacts. It requires observing the twilight sky with two instrument configurations. One observation is taken with the dispersion

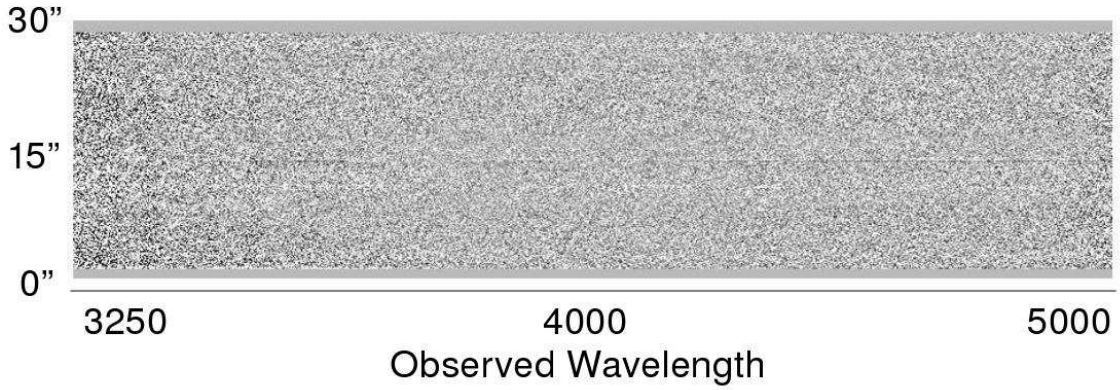

Figure 2.4 A two-dimensional composite spectrogram of 10 galaxies from DLCS reduced with the new pipeline. All objects are masked during averaging so that only clear night-sky slit regions remain. No residual systematic effects are seen as a function of slit position or wavelength.

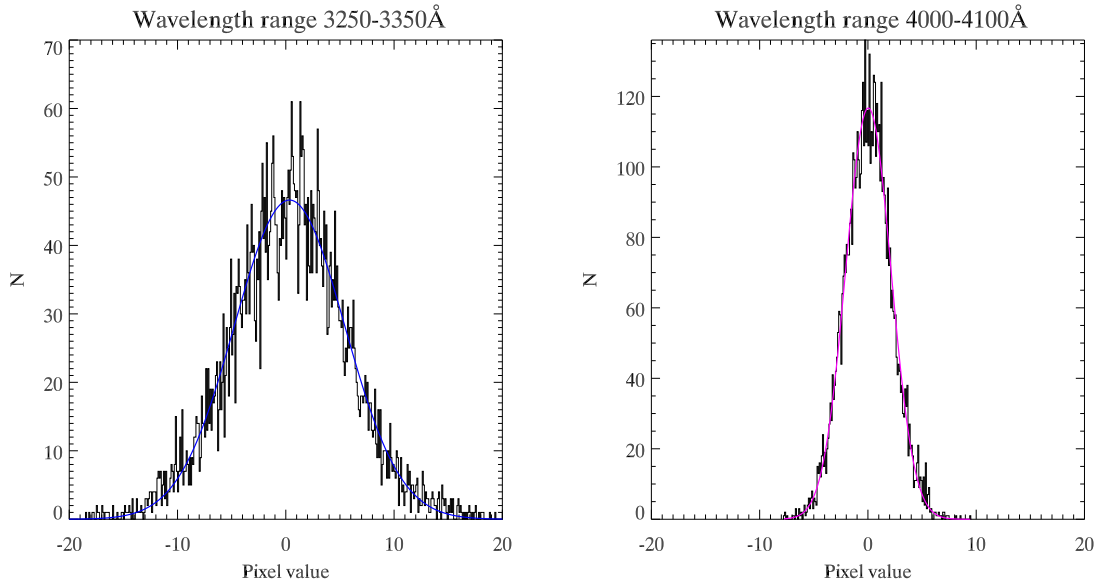

Figure 2.5 Histograms of counts per pixel in selected wavelength regions of a two-dimensional average of background-subtracted night sky shown in Figure 2.4. The distributions are in excellent agreement with pure Gaussian noise with a zero mean.

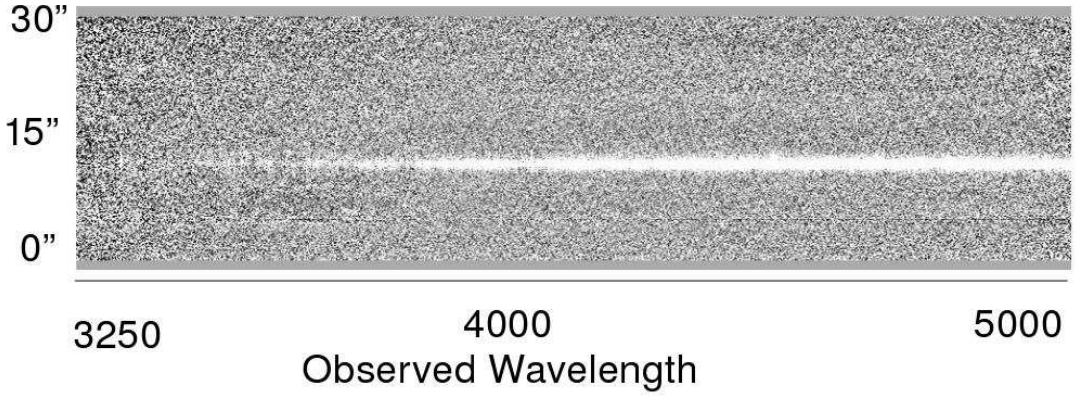

Figure 2.6 A two-dimensional average spectrogram of 10 galaxies from DLCS reduced with the new pipeline. Spectrograms were registered in wavelength and position of the target galaxy before averaging. The residual background fluctuations are stronger than what is observed in Figure 2.4, where spectrograms averaged were registered to slit centers. The bright white trace close to slit coordinate 10″and spanning wavelength range 3350–5000 Å is the average of target galaxy spectra.

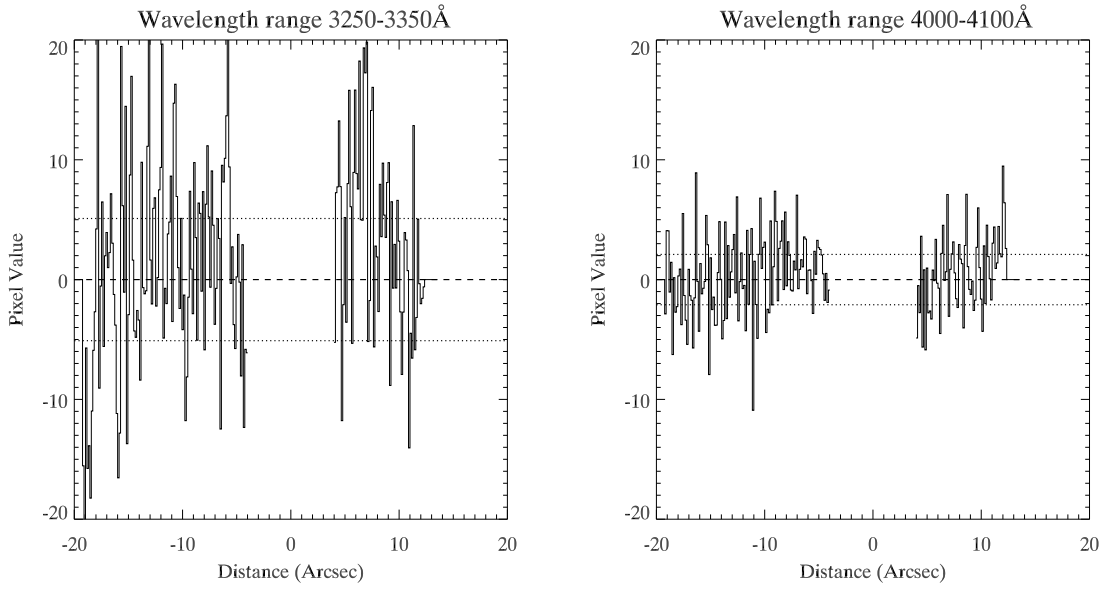

Figure 2.7 Histograms of mean counts per pixel in selected wavelength regions from a two-dimensional background-subtracted composite spectrum shown in Figure 2.6. Pixels within 4” of the object position are excluded. Dotted lines show $\pm 1\sigma$ of Gaussian noise distribution from Figure 2.5. It is apparent that systematic fluctuations remaining are comparable in magnitude to random noise.

setup as intended for science exposures, whereas the other twilight frame is taken with addition of U_n filter in the optical path. The inclusion of the filter allows for longer twilight exposures that provide good count statistics at near-UV wavelengths without contamination by scattered longer wavelength light.

We also presented a simple image rectification scheme that greatly facilitates latter data processing. Slit edges in a multislit spectrogram are traced, and rectification is performed by shifting the pixel columns according to the fitted curve. This rectification also enabled implementation of slit illumination correction, which becomes necessary for high-sensitivity measurements. Slit illumination function can be very irregular due to physical slit defects, making a smooth background fit incur a significant systematic error. The spectrum trace in rectified images follows a straight line, which eliminates the need for object self-tracing, and makes faint object masking a lot easier.

Very deep composite two-dimensional spectrograms have been used to evaluate the quality of background subtraction as a function of slit position, wavelength, and distance from target. We found only a small residual systematic in the composite spectrogram registered according to target position. However, we demonstrate that a good estimate for this residual systematics is the value of the total statistical error, which can be used as a guideline for high sensitivity measurements with LRIS-B in the future.

2.8 Notes on Individual Survey Fields

The the total number of $2.7 < z < 3.6$ targets per survey field is given in column four (N_{obs}) of Table 2.2. After completion of data reduction we have eliminated a total of 15 galaxies from the sample. Our primary concerns were whether any instrument specific defects or object properties might compromise the accuracy of flux measurement in the Lyman continuum. The following three elimination criteria are used:

1. Instrumental defects are apparent in the two-dimensional spectrograms. We discussed earlier in the text our examination into adverse effects that "ghosts" (section 2.5.1 or unrepairable slit illumination irregularity (section 2.5.3) can have on flat fielding and background subtraction. We exclude objects where any such defects are present at pixels below 912Å in the rest frame.

2. The target galaxy might have another object in such proximity that the flux of the two can not be confidently separated during extraction the spectrum.

3. A galaxy is revealed to be a spectroscopic "blend" of non-related objects along one line of sight. Often, no overlapping sources were apparent in the broad band images, but we could securely identify more than one set of high-redshift galaxy absorption lines at significantly different cosmological redshifts. For an example, see Figure 2.8.

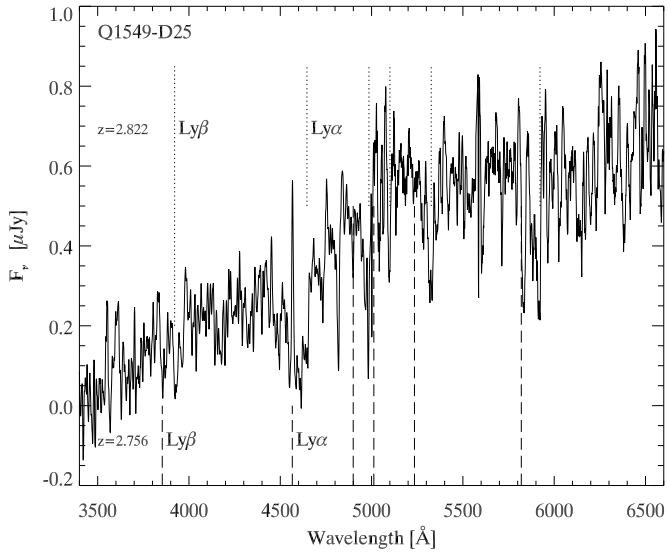

Figure 2.8 Spectrum of object Q1549-D25 identified as a spectroscopic blend of galaxies with $z = 2.755$ and $z = 2.822$. Most prominent spectral features at the two redshifts have been marked. Both galaxies show clear Lyman α (the lower redshift one in emission) and Lyman β lines. Several of the strongest ISM absorption lines at the two redshifts can also been seen.

The number of applicable objects per field is presented in column five of Table 2.2. These DLCS spectra are presented in Figures A.1 to A.30 of the appendix. We proceed with the discussion of slit-mask configuration and object properties in individual fields below.

2.8.1 Objects in the Field Q0100+1300

This field is centered on the background quasar Q0100+1300, (PHL 957, $z = 2.686$). It is one of the three additional survey fields for Lyman-break and $z \sim 2$ BX/BM galaxies, which was observed after the completion of the studies published in Steidel et al. 2003, 2004. As of this date, a total of 31 LBGs and 103 BX galaxies have been spectroscopically confirmed in this field.

In this field we obtained spectra of 15 galaxies $2.7 < z < 3.6$ with integration time split equally among two separate observing runs. We collected 5.2 hrs effective LRIS integration in 2006 December with another 5.1 hrs added in 2007 September (Table 2.2). The latter observing run had the benefit of the newly installed ADC on Keck. Data was reduced separately for each of these runs and spectra were resampled to a common wavelength grid and averaged.

Two-dimensional spectrum of galaxy Q0100-C1 ($R = 24.02$, $z = 3.443$) contained a serendipitous source featuring a relatively bright, spatially resolved emission line (likely Lyman α at $z = 2.21$) and a very faint continuum. Observed wavelength of this Lyman α line corresponds to 878Å in rest frame of C1. Though the spatial separation of the two sources is $1.5''$, we have conservatively excluded C1 from the final DLCS sample. Object Q0100-D16 has a close companion object at a distance

of $\sim 1.7''$. It has also been excluded from DLCS owing to concerns of contamination of the LyC measurement. Object Q0100-BX268 had significant scattered light artifacts in its spectrum and was therefore not included in DLCS sample.

The spectra of remaining 12 galaxies are presented in the appendix, Figure A.11 to A.14.

2.8.2 Objects in the Field Q0256−000

This field is centered on a QSO Q0256−000 ($z = 3.364$) and was part of the $z \sim 3$ survey described in Steidel et al. 2003 (see also Adelberger et al. 2003).

Four out of fifteen galaxies targeted were rejected after spectroscopic observations were completed. Galaxy Q0256-d9 (z=2.849) was eliminated due to presence of a scattered light "ghost" in the flat field (caused by one of the mask alignment boxes). Objects Q0256-d4 and Q0256-m11 were identified as spectroscopic blends after careful examination of their spectra. In Q0256-d4 ($z = 3.67$) we also found an emission line at $z = 2.63$ which we identify as Lyman α based on matching low-ionization absorption lines. Similarly for object Q0256-m11, we find two emission lines which are identified as Lyman α at $z = 2.19$ and $z = 3.09$.

The 2-dimensional spectrum of target Q0256-md34 revealed a previously unknown Lyman α Blob at z=1.870. The spectrum of the blob also reveals prominent C IV and He II emission lines (Figure 2.9). Interestingly, both of these lines appear to be spatially extended over $\sim 2.5''$. The Lyman α line as observed in the 2-dimensional spectrum extends over $4.5''$, or $\sim$ 40kpc at the object redshift. We will discuss this object in more detail in Chapter 4 devoted to Lyman α blobs, but because of flux contamination we exclude Q0256-md34 from the DLCS.

The observation of object Q0256-m9 led to a serendipitous discovery of a companion galaxy with an identical redshift (separated by $3\farcs5$). We present the spectra of the objects as Q0256-m9ap2 and Q0256-m9ap3.

One AGN source, c31 ($z = 3.087$), was included on this mask, and its deep LRIS spectrum is presented in the top panel of Figure A.31. Of note is a detection of rare N IV] 1486 Åemission line, similar to that seen in objects described in recent work by Glikman et al. 2007; Jiang et al. 2008; Vanzella et al. 2009; Raiter et al. 2009

The spectra of 11 galaxies from Q0256−000 are presented in the appendix, Figure A.14 to A.17.

2.8.3 Objects in the Field B20902+34

This field is centered on a famous radio galaxy B20902+34 ($z = 3.392$, Lilly 1988) and was a part of $z \sim 3$ LBG survey. A total of 8.4 hrs of integration were obtained in 2007 November and 2008 April, both of which had the added benefit of the ADC on LRIS.

Only one object from the initial list of 13 galaxies in this field was rejected after data reduction

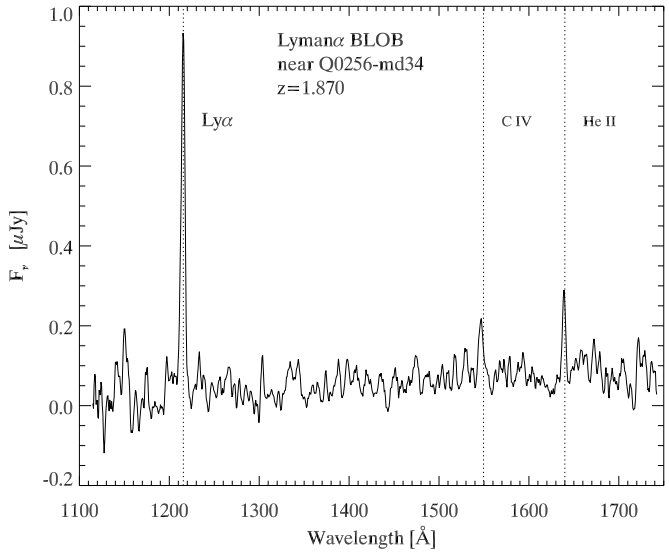

Figure 2.9 Spectrum of Lyman α Blob ($z = 1.870$) serendipitously discovered in the observation of Q0256-md34. Spatially extended emission is seen in both C IV 1549 and He II 1640 emission lines

was completed. The spatial position of Lyman-break galaxy B20902-M2 ($z = 3.054$) coincided with a slit defect, which was not repairable by slit illumination correction.

The slit position used for object B20902-MD27 has revealed a very close companion galaxy with a similar redshift (separated by $2''$). We extract the two components separately, as objects B20902-MD27ap1 and B20902-MD27ap2, and determine redshifts $z = 2.897$ and $z = 2.902$. Since their redshift is so close the possible contamination of LyC flux is not going to significantly affect our conclusions, we include both galaxies in the DLCS sample. As we show later, neither of these is found with a significant detection of LyC.

The spectrum of LBG candidate B20902-M3 ($z = 3.025$) shows high-ionization emission lines indicative off AGN activity (Figure A.31), so it is not included in the galaxy sample.

The spectra of 13 galaxies from Q0256−000, including separate entries for B20902-MD27ap1 and B20902-MD27ap2, are presented in the appendix, Figure A.1 to A.4.

2.8.4 Objects in the Field Q0933+2854

This field is centered on a$z = 3.428$ QSO and was included in the $z \sim 3$ LBG survey. The observations were taken during two separate observing runs, with two different slit-masks (labeled L2 and L3) containing a total of 26 targets for the DLCS sample.

A total of 9.2 hrs LRIS exposure was obtained in 2007 March for 15 targets on the first slit-mask. The second slit-mask was observed for 8.2 hours in 2008 April, and it contained two sources from the first mask (Q0933-MD75 and Q0933-D20). These spectra are are therefore the deepest individual

LBG observations to date.

Five targets were rejected after reduction of the spectroscopic observations for both masks was completed. Galaxies Q0933-C45 ($z = 2.888$) and C28 ($z = 2.921$) were affected by scattered light "ghosts" in LRIS-B data. Two more galaxies, Q0933-M23 ($z = 3.271/3.380$) and Q0933-M18 ($z = 3.02/3.22$) were eliminated as both are found to be cases of two galaxies blended along same line of sight. Source MD47 appeared blended in our data with a lower redshift source, which could possibly contaminate its LyC measurement.

Object Q0100-D16 has a very peculiar spectrum, with a strong Lyman α emission line but almost a total absence of strong ISM absorption lines. Lyman β absorption is present, confirming its redshift as determined by Lyman α, but is is unusually weak. This object will be discussed in Chapter 3 as it is found to be the strongest LyC emitter.

The spectra of 21 galaxies from masks Q0933_L2 and Q0933_L3 are presented in Figures A.17 to A.22.

2.8.5 Objects in the Field Q1009+2956

This is the second of the new fields surveyed for Lyman-break and $z \sim 2$ BX/BM galaxies. It is centered on a QSO at a redshift $z = 2.639$. A total of 132 high-redshift galaxies in this field have been spectroscopically confirmed to date, including 7 BM, 82 BX and 43 LBGs.

Out of 12 targets observed in this field we found one case, galaxy Q1009-C41, having a superposed spectrum with $z = 3.645/3.632$. The spectra of remaining 11 galaxies are presented in Figures A.22 to A.25.

2.8.6 Objects in the Field Westphal (GWS)

This field includes the famous "Groth-Westphal Strip" (or GWS) of the deep HST/WFPC2 mosaic pointing, and was a part of both $z \sim 2$ and $z \sim 3$ surveys for rest-UV selected star-forming galaxies (Steidel et al. 2003, 2004). Data obtained for all 15 initial targets in this field was included in DLCS, and the spectra are presented in Figures A.7 to A.11.

2.8.7 Objects in the Field Q1422+2309

This field is centered on the gravitationally lensed $z = 3.620$ QSO, and the LBG survey observations are described in Steidel et al. 2003. All 12 LyC targets observed in this field were included in DLCS, and their spectra are shown in Figures A.7 to A.11. The observations included a QSO Q1422-d59 $z = 2.833$, whose spectrum is shown in Figure A.31.

2.8.8 Objects in the Field Q1549+1919

Field centered on QSO 1549+1919 $z = 2.843$ is the third additional LBG and BX/BM survey field, with initial observations described in Adelberger et al. 2006. A total of 180 redshifts have so far been spectroscopically determined for 102 BX objects and 78 LBGs.

The spectrum of galaxy Q1549-D25 clearly reveals it as case of spectroscopic blending (Figure 2.8 with ISM absorption redshifts of $z = 2.755$ and $z = 2.822$. We have also included into our observations the QSO Q1549-D10 ($z = 2.916$, Figure A.31), for which Adelberger et al. 2006 have reported a possible detection of fluorescent Lyman α emission coming from a DLA at $z = 2.842$.

The 12 galaxies from Q1549+1919 included in DLCS are presented in Figures A.26 to A.28.

2.8.9 Objects in the Field DSF2237b

Imaging observations and spectroscopic follow-up observations of the field DSF2237b have been described in the LBG survey (Steidel et al. 2003). All 14 galaxies observed in this field were included in DLCS. Their spectra are shown in Figures A.4 to A.7.

2.9 Measurements of the Systemic Redshift

In this section we provide further detail on the determination of systemic redshifts from DLCS spectra (appendix A). Owing to the good signal to noise achieved, we were able to identify and measure a number of low-ionization and high-ionization ISM absorption lines in individual spectra. Low-ionization absorption lines such as Si II λ1260, O I λ1302 + Si II λ1304, C II λ1334 are easily identifiable in a large majority of spectra. In addition we typically can find high-ionization ISM metal lines Si IV $\lambda\lambda 1393, 1402$, C IV $\lambda\lambda 1548, 1550$.

The most prominent feature in all spectra is the Lyman α line, seen in emission or absorption, accompanied with strong Lyman β absorption. It has long been recognized that low-ionization resonance absorption lines from the ISM and high-ionization ISM metal lines are observed at significantly lower velocity than the nebular emission lines (e.g., as determined from Hα emission line of HII regions). Lyman α on the other hand also has a significant velocity offset, but where the ISM appear blue-shifted, Lyman α by rule is seen at a higher velocity with respect to the systemic redshift. Therefore, it was necessary to apply a correction between redshfits determined from ISM absorption and Lyman α emission to the systemic redshift before attempting a measurements in Lyman continuum region of the spectra.

Best-fit transformations described in Adelberger et al. 2005 are reproduced here for clarity. For galaxies with both Lyman α emission and interstellar absorption, we apply:

$$z_{neb} = z_m + 0.070\delta z - 0.0017 - 0.0010(z_m - 2.7), \tag{2.1}$$

where $z_m = 0.5 \times (z_{Ly\alpha} + z_{abs})$ is the mean redshift as determined from Lyman α and ISM absorption lines, and δz is their difference $\delta z = z_{Ly\alpha} - z_{abs}$.

If no prominent Lyman α emission appears in the spectrum, we use the transformation:

$$z_{neb} = z_{abs} + 0.0022 + 0.0015(z_{abs} - 2.7). \tag{2.2}$$

Without deep spectroscopic observations, it would not be possible to derive systemic redshifts as securely as presented here, where identification of ISM absorption lines was possible for all galaxies.

Another major concern for deep LyC surveys is contamination by foreground objects. As discussed in the previous section (§2.8) we found a number of objects which were revealed as line-of-sight blends only after examination of the deep spectra. Based on galaxy number counts in the U band, Siana et al. (2007) estimate that the fraction of $z \sim 3$ galaxies that would have foreground contamination ($0 < z < 3$) within $0.5''$ radius is about 2%. We have found the incidence of such cases to be significantly higher, with 7 blended objects out of 136 galaxies observed (5%, including the blend of Q0256-md34 with the $z = 1.870$ Lyman α blob). We conclude that special care must be taken to investigate the amount possible foreground contamination in studies attempting to detect LyC flux through imaging observations.

Chapter 3

Detection of Lyman Continuum Flux in Galaxies at $z \approx 3$

3.1 Introduction

In this chapter we present measurements of the LyC flux from the DLCS spectroscopic observations. We adopt a conservative approach to estimate the residual systematic error in background subtraction, after which we identify a subsample of galaxies with a detection of LyC flux (§3.2). After a brief review of the various definitions of escape fraction (§3.3), we derive our best estimates for the escape fraction (§3.4) and the implied total ionizing emissivity (§3.5). In Section 3.6 we discuss the effects of variance in IGM opacity on these results.

Following that, we examine the prominent spectral features of LyC detected galaxies, by comparing their average spectrum with an average spectrum for objects where no significant detection of LyC was found (§3.7.1). Section 3.7.2 is devoted to an investigation into the spatial distribution of emergent LyC flux, using a two-dimensional composite spectrogram. Stellar populations of galaxies found with escaping LyC radiation are discussed in §3.8. Last, in §3.9 we identify a number of stellar features in composite spectrum of the full DLCS sample, and report on the first detection of molecular hydrogen (H_2) in spectra of galaxies at high redshift.

3.2 Measurements of the Escaping Flux

As a proxy for the escaping LyC we will use a measurement of the average residual flux in the rest-frame wavelength interval $880-910$ Å (value f_{900}). The choice of this wavelength interval is based on two considerations. First, the mean free path of LyC photon at $z \sim 3$ is estimated to be $\Delta z \sim 0.18$, which corresponds to ~ 30 Å at $z \sim 3$ (Haardt & Madau 1996). The second argument is based on a consideration of LRIS-B sensitivity, which sharply decreases below 3500 Å. The lowest redshift source included in the DLCS sample is at $z = 2.718$ (Q0100-MD6), placing the 880 Å wavelength at

Table 3.1. Properties of galaxies from the Deep Lyman Continuum Sample

Field	Source	RA (J2000)	Dec (J2000)	$\mathcal{R}$	z_{sys}[a]	f_{900}	σ_{900}[c]	f_{1500}[b]	σ_{1500}[d]
Q0100	D2	01:02:57.51	13:14:54.5	24.27	2.8965	-0.011	0.011	0.451	0.016
Q0100	MD6	01:03:01.88	13:16:34.4	24.13	2.7184	-0.003	0.016	0.422	0.015
Q0100	D8	01:03:03.92	13:18:29.8	24.81	2.7352	-0.001	0.017	0.585	0.014
Q0100	C6	01:03:05.79	13:16:41.6	25.31	3.0395	0.016	0.009	0.163	0.012
Q0100	MD20	01:03:06.91	13:15:47.2	25.25	2.7273	0.005	0.015	0.256	0.015
Q0100	C7	01:03:08.22	13:16:29.5	24.39	3.0401	0.004	0.009	0.677	0.013
Q0100	D13	01:03:09.66	13:15:44.0	23.23	2.9806	-0.004	0.010	1.199	0.018
Q0100	MD33	01:03:13.72	13:15:55.2	24.68	2.7186	0.009	0.013	0.497	0.011
Q0100	D14	01:03:14.65	13:15:11.2	24.57	2.9716	0.006	0.009	0.426	0.013
Q0100	C15	01:03:21.35	13:15:48.1	25.49	2.9295	0.022	0.009	0.269	0.015
Q0100	M11	01:03:22.03	13:14:44.6	24.64	3.4451	-0.002	0.006	0.423	0.013
Q0100	D21	01:03:26.22	13:15:04.3	23.82	2.8203	-0.024	0.010	0.669	0.011
Q0256	md24	02:58:51.45	00:10:31.6	23.97	2.9786	-0.020	0.015	0.613	0.016
Q0256	c16	02:58:53.11	00:10:43.4	24.22	2.9786	-0.014	0.015	0.585	0.018
Q0256	m16	02:58:55.43	00:11:37.8	25.44	3.2270	0.009	0.012	0.160	0.017
Q0256	c21	02:58:58.82	00:11:25.3	24.48	3.2270	-0.004	0.012	0.333	0.017
Q0256	c17	02:58:59.79	00:10:52.3	23.89	3.2810	0.011	0.011	0.767	0.019
Q0256	m20	02:59:04.16	00:12:35.6	24.42	3.2290	-0.018	0.012	0.529	0.016
Q0256	c32	02:59:06.58	00:13:17.5	24.52	3.2260	-0.007	0.012	0.455	0.021
Q0256	md46	02:59:11.80	00:13:26.0	24.38	2.9120	0.010	0.014	0.399	0.019
Q0256	m9ap2	02:59:09.22	00:09:21.9	24.48	3.2780	-0.010	0.010	0.346	0.017
Q0256	m9ap3	02:59:09.22	00:09:21.9	24.48	3.2780	0.011	0.010	0.411	0.016
Q0256	d5	02:59:16.29	00:10:40.7	23.60	3.0870	-0.015	0.012	0.473	0.016
B20902	M11	09:05:19.58	34:09:04.0	24.19	3.2999	-0.024	0.016	0.727	0.014
B20902	MD21	09:05:20.08	34:07:19.7	24.18	2.9916	-0.031	0.020	0.503	0.012
B20902	C5	09:05:23.10	34:08:59.4	24.70	3.1008	0.015	0.018	0.371	0.012
B20902	MD32	09:05:26.24	34:09:28.8	24.03	2.8656	0.006	0.024	0.551	0.011
B20902	MD25	09:05:25.82	34:07:44.4	23.81	2.8935	-0.012	0.023	0.783	0.013
B20902	C7	09:05:30.11	34:09:07.7	24.52	3.1911	-0.022	0.017	0.341	0.015
B20902	D8	09:05:31.24	34:08:48.8	24.24	2.8658	-0.035	0.023	0.849	0.014
B20902	MD34	09:05:34.20	34:09:34.4	24.44	3.0274	-0.017	0.022	0.370	0.014

3272 Å, where the instrument efficiency drops to 16%.

Figure 3.1 presents the measured values of f_{900}, with objects grouped and ordered as they were located on separate LRIS slit-masks. The values of f_{900} and its associated statistical error (σ_{900}) for DLCS galaxies are tabulated in Table 3.1. Also shown are measurements of the continuum flux in the rest-frame interval 1450–1550 Å, which will be used later on as an indicator of the intrinsic number of ionizing photons produced in these objects. Table 3.2 gives the corresponding measurements for the 4 AGN objects in our sample.

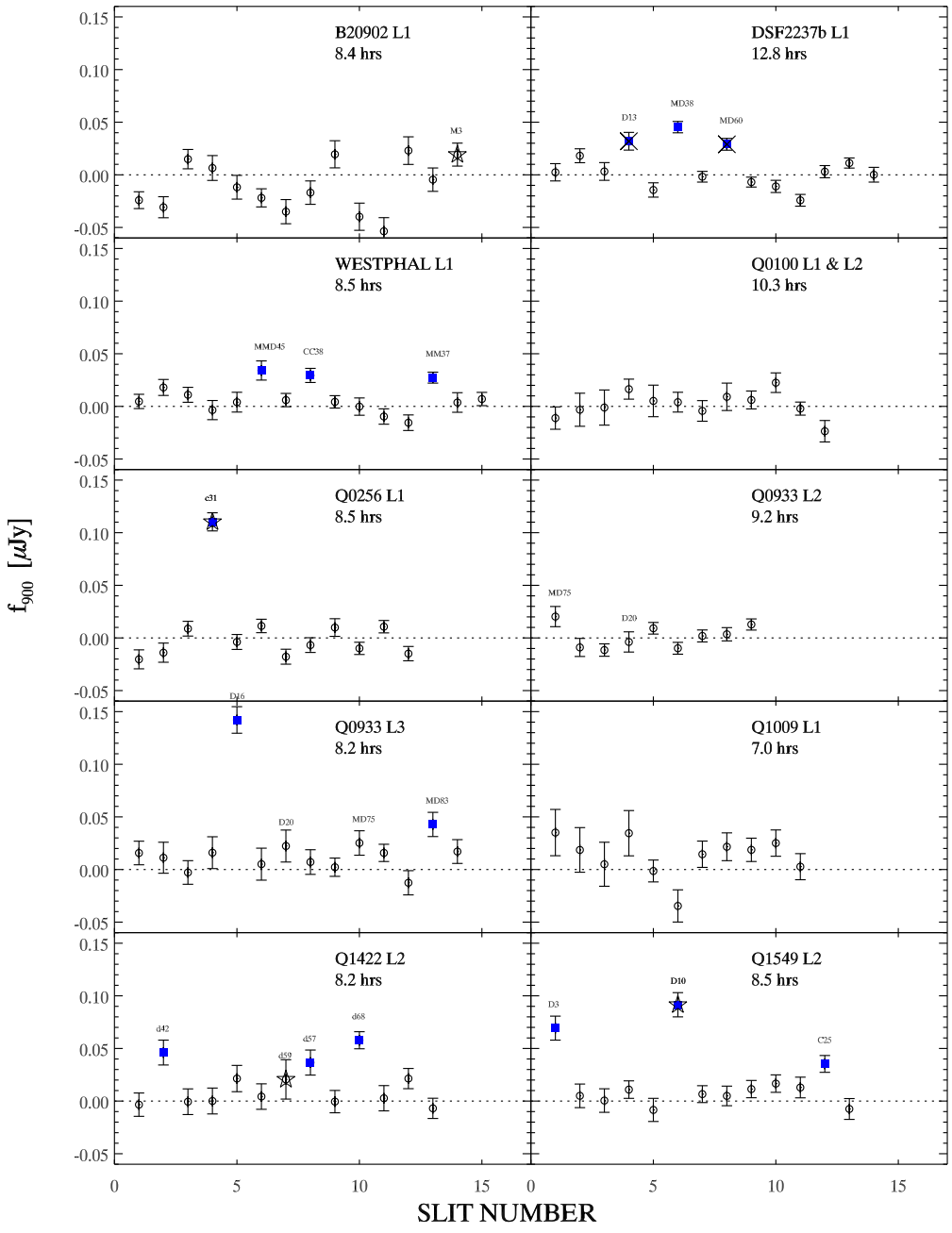

Figure 3.1 Measurements of LyC flux (f_{900}) for 121 Lyman break galaxies (circles) and 4 AGN (star symbols) from the DLCS sample. The ordering of objects follows their relative placement on the original slit masks. Total exposure times in hours per slit-mask are indicated under panel titles. Error shown are 1σ statistical errors derived from sky brightness and detector noise. Objects with "first cut" detection of f_{900} (13 galaxies and 2 AGN) are marked with square (blue) symbols. After the revision of errors based on the distribution of f_{900} for non-detections, sources DSF2237b-D13 and DSF2237b-MD60 have been excluded from LyC detections (shown crossed out). Note that galaxies Q0933-MD75 and Q0933-D20 (labeled) have been observed twice, on masks L2 and L3.

Table 3.1 (cont'd)

Field	Source	RA (J2000)	Dec (J2000)	$\mathcal{R}$	z_{sys}[a]	f_{900}	σ_{900}[c]	f_{1500}[b]	σ_{1500}[d]
B20902	MD24	09:05:34.19	34:07:40.4	25.20	2.8977	0.019	0.026	0.232	0.011
B20902	MD27ap1	09:05:37.25	34:08:17.5	24.43	2.8970	-0.040	0.026	0.256	0.013
B20902	MD27ap2	09:05:37.16	34:08:17.9	24.60	2.9017	-0.054	0.026	0.381	0.011
B20902	D10	09:05:41.13	34:09:34.1	25.47	2.8963	0.023	0.026	0.366	0.014
B20902	C4	09:05:45.79	34:08:18.0	24.52	3.0259	-0.005	0.022	0.380	0.011
Q0933	MD39	09:33:20.63	28:44:42.7	23.95	2.9871	-0.009	0.015	0.305	0.012
Q0933	C27	09:33:27.29	28:44:37.1	25.29	3.5424	-0.011	0.014	0.286	0.017
Q0933	C31	09:33:41.37	28:45:36.5	24.70	3.2250	0.009	0.009	0.275	0.018
Q0933	M5	09:33:40.07	28:43:08.5	24.25	3.1737	-0.010	0.015	0.446	0.014
Q0933	D13	09:33:43.86	28:44:27.3	25.19	3.1644	0.002	0.009	0.204	0.012
Q0933	M16	09:33:46.24	28:45:06.7	24.34	3.0381	0.004	0.009	0.523	0.015
Q0933	M7	09:33:48.54	28:43:37.5	24.43	3.4909	0.013	0.009	0.220	0.014
Q0933	C15	09:33:23.32	28:43:07.5	24.83	3.1639	0.016	0.010	0.555	0.018
Q0933	C18	09:33:34.24	28:43:23.4	24.68	2.9285	0.011	0.008	0.530	0.017
Q0933	C22	09:33:32.09	28:43:42.0	24.86	3.1627	-0.003	0.009	0.600	0.017
Q0933	D12	09:33:33.92	28:44:18.1	24.24	2.9236	0.016	0.011	0.647	0.016
Q0933	D16	09:33:30.55	28:44:53.5	25.17	3.0430	0.142	0.015	0.284	0.014
Q0933	MD49	09:33:20.04	28:45:28.7	25.01	2.9156	0.005	0.011	0.470	0.016
Q0933	D20	09:33:31.80	28:46:00.6	24.70	2.9195	0.010	0.015	0.585	0.009
Q0933	D21	09:33:36.08	28:46:44.4	25.26	2.9108	0.007	0.013	0.416	0.017
Q0933	D23	09:33:23.44	28:47:17.1	24.27	3.2270	0.002	0.015	0.577	0.015
Q0933	MD75	09:33:24.42	28:47:46.0	24.49	2.9131	0.023	0.010	0.262	0.011
Q0933	D26	09:33:25.07	28:48:24.4	24.72	3.2653	0.016	0.015	0.331	0.016
Q0933	M31	09:33:21.85	28:49:09.8	24.67	2.9159	-0.013	0.012	0.162	0.016
Q0933	MD83	09:33:21.51	28:48:46.4	24.91	2.8790	0.043	0.009	0.305	0.015
Q0933	D30	09:33:25.73	28:49:37.8	23.66	2.9128	0.017	0.023	0.666	0.017
Q1009	BX11	10:11:39.00	29:41:01.4	24.16	2.7662	0.035	0.012	0.291	0.019
Q1009	C7	10:11:42.92	29:41:04.4	24.65	2.7803	0.019	0.008	0.409	0.017
Q1009	D5	10:11:44.39	29:40:20.9	24.43	2.7793	0.005	0.011	0.535	0.016
Q1009	MD12	10:11:46.03	29:42:08.8	23.93	2.7763	0.035	0.011	0.593	0.016
Q1009	C16	10:11:50.21	29:42:19.2	24.64	3.3013	-0.001	0.011	0.595	0.018

Table 3.1 (cont'd)

Field	Source	RA (J2000)	Dec (J2000)	$\mathcal{R}$	z_{sys}[a]	f_{900}	σ_{900}[c]	f_{1500}[b]	σ_{1500}[d]
Q1009	D12	10:11:56.59	29:41:48.4	24.37	2.9095	-0.035	0.022	0.758	0.018
Q1009	C26	10:11:58.05	29:40:59.6	23.81	3.0629	0.015	0.021	0.659	0.019
Q1009	C31	10:12:01.19	29:42:41.4	25.25	3.0374	0.022	0.021	0.353	0.018
Q1009	D17	10:12:03.49	29:39:50.1	23.61	3.2139	0.019	0.021	0.947	0.020
Q1009	C36	10:12:03.92	29:41:52.4	24.10	3.0629	0.025	0.010	0.432	0.016
Q1009	C46	10:12:10.89	29:42:00.9	24.43	3.0637	0.003	0.015	0.241	0.014
Westphal	CC17	14:17:55.65	52:25:41.7	24.20	3.1775	0.005	0.007	0.441	0.012
Westphal	CC16	14:18:12.33	52:25:20.9	24.91	3.0711	0.018	0.008	0.373	0.010
Westphal	MMD34	14:18:05.72	52:26:07.3	24.96	3.1405	0.011	0.007	0.374	0.013
Westphal	CC24	14:18:04.12	52:26:29.8	23.79	2.9225	-0.004	0.009	0.739	0.012
Westphal	CC31	14:17:53.09	52:28:07.9	24.49	2.9236	0.004	0.009	0.452	0.012
Westphal	MMD45	14:18:19.81	52:27:06.7	24.00	2.9366	0.034	0.009	0.394	0.013
Westphal	CC32	14:18:14.45	52:28:04.7	24.17	3.1921	0.006	0.006	0.699	0.014
Westphal	CC38	14:18:03.80	52:29:04.6	24.46	3.0723	0.029	0.007	0.519	0.011
Westphal	CC46	14:18:00.17	52:29:50.7	23.65	3.2597	0.004	0.006	1.017	0.020
Westphal	MM38	14:18:04.06	52:29:52.3	24.86	2.9255	0.000	0.008	0.260	0.009
Westphal	CC41	14:18:20.50	52:29:18.9	24.95	3.0260	-0.010	0.007	0.324	0.011
Westphal	DD28	14:18:24.84	52:29:25.3	23.91	3.0197	-0.015	0.007	0.411	0.008
Westphal	MM37	14:18:26.23	52:29:42.8	24.43	3.4200	0.027	0.005	0.574	0.012
Westphal	CC53	14:18:22.15	52:30:17.3	25.07	2.8069	0.004	0.009	0.313	0.013
Westphal	CC55	14:18:20.77	52:30:42.7	24.34	3.2060	0.007	0.006	0.559	0.016
Q1422	c49	14:24:36.11	22:52:41.3	24.89	3.1829	-0.003	0.013	0.328	0.014
Q1422	d42	14:24:27.72	22:53:50.7	25.32	3.1399	0.046	0.013	0.372	0.012
Q1422	c63	14:24:30.18	22:53:56.2	25.85	3.0607	-0.001	0.011	0.202	0.013
Q1422	d45	14:24:32.20	22:54:03.0	24.11	3.0705	0.000	0.013	0.953	0.014
Q1422	d53	14:24:25.53	22:55:00.4	24.23	3.0853	0.021	0.012	0.425	0.012
Q1422	c70	14:24:33.63	22:54:55.2	25.45	3.1281	0.004	0.011	0.248	0.013
Q1422	d57	14:24:43.24	22:56:06.6	25.71	2.9412	0.037	0.012	0.143	0.016
Q1422	c84	14:24:46.16	22:56:51.4	24.70	2.9744	-0.001	0.012	0.383	0.015
Q1422	d68	14:24:32.94	22:58:29.1	24.72	3.2838	0.058	0.012	0.346	0.017
Q1422	c101	14:24:42.28	22:58:37.8	24.17	2.8755	0.003	0.013	0.599	0.011

The flux error bars shown are statistical errors based solely on the value of sky background in the data and the read noise of LRIS-B detectors. A representative value for this initial estimate of flux error is $\sigma = 0.01$ μJy. It can be seen that the majority of objects have f_{900} flux consistent with zero within 1–2σ of this statistical error. However, we caution that these error estimates do not include the systematic uncertainty associated with background subtraction. As we show below, this additional contribution to the uncertainty is roughly comparable to the above error based on counting statistics.

Grouping observations by slit-mask allows us to monitor for the presence of systematic errors from mask to mask. These can be caused by biased background estimates, presence of scattered light and a number of other factors related to the instrument setup for a given slit-mask. Systematic overestimate of background level was noted for a sample of 14 sources presented in Shapley et al. (2006) (S06). These authors observed that the flux of objects without significant detection of LyC flux was centered around an unphysical negative value (cf. their Figure 5).

We have invested considerable effort to improve the data reduction process, specifically focusing on flat-fielding at wavelengths below 4000 Å and background subtraction (as described in detail in §2.5). Special care was given to the removal of sources of systematic error. As we show below, we have sufficient reason to believe that our new data reduction procedure is successful in decreasing systematic error below the value of the random errors.

As a first step in the examination of random and systematic errors, we have selected as tentative Lyman continuum detections those objects with f_{900} greater than 3σ of the statistical error. This selects 13 galaxies and 2 AGN as candidate objects where LyC is detected. We will call this sample "first cut." However, we will re-evaluate the significance of the detection based on an investigation of the distribution of f_{900} values for the remaining objects. In the study of S06, only 1 out of 14 objects were confirmed with detected LyC down to a similar flux sensitivity. Therefore, the most conservative assumption we can make is that the majority of DLCS objects should have a flux consistent with zero, if our error estimates are accurate. In the absence of other noise contributions the standard deviation of f_{900} values should be roughly equal to the estimated error on a single measurement.

Excluding "first cut" objects, the standard deviation of f_{900} flux for objects on four out of ten masks (B20902 L1, DSF2237b L1, Q0256 L1 and Q0933 L2) is larger than the estimated statistical error by a factor of 1.5 to 2.0. One of the most likely sources of larger systematic error is background subtraction in data that has not been optimally flat-fielded. As we have discussed in §2.5.1, adequate flat-fielding below 4000 Å becomes increasingly difficult, and we have been progressively making improvements to the process throughout the duration of the survey. Data from masks observed prior to April 2008 have not had the benefit of the observational approach that is required for application of our best flat-fielding algorithm. However, increased scatter of f_{900} is not observed

Table 3.1 (cont'd)

Field	Source	RA (J2000)	Dec (J2000)	$\mathcal{R}$	z_{sys}[a]	f_{900}	σ_{900}[c]	f_{1500}[b]	σ_{1500}[d]
Q1422	d81	14:24:31.44	22:59:51.5	23.41	3.1010	0.021	0.012	0.814	0.015
Q1422	d78	14:24:40.48	22:59:35.3	23.77	3.1030	-0.007	0.012	0.655	0.012
Q1549	D3	15:51:43.71	19:09:12.4	24.22	2.9362	0.069	0.011	1.510	0.018
Q1549	C8	15:51:45.39	19:08:49.9	25.05	2.9396	0.005	0.008	0.474	0.018
Q1549	D7	15:51:46.25	19:09:50.1	24.31	2.9352	0.001	0.012	0.781	0.021
Q1549	C10	15:51:48.42	19:09:25.0	24.84	3.1878	0.011	0.010	0.640	0.020
Q1549	C9	15:51:46.71	19:11:52.4	23.55	2.9204	-0.008	0.010	1.060	0.018
Q1549	D16	15:51:54.85	19:11:31.1	24.05	3.1317	0.007	0.011	0.815	0.015
Q1549	C17	15:51:55.28	19:12:19.5	24.85	2.9355	0.005	0.011	0.478	0.014
Q1549	C19	15:52:00.20	19:10:08.7	24.78	3.1608	0.011	0.011	0.589	0.014
Q1549	M22	15:52:02.71	19:09:40.1	24.85	3.1544	0.017	0.008	0.270	0.016
Q1549	C22	15:52:03.84	19:09:43.2	24.61	2.9626	0.013	0.011	0.712	0.023
Q1549	C25	15:52:06.07	19:11:28.4	24.83	3.1508	0.035	0.008	0.529	0.017
Q1549	C27	15:52:07.04	19:12:19.3	24.51	2.9241	-0.007	0.009	0.634	0.016
DSF2237b	MD22	22:39:23.08	11:48:57.5	24.36	2.9265	0.002	0.016	0.624	0.015
DSF2237b	C2	22:39:31.97	11:47:58.8	24.95	3.1409	0.018	0.013	0.348	0.017
DSF2237b	C7	22:39:32.97	11:48:17.6	25.10	2.9205	0.003	0.017	0.246	0.015
DSF2237b	D13	22:39:27.58	11:49:45.3	24.96	2.9212	0.032	0.017	0.520	0.015
DSF2237b	C16	22:39:36.50	11:49:21.5	24.52	3.1301	-0.014	0.014	0.448	0.014
DSF2237b	MD38	22:39:35.65	11:50:25.6	24.19	3.3278	0.045	0.011	0.748	0.014
DSF2237b	M15	22:39:30.87	11:51:38.8	25.12	3.4019	-0.002	0.010	0.196	0.013
DSF2237b	MD60	22:39:28.10	11:52:57.7	24.94	3.1413	0.029	0.011	0.402	0.015
DSF2237b	C25	22:39:38.73	11:51:33.5	24.45	3.3792	-0.007	0.009	0.406	0.017
DSF2237b	C29	22:39:34.66	11:52:39.0	24.97	3.0995	-0.011	0.012	0.391	0.014
DSF2237b	M20	22:39:38.88	11:52:22.1	24.20	3.1439	-0.024	0.011	0.471	0.014
DSF2237b	C27	22:39:42.94	11:52:26.7	24.21	3.0835	0.003	0.012	0.760	0.011
DSF2237b	M29	22:39:41.58	11:54:03.7	23.97	3.3914	0.011	0.010	0.545	0.014
DSF2237b	MD84	22:39:35.15	11:55:30.2	23.62	2.8955	0.000	0.014	0.976	0.019

[a]Inferred systemic redshift (see §2.9)

[b]Mean continuum flux at 1450–1550 Å in the rest-frame

[c]Includes both statistical and systematical error estimate

[d]Statistical error estimate

Table 3.2. Properties of QSOs and AGN from the Deep Lyman Continuum Sample

Field	Source	RA (J2000)	Dec (J2000)	$\mathcal{R}$	z_{sys}	f_{900}	σ_{900}	f_{1500}	σ_{1500}
B20902	M3	09:05:45.60	34:05:26.3	24.54	3.026	0.019	0.022	0.418	0.012
Q0256	c31	02:58:57.91	00:12:46.1	24.44	3.063	0.110	0.015	0.392	0.016
Q1422	d59	14:24:24.39	22:56:19.9	24.48	2.833	0.021	0.019	0.563	0.011
Q1549	D10	15:51:49.47	19:10:41.0	23.38	2.916	0.091	0.011	0.714	0.019

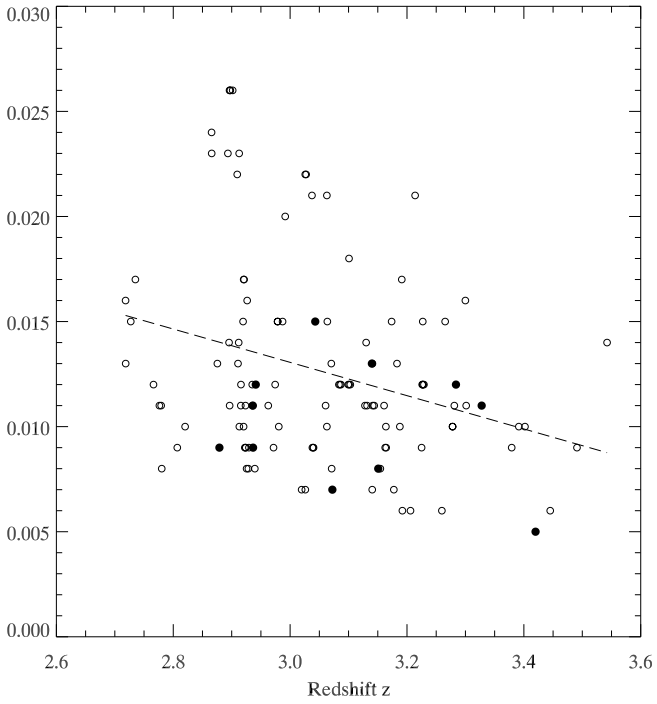

Figure 3.2 Improved estimates for the uncertainty of LyC flux measurements (σ_{900}), after analysis of systematical errors. Values for galaxies with a detection of LyC flux at $\geq 3\sigma$ significance are marked with solid symbols. The dashed line is a linear fit used to model σ_{900} for simulations in Section 3.6.

in masks Q0100 L1&L2 and Q1009 L1, which were also observed prior to introducing the optimal flat-fielding strategy. However, in their case the random errors from the counting statistics alone are already larger than typical ($\sim 0.012 - 0.015$ μJy). This leads us to conclude that the errors introduced by suboptimal flat-fielding are not larger than ~ 0.01 μJy. For data taken after April 2008 (masks WESTPHAL L1, Q0933 L3, Q1422 L2 and Q1549 L2, see Table 2.2) the scatter in flux measurements (excluding "first cut" objects) is in good agreement with the estimate of random error, indicating that the flat-fielding problems and associated systematics were successfully eliminated.

In the analysis that follows we will increase the errors for f_{900} to match the standard deviation in flux of all objects without "first cut" LyC detection. The improved error estimates and their apparent anti-correlation with object redshift (due to increase in LRIS-B efficiency with wavelength) are presented in Figure 3.2. According to these final error estimates, the mean value of f_{900} (excluding "first cut") is not significantly different from zero for any of the masks observed. The most discrepant case is in the field B20902 L1, where the mean is negative f_{900} at $\sim 1.6\sigma$. We find that all but two of our "first cut" objects remain above the 3σ significance level in f_{900} after applying the increased error estimates. "First cut" objects DSF2237b-D13 and DSF2237b-MD60 were degraded to a significance of 1.8σ and 2.6σ, respectively, so that the final sample of LyC detections consist of 11 galaxies and

2 AGN.

Figures 3.3 and 3.4 show R band image cutouts for these 11 galaxies. The slit positions used in the deep spectroscopic observations are also indicated. We find no other objects which are in sufficient proximity to these galaxies to be a possible source of contamination. Blending of the target galaxy with objects in the foreground is an important concern for imaging studies of LyC, as noted by Iwata et al. (2009). Owing to the spectroscopic nature of DLCS and quality of our data we are able to avoid this source of crude error. As discussed at length in §2.9, we have observed a substantial number of cases of source blending in the spectra of our initial sample ($\sim 5\%$), which would not be identified in imaging observations alone. This fraction of blends is comparable to the expected number of galaxies with significant LyC ($< 10\%$, based on results of Shapley et al. (2006)).

The DLCS spectra are deep enough that we can securely identify a number of ISM absorption lines in every spectrum individually. This allows for a confident determination of systemic redshifts (Table 3.1), after applying a shift to account for the typical velocity difference between ISM absorption and nebular emission lines (Adelberger et al. 2005). The 1σ rms for this empirical transformation between ISM absorption line redshift and systemic redshift corresponds to 1 Å in the rest-frame. Therefore we proceed with the analysis of f_{900} confident that the flux error introduced by any redshift uncertainty is negligible.

3.3 Definition of the Escape Fraction of LyC

The common definition of escape fraction, used mostly in theoretical studies of reionization, is simply the fraction of produced Lyman continuum photons that is able to escape into the IGM (Wyithe & Cen 2007; Wise & Cen 2009, and references therein). This value has been also named the *absolute* escape fraction (f_{esc}). In order to determine f_{esc} a measure of the intrinsic number of ionizing photons is necessary. SED models of young stellar populations have so far been used for this purpose, applying a normalization based on measurements of UV continuum at longer wavelengths (typically ~ 1500 Å). However, the shape of the stellar spectra for O/B stars in this wavelength range (on which such models rely) is still not well understood, and direct observations at present do not exist. To circumvent this problem, observational studies usually place constraints on the the *relative* escape fraction, as initially defined by Steidel et al. (2001):

$$f_{esc,rel} = \frac{(L_{1500}/L_{900})_{int}}{(f_{1500}/f_{900})_{corr}}, \tag{3.1}$$

where

$$(f_{1500}/f_{900})_{corr} = \frac{f_{1500}}{f_{900} \times e^{\tau_{IGM}}} \tag{3.2}$$

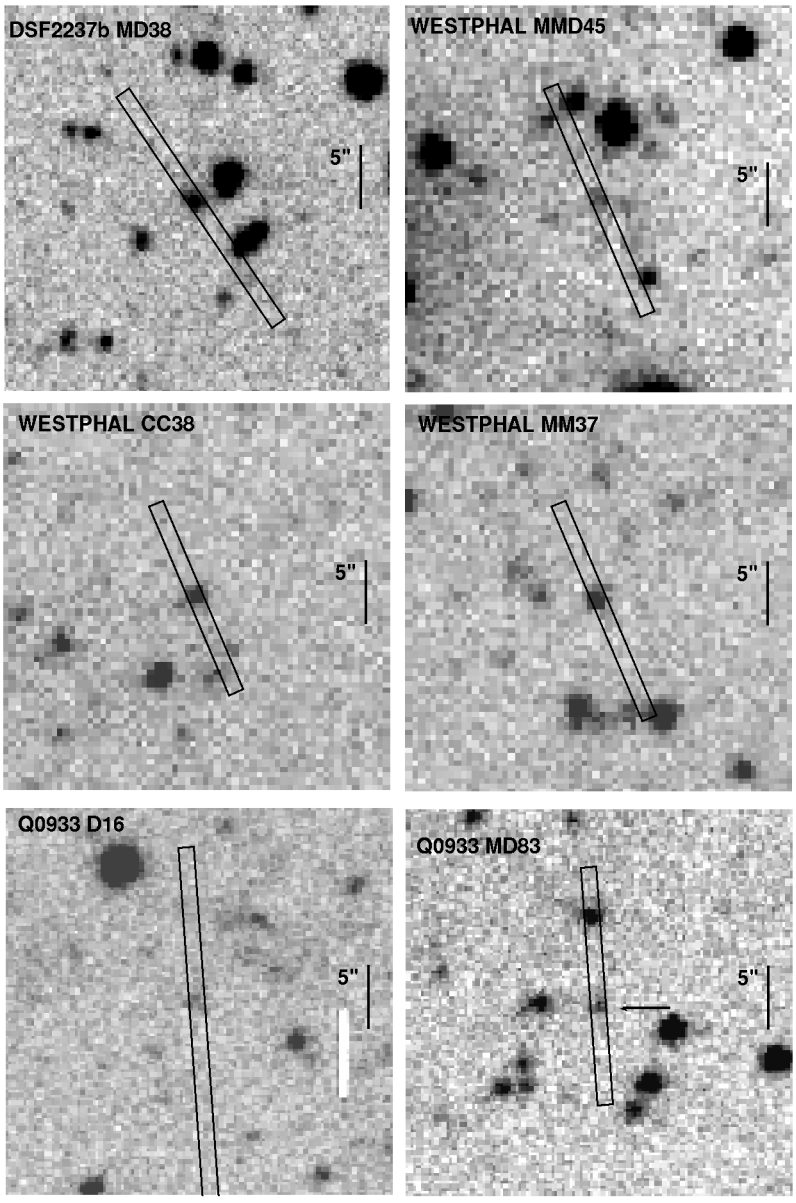

Figure 3.3 Cutouts from the $\mathcal{R}$ band imaging for 11 galaxies with detected LyC emission. The extent of the slit used in deep spectroscopic observations are indicated with black rectangles. Images are $30''$ on a side.

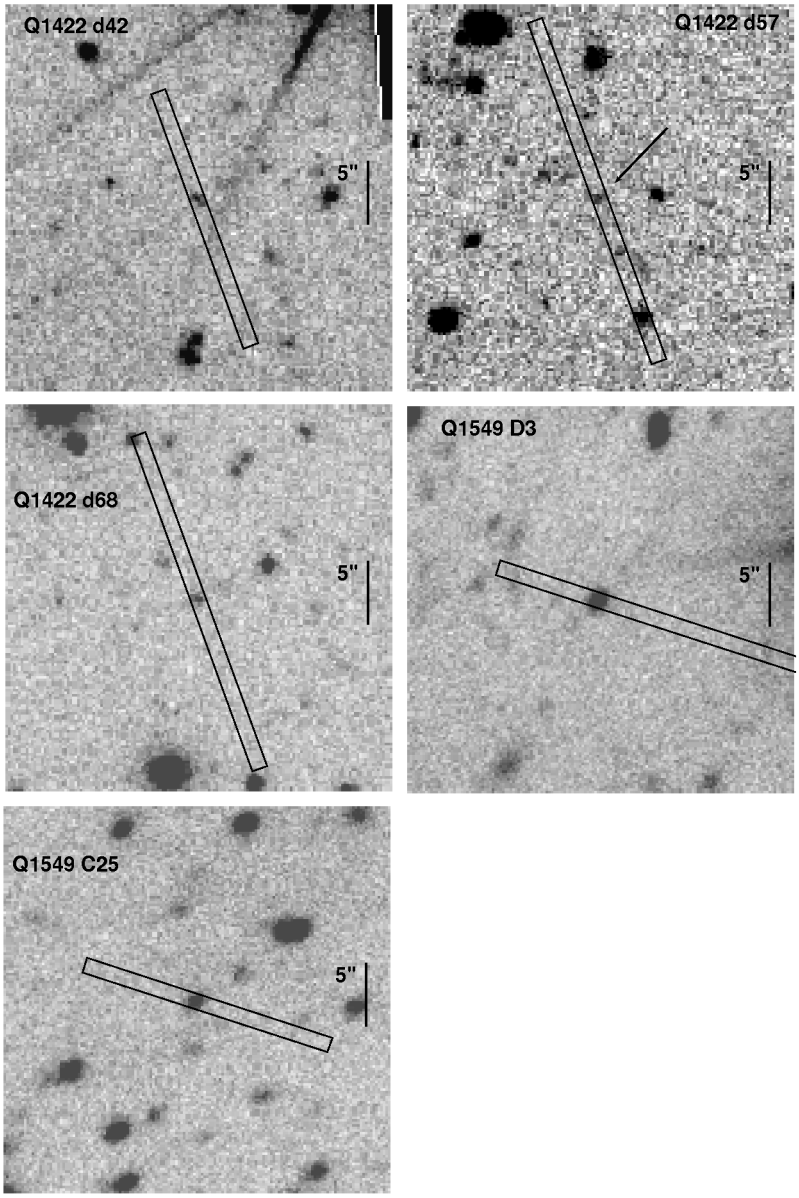

Figure 3.4 continued from Figure 3.3

is the ratio between observed f_{1500} flux and LyC flux corrected upward for the attenuation by the IGM. The term $(L_{1500}/L_{900})_{int}$ represents the intrinsic ratio of non-ionizing UV to ionizing specific intensity produced in the galaxy, and depends to a large extent on models of the Lyman-break in the spectra of the hottest stars. Integrated over the stellar population of a star-forming galaxy, the break in the spectrum at 912 Å will surely depend on the IMF and metallicity. Siana et al. (2007) show the evolution of $(L_{1500}/L_{900})_{int}$ based on Starburst99 (Leitherer et al. 1999) and BC03 (Bruzual & Charlot 2003) population synthesis models, concluding that the expected value for the intrinsic break from stars is $(L_{1500}/L_{900})_{int} \sim 6$. On the other hand, Iwata et al. (2009) find that for the bluest model galaxy generated by Starburst99 (top-heavy IMF, low metallicity, no dust) this value can decrease to $(L_{1500}/L_{900})_{int} \sim 1.09$. Clearly this number remains the most significant source of uncertainty for estimating f_{esc}.

The advantage of $f_{esc,rel}$ over the absolute escape fraction is in that it can be defined with respect to a UV continuum luminosity accessible to direct observations. For star-forming galaxies at $z \sim 3$, the continuum flux at 1500 Å used in equation (3.2) can easily be determined from observations (i.e., by broadband photometry).

For easier comparison with earlier studies (Steidel et al. 2001; Inoue et al. 2005), for the remainder of analysis in this section we adopt a value $(L_{1500}/L_{900})_{int} = 3$. To convert the relative to absolute escape fraction, we need to correct for the amount of differential extinction by dust between 1500 and 900 Å. Following Siana et al. (2007) we use the relation :

$$f_{esc} = 10^{-0.4\times10.33E(B-V)} f_{esc,rel}, \tag{3.3}$$

where the extinction has been assumed to follow a Calzetti law (Calzetti 1997). Therefore in order to derive its value we need to also estimate the amount of dust extinction and assume a form of the reddening law.

Using supporting photometric observations in the near-IR and mid-IR (Section 3.8), we were able to derive model parameters describing the stellar populations in more than a half of the DLCS sample. We demonstrate in §3.8 that LyC detections are made preferentially among galaxies with low inferred extinction ($E(B-V) \leq 0.1$) and low star-formation rate. For the derivation of f_{esc} (equation (3.3)) we conservatively assume $E(B-V) = 0.1$. This would imply a scaling relation $f_{esc} = 0.39 \times f_{esc,rel}$, and we proceed with using this relation for f_{esc} in the discussion that follows.

To remain consistent with the derivation o luminosity function for LBGs at $2.7 \leq z \leq 3.4$ presented in Reddy et al. (2008), we have used the apparent magnitude $\mathcal{R}$ of our galaxies to derive their absolute luminosity M_{1700} :

$$M_{AB}(1700\text{Å}) = \mathcal{R} - 5log(d_L/10\text{pc}) + 2.5log(1+z), \tag{3.4}$$

where d_L is the luminosity distance to redshift z. The effective wavelength of the $\mathcal{R}$ band pass is $\lambda_{eff} = 6830\,\text{Å}$, which for the mean redshift in the DLCS sample galaxies is close to 1700 Å in the rest-frame. The magnitude corresponding to the "break" in the power-law of LBG luminosity function given by Reddy et al. (2008) is $M_* = -21.1$. We will use this value interchangeably with the corresponding break luminosity (L_*).

3.4 Measurements of the LyC Escape Fraction

The measurements of f_{900} for the 11 LyC detections are shown in Figure 3.5 (upper panel) as a function of their continuum flux at 1500 Å (f_{1500}). The only other currently available measurement of this kind is the LyC leaking galaxy C49 discovered by S06 (and confirmed by Iwata et al. (2009)), which we include in the plot.[1] Apart from the apparent outlier flux of Q0933-D16 ($f_{900} = 0.141\,\mu$Jy), the majority of the measurements lie close to a constant flux of $f_{900}^{det} = 0.042 \pm 0.013\,\mu$Jy, implying a rapid increase of the observed ratio f_{900}/f_{1500} toward fainter continuum flux.

The lower panel of Figure 3.5 shows the 3σ upper limits on the f_{900} flux from the remainder of the DLCS sample. Of these, $\sim 20\%$ of sources have LyC flux upper limits above the mean observed value for the detected sample. Our observations of these objects might simply not be deep enough to have detected flux levels similar to that observed in detected sample. However, the clipped mean value of the 3σ upper limits for this sample of objects as a whole is lower than the average detected flux, $f_{900}^{lim} = 0.033 \pm 0.008\,\mu$Jy. This value will be used to estimate an upper limit on observed LyC emission for the remaining galaxies that are not individually detected.

The values of f_{1500}/f_{900} and inferred f_{esc} for 11 galaxies with LyC detection are tabulated in Table 3.3. We observe a broad range in f_{1500}/f_{900}, from 2.0 (object Q0933-D16) to 21.9 (Q1549-D3). This is in excellent agreement with the results of Iwata et al. (2009), who observe a range $2.3 < f_{1500}/f_{900} < 23.8$ in seven LBGs with detected LyC.

Figure 3.6 shows the distribution of absolute magnitude at rest frame 1700 Å (M_{1700}) for the galaxies with and without LyC detection. Results of two-sided Kolmogorov-Smirnov tests comparing the absolute magnitude distribution of LyC detections and the full sample, show that they are consistent with having been drawn from the same distribution (probability $\geq 70\%$). The same conclusion holds if we compare the distribution of absolute magnitude for just those sources in DLCS for which the 3σ upper limit is below the mean observed $f_{900}^{det} = 0.042\ \mu$Jy (84 sources in total). It appears that the likelihood of a galaxy leaking a flux detectable in our survey is independent of its luminosity.

Figure 3.7 shows the inferred values of f_{esc} as a function of galaxy luminosity (in units of break luminosity L_*). Under the assumptions given earlier, we find typical value f_{esc} in brighter objects

[1] Note that the spectrum of C49 was obtained by Shapley et al. (2006) using an identical instrument setup as in the present survey.

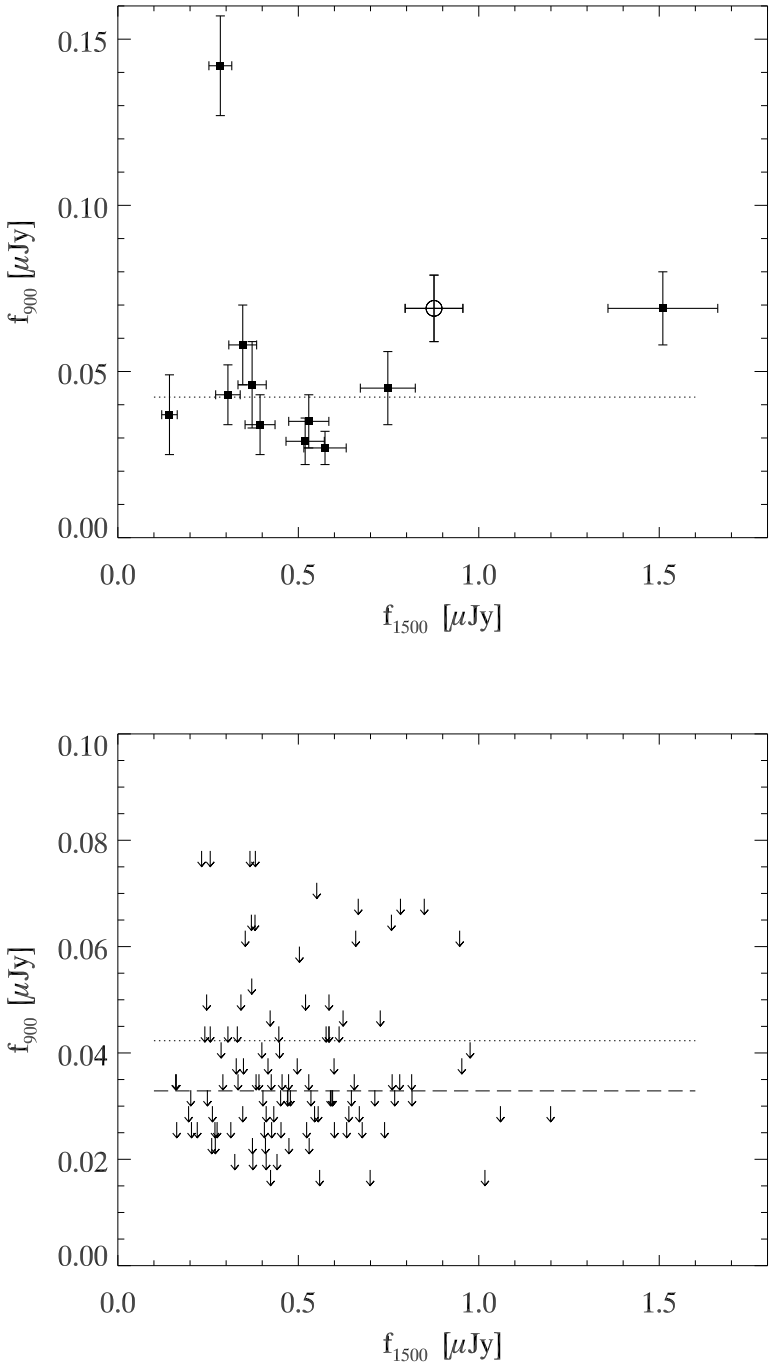

Figure 3.5 Measurements and 3σ upper limits for LyC flux f_{900} for galaxies in the DLCS sample, as a function of continuum luminosity (f_{1500}. *Upper panel :* Observed flux f_{900} for the 11 LyC detections. Error bars shown are 1σ. The dotted line shows a clipped mean of $\langle f_{900}^{det} \rangle = 0.042$ μJy. *Lower panel :* Upper limits on f_{900} (3σ) for galaxies without LyC detection (arrows). The dotted line shows the clipped average flux $\langle f_{900} \rangle$ of the 11 detections, as in the upper panel. The dashed line is a clipped mean of the 3σ upper limits, $\langle f_{900}^{lim} \rangle = 0.33$ μJy. Note the different y-axis scale for the two panels.

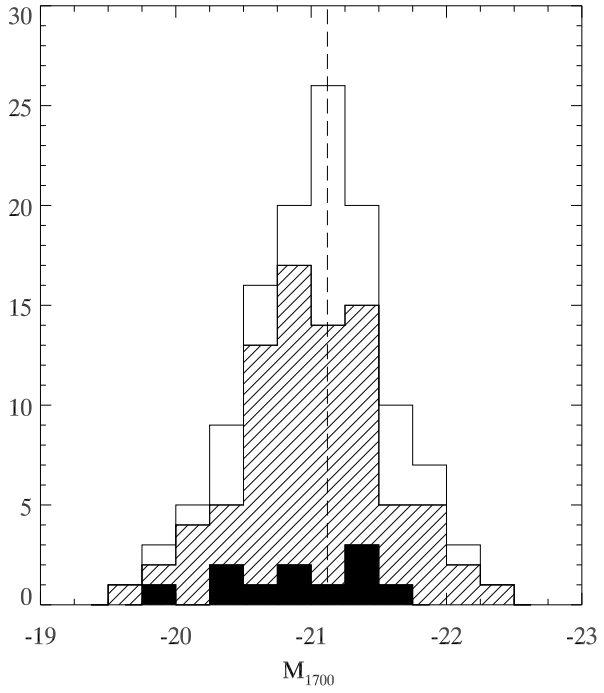

Figure 3.6 Distribution of absolute magnitude M_{1700} for galaxies with LyC detection (black solid) compared to the full DLCS sample (white, background). The shaded histogram is the subset of DLCS sample for which the 3σ limit on f_{900} measurement is below the mean observed flux in LyC detections ($3\sigma \leq \langle f_{900} \rangle = 0.042$ μJy). Two-sided Kolmogorov-Smirnov statistics suggests a high probability ($\geq 70\%$) that all three are representative of the same distribution. Vertical dashed line indicates the position of the break luminosity in the $z \sim 3.0$ LBG luminosity function ($M_* = -21.1$, (Reddy et al. 2008)).

to be $f_{esc} = 20\%$. Though at faint continuum flux levels we are naturally biased toward objects with a higher f_{esc}, it is still striking that there are no objects brighter than L_* with escape fractions significantly greater than 20%. The median escape fraction for 7 LBGs reported in Iwata et al. (2009) is also found to be $f_{esc} \sim 20\%$ under same assumptions.

A much higher value of f_{esc} appears to be common for fainter objects. As expected from the observed similarity in the detected flux f_{900} for all objects, the escape fraction shows an inversely proportional increase at lower luminosities, reaching values of 100% at $L \sim 0.2L_*$. One object (Q0100-D16) apparently has an unphysical value of $f_{esc} > 100\%$. We caution that this is true only given the typical assumptions regarding the intrinsic spectrum of hot stars and the IGM opacity, as explained in §3.3.

We proceed with the derivation of the average escape fraction observed in the DLCS sample. Thus far, theoretical investigations of galaxy formation have commonly relied on a single value of f_{esc} for all galaxies. Our findings show what appears to be a strong trend of f_{esc} with luminosity, although at the same time the relative number of galaxies emitting LyC does not seem to depend

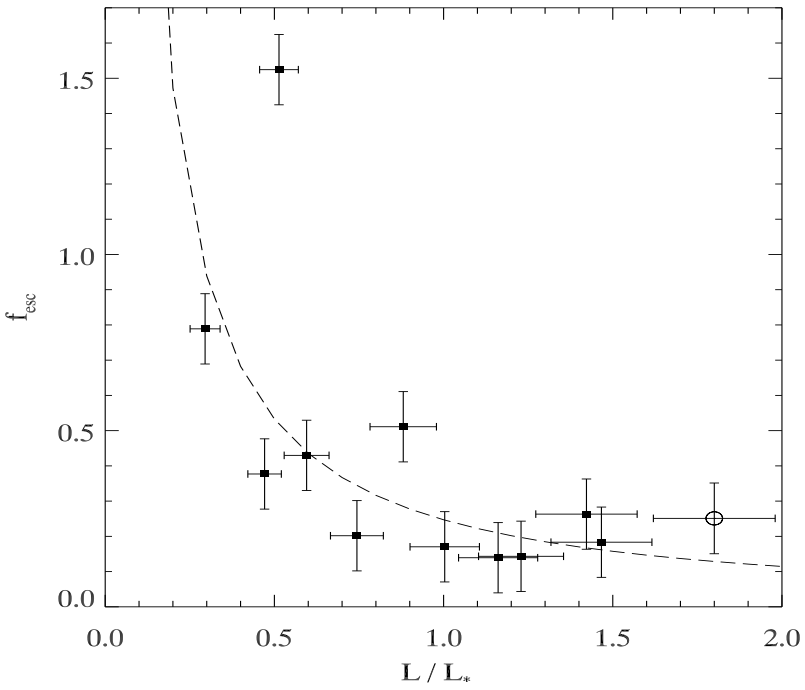

Figure 3.7 The observed luminosity dependence of absolute escape fraction (f_{esc}) of ionizing radiation for 11 LyC detections. The x-axis is shown in terms of the break luminosity in $z \sim 3$ luminosity function (L_*). The empty circle shows the object C49 from Shapley et al. (2006). A best fit function of the form $f_{esc} \sim L^{-1}$ is shown as a dashed line.

on luminosity to a noticeable extent. It is not clear how this trend continues below our luminosity limit of $\sim 0.2L_*$. Therefore the average f_{esc} values we provide in Table 3.4 should be taken with caution.

For the 11 detections the average value of is $f_{esc} \sim 43\%$, whereas for the full sample of 121 galaxies it is lowered to 5%. The average f_{900} flux from 110 galaxies without LyC detection in individual spectra, and find that it is below 3σ significance. Therefore we only place an upper limit of $\leq 2\%$.

However, taking into account that fainter sources seem to be comparatively stronger LyC leakers, we calculated a separate average for galaxies with $L < L_*$ that had no detectable f_{900} individually. We find a detection of f_{900} at 4σ significance, and an implied $f_{esc} \sim 5\%$. This suggests that there were a number of galaxies in our sample among those fainter than $L < L_*$ that were just below the detection threshold for our sensitivity limit.

Table 3.3. Measurements of the Lyman Continuum Escape Fraction

Field	Object	L (L_*)[a]	(f_{1500}/f_{900})[b]	f_{esc}[c]
DSF2237b	MD38	1.5	16.6 ± 4.1	0.18
WESTPHAL	MMD45	1.4	11.6 ± 3.1	0.26
WESTPHAL	CC38	1.0	17.9 ± 4.3	0.17
WESTPHAL	MM37	1.2	21.3 ± 4.0	0.14
Q0933	D16	0.5	2.0 ± 0.2	1.52
Q0933	MD83	0.6	7.1 ± 1.5	0.43
Q1422	d42	0.5	8.1 ± 2.3	0.38
Q1422	d57	0.3	3.9 ± 1.3	0.79
Q1422	d68	0.9	6.0 ± 1.3	0.51
Q1549	D3	1.2	21.9 ± 3.5	0.14
Q1549	C25	0.7	15.1 ± 3.5	0.20

[a]Based on R magnitude and a break luminosity $M_{AB}(1700\text{Å}) = -21.1$

[b]Observed flux ratio. The error estimate includes systematic error.

[c]Assuming IGM opacity $e^{-\tau} = 0.38$ and $(L_{1500}/L_{900})_{int} = 3.0$

Table 3.4. Average Lyman Continuum Escape Fraction

Subsample	N[a]	$\langle L \rangle (L_*)$	$\langle f_{1500}/f_{900} \rangle$	$\langle f_{esc} \rangle$
Detections	11	0.9	7.1 ± 0.6	0.43
All non-detections	110	1.1	≥ 160	≤ 0.02
$0.2 < L < L_*$	56	0.4	58 ± 14	~ 0.05
Full sample	121	1.1	64 ± 8	~ 0.05

[a]Number of galaxies

3.5 Limits on the Total Ionizing Flux

We now use the results of the f_{900} measurements to derive an estimate of the total ionizing emissivity from galaxies at $z \sim 3.0$, by integrating the observed f_{900} flux over the well-constrained luminosity function for $z \sim 3$ star-forming galaxies (Reddy et al. 2008). We proceed with the assumption that the likelihood of observing LyC is to first order independent of absolute magnitude, as implied by our earlier analysis. In the sample of 84 objects for which our sensitivity is above $f_{900}^{det} = 0.042\,\mu$Jy, the frequency of LyC detections is $p = 11/84 = 13 \pm 4\%$. Note that this is still consistent with a situation where fainter sources "leak" a higher fraction of the ionizing photons produced in their star-forming regions, as the nature of our survey is subject to detection threshold in flux, not in f_{900}/f_{1500} flux ratio.

Integrating the LBG luminosity function of Reddy et al. (2008), we find the comoving density of galaxies brighter than $M_{1700} = -19.5$ (or $0.2L_*$) to be $\rho_{gal} = 2.4 \pm 1.5 \times 10^{-3} Mpc^{-3}$. The median IGM transmission for ionizing photons over the f_{900} wavelength range ($880 - 910$ Å) is $e^{-\tau} \sim 52\%$ (mean $e^{-\tau} \sim 38\%$) so that if $p = 13 \pm 4\%$ of LBGs at $\langle z \rangle = 3$ allow f_{900}^{det} to escape, their total comoving ionizing emissivity at rest frame 900 Å is given by:

$$\varepsilon_\nu = p \times \rho_{gal} \times \frac{f_{900}^{d} et}{(1 + \langle z \rangle)} \times 4\pi d_L^2 \times e^{\tau_{IGM}}. \tag{3.5}$$

For the values assumed above we obtain $\varepsilon_\nu = 4.6 \pm 3.2 \times 10^{24}$ ergs s^{-1} Hz^{-1} Mpc^{-3}. This value represents a firm lower limit on the contribution of star-forming galaxies to total comoving emissivity of ionizing radiation at $z = 3$.

For a LyC photon mean free path length of $\Delta z = 0.18$, we can calculate the proper specific intensity of the ionizing radiation as

$$J_\nu \approx \frac{1}{4\pi} \times (\frac{dl}{dz})_{z=3} \times \Delta z \times (1+z)^3 \times \varepsilon_\nu, \tag{3.6}$$

where dl/dz is the proper length interval in our assumed cosmology evaluated at $z = 3$ and $(1 + z)^3$ adjusts from comoving to proper emissivity. We obtain a lower limit of $J_\nu = 1.1 \pm 0.8 \times 10^{-22}$ ergs s^{-1} Hz^{-1} cm^{-2} sr^{-1}.

A firm upper limit on J_ν can be estimated by considering that the remaining 87% of Lyman-break galaxies cannot emit more than $f_{900}^{lim} = 0.032\ \mu$Jy on average. This contribution could increase the estimate of J_ν at most by a factor of six, to $J_\nu \sim 6 \times 10^{-22}$ ergs s^{-1} Hz^{-1} cm^{-2} sr^{-1}.

The photoionization rate is related to specific intensity J_ν as:

$$\Gamma_{HI} = 4\pi \times \int_{\nu_{912}}^{\infty} \frac{J_\nu}{h\nu} \sigma_{HI}(\nu) d\nu. \tag{3.7}$$

Most recent estimates of the metagalactic hydrogen ionization rate give a value $\Gamma = 0.5 \pm 0.1 \times$

$10^{-12}s^{-1}$ (Faucher-Giguère et al. 2008). Adopting a spectral slope for J_ν of $\nu^{-1.8}$ (Madau et al. 1999), this ionization rate corresponds to $J_\nu \sim 2 \times 10^{-22}$ ergs s^{-1} Hz^{-1} cm^{-2} sr^{-1}. This estimate would need to be adjusted by a factor of two if the spectral slope of the ionization field is varied between ν^{-3} and ν^{0}.

Hunt et al. (2004) estimate the contribution of QSOs to ionizing flux at $z = 3$ to be $J_\nu^{QSO} \sim 2 \times 10^{-22}$ ergs s^{-1} Hz^{-1} cm^{-2} sr^{-1}. Siana et al. (2008) derive a similar value of $J_\nu^{QSO} \sim 1.5 \times 10^{-22}$ ergs s^{-1} Hz^{-1} cm^{-2} sr^{-1}. On the face of it, the contribution of galaxies to the ionizing background is at least half of the amount supplied by QSOs. Given all the uncertainties involved in the estimate of the total photo-ionization rate at $z = 3$, it is clear that QSOs and star-forming galaxies together can definitely produce enough ionizing radiation to keep the IGM ionized.

3.6 Effects of Variation in IGM Opacity

As can be seen from equations (3.1)–(3.3), the uncertainty in the amount of IGM attenuation along the line of sight to a given galaxy directly translates into the uncertainty of the inferred escape fraction. We have no means of independently estimating the IGM optical depth at the LyC in individual objects. Therefore it is a legitimate concern whether or not the average IGM optical depth is applicable for all 11 objects with LyC detection.

Predictions for the distribution of the IGM opacity made using empirical distributions of absorbing gas properties (Madau 1995; Bershady et al. 1999; Inoue & Iwata 2008). For example, at a redshift $z = 3.06$ (basically equal to the mean redshift of our spectroscopic sample $z = 3.05$), S06 demonstrate that IGM transparency at the rest-frame 900 Å has an expected mean of $e^{-\tau_{IGM}} = 0.38$. However, individual realizations of transparency can range anywhere between 0.03 and 0.62 (in a 95% confidence interval). These values were derived using a Monte-Carlo simulation of IGM absorbers based on Bershady et al. (1999) MC-NH model (see Figure 9 of S06). Such a broad range of possible values can severely compromise any derivation of unabsorbed 900 Å flux based on the mean expected IGM transparency alone. Below the Lyman continuum, the IGM transparency models are very sensitive to numbers of Lyman limit systems (Iwata et al. 2009). Therefore, a detected source could be along a line of sight having typical Ly α forest opacity distribution, but clearer than average lines of sight when it comes to Lyman limit systems.

We can, however, investigate this bias by comparing the distribution of LyC detections in our sample with a simulated efficiency of our spectroscopic survey in luminosity and redshift space which would incorporate a model for the variance in the IGM absorption.

The sensitivity achieved for f_{900} flux measurements in this work depends, for the most part, on sky brightness at observed wavelengths corresponding to 900Å in the rest-frame, which is a direct function of target redshift (Figure 3.2). Adopting a value for the ratio $(L_{1500}/L_{900})_{int} = 3$, and

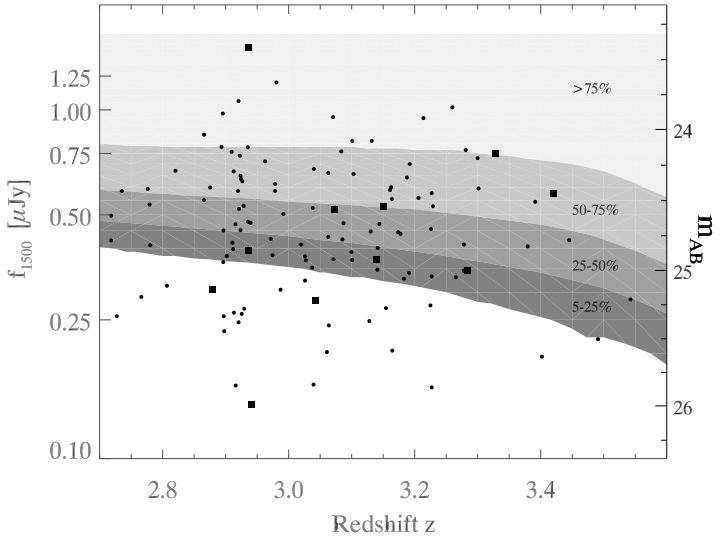

Figure 3.8 Probability of occurrence of lines of sight in the IGM having an opacity lower than necessary to attenuate LyC flux below our survey sensitivity limit (assuming constant $f_{esc} = 20\%$). The shaded regions outline the $[f_{1500}, z]$ parameter space for which this probability is in the intervals $5\% - 25\%$, $25\% - 50\%$, $50\% - 75\%$ and $\geq 75\%$. The square symbols show 11 LyC detections and the rest of the DLCS sample is shown with dots. See discussion in Section §3.6

a constant $f_{esc} = 20\%$, for any given continuum luminosity f_{1500} we can make a prediction of the observed flux f_{900}. We perform this calculation for a grid of points in $[f_{1500}, z]$ parameter space, and at each point we evaluate the probability that the IGM opacity is lower than would be required to decrease the inferred f_{900} flux below our $3\sigma_{900}(z)$ detection limit. To obtain the probability distributions of IGM opacity in the LyC for the full redshift range covered by our sample, we have repeated the Monte-Carlo simulations described in S06 at regular redshift intervals $z = 2.7$ to $z = 3.6$ (in increments $\Delta z = 0.1$).

The results of this analysis are presented in Figure 3.8. We see that for continuum flux levels above ~ 0.8 μJy, for more than 75% of the lines of sight in the IGM we would still be able to detect the inferred f_{900} flux, given the assumption of a constant $f_{esc} = 20\%$. However, we have observed 11 objects in this region of the parameter space, but found only 1 detection. This suggests that for the brighter objects the sample average escape fraction is significantly lower than the assumed 20%. On the other hand, going to the faintest luminosities, we detect LyC in 3 out of 25 objects where less than 5% of the IGM lines of sight are clear enough not to attenuate their flux below our detection limit. Clearly, the assumption of $f_{esc} = 20\%$ for these objects is too low.

Changing the assumed value of constant f_{esc} for all objects in this analysis only shifts the probability bands with respect to the continuum luminosity scale. Shown in Figure 3.9 are the results of the assuming a constant $f_{esc} = 30\%$. A larger f_{esc} does not alleviate the problem that we

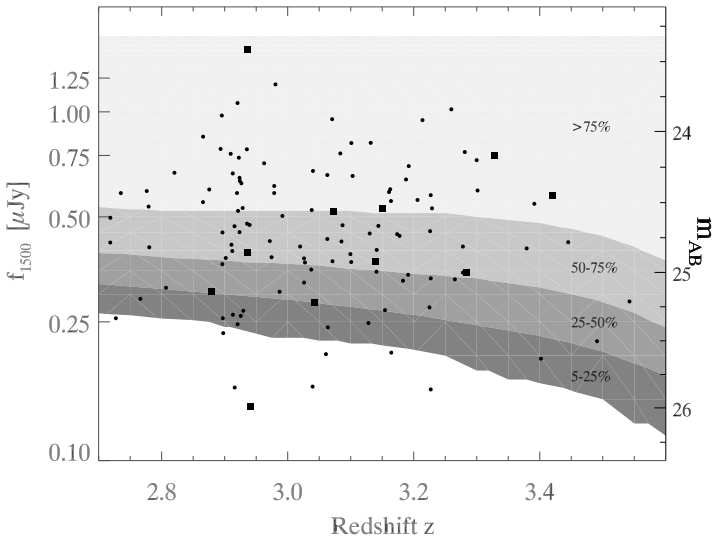

Figure 3.9 As in Figure 3.8, but for $f_{esc} = 30\%$.

detect LyC in too few bright objects and comparatively too many among the faint ones. We conclude that the considerations of variance in IGM transparency may only scale the inferred escape fraction for individual objects, but can not alter our conclusion that we observe luminosity dependence of LyC escape, in a sense that fainter galaxies appear to show a higher escape fraction of LyC radiation.

3.7 Composite Spectra of DLCS Galaxies

We now turn to the investigation of spectral properties of galaxies with measured escaping LyC radiation. The apparent similarity in the range of luminosity and redshift for galaxies with and without detected LyC allows for a direct comparison of the average spectrum for these two samples. Any differences observed between the two average spectra are likely related to distinctive physical conditions which allow Lyman continuum radiation to escape into the IGM.

3.7.1 One-Dimensional Composite Spectra

All extracted one-dimensional spectra of DLCS galaxies are scaled according to the value of continuum flux f_{1500}. After shifting into rest-frame, the spectra are resampled to a common wavelength grid using spline interpolation and averaged an iterative median clipping rejection algorithm. In this process the mean value is established after outliers with values differing more than 3σ from the initial median flux are rejected. This rejection algorithm decreases the noise in the composite spectra and we have verified that none of the conclusions are altered if we apply a plain average.

Figure 3.10 presents a global overview of spectral features in the composite spectra of galaxies

with and without significant LyC flux for wavelengths in the range $860-1200$ Å in the rest-frame. We observe a close similarity for the continuum flux decrement observed in the $1050-1170$ Å range (D_A) of the two composites. The strength of absorption in this wavelength interval is mostly determined by the number of low column density ($N(HI) < 10^{15} cm^{-2}$) systems in the Lyman alpha forest. The continuum flux for "LyC detected" composite in the range $930-1040$ Å becomes increasingly higher than the "LyC not detected" composite spectrum in the range $930-1040$ Å . This becomes very prominent at wavelengths below Lyman γ. The "Lyc not detected" composite spectrum shows the clear onset of blending of absorption lines caused by higher Lyman series transitions than Ly_7 (926.2 Å, see inset in Figure 3.10). The flux in this composite spectrum decreases to a value very close to zero around 920 Å. This is a secure observational result, as gap of 8 Å before the onset of Lyman continuum in the rest-frame translates to ~ 32 Å in observed frame, which is more than 4 times the value of the LRIS-B spectroscopic resolution, and also more than 8 times greater than the wavelength interval corresponding to 1σ rms for spectroscopic redshift.

Contrary to this, the flux seen in the composite of galaxies with detected LyC radiation does not have a sharp decrease below Ly_7, but retains an average value of $\sim 0.1 f_{1500}$. At wavelengths just below the onset of Lyman continuum, it shows an increase to an average value $f_{900} \sim 0.14 f_{1500}$, as expected from the values of f_{900} for individual sources presented earlier.

Figure 3.11 shows the two composite spectra in the wavelength interval $1250-1600$ Å, where the most prominent features are ISM absorption lines. We observe that the strength of the absorption lines is systematically weaker in the LyC composite. This is likely an indication of the average covering fraction of the absorbing material, which could very well be causally related to LyC escape. The inset of Figure 3.11 focuses on Lyman α, with the LyC detected sample showing significantly stronger emission on average. Though the detailed radiative transfer analysis of Lyman α trough a multi-phase ISM is very complex, we do know that this emission line is easily quenched by dust. As we will demonstrate further in Section 3.8, there is strong evidence that we detect LyC preferentially in galaxies with very low value of dust extinction.

3.7.2 Two-Dimensional Composite Spectrum of LyC Detections

The composite described in the previous chapter is an average of spectra extracted using a 10-pixel wide aperture ($1.35''$ on LRIS-B). As a consequence, any information about the spatial flux distribution below the scale of the aperture width is lost, together with any flux that may be detectable outside of the extraction aperture.

Iwata et al. (2009) report on the finding that there is a significant positional offset between the origin of Lyman continuum flux and the bulk of photons at longer UV wavelengths. These authors used imaging in narrow-band ($NB359$) matching the wavelength of LyC for a large sample of galaxies located in the SSA22 proto-cluster ($z = 3.09$). Images in the R-band were used to estimate the UV

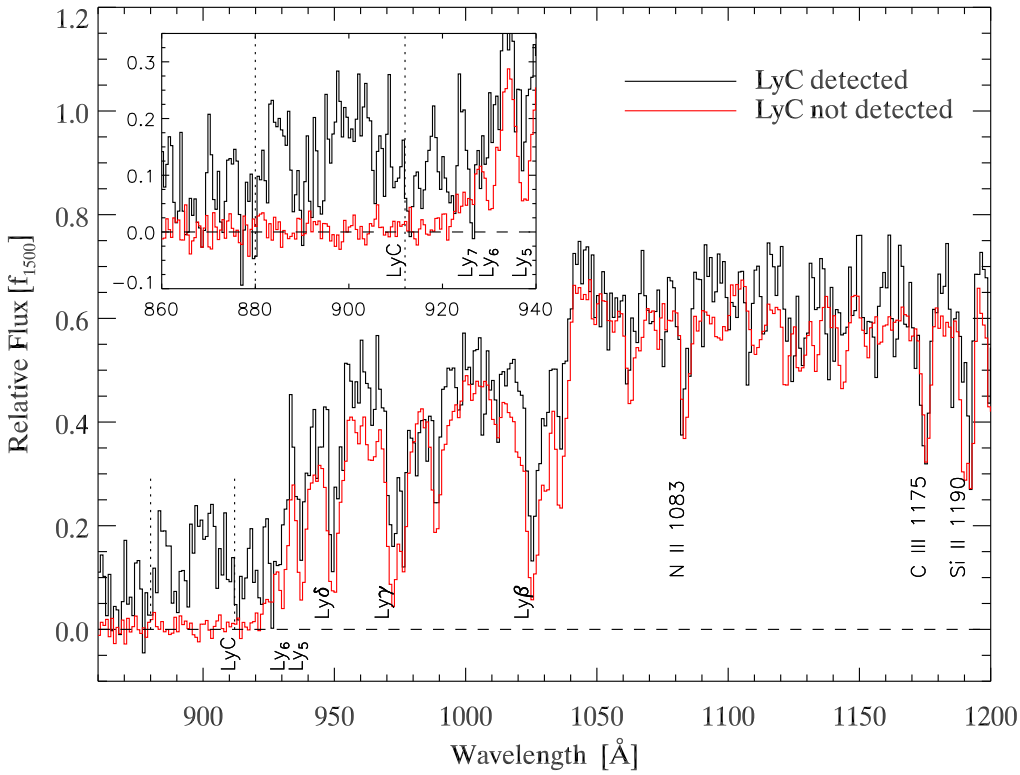

Figure 3.10 Comparison of two composite spectra obtained from the sample of 11 galaxies with detected LyC flux (black line) and from the sample of 110 galaxies without significant LyC flux (red line). The flux is units of f_{1500}. Spectra are re-binned to a resolution of 1 Å per pixel in rest-frame for clarity. The inset focuses on the wavelength interval 860–920 Åwith the spectra sampled at 0.5 Å per pixel. Dotted lines mark the interval 880–912 Åwhere f_{900} measurement is obtained. Several of the strongest absorption features are labeled. Higher Lyman series transitions than Lyδ are labeled with Ly_5, Ly_6 and Ly_7.

continuum luminosity. Iwata et al. (2009) find 17 objects with significant escaping LyC radiation and discover that the average positional offset between the NB359 and the R-band images for these galaxies is $0''.97$. Higher resolution images taken with *HST/ACS* have showed that many of LyC detected galaxies have a multiple component structure, and that Lyman continuum emission appears to be associated with only a fraction of these components.

The slit width used for DLCS observations is $1''.2$, comparable to the average offset of escaping LyC flux found by Iwata et al. (2009). This raises concerns if we might be missing a significant amount of escaping radiation. Some LyC flux could conceivably come from regions of the galaxy outside of the center of our slit, or outside the extraction aperture, decreasing the number of galaxies where we can detect the LyC.

To investigate this, we have created another composite spectrum of LyC detections, this time using the full 2-dimensional (2-D) background-subtracted spectrograms for each source. The spec-

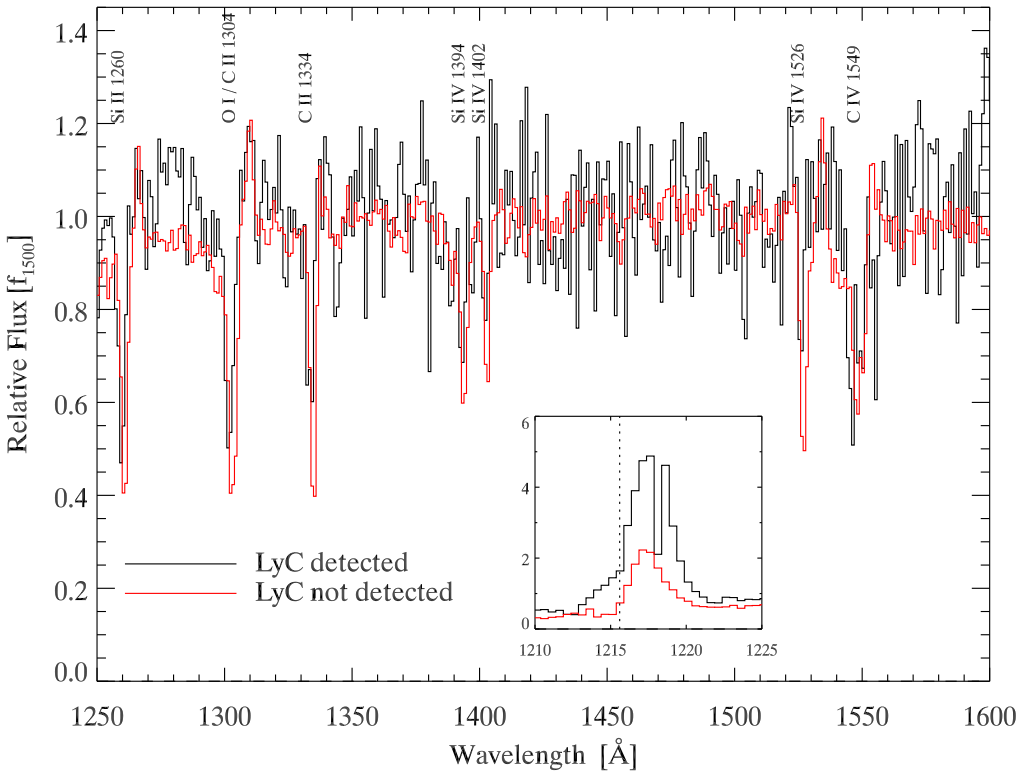

Figure 3.11 Same as in Figure 3.10, here showing the wavelength interval 1250–1600 Å in the rest-frame. Spectra are re-binned to a resolution of 1 Å per output pixel, and the composite of sources without LyC detection has been shifted by 1 Å for clarity. The inset shows the relative strengths of Ly α line, with spectra sampled at 0.5 Å per pixel (no shift applied). The dotted line in the inset is at Ly $\alpha = 1215.6$ Å. Strongest absorption features are labeled.

trograms were resampled to a common wavelength grid in the rest-frame. After flux calibration and galactic extinction correction were applied, the pixel counts in these 2-D spectra were scaled according to the f_{1500} flux measurements obtained earlier. All other objects found in the slit apart from the DLCS target were masked, and individual spectrograms were registered and averaged using min-max rejection.

Figure 3.12 shows the spatial distribution of the detected flux in selected wavelength intervals, obtained from this 2-D composite. We use the median flux from the range 950–1190 Å as an guideline for the spatial profile of continuum radiation in the UV. The full width at half maximum (FWHM) for this spatial profile is $1\farcs1$. In comparison, the median flux from the wavelength interval 880–910 Å, where LyC measurement is performed, shows a much more extended shape, with a FWHM of $\sim 2''$. We also show the median flux centered on Ly α for comparison. It has already been reported in the literature that Ly α emission is significantly more extended than the continuum radiation for $z \sim 3$ galaxies (Hayashino et al. (2004); also see results of the study in Chapter 4). We also see a

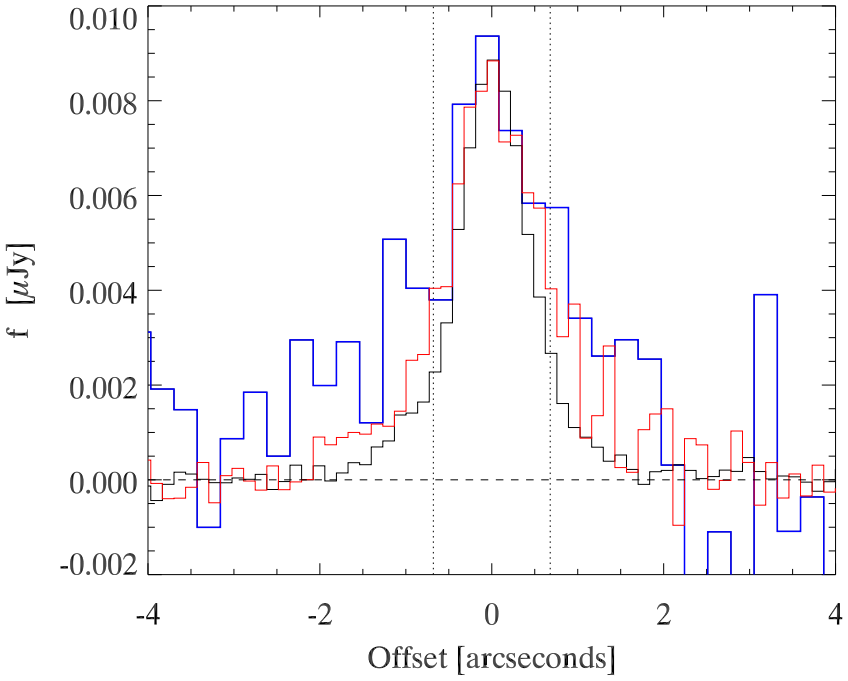

Figure 3.12 Spatial distribution of emission from the 2-dimensional composite spectrogram of galaxies with LyC detection. Blue histogram shows the median flux in the the rest-frame LyC wavelength range ($880-910$ Å), binned by a factor of 2 in the spatial direction. Black and red histograms show the median flux distribution in 950–1190 Å and Lyman α (1211–1220 Å) range, scaled to same peak value for clarity. Dotted lines show the extent of our spectroscopic aperture used for measuring f_{900} in individual objects. The flux outside this aperture is comparable to f_{900}. Emerging LyC flux is observed up to a distance of $2''$ (16 kpc). Average Ly α emission is seen to be slightly broader than continuum.

slight indication of extended Ly α in the average 2-D composite spectrum of LyC detections.

Though there is significant noise in the LyC profile shown in Figure 3.12, as we are reaching the sensitivity limit where systematical errors become important, we find that a larger FWHM for the extent of LyC radiation is a robust result. The LyC flux measured from the 2-d composite in an aperture twice as wide as used in for individual spectra is $\sim 50\%$ larger.

Our results support the findings of Iwata et al. (2009) and have several important consequences. First, careful considerations of this positional offset will have to be made in future spectroscopic studies of LyC. Second, our estimates for the contribution to total ionizing radiation from galaxies may need to be enlarged by 50% accordingly. These findings also open up crucial questions about the nature of the mechanism by which LyC escapes from galaxies. Another question that remains to be answered is whether the stars responsible for bulk of the LyC have a different spatial distribution from those that emit the bulk of UV radiation.

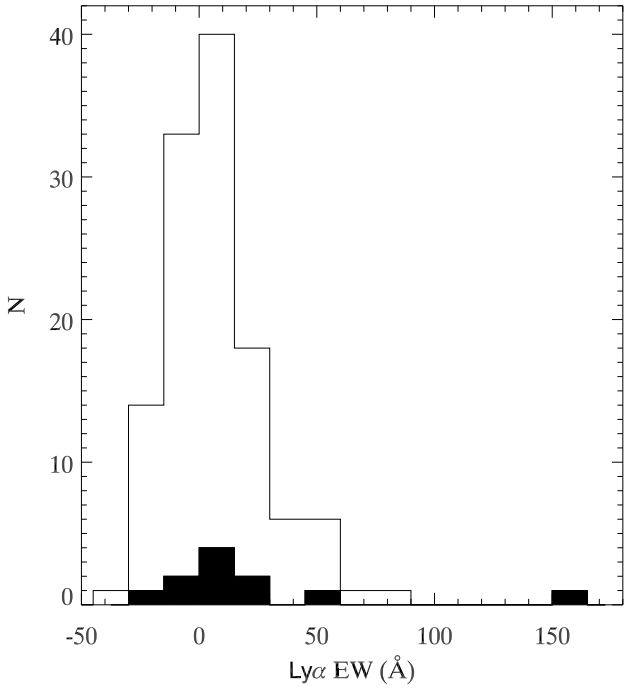

Figure 3.13 Distribution of Ly α rest-frame equivalent width as measured from the DCLS spectra. Measurements of Lyman α for the 11 galaxies with detected Lyman continuum flux are presented by the solid histogram.

3.8 Stellar Populations of Galaxies with LyC Detection

In this section we present a cursory investigation into stellar populations of galaxies with detected Lyman continuum leakage. Rest frame UV photometry alone (observed bands U_n, G, R) does not provide enough information to distinguish between galaxies which are dominated by a recent star formation episode but have been considerably reddened by dust, from those that are redder primarily due to a substantial contribution to total luminosity coming from older stars. Some estimates of the amount of dust extinction for $z \approx 3$ galaxies can be derived using observed $G - R$ color alone (corrected for Ly α equivalent width and IGM opacity), but this would require assuming a fixed common age for the stellar populations of all galaxies (Adelberger & Steidel 2000). In order to be able to break the age-reddening degeneracy, supporting near-infrared (rest-frame optical at $z \approx 3$) observations are necessary.

Portions of five fields from which our DLCS targets were chosen (Q0100, Q0933, Q1009, Q1422 and Q1549) were imaged with $WIRC$ on the 200-inch telescope at Mt.Palomar in K_s (Erb et al., in preparation). Imaging in near-IR J band is available for fields Q1549 and Q1009 from the same work. Additionally, Spitzer IRAC photometry in at least one of the four channels (3.6,4.5,5.8 and 8.0 μm) is publicly available for 18 sources from fields Q1549 and WESTPHAL. Lastly, 5 sources (B20902-

M11, B20902-MD21, B20902-MD32, DSF2237b-M20 and WESTPHAL-CC32) were observed in J and Ks bands with NIRC on W. M. Keck I Telescope and photometry published in Shapley et al. (2001). All of these supplementary observations gave us at least one broadband photometry point longward of the age-sensitive Balmer break (3646 Å in rest-frame) for a total of 62 out of 122 DLCS galaxies. This subsample includes five sources with detected Lyman continuum flux (Q1549-D3, Q1549-C25, Q1422-d42, Q1422-d68 and WESTPHAL-CC38).

We proceeded to fit model galaxy SEDs obtained with Bruzual & Charlot (2003) population synthesis code to the available broadband photometry data. Our approach is identical to SED modeling presented in Shapley et al. (2001) and we refer the reader to their section 5.2 for details. Here we will just briefly recapitulate the procedure for clarity. Only models with a constant star formation history are considered. Prior to SED fitting we applied a correction to the $G - R$ color for the strength of Ly α line emission or absorption using equivalent width measurements obtained from our deep spectroscopy (Figure 3.13). We have also assumed that Solar metallicity, Salpeter IMF with a range of $0.1 - 125\,\mathrm{M}_{\odot}$ and a Calzetti extinction law (Calzetti 1997) are satisfactory for this analysis. More rigorous approach to stellar population modeling of DLCS galaxies is beyond the scope of this paper.

The SED fitting algorithm returns estimates of extinction (parametrized by $E(B-V)$), age since the onset of most recent episode of star formation (t_{sf}) and the continuous star formation rate ($\Psi(t) = \Psi_0$). We have applied a constraint on the best-fit result for the age t_{sf} to be greater than the dynamical timescale of star-forming regions in LBGs at $z \sim 3$, which is estimated at about 30 Myr. An age for an average stellar population lower than the dynamical timescale would be unphysical for reasons of causality.

In Figure 3.14 we present best-fit values for $E(B-V)$ and constant star formation rate Ψ_0. The median values of model parameters we obtain for this sample of 62 galaxies are $\langle E(B-V)\rangle = 0.14, \langle \Psi_o \rangle = 57h^{-2}\,\mathrm{M}_{\odot}/\mathrm{yr}, \langle t_{sf}\rangle = 360$ Myr. Both the median and the range of model parameters are very similar to values obtained in Shapley et al. (2001), for a somewhat larger sample of LBGs ($\langle E(B-V)\rangle = 0.15, \langle \Psi_o \rangle = 45\,\mathrm{h}^{-2}\,\mathrm{M}_{\odot}/\mathrm{yr}, \langle t_{sf}\rangle = 320\,\mathrm{Myr}$). However, we caution the reader to take these results only as a guideline. The supporting near-IR observations we have compiled were not uniform in depth, and there were differing number of near-IR points available per source. For this reason, the confidence with which SED fitting was able to constrain stellar population parameters varies among sources presented. Additionally, the values of these parameters would change to a certain extent under different SED modeling assumptions. For these reasons we will proceed in this analysis taking just the relative ordering of galaxies in $E(B-V)$ and Ψ_0 values, which should be generally robust under different model assumptions and with respect to uncertainties in best-fit parameters.

We can observe the same correlations between results for best-fit SED model parameters as

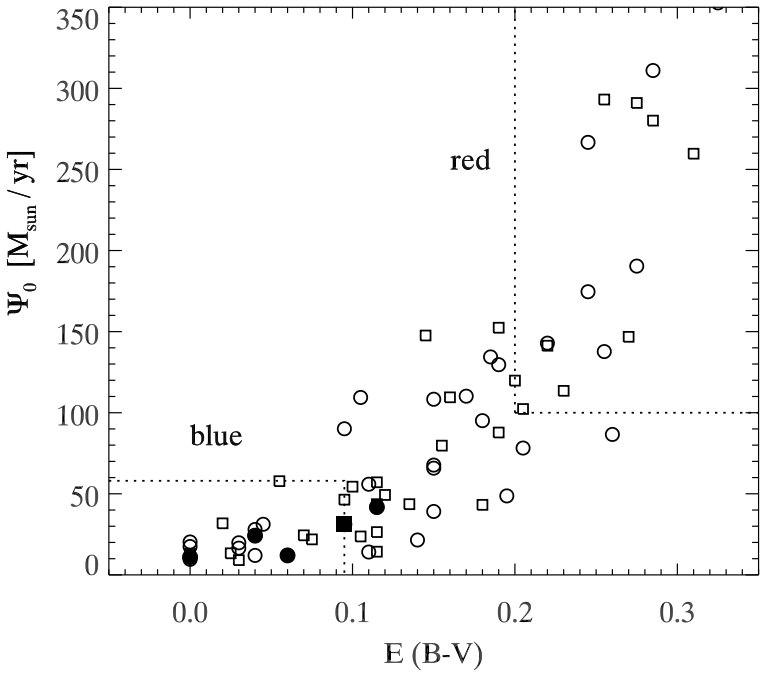

Figure 3.14 Best-fit values for dust extinction ($E(B-V)$) and constant star-formation rate (Ψ_0) obtained for a subsample of 62 galaxies. Galaxies for which only U_n, G, R, K_s photometry was available are shown as square symbols, while those for which a measurement in at least one IRAC band was available are marked with a circle symbol. Five sources with detected Lyman continuum flux are marked with solid symbols. Dashed lines separate the top and bottom quartile in this distribution, taking into account only galaxies without LyC detection. Labeled as the "blue" star-formation (SF) sample are 15 galaxies within $0 < E(B-V) < 0.095$ and constant star-formation rate $\Psi_o < 58h^{-2}M_\odot/yr$. The "red" star-formation subsample are 15 galaxies with best-fit SED parameters in the range $E(B-V) > 0.2$ and $\Psi_o > 100h^{-2}M_\odot/yr$.

discussed at length in Shapley et al. (2001). Galaxies with higher values of best-fit continuous star formation rate have both higher amount of dust extinction (Figure 3.14) and lower age since the onset of the last star formation episode t_{sf}. Additionally, there is a significant correlation between the age of star-formation t_{sf} and $E(B-V)$, in the sense that galaxies with with less prominent Balmer break (i.e., a higher luminosity contribution from short-lived hot stars) also require more dust extinction in order to match the rest-UV photometry. These findings support the assumption that our deep spectroscopic sample is fully representative of Lyman-break galaxy population at $z \sim 3$ that has been studied previously.

Dashed lines in Figure 3.14 outline two regions with limits chosen such that each contains exactly 15 galaxies with no detection of Lyman continuum flux, representing top and bottom quartile of the distribution in $(E(B-V), \Psi_o)$ values. We will call these two comparison subsamples of non-leaking galaxies "red" and "blue," the former showing significantly stronger dust extinction. For

the subsample of 15 "blue" sources the average values are $t_{sf} = 1383Myr$, $E(B-V) = 0.03$ and $\Psi_o = 22h^{-2}M_\odot/yr$, whereas for the 15 "red" galaxies they are $t_{sf} = 177Myr$, $E(B-V) = 0.26$ and $\Psi_o = 220h^{-2}M_\odot/yr$. Note that labels "red" and "blue" refer only to the inferred value for the amount of dust extinction. Rest-UV and optical photometry is dominated by radiation from early-type (O/B and A spectral class) stars and therefore it cannot provide good constraints on age of the global stellar population and, consequently, total stellar mass.

Large filled symbols in Figure 3.14 show the positions of five galaxies with detected Lyman continuum flux. It is immediately apparent that all five of these galaxies have among the lowest best-fit star-formation rate and below average dust extinction. There is currently no near-IR photometry available for the other 6 Lyman continuum leaking galaxies and thus their $E(B-V)$ and star-formation rates could not be derived and compared using the same approach. Here we are forced to employ an indirect approach in order to examine if all LyC detections have low values for continuous star-formation rate and dust extinction as well. Shapley et al. (2001) have demonstrated that several distinguishing characteristics can be observed in the rest-UV spectra of "red" and "blue" star-formation galaxies. Most prominent of those are the different strengths of Ly α emission and low-ionization ISM absorption lines. Spectra of "red" galaxies with higher than average extinction and high continuous SFR feature a Ly α line with a mixture of an emission and absorption component, resulting in low average equivalent width. On the other hand the "blue" star-formation galaxies are observed to have much stronger Ly α emission, possibly as a result of lower dust content which would otherwise scatter and absorb Ly α. In addition, low-ionization ISM absorption lines are seen to be significantly stronger in "red" galaxies. One possible interpretation of this trend is that higher star-formation rates produce a broader range of velocities in the interstellar medium, owing to stronger shock heating by supernovae. Low-ionization ISM absorption lines observed in rest-UV should be optically thick and therefore sensitive to differences in velocity width (rather than column density), producing the observed relation with star-formation rate. The correct interpretation of such qualitative trends in Ly α emission and ISM absorption is not yet clear. Regardless, existence of these correlations allows us to investigate the place of LyC leaker galaxies within these two populations.

Average spectra obtained from the "red" and "blue" samples and from all 11 galaxies with LyC detection are compared in Figure 3.15 and Figure 3.16. Ly α emission is observed to be strongest for "blue" galaxies ($EW \sim 19$ Å) followed closely to that seen in for LyC "leakers" ($EW \sim 16$ Å). On the other hand, the average "red" galaxy has a substantially weaker Ly α , with $EW \sim 3$Å (red dashed line). The difference in average extinction between the "red" and "blue" comparison samples as obtained from broadband SED fitting ($\Delta E(B-V) = 0.23$) is clearly demonstrated by the slopes of their spectral continua as well. On the other hand, we observe a very similar continuum slope for LyC leakers and the "blue" galaxies, suggesting similar average $E(B-V)$. The same similarity is

seen in the strength of low-ionization ISM absorption lines; they are equal for the "blue" and LyC detected apparently stronger in the "red" comparison sample.

The values of best-fit SED model parameters for 5 LyC leakers (Figure 3.14) indicate these galaxies are among those with the lowest observed star-formation rate and amount of dust extinction. This is further supported by the close similarity in strength of Ly α emission, continuum shape and ISM absorption features with the "blue" comparison sample. Though qualitative in nature, the analysis above suggests that all LyC leakers are likely characterized by very low star-formation rate and low dust extinction.

3.9 Stellar Lines and Detection of Molecular Hydrogen

In this section we briefly report on the observation of many weaker ISM and stellar features that are now accessible to investigation owing to the unprecedented depth achieved in the composite spectrum of all DLCS galaxies.

Figure 3.17 shows an identification chart with a number of ISM and stellar features (wavelength range 1000–1180 Å). The list of lines identified is based on model synthetic line spectra of star-forming galaxies presented in Robert et al. (2003). Figure 3.17 is based on Figure 9 in Robert et al. (2003) for easier comparison. Most prominent absorption lines originating in the ISM are labeled on top. A number of transitions of Fe, C, N, Ar, P, O and Si match the features seen in the composite spectrum. Absorption lines which originate in atmospheres of O/B stars are marked on the bottom of the plot. Besides strong stellar absorption features (O VI,C III) we find clear signatures of stellar S IV, P V and N IV. As a more quantitative description is beyond the scope of this work, we use this identification chart only as a demonstration that the Lyman α forest has been sufficiently removed in the average of the full DLCS galaxy sample. Most features remaining in the composite below 1215 Å can be attributed to real absorption lines with a high degree of certainty. This opens up, for the very first time, the possibility of a closer study of O/B stellar atmospheres at redshifts $z \approx 3$.

In Figure 3.18 we show the composite of all DLCS spectra in the wavelength range 920–1020 Å (middle panel). The bottom panel shows a model spectrum by Walborn et al. 2002, containing selected metallic lines convolved with an H I absorption spectrum. The strength of metal line transitions is based on Large Magellanic Cloud abundances (Walborn et al. 2002). A shift of -300 km/s has been applied to match the Lyman series in the DLCS composite. The top panel shows a model of Lyman-Werner absorption bands of H_2 together with H I absorption lines, from the same authors. We have chosen $N(H_2) = 5 \times 10^{19}$ cm^{-2} just for the sake of illustration of H_2 transition wavelengths and relative strengths. Note that both model spectra have been scaled to a continuum of 0.5 for clarity, whereas the composite has a continuum level of 1.0 as in Figure 3.17.

We select four wavelength regions in the DLCS composite, which according to the LMC spectrum

model are expected to be relatively clear of H I and metal absorption. These are 941–944 Å, 956–960 Å, 979–986 Å and 992–1020 Å. Absorption features in all four of these intervals are clearly present, and we attribute them to H_2 in the ISM. If these identifications are correct, this would be the first direct identification of H_2 UV absorption bands in average star-forming galaxies at high redshift. Searches for UV absorption features of molecular hydrogen at high redshift have so far been limited to spectra of damped Lyman α absorbers (Noterdaeme et al. 2008; Cui et al. 2005; Ge et al. 2001; Petitjean et al. 2000) and GRB host galaxies (Prochaska et al. 2009; Sheffer et al. 2009).

Due to the complex nature of the H_2 spectrum, high degree of blending in the transitions and the uncertain position of the continuum, we did not attempt to model physical parameters of the H_2 gas. However, based on the continuum level in the longest "clear" wavelength region 992-1020 Å, where a presence of saturated H_2 bands is likely, we can place a tentative upper limit to the covering fraction of H_2 gas at about 25–30%. Certainly, a much more thorough analysis of H_2 is possible, and should be performed in the future, including detailed models of ISM with multiple component atomic and molecular gas densities and temperatures (for example, see Browning et al. 2003).

3.10 Summary and Conclusions

We presented deep optical spectroscopic observations for 121 star-forming galaxies at $z \approx 3$. Our sample spans a broad range in redshift ($2.7 < z < 3.6$) and UV continuum luminosity $0.2 < L/L_* < 1.6$.

In spite of the high quality of individual spectra achieved, measurement of LyC radiation from spectroscopic observations remains very technically challenging. Utmost care must be given in quantifying the statistical and systematic errors involved. A major benefit of spectroscopic data lies in the ability to identify and reject cases of unrelated sources blended along the line of sight. We find that this type of foreground contamination is very significant ($\approx 5\%$), and this would severely affect any measurement of LyC based on imaging data alone.

After careful estimates of statistical and systematic errors, we find 11 individual star-forming galaxies with $> 3\sigma$ detection of LyC photons. We derive the escape fraction through the ratio of the observed LyC flux in the 880–910 Å range and the continuum luminosity at 1500 Å, the latter also being directly determined from our spectra. Under standard assumptions about the shape of SED for populations of young and hot stars, we find a broad range of f_{esc} in our sample, from 14% to 150%. As has been also noted in previous studies, we find cases with unphysical value $f_{esc} > 100\%$, indicating that standard assumptions about the value of intrinsic Lyman break in O/B stellar populations are not always applicable.

The mean value for 11 LyC detections is found to be $f_{esc} = 43\%$. Objects brighter than the luminosity of the break in $z \approx 3$ galaxy luminosity function have on average a lower escape fraction

$f_{esc} \approx 20\%$. A strong preference for higher values of escape fraction is observed for fainter galaxies, though the relative number of galaxies with LyC detection seems to be independent of UV continuum luminosity. To our sensitivity limit, we find that about $13 \pm 4\%$ of galaxies have detectable LyC flux.

We study the effect of the broad range in IGM attenuation for different lines of sight at $z \approx 3$. Though it is recognized that individual objects can lie along lines of sight which have significantly different IGM opacity than the mean, we find that our observation of higher escape fraction for fainter objects is robust for the sample. Put simply, the apparent dearth of galaxies brighter than L_* with $f_{esc} > 30\%$ is difficult to explain away by considerations of variability in IGM attenuation.

We derive that the integrated contribution of galaxies to ionizing radiation at $z \approx 3$ is $J_\nu > 1.1 \pm 0.8 \times 10^{-22}$ ergs s^{-1} Hz^{-1} cm^{-2} sr^{-1}. This is very close to the value observed for QSOs at the same redshift $J_\nu^{QSO} \approx 2 \times 10^{-22}$ ergs s^{-1} Hz^{-1} cm^{-2} sr^{-1}. We find that galaxies and AGN together produce enough LyC photons to keep the hydrogen in the Universe ionized.

An analysis of composite spectra of the LyC detections reveals that these objects have a stronger than average Lyman α emission but significantly weaker ISM absorption lines. As most ISM absorption lines are heavily saturated, this observation would imply a larger covering fraction of the absorbing gas in galaxies without LyC detection. Note that this logical correlation came out only in the composite of $> 3\sigma$ LyC detections, and therefore provides further credibility to individual LyC detections. Another notable difference of the composite spectra is in the appearance of Lyman series absorption lines. In particular, below 920 Åthe higher Lyman transitions start to blend, but we find that the "LyC detected" composite has significant escaping flux, whereas the "LyC non-detected" is fully absorbed. This independently suggests that there is a significant difference in the covering fraction of absorbing gas in the two samples.

A composite spectrum of $L > L_*$ galaxies without individual LyC detection places a firm upper limit on their average escape fraction $f_{esc} \leq 2\%$. On the other hand, we find a significant detection of LyC in the composite of fainter $0.2 < L < L_*$ galaxies, $f_{esc} \leq 5\%$. The reason for the apparent lack of brighter objects with intermediate values of escape fraction $2\% < f_{esc} < 14\%$ is not clear at this time. One possibility could be that this is a consequence of a relatively short timescale during which galaxies exhibit strong escaping LyC.

We investigated the spatial distribution of escaping LyC radiation using a 2-dimensional composite spectrum. We observe a significantly broader spatial extent of LyC radiation as compared to UV continuum. The profile of LyC radiation apparently extends 10 kpc more than the UV continuum. This supports earlier findings from LyC imaging that the regions emitting LyC can be spatially separated from centroid of the galaxy, as defined by the bulk of the UV continuum. It remains to be answered if this is an indication of the physical conditions in the ISM that allow the ionizing radiation to escape, or that the distribution of the stars producing LyC is substantially different

from those that emit most of the UV continuum. In any case, due to the nature of our survey, it is likely that our flux measurements are missing a fraction of the escaping LyC light. Taking this into account, the values for the contribution of galaxies to total ionizing budget could be revised upwards by as much as a factor of two.

The availability of supporting near-IR and mid-IR observations for about a half of our sample, including five objects with LyC detection, allowed us to derive stellar population parameters using SED modeling. All five objects are found to have low values of dust extinction ($E(B-V) \leq 0.1$) and star-formation rate ($\Psi_o < 58h^{-2}M_{\odot}/yr$). We extend this conclusion to all objects with LyC detection by a comparison with the average spectra of objects chosen from opposing ends of the $(E(B-V), \Psi_o)$ distribution. Composite spectrum of all 11 detections is very similar to a composite spectrum of galaxies without LyC chosen to have the lowest values of ($E(B-V)$ and Ψ_o). This striking resemblance is reflected in shape of the continuum, Lyman α emission and ISM absorption lines. On the other hand, the average spectrum of 11 LyC detections is significantly different from the average spectrum for galaxies with highest values of dust extinction and star-formation rate in all three of these respects. Further studies will have to address the question of why only a fraction of galaxies with low ($E(B-V)$ have detectable LyC flux. Apparently, the luminosity averaged value of dust extinction does not fully correlate with the gas covering fraction. It seems that more detailed models of gas and dust distribution in star-forming regions at high redshift are needed in order to address these questions. For this purpose, space-based observations of local star-forming galaxies in the far-UV are going to provide important insights.

The average spectrum of the full DLCS sample provides the most in-depth look to date into the structure of the ISM of galaxies at $z \approx 3$. We also tentatively identify a number of comparatively weaker stellar absorption features, opening up for the first time the possibility for detailed studies of O/B stellar atmospheres at high redshift. Furthermore, in several spectral regions free of strong H I and metal lines, we find absorption features that can be attributed to H_2 Lyman-Werner absorption bands. This is the first time that H_2 is directly observed in spectra of average star-forming galaxies at $z \approx 3$.

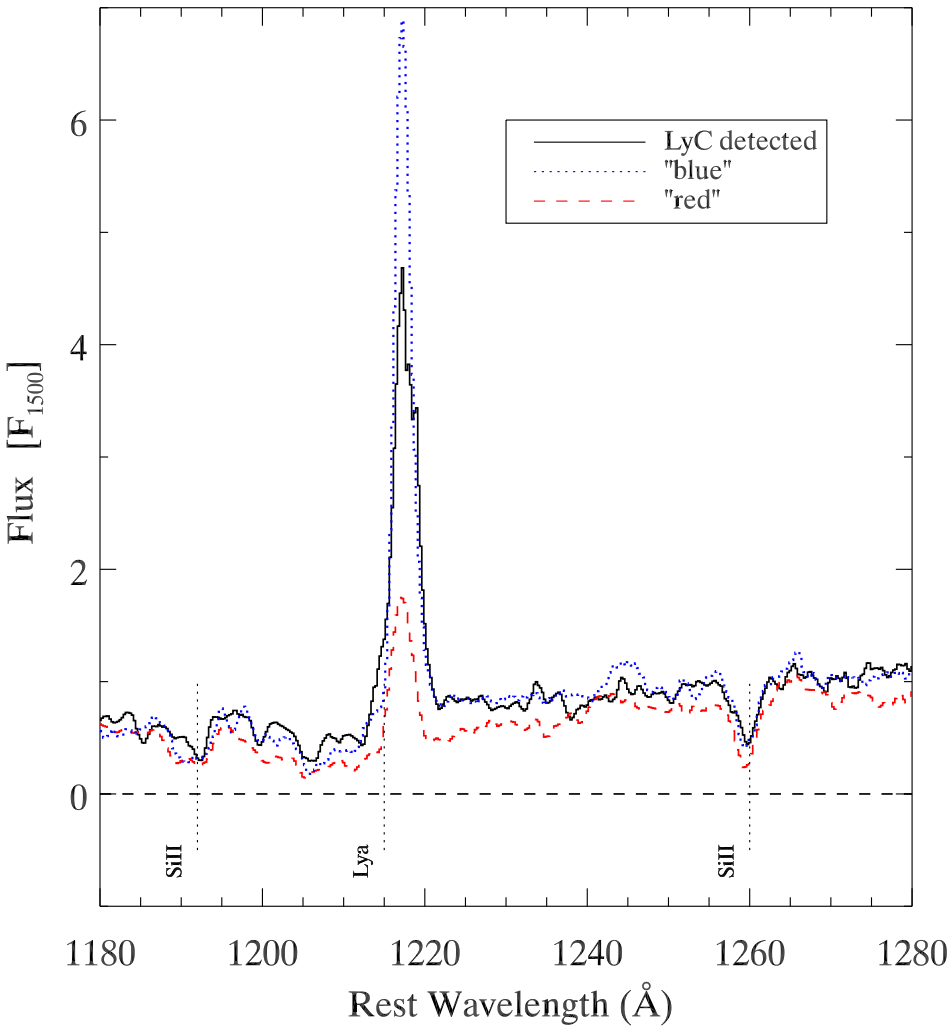

Figure 3.15 Average spectra of 11 galaxies with Lyman continuum detection (black solid line) and of two subsamples of galaxies without detectable LyC taken from the top and bottom quartiles in $(E(B-V),\Psi_o)$ distribution of Figure 3.14. Blue dotted line shows the average spectrum of 15 "blue" galaxies in terms of the value of best-fit E(B-V). Red dashed line is an average of 15 "red" galaxies in E(B-V) with no detectable Lyman continuum flux. All spectra are normalized to the value of mean flux at 1500Å . Equivalent widths of Ly α emission are $EW_0 \sim 14$ Å, 18 Å and 3 Å for the LyC detected, "blue" and "red" average spectrum respectively.

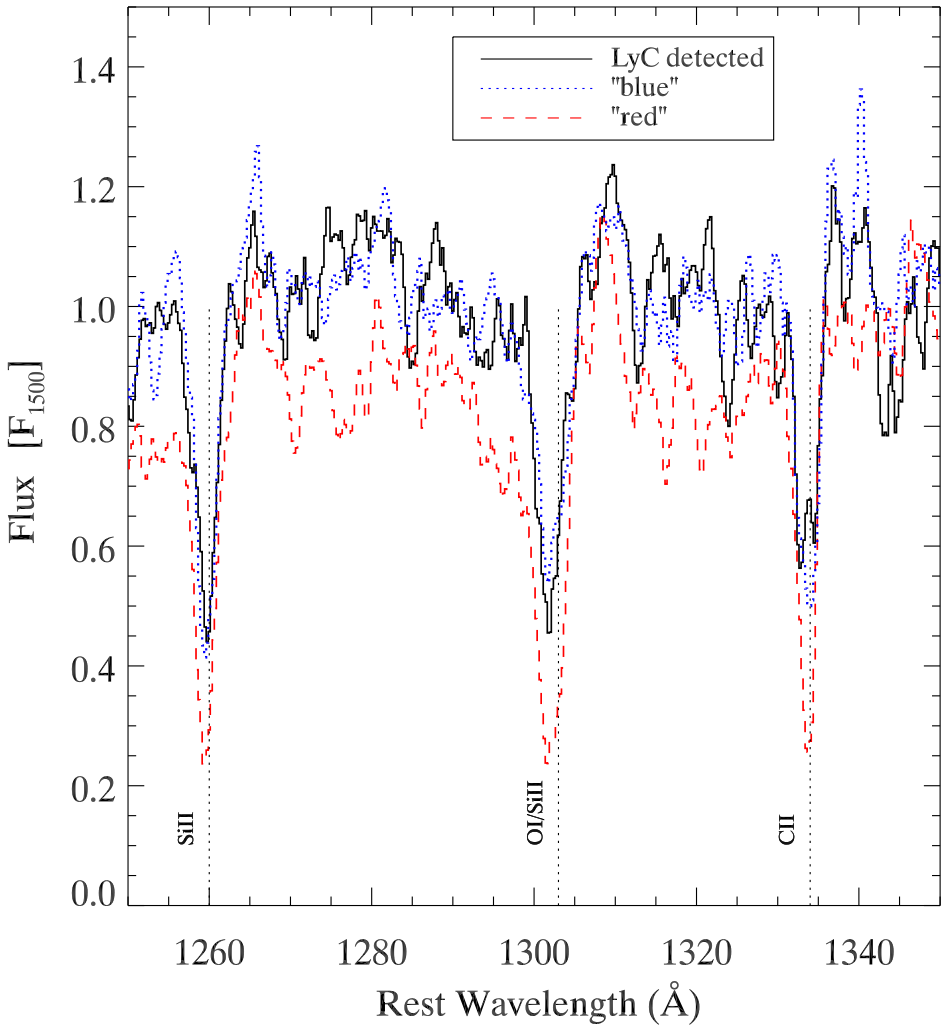

Figure 3.16 Same as in Figure 3.15, here focusing on a wavelength region containing ISM absorption lines Si II 1260, O I / Si II 1303 and C II 1334, The continuum shape and strengths of these absorption lines between the "blue" star-formation subsample without significant leaking LyC (blue dotted line) and average spectrum for all 11 galaxies with detected LyC flux (black solid line) are indistinguishable. The difference in amount of dust extinction as determined by SED fitting to broadband photometry is also apparent here in the a markedly redder continuum slope observed for the "red" galaxies (red dashed line).

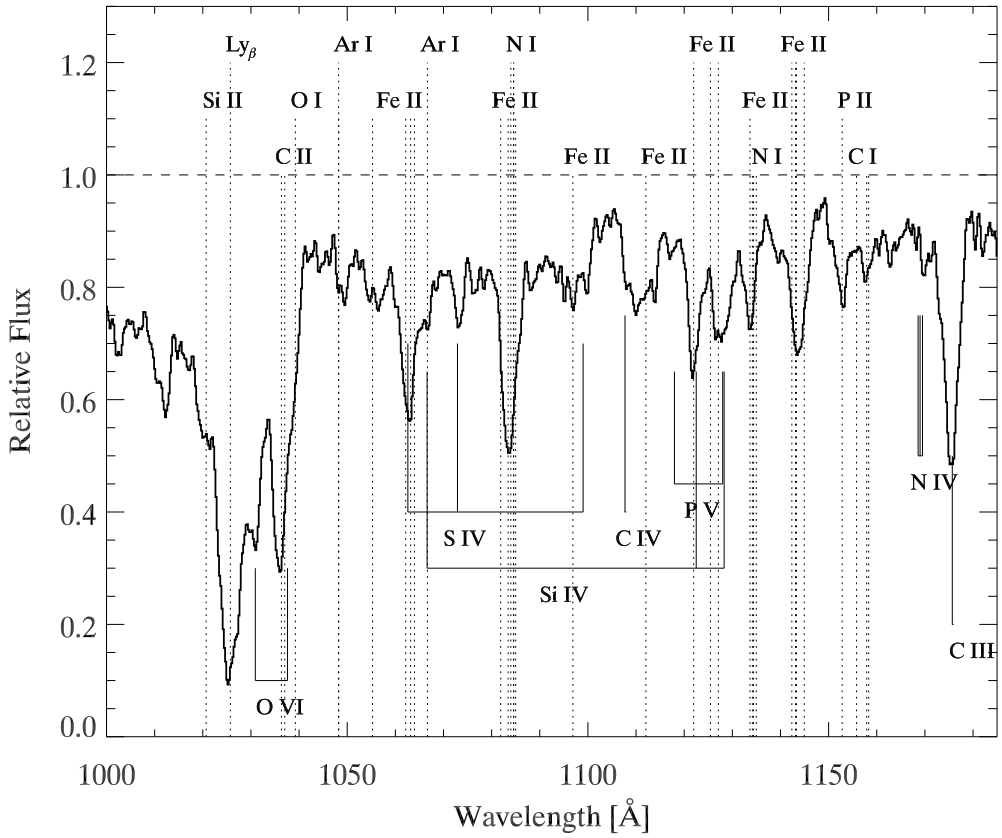

Figure 3.17 Interstellar and stellar absorption features identified in the composite spectrum of all 121 DLCS galaxies. Shown here is the wavelength range $1000 - 1180$ Å. The composite spectrum is normalized to unity at 1500 Å and is corrected for average IGM absorption. Most prominent absorption lines originating in the ISM are labeled on top, with dotted lines indicating separate transitions. Absorption lines that have a component of stellar origin are labeled below and marked with solid vertical lines. Compare with Figure 9. of Robert et al. (2003).

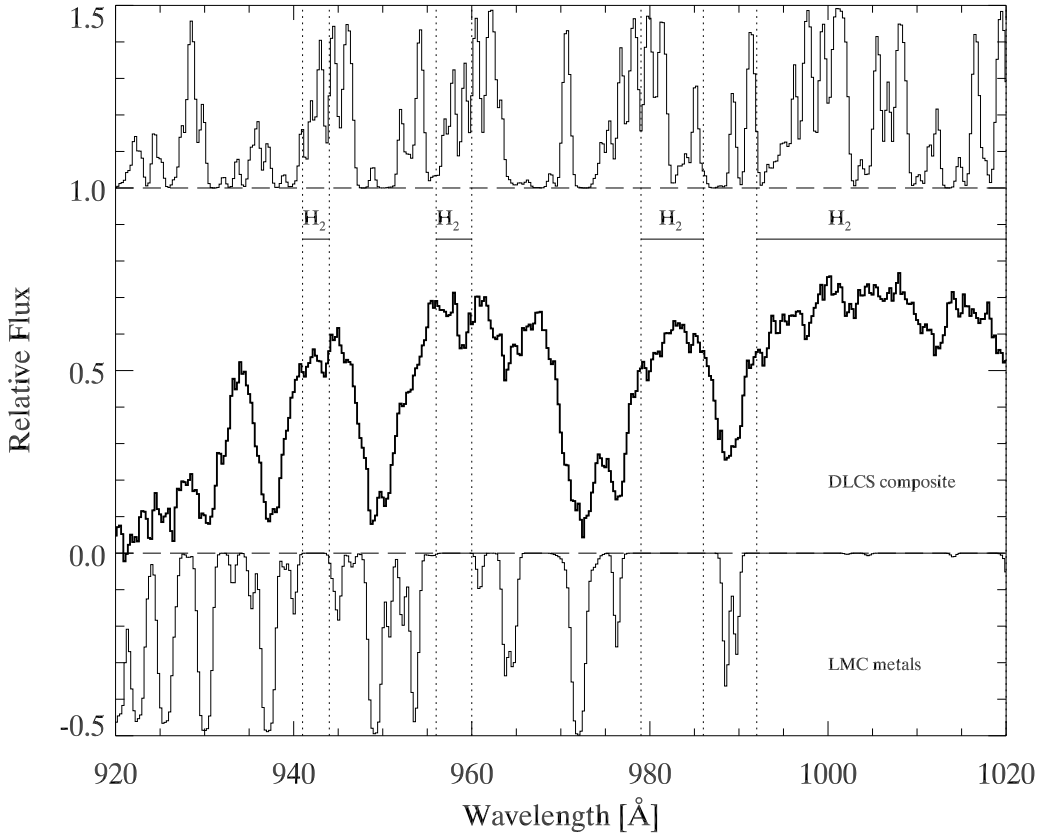

Figure 3.18 Identification of molecular hydrogen absorption bands of in the composite spectrum of DLCS sample galaxies (middle). Shown here is the wavelength range $920-1020$ Å. DLCS composite is normalized to unity at 1500 Å and corrected for average IGM absorption. Lower spectrum is the model of H I absorption for the Large Magellanic Cloud with selected metallic lines (Walborn et al. 2002). A shift of $v = -300\,\mathrm{km\,s^{-1}}$ has been applied to match the Lyman series in the DLCS composite. Upper spectrum is the H I and H_2 model for LMC with $N(H_2) = 5 \times 10^{19}\,\mathrm{cm^{-2}}$ from the same authors. No velocity shift has been applied. The two model absorption spectra have been smoothed and resampled to match DLCS composite resolution, scaled by 0.5 and shifted in y-axis for clarity. Though most of the DLCS composite spectrum appears to be dominated by absorption features of H I and metals in the ISM, there are several clear wavelength "windows" (labeled as H_2) where Lyman-Werner absorption bands of molecular hydrogen appear.

Part II

Lyman α and H α Emitters in the $z = 2.3$ Proto-Cluster

Abstract

We present two deep narrow-band imaging surveys for Lyman α and H α emitters in the HS1700+64 field which contains the significant galaxy overdensity at $z = 2.3$. We detect 119 Lyman α emitters and discovered 6 large Lyman α "blobs," having sizes from 50 to 100 kpc. This makes the field HS1700+64 the richest concentration of large blobs known to date.

Follow-up optical spectroscopic observations obtained at W. M. Keck Observatory have confirmed a total of 47 Lyman α emitters. The blobs and Lyman α emitters appear to form a structure extending over $\sim$ 12 Mpc (comoving). Supporting spectroscopic and imaging observations used for rest-UV continuum selection of star-forming galaxies ($z \sim 2$ "BX" and Lyman-break galaxies) uncover that all but one of the blobs are associated with a continuum selected object.

Optical spectroscopy of 16 H α emitters shows their Lyman α line predominantly in absorption. However, a deep composite image of 16 H α emitters formed from their Lyman α narrow-band image reveals that they have spatially extended emission detected with a radius > 40 kpc.

The integrated La emission of H α selected galaxies amounts to the equivalent of a rest equivalent width of ≈ 33 Å – a line strength that would be classified as a Lyman α emitter (LAE) if the Ly α flux were of higher surface brightness.

This observation confirms and extends earlier suggestions (Hayashino et al. 2004) that spatially extended Lyman α emission is present around star-forming galaxies that would not be selected as LAEs. We suggest that this extended Lyman α "glow" is a generic feature of star-forming galaxies at high redshift, whether or not a galaxy exhibits Lyman α emission in a slit spectrum or relatively shallow narrow band image.

Chapter 4

The $z = 2.3$ Protocluster in Lyman α and Hα Narrow Band Imaging

4.1 Introduction

Numerous observational studies over the last decade have firmly established that $z \sim 2 - 3$ corresponds to the epoch when the peak of star-formation activity in the Universe is reached (Madau et al. 1996; Steidel et al. 1999; Bouwens et al. 2007; Reddy & Steidel 2009, and references therein) In this important redshift range two fields containing an significant overdensity of galaxies have been studied in depth. These are the $z = 3.09$ proto-cluster in the field SSA22 (Steidel et al. 1998) and the $z = 2.3$ proto-cluster in the field of the $z = 2.7$ quasar HS1700+64 (Steidel et al. 2005). The former was identified in a spectroscopic survey of photometrically selected "Lyman break" galaxies (LBG), which efficiently identifies candidate objects in the redshifts range $z = 2.5-3.5$ (Steidel et al. 2003). A similar spectroscopic survey of candidate star-forming galaxies targeting the redshift range $z = 2.3 \pm 0.4$ ("BX" galaxies, Steidel et al. (2004)) lead to the discovery of the $z = 2.3$ proto-cluster. These two structures became apparent as sharp "peaks" in the redshift distribution of confirmed high-redshift galaxies, with an overabundance of objects by factors of 6 and 7 (respectively) as compared to the "field."

A very efficient technique for identifying galaxies undergoing strong episodes of star formation is based on imaging in a narrow band centered on the redshifted Lyman α (Ly α) wavelength. An unexpected outcome of deep narrow-band imaging in the SSA22 proto-cluster field has been the discovery of two giant and luminous diffuse Ly α emission objects (Ly α "blobs," Steidel et al. (2000, hereafter S00). With their physical size extending over 100kpc and a Ly α brightness of $\sim 10^{-15} ergs^{-1} cm^{-2}$, these blobs were extremely puzzling as no obvious source of such powerful UV radiation was found. There are only a handful of $\sim$ 100kpc sized Lyman α blobs known to

date. In this work we present a discovery of six large Lymanα blobs found in the proto-cluster field HS1700+64 at $z = 2.3$

4.2 Imaging Observations

In this section we describe two new sets of imaging observations for the field of the z=2.3 proto-cluster, centered on the bright QSO HS1700+64 ($z_Q = 2.751$). Deep optical narrow-band imaging centered at 4010 Å, which was designed to match Ly α from the known galaxy overdensity at $z = 2.30$ presented in Section § 4.2.1. In Section 4.2.2 we present deep near-infrared narrow-band imaging in the $Br\gamma$ filter ($2.169\mu m$). This band pass is well matched to the H α line at z=2.3. Later on in Section § 4.5 we present the results of a spectroscopic followup of candidate Ly α emitters with a special focus on 6 large Ly α emission "blobs" we have discovered.

Details of the optical and near-infrared broad band imaging ($U_n, G, \mathcal{R}$ and J, K_s) of the HS 1700+64 field have been presented in an earlier publications (Shapley et al. 2005; Erb et al. 2006a). Here we briefly summarize the key properties of the final imaging products for clarity.

Deep imaging in U_n, G, and $\mathcal{R}$ photometric system (see Steidel et al. 2003, for details) was obtained in a $16' \times 16'$ region centered on HS 1700+64, with a plate scale of $0''.236$. The filters used have the following effective wavelengths and band-pass widths : $\lambda_{U_n} = 3550$ Å (600 Å), $\lambda_G = 4780$ Å (1100 Å) and $\lambda_{\mathcal{R}} = 6830$ Å (1250 Å). The final image quality in all three bands is $FWHM \sim 0''.9$. The surface brightness limits for a flux detection at 3σ significance are $U_n = 27.7$ mag arcsec^{-2}, $G = 27.8$ mag arcsec^{-2} and $\mathcal{R} = 27.0$ mag arcsec^{-2}. This corresponds to $U_n = 26.6$, $G = 26.7$ and $\mathcal{R} = 25.9$ for a $3''$ diameter aperture.

A sub-portion of the field with optical coverage, having a size of $8.5' \times 8.5'$ was observed in near-infrared J and K-short (K_s) bands. The surface brightness limit achieved (3σ) is $K_s = 23.0$ mag arcsec^{-2} (Vega magnitude) or $K_s = 22.0$ for a $3''$ diameter aperture. The J band photometry limit was estimated to have a 3σ limit at ~ 24.0 (Erb et al. 2006a).

4.2.1 Optical Narrow-Band Imaging (Ly α)

Narrow-band imaging data were obtained using LFC Wide-Field Imager on the Hale 200-inch telescope at Palomar Observatory during three clear nights in July 2007. The LFC camera is an array of six 2048×4096 pixel back-side illuminated SITe CCDs, covering a field of view that is approximately $24'$ in diameter. The plate scale is $0''.18$/pixel, providing an image scale of $0''.36$/pixel in the 2×2 binned readout mode, which was used for our observations.

The LFC camera was equipped with a custom-made filter with high throughput in a narrow-band centered on $\lambda_{eff} = 4010$ Å and a width of FWHM = 90 Å (Figure 4.1). During the course of the observing run the seeing at 4010 Å was varying in the range $0''.9$ to $1''.7$, but the majority

of exposures were obtained in $\sim 1\farcs2$ seeing conditions. The single exposure time was 1800 seconds and a random dithering pattern was applied between exposures. The data were reduced according to standard procedures in IRAF using the Mosaic Data Reduction Package (MSCRED). Flat-field images were created from twilight sky observations.

In producing the final deep narrow-band image we have combined a total of 46 frames to reach an effective exposure time of 22.3 hrs. Flux calibration was performed based on nightly observations of the spectrophotometric standard star Feige 67 (Massey et al. 1988). The photometric limits achieved in the final narrow-band mosaic are $NB = 26.8$ for a 3σ significance detection in a $3''$ diameter aperture, equivalent to $NB \sim 27.8$ mag arcsec^{-2}.

To obtain an estimate of the continuum level near Ly α we make use of broadband photometry measurements. The peak transmission of the 4010 Å filter is located right in between transmission bands of the U_n and G filters (Figure 4.1). We can therefore derive a prediction of the narrow-band flux, in the absence of strong lines in the spectrum, using a linear combination of two broadband measurements that is very close to a simple average :

$$UG(4010) = 0.63 \times U_n + 0.37 \times G. \tag{4.1}$$

The two coefficients in this equation are easily derived considering the effective wavelengths of the U_n and G filters. This value we will call the "UG continuum" magnitude.

By the same formula we create a "UG continuum" image, which provides an estimate for the spatial extent and shape of the continuum flux at 4010 Å. Prior to averaging, the existing U_n and G images were scaled to a common zero point and slightly smoothed to match the seeing obtained for the final 4010 Å narrow-band image ($FWHM = 1\farcs2$). The resulting UG continuum image is somewhat deeper than U_n and G separately, reaching a 3σ brightness limit of $UG = 28.1$ for aperture photometry with a 3" diameter. We re-sample and spatially register the 4010 Å narrow-band mosaic to match the pixel scale and size of the UG continuum image. After trimming off edges and a small region dominated by the scattered light of a bright star, the final common area for the narrow-band and UG continuum coverage is 219 arcmin^2 (Figure 4.3).

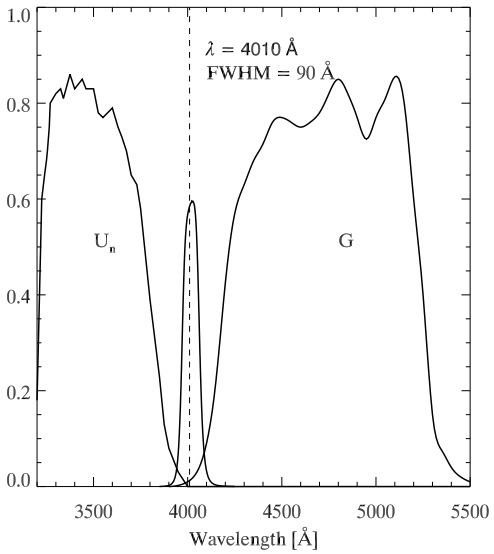

Figure 4.1 Filter transmissions for the U_n, 4010 Å narrow-band and G band passes.

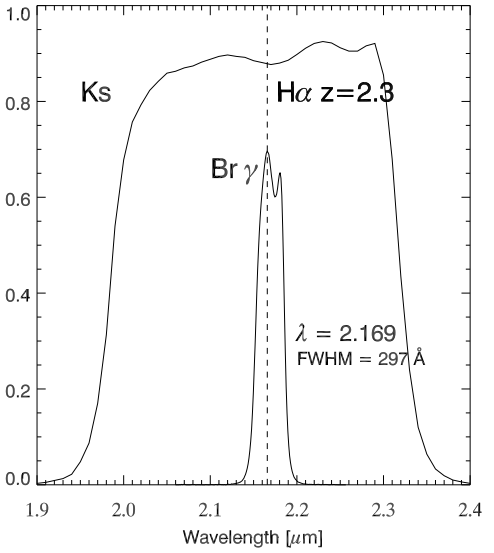

Figure 4.2 Transmission of the K_s and Br γ filters for the WIRC camera on the Palomar 5.1m Hale telescope. The wavelength of H α at z=2.3 is indicated with a vertical dashed line.

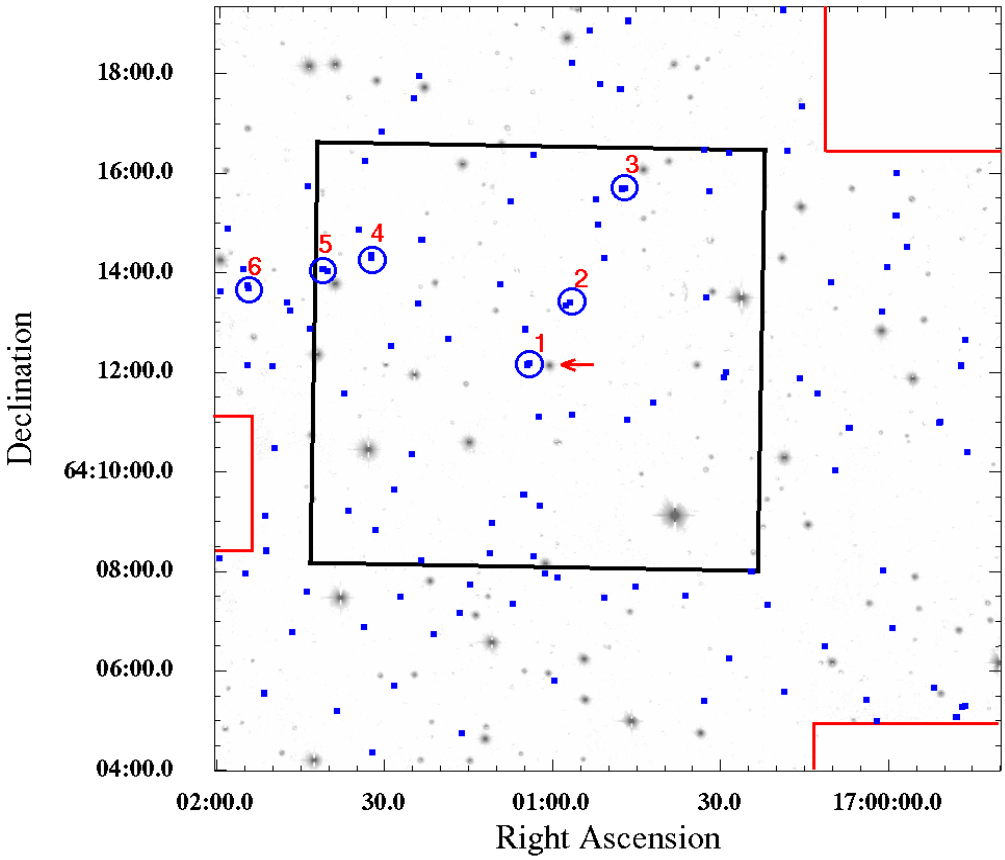

Figure 4.3 Field map of the 4010 Å narrow-band and near-infrared imaging coverage (black box). The background quasar HS1700+64 is marked with a red arrow. Blue square symbols mark the positions of Ly α excess candidates, with 6 Ly α blobs marked with large blue circles and numbered according to the distance from line of sight to HS1700+64. Red boxes mark regions without 4010 Å imaging coverage.

4.2.2 Near-IR Narrow-Band Imaging (H α)

Near-infrared imaging was obtained with the Wide Field Infrared Camera (WIRC; Wilson et al. (2003)) on the Palomar 5.1m Hale telescope in August 2004 and May 2005. We obtained a total of 22 hrs effective exposure with the Brγ ($\lambda = 2.17\mu m$, $FWHM = 297$ Å) filter. The same $8.5' \times 8.5'$ field as covered by previous broadband J and K_s imaging was targeted. Objects detected in Br γ with a 3σ significance have a magnitude of $NB_{Br\gamma} = 21.8$ (Vega).

4.3 Narrow-Band Source Catalogs

4.3.1 Catalog of Ly α Emitter Candidates

The source catalog for optical narrow-band imaging was obtained using SExtractor version 2.4.4 (Bertin & Arnouts 1996) with photometry performed in dual-image mode. Primary detection was carried out in the 4010 Å narrow-band image. Isophotal apertures as determined by the pixel area of the narrow-band detection were used for measurements in U_n,G and UG continuum images. However, as the value of flux measured in an isophotal aperture is somewhat sensitive to the choice of detection threshold above background, we have used MAG_AUTO as a more robust measure of the "total" narrow-band flux (which is labeled NB in all discussion that follows). For calculation of colors $(NB - UG)$ and $(U_n - G)$ we employ isophotal magnitude measurements. The catalog of narrow-band detected sources contains ~ 6700 entries down to a limiting $NB = 25.5$.

From this catalog we select Ly α emitter candidates using an improved color-excess criterion described below. A number of previous surveys for Ly α emitters (Steidel et al. 2000; Cowie & Hu 1998) have selected objects based on the simple requirement that the flux in the narrow-band is about 2 times higher than the continuum flux estimate. This would correspond to:

$$(NB - UG) \leq -0.75, \tag{4.2}$$

using the "UG continuum" magnitude as defined in this work. In the case of Ly α emission in the 4010 Å filter, equation 4.2 also imposes a requirement on the Ly α equivalent width of $W_\lambda \geq 90$ Å (observed frame). However, it is important to note that the color and equivalent width cuts are equivalent only for sources with a continuum value at observed-frame 4010 Å which is well approximated with the average of values measured at 3550 and 4780 Å. This is a somewhat crude approximation for galaxies with redshifts spanning $2.0 \leq z \leq 2.5$, as the U_n passband becomes increasingly blanketed by the Ly α forest. Therefore, a more robust approach to defining an "excess" of narrow-band flux is to do so with respect to the mean $(NB - UG)$ value observed for sources in this redshift range.

Figure 4.4 presents the full catalog of narrow-band detected sources with their observed $(U_n - G)$ and $(NB - UG)$ colors. According to the broad-band color criteria optimized for selecting star-forming galaxies at $2.0 \leq z \leq 2.5$ ("BX" galaxies of Steidel et al. 2004; Adelberger et al. 2004) they are mostly to be found within the range $0 \leq U_n - G \leq 1.4$. We can thus introduce an adjustment to the observed narrow-band excess color $(NB - UG)$, so that it is equal to zero for the bulk of the objects.

$$(NB - UG)_{corr} = (NB - UG) - f(U_n - G). \tag{4.3}$$

The new narrow-band excess selection cut used for the selection of Ly α emitter candidates in

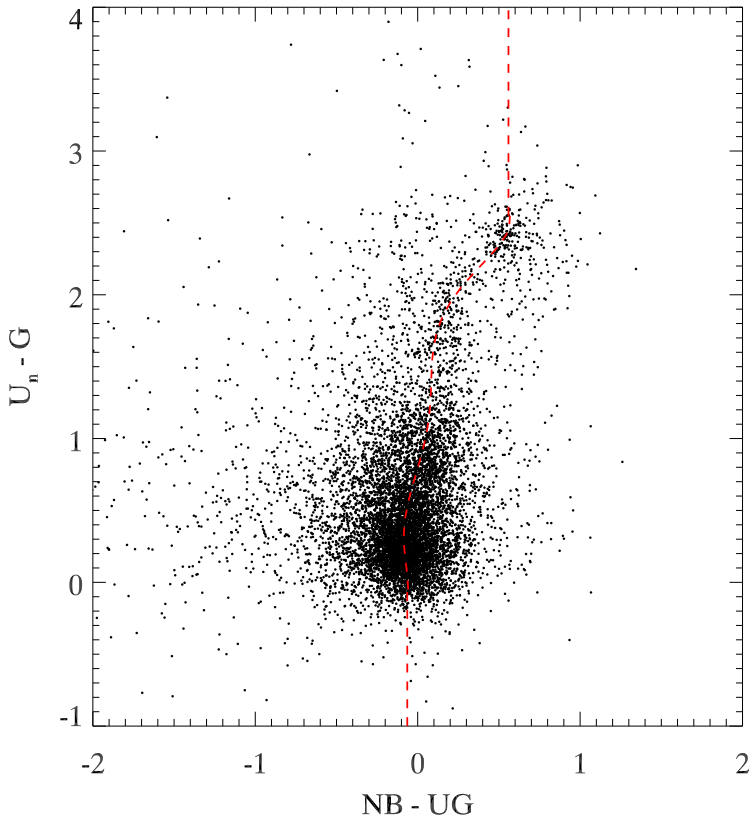

Figure 4.4 Color-color diagram of all 4010 Å sources in HS 1700+64 field. Magnitudes are measured in identical isophotal areas as initially detected in the 4010 Å narrow-band image. A smooth fit to the mode of to the locus of objects in (NB-UG) color has been shown with the red dashed line. For rare objects having color (U_n-G)$\leq$ 0 and (U_n-G)$\geq$ 2.5 we assume a constant value of -0.06 and 0.55 respectively.

this work is then :

$$(NB - UG)_{corr} \leq -0.75, \tag{4.4}$$

The fit through the bulk of the objects in $(NB-UG)$ shown in Figure 4.4 empirically defines the function $f(U_n-G)$ which is used as the correction term in Equation 4.3. Note that this correction is relatively small for a great majority of objects, staying within the range $-0.06 \leq f(U_n - G) \leq 0.11$ for $0 \leq U_n - G \leq 1.4$.

Applying Equation 4.4 to the narrow-band catalog selects a total of 119 objects brighter than $NB = 25.5$. The full list of narrow-band excess candidates with their celestial coordinates, magnitudes, spectroscopic redshifts and cross identifications (see Section 4.5 and 4.6) is presented in Table 4.1.

Figure 4.5 shows the $U_n - G$ color distribution for all Ly α emitter candidates compared to those

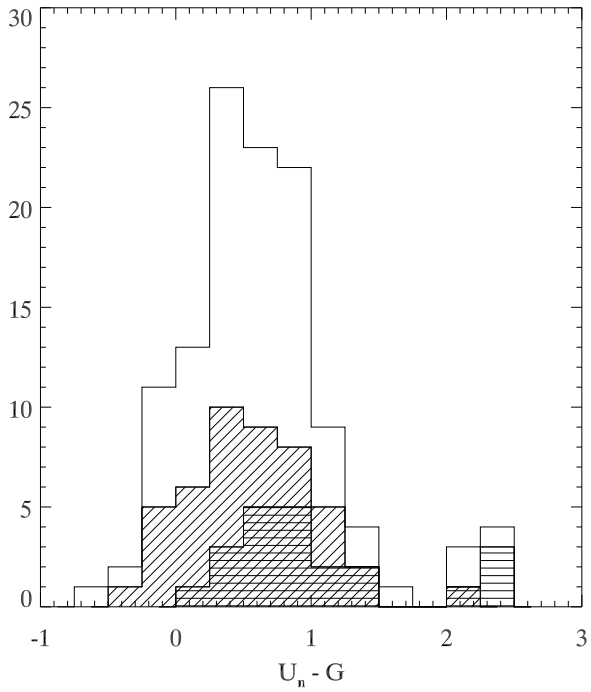

Figure 4.5 Distribution of all 119 narrow-band excess objects in $U_n - G$ color. Diagonally shaded histogram is for objects with spectroscopic redshift confirmed to be at $z \sim 2.3$. The histogram with horizontal shading shows the distribution of $(U_n - G)$ for 22 objects that also satisfy "BX" continuum selection criteria. We see that the $(U_n - G)$ color for confirmed star-forming galaxies spans a broader range than $0 \leq (U_n - G) \leq 1.4$. One cause of this could be that the broad-band magnitude measurements are forced to a region determined by the 4010 Å isophote.

that were later spectroscopically confirmed to have a redshift $z \sim 2.3$ (Section 4.5). There are 7 confirmed $z = 2.3$ galaxies with $(U_n - G) \geq 1.0$ and for about half of them the correction term introduced in Equation 4.3 was decisive for including them in the narrow-band excess catalog.

The width of the 4010 Å filter allows for the detection of Ly α line emission in the redshift range $z = 2.24$ to $z = 2.36$. Therefore the comoving volume probed by the 4010 Å imaging is roughly $25 \times 25 \times 157$ Mpc, or $V \approx 10^5$ Mpc^3.

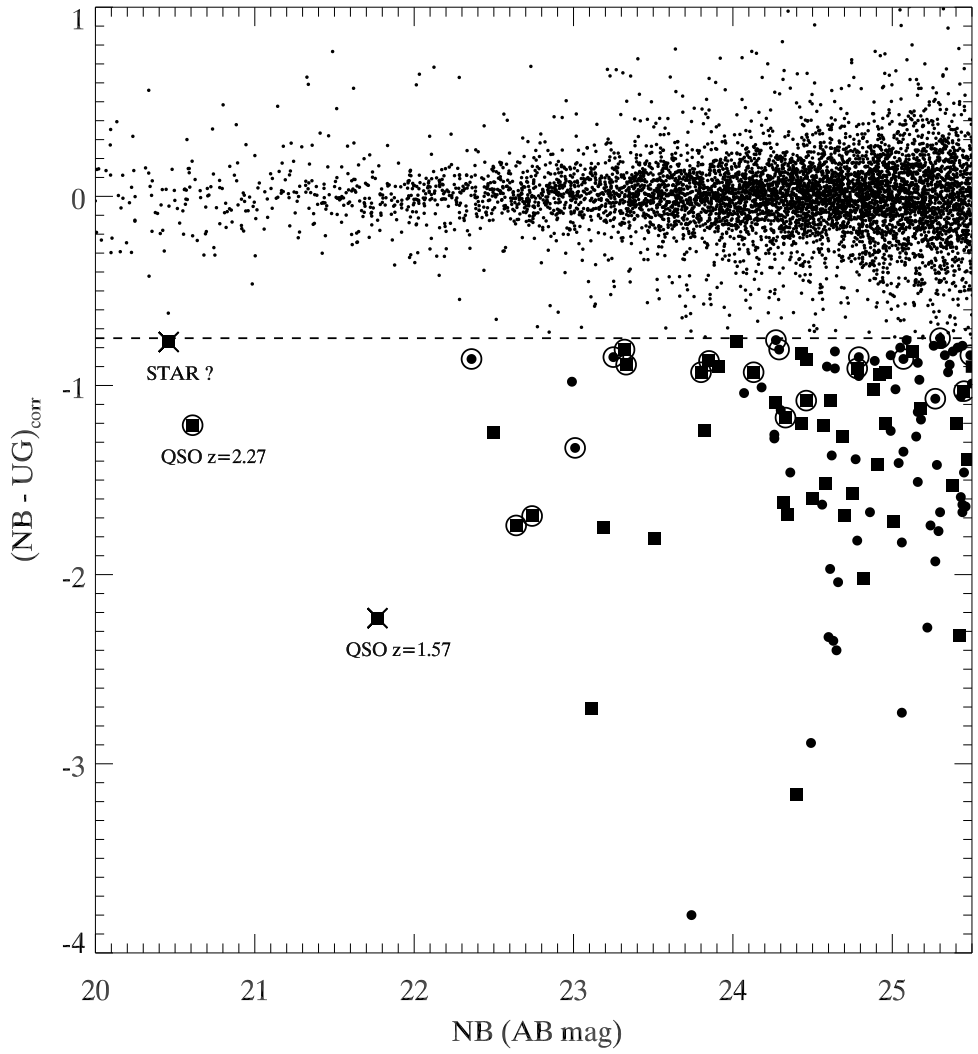

Figure 4.6 Narrow-band excess $(NB-UG)_{corr}$ for objects in HS 1700+64 field. Objects satisfying (NB-UG)$_{corr} \leq -0.75$ (dashed line) are marked with larger symbols. Objects that have a spectroscopically confirmed redshift in the interval $2.24 \leq z \leq 2.36$ are marked with square symbols. A total of 22 objects whose broad-band colors also satisfy "BX" selection criteria are circled. Three objects have been classified as QSO/AGN with redshifts outside of the "spike" after followup spectroscopy (labeled and crossed out).

Table 4.1. Catalog of 4010 Å narrow-band selected Ly α emitter candidates in the field HS 1700+64

RA (J2000)	DEC (J2000)	Name	NB (AB mag)	Δ [a]	U_n (AB)	G (AB)	z_{em}	z_{abs}	Comment
17:01:34.86	+64:14:52.6	BNB001	20.46	-0.77	21.72	20.67	0.000	0.000	STAR ?
17:00:32.83	+64:05:24.9	BNB003	20.61	-1.21	22.12	21.68	2.269	2.281	BX116, QSO
17:00:53.21	+64:18:53.0	BNB004	21.77	-2.23	24.33	23.88	1.569	···	QSO
17:00:01.98	+64:05:00.1	BNB006	22.36	-0.86	24.37	23.39	···	···	BX91
17:01:32.51	+64:14:17.8	BNB007	22.50	-1.25	24.82	23.61	2.322	···	BLOB-4
17:01:59.63	+64:08:15.3	BNB009	22.64	-1.74	24.82	24.11	2.299	···	BX372
17:00:52.14	+64:15:28.9	BNB010	22.74	-1.69	25.25	24.36	2.284	2.296	MD157, AGN
17:00:18.37	+64:19:17.3	BNB013	22.99	-0.98	25.09	22.82	···	···	···
17:01:07.00	+64:07:21.0	BNB014	23.01	-1.33	24.72	24.33	···	···	BX287
17:01:54.64	+64:13:40.8	BNB015	23.11	-2.71	27.82	25.73	2.299	···	BLOB-6
17:01:04.08	+64:12:11.9	BNB016	23.19	-1.75	25.96	25.09	2.290	2.260	BLOB-1
17:01:33.69	+64:06:53.1	BNB017	23.25	-0.85	24.58	24.26	···	···	BX239
17:00:50.59	+64:07:28.6	BNB018	23.32	-0.81	24.77	24.12	2.317	···	BX313
17:01:43.58	+64:12:52.6	BNB019	23.33	-0.89	25.10	24.01	2.291	2.277	BX754
17:01:41.21	+64:14:03.9	BNB021	23.51	-1.81	26.40	25.40	2.269	2.264	BLOB-5
17:00:46.92	+64:15:42.4	BNB022	23.74	-3.80	27.82	27.16	2.293	···	BLOB-3
17:01:54.63	+64:12:08.3	BNB023	23.80	-0.93	25.62	24.29	2.286	···	BX689
17:00:29.12	+64:11:54.4	BNB024	23.82	-1.24	25.62	24.84	2.293	···	···
16:59:59.10	+64:06:51.4	BNB026	23.85	-0.87	25.55	25.04	2.279	···	BX235
17:00:46.22	+64:19:04.1	BNB027	23.91	-0.90	25.95	24.89	2.295	···	···
17:01:51.27	+64:08:24.7	BNB029	24.02	-0.77	25.32	24.71	2.298	···	···
16:59:50.36	+64:11:00.7	BNB030	24.07	-1.04	25.99	25.41	···	···	···
17:00:06.70	+64:10:52.8	BNB032	24.13	-0.93	26.05	25.18	2.290	2.227	BX579
16:59:50.62	+64:10:58.8	BNB033	24.18	-1.01	26.32	25.87	···	···	···
17:00:51.39	+64:17:47.5	BNB034	24.26	-1.28	26.03	25.79	···	···	···
17:01:21.15	+64:06:44.6	BNB035	24.26	-1.26	26.10	25.71	···	···	···
17:01:18.71	+64:12:40.1	BNB036	24.27	-1.09	25.93	25.35	2.298	2.280	···
17:01:32.10	+64:04:22.0	BNB037	24.27	-0.76	26.28	23.99	···	···	MD6
17:01:16.53	+64:07:10.8	BNB038	24.29	-0.81	25.65	24.66	···	···	BX267
16:59:56.18	+64:14:31.2	BNB039	24.30	-1.13	26.01	25.64	···	···	···
17:00:47.44	+64:15:41.8	BNB040	24.32	-1.62	27.49	27.27	2.291	···	BLOB-3
17:01:04.51	+64:12:09.7	BNB041	24.33	-1.17	27.37	26.18	2.295[b]	2.297	MD109, BLOB-1
17:01:31.70	+64:08:50.1	BNB042	24.34	-1.68	26.24	26.39	2.275	···	···
16:59:46.65	+64:05:16.0	BNB043	24.36	-1.46	27.07	26.13	···	···	···
17:00:18.43	+64:05:35.1	BNB044	24.40	-3.16	27.65	27.79	2.274	···	···
17:00:09.23	+64:10:01.6	BNB045	24.43	-1.20	26.54	26.20	2.315	···	···
17:00:56.50	+64:18:13.2	BNB046	24.43	-0.83	25.86	25.44	2.300	···	···
17:00:31.75	+64:15:38.8	BNB047	24.46	-0.86	25.89	25.96	2.297	···	···
17:01:51.35	+64:09:06.2	BNB048	24.46	-1.08	26.05	25.82	2.296	···	BX441
17:01:05.11	+64:09:33.6	BNB050	24.49	-2.89	27.82	27.69	···	···	···
17:00:36.17	+64:07:30.6	BNB051	24.50	-1.60	26.79	26.33	2.313	···	···
16:59:51.63	+64:05:39.9	BNB054	24.56	-1.63	27.15	26.46	···	···	···
17:01:33.71	+64:16:15.2	BNB055	24.57	-1.21	26.54	25.79	2.307	2.290	···
17:00:59.06	+64:07:53.0	BNB056	24.58	-1.52	26.69	26.21	2.312	···	···

Table 4.1 (cont'd)

RA (J2000)	DEC (J2000)	Name	NB (AB mag)	Δ [a]	U_n (AB)	G (AB)	z_{em}	z_{abs}	Comment
17:01:54.75	+64:13:44.3	BNB058	24.59	-0.90	26.76	26.46	···	···	BLOB-6?
17:01:38.44	+64:05:11.6	BNB059	24.60	-2.33	27.26	27.30	···	···	
17:00:56.36	+64:11:09.4	BNB060	24.61	-1.97	27.74	27.51	···	···	···
17:01:36.44	+64:09:13.0	BNB061	24.61	-1.08	26.63	26.28	2.340	···	···
17:01:40.43	+64:14:01.5	BNB062	24.62	-1.37	27.49	26.08	···	···	BLOB-5?
17:01:28.21	+64:05:42.9	BNB064	24.63	-2.35	27.82	27.37	···	···	···
17:00:32.26	+64:13:30.6	BNB065	24.64	-0.82	26.54	25.89	···	···	···
17:01:01.35	+64:07:58.6	BNB066	24.64	-0.91	27.35	25.12	···	···	···
17:00:46.58	+64:11:03.5	BNB067	24.65	-2.40	27.47	27.54	···	···	···
16:59:45.57	+64:10:23.9	BNB068	24.66	-2.04	27.30	26.79	···	···	···
17:00:56.85	+64:13:24.7	BNB070	24.69	-1.27	26.55	26.91	2.307	···	BLOB-2
17:01:32.61	+64:14:21.5	BNB071	24.70	-1.69	27.35	26.44	2.288	···	BLOB-4?
17:00:50.59	+64:14:18.9	BNB075	24.75	-1.57	27.43	26.48	2.308	···	···
16:59:46.16	+64:05:17.1	BNB076	24.77	-1.39	26.97	26.62	···	···	···
17:01:28.34	+64:09:38.5	BNB077	24.78	-0.91	26.26	25.57	2.279	···	BX479
17:01:16.20	+64:04:44.9	BNB078	24.78	-1.82	27.04	26.51	···	···	···
16:59:59.76	+64:14:06.6	BNB079	24.79	-0.95	26.37	25.97	···	···	···
16:59:46.56	+64:12:07.8	BNB080	24.79	-0.85	27.40	25.02	···	···	D40
17:00:56.47	+64:13.27.2	BLOB-2c	24.80	-1.2[c]	···	···	z=2.3082	···	BLOB-2
17:01:03.42	+64:16:23.1	BNB083	24.82	-2.02	27.60	27.31	2.308	···	···
17:00:17.74	+64:16:27.4	BNB086	24.86	-1.67	27.43	26.61	···	···	···
17:01:27.24	+64:07:29.5	BNB088	24.88	-1.02	26.49	26.14	2.301	···	···
17:01:58.27	+64:14:53.1	BNB089	24.89	-0.87	26.94	26.28	···	···	···
17:00:32.62	+64:16:28.4	BNB093	24.91	-1.42	27.22	26.99	2.327	···	···
17:01:23.46	+64:14:40.3	BNB095	24.92	-0.94	26.66	25.74	2.314	···	···
17:00:45.02	+64:07:42.3	BNB097	24.96	-1.20	27.06	26.81	2.321	···	···
17:01:49.84	+64:10:28.5	BNB098	24.96	-0.93	26.64	26.46	2.340	···	···
17:01:03.33	+64:08:18.5	BNB100	24.99	-0.84	27.42	26.16	···	···	···
17:01:59.54	+64:13:37.7	BNB101	24.99	-1.24	26.69	26.33	···	···	···
17:00:51.79	+64:14:58.9	BNB104	25.01	-1.72	27.02	27.07	2.295	···	···
17:00:28.29	+64:06:15.9	BNB105	25.02	-1.02	27.00	26.35	···	···	···
17:00:28.21	+64:16:24.6	BNB106	25.04	-1.41	27.82	26.75	···	···	···
17:00:00.80	+64:13:13.1	BNB108	25.05	-0.80	27.35	25.80	···	···	···
17:01:02.23	+64:09:19.9	BNB109	25.06	-1.83	27.82	27.14	···	···	···
17:01:55.51	+64:14:03.5	BNB110	25.06	-2.73	27.82	26.93	···	···	···
17:01:54.93	+64:07:57.3	BNB111	25.07	-0.86	26.59	25.95	···	···	BM290
17:00:28.75	+64:12:00.6	BNB112	25.07	-1.35	27.02	26.78	···	···	···
17:01:28.88	+64:12:32.0	BNB113	25.09	-0.76	26.66	25.78	···	···	···
17:01:47.62	+64:13:24.0	BNB115	25.13	-0.82	26.78	26.31	2.308	···	···
17:01:50.14	+64:12:06.8	BNB118	25.15	-1.27	27.21	26.25	···	···	···
17:01:23.42	+64:08:13.6	BNB119	25.16	-0.88	27.03	26.05	···	···	···
17:01:02.46	+64:11:06.9	BNB120	25.16	-1.14	27.27	26.65	···	···	···
17:01:51.53	+64:05:32.8	BNB121	25.16	-1.51	27.31	27.82	···	···	···
17:00:11.26	+64:06:30.2	BNB125	25.17	-0.97	27.19	26.43	···	···	···

Table 4.1 (cont'd)

RA (J2000)	DEC (J2000)	Name	NB (AB mag)	Δ [a]	U_n (AB)	G (AB)	z_{em}	z_{abs}	Comment
17:00:00.78	+64:08:01.6	BNB127	25.18	-1.12	26.89	26.69	2.269	···	···
17:01:11.22	+64:08:22.7	BNB128	25.18	-1.18	27.15	26.73	···	···	···
17:01:14.69	+64:07:45.1	BNB130	25.22	-2.28	27.82	27.96	···	···	···
17:01:30.71	+64:16:50.8	BNB133	25.24	-1.74	27.66	27.60	···	···	···
17:01:24.04	+64:17:56.9	BNB136	25.26	-0.79	27.13	25.96	···	···	···
16:59:58.15	+64:15:08.9	BNB137	25.27	-1.93	27.82	27.72	···	···	···
17:00:12.36	+64:11:35.3	BNB138	25.27	-1.07	27.82	25.39	···	···	D37
17:01:43.93	+64:15:43.9	BNB139	25.28	-1.42	26.91	27.19	···	···	···
17:01:10.73	+64:08:58.5	BNB140	25.29	-1.77	27.68	27.77	···	···	···
17:01:24.96	+64:17:31.0	BNB141	25.30	-1.67	27.82	27.47	···	···	···
17:01:46.51	+64:06:46.9	BNB142	25.30	-0.75	26.99	26.02	···	···	BX226
17:01:24.17	+64:13:23.5	BNB143	25.31	-0.78	27.29	26.44	···	···	···
17:00:03.84	+64:05:25.3	BNB145	25.33	-0.84	27.20	26.66	···	···	···
17:01:47.00	+64:13:14.1	BNB148	25.35	-0.93	27.30	26.50	···	···	···
17:00:24.31	+64:08:00.2	BNB149	25.36	-0.89	27.38	26.92	···	···	···
17:00:09.80	+64:13:48.4	BNB152	25.38	-0.82	26.71	26.58	···	···	···
17:01:04.84	+64:12:52.4	BNB153	25.38	-1.53	27.32	27.35	2.291	2.250	···
17:01:07.45	+64:15:26.5	BNB155	25.40	-1.20	27.41	27.23	2.290	···	···
17:00:47.71	+64:17:41.6	BNB156	25.41	-0.80	27.49	26.69	···	···	···
17:00:21.51	+64:07:20.2	BNB157	25.42	-2.32	27.82	27.20	2.317	···	···
17:00:15.03	+64:17:21.0	BNB158	25.43	-1.06	27.82	26.81	···	···	···
16:59:47.73	+64:05:04.0	BNB159	25.43	-1.59	27.82	27.96	···	···	···
17:01:43.95	+64:07:35.0	BNB162	25.44	-1.63	27.82	27.83	···	···	···
17:01:25.10	+64:10:21.8	BNB163	25.44	-0.79	27.49	26.99	···	···	···
16:59:45.88	+64:12:38.7	BNB164	25.44	-1.67	27.82	27.38	···	···	···
17:00:41.96	+64:11:24.3	BNB165	25.45	-1.03	27.82	26.50	2.333[b]	···	MD94, AGN
17:00:59.62	+64:05:49.4	BNB167	25.45	-1.46	27.82	27.00	···	···	···
16:59:57.94	+64:16:00.6	BNB170	25.46	-1.64	27.82	27.51	···	···	···
17:00:57.50	+64:13:21.0	BNB171	25.47	-1.39	27.45	26.92	2.293	···	BLOB-2?
17:00:15.46	+64:11:53.1	BNB173	25.49	-0.84	27.76	25.65	···	···	···
17:01:09.30	+64:13:46.1	BNB174	25.50	-0.90	27.74	27.06	2.335	···	···
17:01:37.40	+64:11:34.1	BNB175	25.50	-0.99	27.78	27.19	2.442	···	···

[a] $\Delta = (NB - UG)_{corr}$. This is the narrow-band excess $(NB - UG)$ corrected for the $U_n - G$ color term of the locus, as given in Equation 4.3

[b] Emission redshift based on H_α

[c] This core of Blob-2 was added to the catalog manually.

4.3.2 Catalog of H α Emitter Candidates

We proceed to obtain a catalog of candidate H α emitters from the Br γ imaging following a similar approach as with selection of 4010 Å "excess" sources. The K_s and Br γ images were spatially registered and photometry was obtained in dual-image mode using narrow-band as the detection image. This yields a catalog of $\sim$ 1250 sources brighter than $NB_{Br\gamma} \leq 20.5$ (Vega magnitude). In Figure 4.8 we show these measurements of $NB_{Br\gamma} - K_s$ color. Since the Br γ and K_s filters overlap, the K_s magnitude was corrected for the $NB_{Br\gamma}$ flux contribution.

We find a total of 83 sources brighter than $NB_{Br\gamma} \leq 20.5$ whose photometry formally satisfies the condition :

$$NB_{Br\gamma} - K_s \leq -0.75. \tag{4.5}$$

The Brγ filter has a $FWHM = 297$ Å and therefore the above equation is also equivalent to a requirement of $W_\lambda \geq 300$ Å (observed) for H α at $z = 2.30 \pm 0.03$. The total comoving volume at

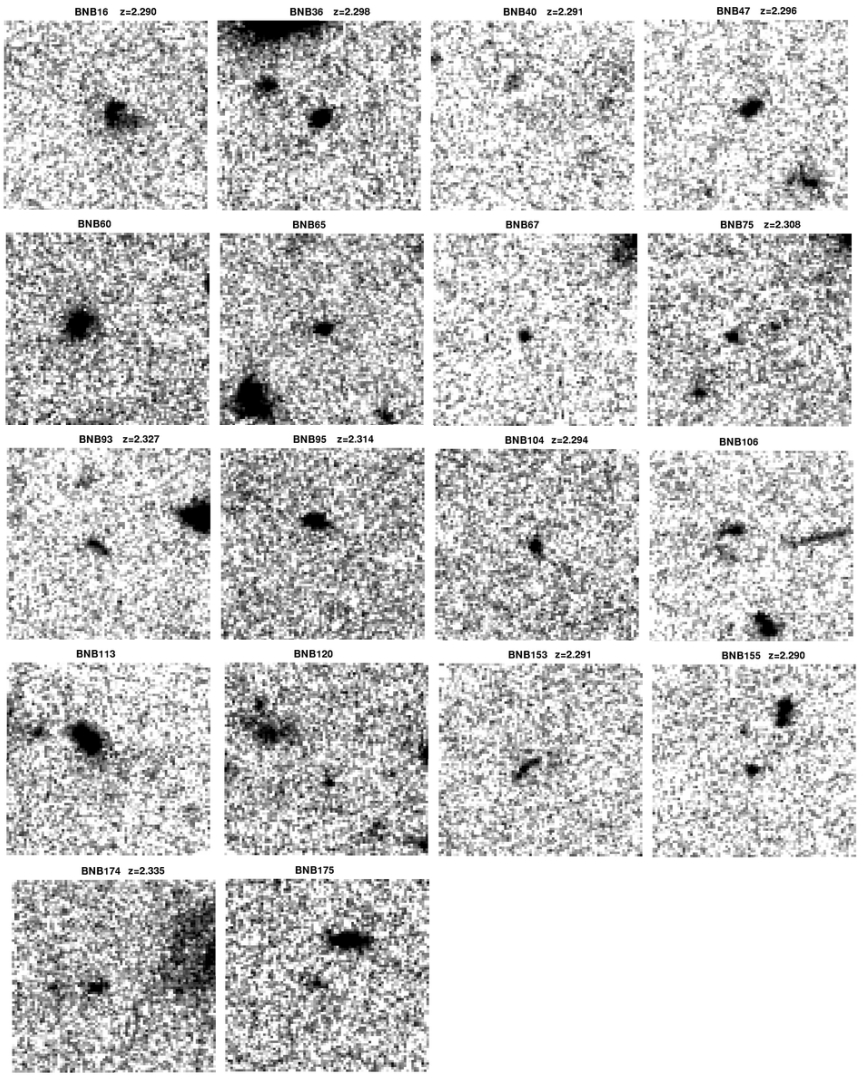

Figure 4.7 Cutouts from HST imaging coverage of HS1700+64 proto-cluster field centered on positions of Ly α emitters. The images were taken with ACS and F814W filter. Field size is $3''$, and redshifts are indicated where available. The typical observed FWHM of a single Ly α emitter is $\sim 0''.15$. Compare with Figure 4.9.

Table 4.2. Candidate H α emitters matching rest-UV continuum selection

RA (J2000)	DEC (J2000)	Name	$NB_{Br\gamma}$ (AB mag)	$NB_{Br\gamma} - K_s$ (AB mag)	$W_{\lambda 0}$(H α) (Å)	z_{em}	z_{abs}	Comment
17:00:52.23	64:15:29.0	HaNB1	18.82	1.17	204	2.293	2.292	MD157, [a]
17:00:47.65	64:09:44.5	HaNB3	18.86	1.17	204	2.2883	···	MD69 [b]
17:01:22.17	64:12:19.1	HaNB4	18.93	1.30	241	···	2.296	BX710
17:01:33.84	64:14:17.7	HaNB5	19.29	1.94	492	···	2.291	BX909
17:01:00.25	64:11:55.3	HaNB8	19.39	0.93	145	2.3148	···	MD103 [b]
17:01:21.61	64:14:18.2	HaNB10	19.43	1.56	331	···	2.289	BX913
17:01:16.15	64:14:19.6	HaNB12	19.47	1.03	167	2.3069	···	BX917 [b]
17:01:15.79	64:10:26.9	HaNB14	19.54	1.21	216	2.296	2.289	BX563
17:00:32.12	64:12:24.3	HaNB17	19.71	2.43	N/A[d]	3.317	3.314	C34
17:01:17.90	64:14:40.5	HaNB18	19.72	0.77	109	···	2.305	BX951
17:01:21.32	64:12:20.4	HaNB19	19.73	1.30	241	2.2959	···	BX711 [c]
17:00:52.95	64:14:35.8	HaNB26	19.87	1.42	280	···	2.296	BX939
17:01:14.31	64:10:59.5	HaNB28	19.91	1.40	275	···	···	BM490
17:01:22.42	64:11:52.0	HaNB29	19.91	0.82	120	···	···	BX705
17:01:17.80	64:13:54.9	HaNB31	19.93	0.80	117	···	2.308	BX879
17:01:31.15	64:13:29.1	HaNB35	19.99	1.08	181	···	2.290	BX810
17:01:02.96	64:13:54.2	HaNB40	20.08	1.15	N/A	···	1.843	BX846
17:00:35.57	64:14:59.8	HaNB41	20.09	1.48	302	2.2967	···	BX991 [c]
17:01:26.45	64:12:16.1	HaNB49	20.16	1.00	161	···	···	MD110
17:00:33.95	64:14:21.4	HaNB51	20.16	2.46	767	2.301	2.296	BX919
17:01:31.38	64:12:58.1	HaNB56	20.25	0.77	109	2.296	2.289	BX763
17:01:03.73	64:12:20.1	HaNB57	20.26	1.27	N/A	2.4213	···	BX759 [b]
17:00:48.26	64:10:05.6	HaNB61	20.32	0.97	154	2.3089	···	BX505 [b]
17:00:50.65	64:15:26.7	HaNB73	20.36	0.96	151	···	···	BX1039
17:01:28.67	64:15:25.6	HaNB75	20.39	1.81	430	···	···	BX1035
17:01:03.94	64:14:45.9	HaNB76	20.40	1.00	161	···	···	BM759
17:01:26.30	64:08:42.3	HaNB85	20.44	0.87	131	···	···	BM348
17:01:19.01	64:11:40.0	HaNB91	20.49	1.42	280	···	2.298	BX649
17:01:22.80	64:15:16.9	HaNB93	20.49	0.99	158	···	···	BM801

[a] This source is classified as an AGN.

[b] H α emission redshift from NIRSPEC spectroscopy, (Erb et al. 2006b)

[c] H α emission redshift from NIRSPEC spectroscopy, unpublished

[d] Estimated equivalent width of [OIII] is $W_{\lambda 0} \sim 500$ Å

z=2.3 probed by the Brγ excess selection is roughly $14 \times 14 \times 80$ Mpc or $V \approx 15700\,\mathrm{Mpc}^3$, about 6 times smaller than for the full catalog of Ly α emitters.

Figure 4.9 shows image cutouts of a fraction of H α candidates with *HST* ACS imaging coverage. We observe a range of continuum morphologies, from large diffuse objects (HaNB18), over multiple component sources (HaNB3) to single compact objects (HaNB76). Earlier studies of the morphologies of star-forming galaxies at $z \gtrsim 2-3$ have found no significant correlation between the appearance in continuum imaging and stellar mass, star formation rate or the strength of galaxy-scale outflows (Law et al. 2007). However, in a study of the morphologies of the members of the $z = 2.3$ proto-cluster (Peter et al. 2007), it was found that dustier galaxies have more nebulous UV morphologies. Unfortunately, more quantitative comparison of the appearance of Ly α (Figure 4.7) and H α emitters in the ACS data is difficult due to the large difference in the continuum brightness of the two samples.

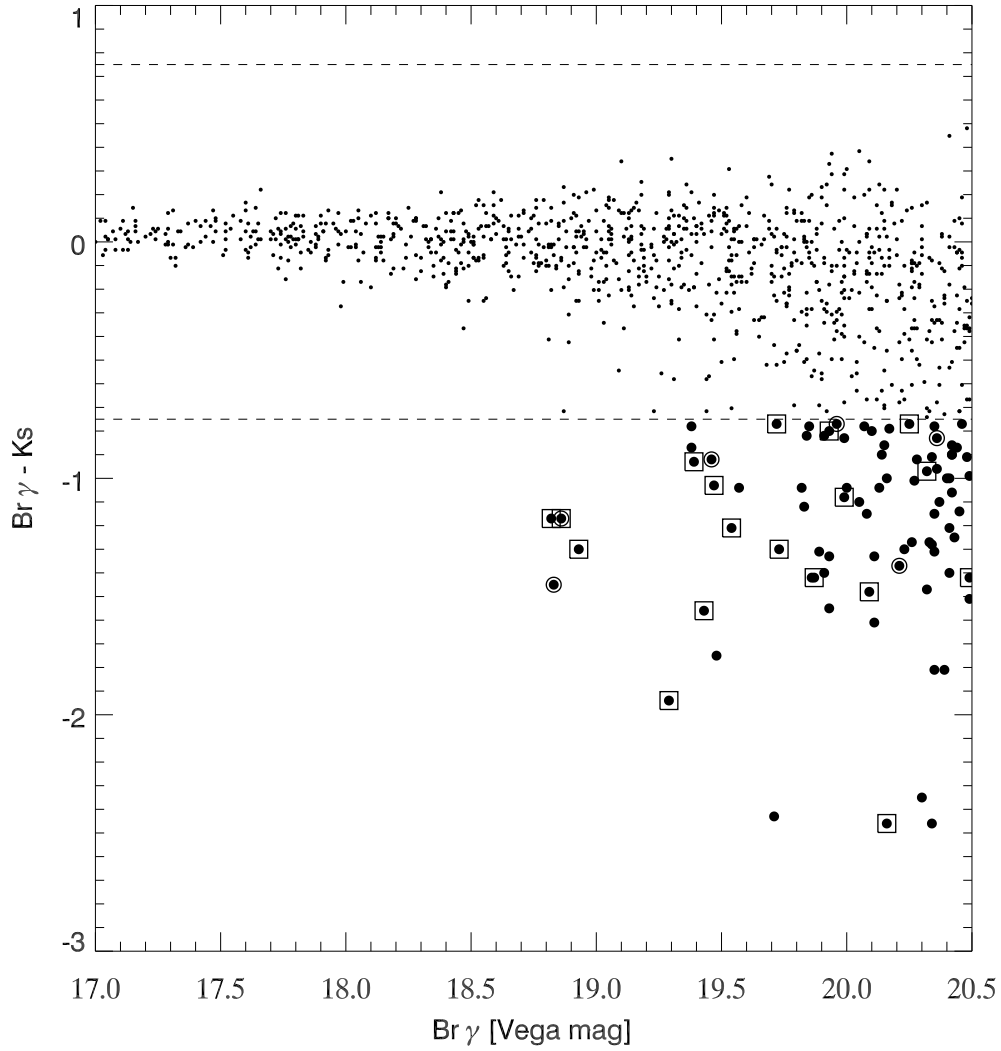

Figure 4.8 Near-infrared narrow-band excess ($Br\gamma - K_s$) of objects from a portion of HS1700+64 field with near-infrared imaging coverage. Objects satisfying $Br\gamma - K_s \leq -0.75$ are marked with larger symbols. Objects that have a spectroscopically confirmed redshift in the redshift interval $2.27 \leq z \leq 2.33$ are marked with additional square symbols. Circles mark 6 objects that are also classified as DRGs.

Table 4.3. DRG objects matching H α or Ly α selection criteria

RA	DEC	Name	Match[a]	K_s	$J-K_s$	z_{em}	z_{abs}	Comment
17:01:18.76	64:08:20.2	DRG6	HaNB53	20.95	2.84	···	···	···
17:00:47.61	64:09:44.5	DRG20	HaNB3	19.93	2.74	···	2.286	MD69
17:01:04.22	64:10:44.1	DRG29	HaNB72	19.87	2.43	···	···	···
17:00:42.04	64:11:24.2	DRG34	BNB165	19.55	2.48	2.333	···	MD94,AGN
17:01:04.05	64:12:11.7	DRG38	BNB16	20.35	3.12	2.290	2.260	BLOB536
17:00:58.06	64:13:10.3	DRG46	HaNB2	19.88	2.54	···	···	···
17:01:19.37	64:14:37.7	DRG55	HaNB33	20.44	2.57	···	···	···
17:01:33.64	64:14:37.8	DRG56	HaNB11	20.12	2.42	···	···	···
17:01:32.75	64:14:21.7	DRG72	BNB71	20.92	3.76	2.282	···	···

[a]Name of matching H α or Ly α selected object.

4.4 Catalog of DRG objects

The available near-infrared photometry (J, K_s) allowed for the creation of a catalog of Distant Red Galaxy candidates (DRG, Franx et al. (2003)) by using the $(J-K_s) > 2.3$ criterion. It has been found that this color cut, which attempts to identify objects with a prominent 4000Å or Balmer break feature in their SED, is efficient in identifying high-redshift galaxies that are heavily reddened or have a dominant old stellar population. However, obtaining redshifts for a large sample of these objects has proved to be difficult (Wuyts et al. 2009; Kriek et al. 2006) mainly due to their faintness in the optical and lack of multiplexing capability in the near-infrared.

In the portion of the field with near-IR imaging coverage we find 75 sources that satisfy the $J-K_s > 2.3$ selection down to $K_s = 21.0$ (Vega). The DRG selection was designed to identify galaxies at redshifts $z > 2$, however, Wuyts et al. (2009) show that the distribution in redshift of these sources has a broad range, from $z = 1.2$ to $z = 3.7$. By matching the positions of Ly α and H α emitter candidates with DRG candidates, we find that 6 out of 83 objects (7%) passing the H α selection are also selected with the DRG criterion. Similarly, 3 out of 37 (8%) of Ly α emitters (within the near-infrared imaging coverage) are also selected as DRGs. Out of these 9 matches to Ly α or H α selection we find that 4 objects have already determined redshifts at $z \sim 2.3$ (Table 4.3).

If we assume that he remaining 5 DRG matches are also at a redshift $z \sim 2.3$, this would imply that a fraction of $\geq 11\%$ of all $J-K_s > 2.3$ objects in this field is at the proto-cluster redshift. Our current understanding about the redshift distribution of sources selected with the DRG criteria is based on very small samples (Wuyts et al. 2009). For this reason it is not yet possible to establish whether or not the number of DRG candidates in the proto-cluster represents an over-density in a similar amount as observed in the number of "BX" galaxies.

The selection of DRG objects in this work has been performed only for extending the "reach" of continuum selection, so that it can be studied in comparison to H α and Ly α objects. As we will see later when describing the newly discovered Ly α blobs, 2 out of 4 blobs within the near-infrared survey are found to incorporate a source passing the DRG criteria. In case of BLOB-3, object DRG64

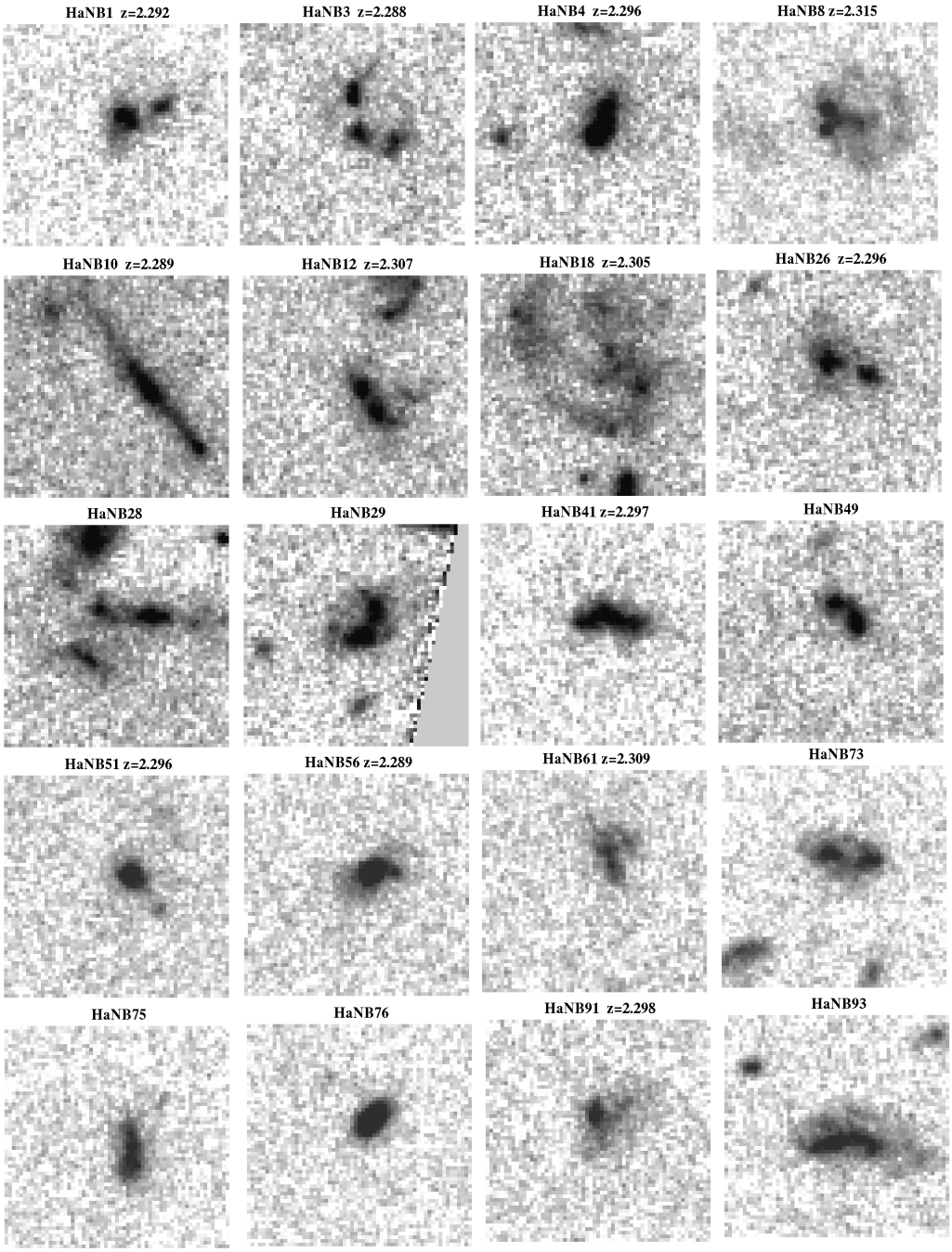

Figure 4.9 Cutouts from HST imaging coverage of HS1700+64 proto-cluster field centered on positions of H α emitters. The images were taken with ACS and F814W filter. Field size is $3''$, and redshifts are indicated where available.

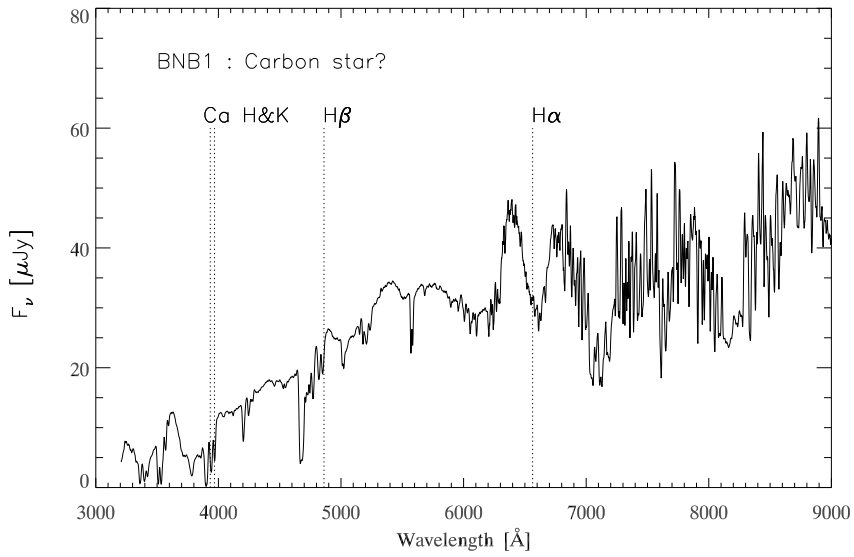

Figure 4.10 The puzzling spectrum of BNB1, the brightest source from the 4010 Å excess catalog. We tentatively identify it as a likely late-type carbon star based on the presence of Ca H&K and H α and longward broad absorption features.

is found close to the "core" as determined by Ly α emission, and it is the only continuum selected source that is likely related with the blob. This underscores the importance of deep multi-wavelength broad-band coverage in conjunction with narrow-band surveys.

4.5 Optical Spectroscopy of Ly α Candidates

Optical follow-up spectroscopy of candidate Ly α emitters (Section § 4.3.1) has been obtained using Low Resolution Imaging Spectrometer (LRIS, Oke et al. (1995); Steidel et al. (2004)) on Keck I telescope. The observation were carried out over the course of several separate observing nights in September 2006[1], September 2007, June 2008 and September 2009.

For observing runs concluding with June 2008 the configuration included "d680" dichroic as the beam-splitter and the 400/3400 grism as the dispersive element on the blue arm spectrograph (LRIS-B). The masks were designed with 1.″2 wide slits, and LRIS-B data was binned by a factor of 2 in dispersion direction during readout. This provides a spectroscopic resolution of FWHM= 8.2 Å, which for Ly α observed at $z \sim 2.3$ corresponds to a velocity resolution of $\sim$ 600km s^{-1}. For the September 2009 observing run LRIS-B was also configured with the "d680" dichroic but this time we employed the 600/4000 grism. Slits used were 1.″2 wide and data was binned by 2 in the dispersion direction during readout. Final spectral resolution for September 2009 LRIS-B data is

[1]The candidates observed in September 2006 were based on an earlier attempt at creating a catalog of narrow-band excess targets, preceding deep imaging data obtained in July 2007 and presented in this work

$FWHM = 4.5$ Å ($\sim 300 \mathrm{km\,s^{-1}}$). Note that all of the above spectroscopic resolution estimates are based on a slit width of $1''.2$, but the seeing disk of the sources during our observations was commonly below $1''.0$, so the resolution element is then $\geq 20\%$ smaller.

We have collected follow-up optical spectroscopic observations for 49 of the 119 objects from the 4010 Å narrow-band excess catalog (Table 4.1). The choice of sources was based on considerations of brightness in narrow-band (with brighter sources having higher priority) and optimal mask geometry.

Only two interlopers were found with redshifts other than $z \sim 2.3$. The first of those is BNB1, the brightest narrow-band excess candidate ($NB = 20.46, \mathcal{R} = 19.9$). It has an unusual optical spectrum and we tentatively identify it as a late-type carbon star based on the presence of Ca H&K lines, and the broad absorption bands at 8000Å. The spectrum of BNB1 is shown in Figure 4.10. No prominent emission feature is seen at 4010 Å so we assume that this object has passed the narrow-band excess selection owing to flux variability between the epochs of narrow-band and continuum imaging. The other interloper is BNB4 and its optical spectrum identifies it as a quasar at $z = 1.569$. This quasar made the narrow-band excess selection due to the presence of CIV 1549 emission line at 4010 Å with $\mathrm{W}_\lambda \sim 120$ Å (observed frame).

Therefore we can be reasonably confident that our 4010 Å catalog has a very small fraction of interloper objects ($\sim 4\%$) at redshifts other than $z \sim 2.3$. This claim is also supported by the appearance of 4010 Å excess sources in deep HST ACS imaging data of the HS1700+64 field (Peter et al. 2007). Figure 4.7 shows 18 sources from our 4010 Å excess catalog found in the ACS imaging coverage. The effective wavelength of the filter used (F814W) for these data is 8332Å, and the filter band pass at $z = 2.3$ would correspond to $2150 - 2900$ Å in the rest-frame. The majority of Ly α emitters are very faint in the continuum ($R \sim 26 - 27$) and appear to have small angular size ($FWHM \sim 0''.15$) in these images, making it very unlikely for them to be low-redshift interlopers.

Three sources from the 4010 Å excess catalog have optical spectra that show clear signatures of AGN activity. Object BNB3 is identified as a $z = 2.269$ quasar with broad lines in both emission and BAL absorption. Objects BNB10 ($z = 2.284$) and BNB165 ($z = 2.333$) we classify as AGN galaxies based on the presence of high-ionization emission lines.

Of the remaining 44 sources with optical spectroscopy observations, 5 are found to be associated with large clouds of extended Ly α emission (Ly α "blobs"). We will present their spectra and discuss these sources in detail in Section § 4.8. The other 39 objects have been identified as Ly α emitters with redshifts within $2.26 \leq z \leq 2.34$. The Ly α line profiles are presented in Figures 4.11 and 4.12.

Below we will address in more detail a few of the more interesting findings from the spectroscopic follow-up. From 21 spectra taken with the lower resolution setup (grism 400/3400) we find 6 where Ly α line is resolved. These are BNB009, BNB019, BNB021, BNB061, BNB095 and BNB115. Object BNB009 is also interesting in that it has a very strong Ly α line (rest-frame $EW \geq 120$ Å) but also a detected CIV 1549 emission line. Object BNB019 has a broad Ly α emission with an implied velocity

width of $FWHM = 1200\mathrm{km\,s^{-1}}$, and it is spatially extended over more than $3''$ (25kpc) in the slit direction. This source is found right at the very edge of our narrow-band image, so it is possible that it is related to one more large Ly α blob missed by the present survey. For object BNB95 the emission feature identified as Ly α is most likely double peaked, with components differing by about $1000\mathrm{km\,s^{-1}}$. A total of 18 spectra was observed with LRIS-B in the higher resolution setting (grism 600/4000). We find 5 where Ly α line width is in the $300 - 600\mathrm{km\,s^{-1}}$ range, others are unresolved. In summary, we observe a range of velocity widths, from $300\mathrm{km\,s^{-1}}$ (for our higher resolution observations) to strong, spatially extended emission with $FWHM = 1200\mathrm{km\,s^{-1}}$.

Continuum flux has been detected in only a handful of emitters, as we have used only moderate exposure times for quick confirmation of Ly α candidates. No optical spectroscopy was obtained for BNB165 and BNB41 and their redshift given in Table 4.1 were determined based on the measurement of H α in near-infrared (Erb et al. 2006a).

The distribution of Ly α emission redshifts after the spectroscopic follow-up is shown in Figure 4.13. We identified 31 Ly α emitters within the redshift interval $z = 2.300 \pm 0.015$. Another 31 rest-UV continuum selected objects *without* a match in the Ly α emitter catalog have been identified within this redshift over-density. Approximately two thirds of such objects (total of 21) have no detectable Ly α emission and their redshifts have been established based on strong ISM absorption lines. With our Ly α emitter survey we have succeeded in doubling the number of known objects in the z=2.3 proto-cluster.

4.6 Comparison of Ly α and H α with Rest-UV Continuum Selection

Independently of our 4010 Å and Br γ narrow-band surveys, follow-up spectroscopy of star-forming galaxy candidates selected according to their rest-UV continuum photometry $(U_n, G, \mathcal{R})$ has been ongoing for the past several years. These include $z \sim 2$ star-forming galaxy candidates (according to BX/BM broad-band color selection criteria, Steidel et al. (2004)) and $z \sim 3$ LBG candidates (C, D, M, MD broad-band color cuts of Steidel et al. (2003)). The magnitude limit for both of these catalogs is $\mathcal{R} \leq 25.5$.

As of the time of writing of this chapter, spectroscopic observations in $16' \times 16'$ optical survey area centered on HS 1700+64 have provided redshift determinations for 215 objects spanning the range of $1.5 \leq z \leq 3.5$. Within the galaxy over-density redshift interval $z = 2.300 \pm 0.015$, as initially defined by Steidel et al. (2005), there are now a total of 37 rest-UV continuum objects identified. These are mostly satisfying BX color cuts (32 objects), with 4 more MD and 1 C object. There are about 1450 BX candidates in the optical survey field, and so the projected number of continuum selected proto-cluster members brighter than ($\mathcal{R} = 25.5$) can be estimated to be ~ 215.

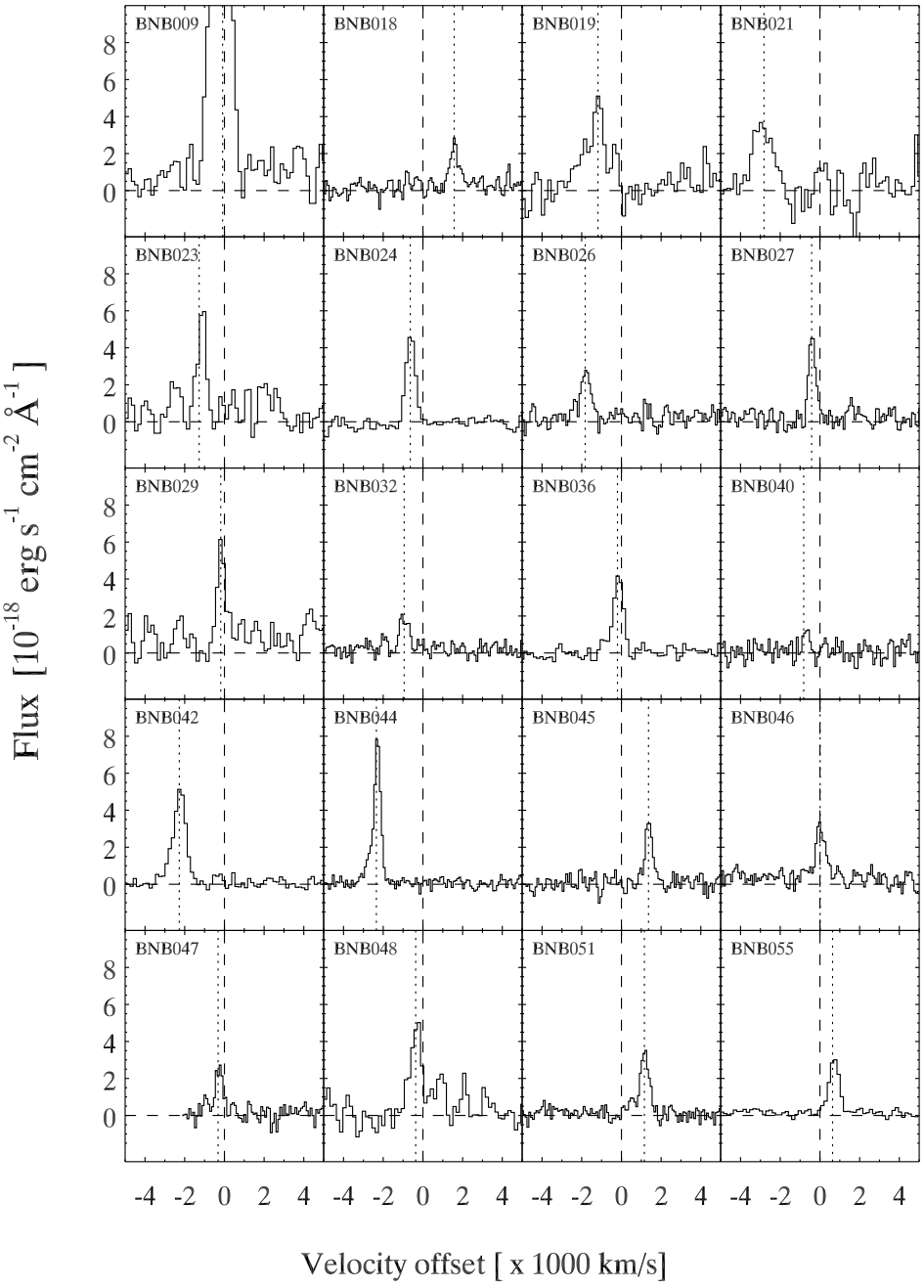

Figure 4.11 Follow-up optical spectra of 4010 Å sources. In all cases shown we find a single prominent emission feature and identify it as Ly α at $z \sim 2.3$. The x-axis shows the velocity offset from $z = 2.30$. Object BNB009 has a very strong Ly α emission that peaks at 4×10^{-17} erg s^{-1} cm^{-2} Å^{-1}.

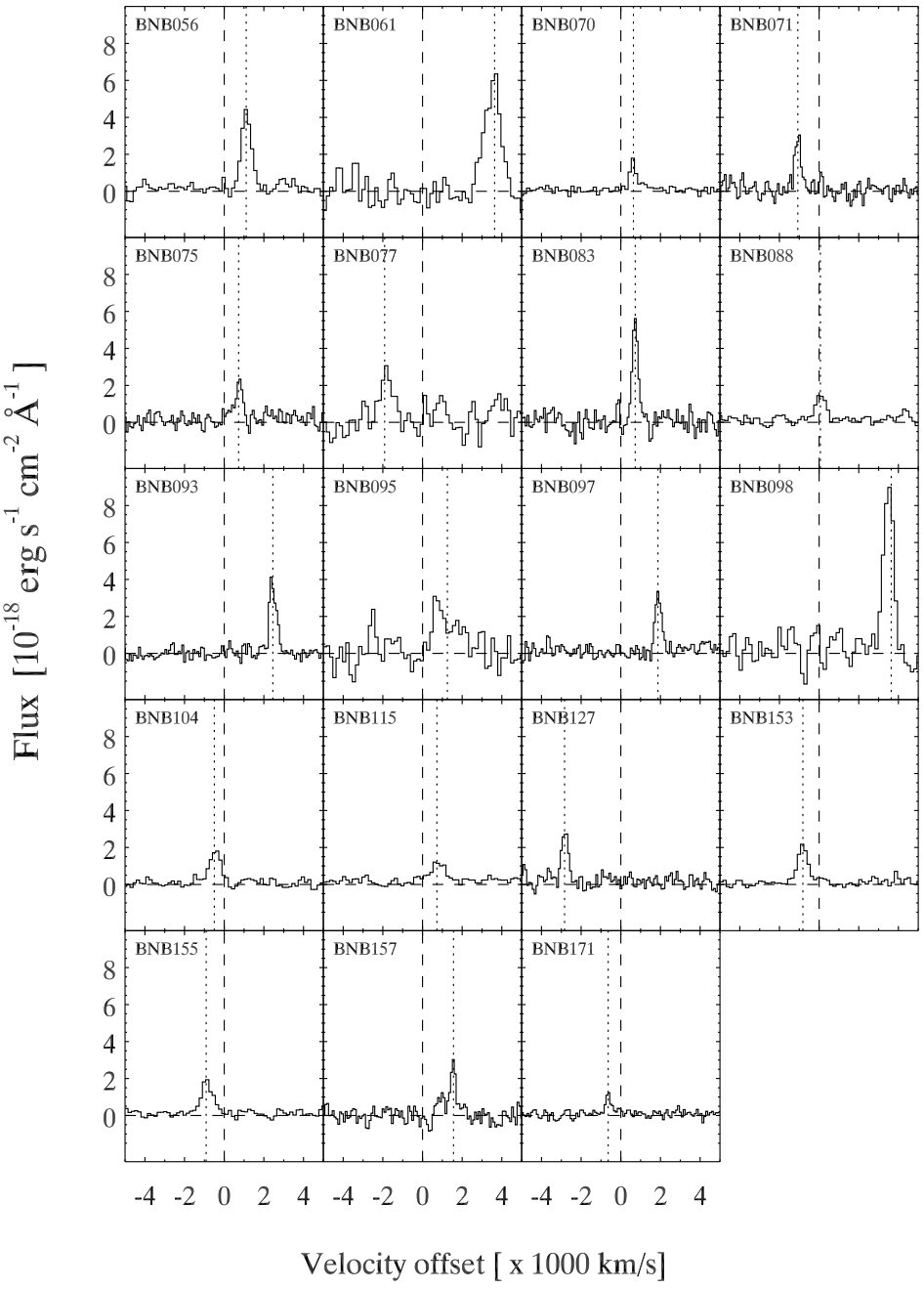

Figure 4.12 Continued from Figure 4.11.

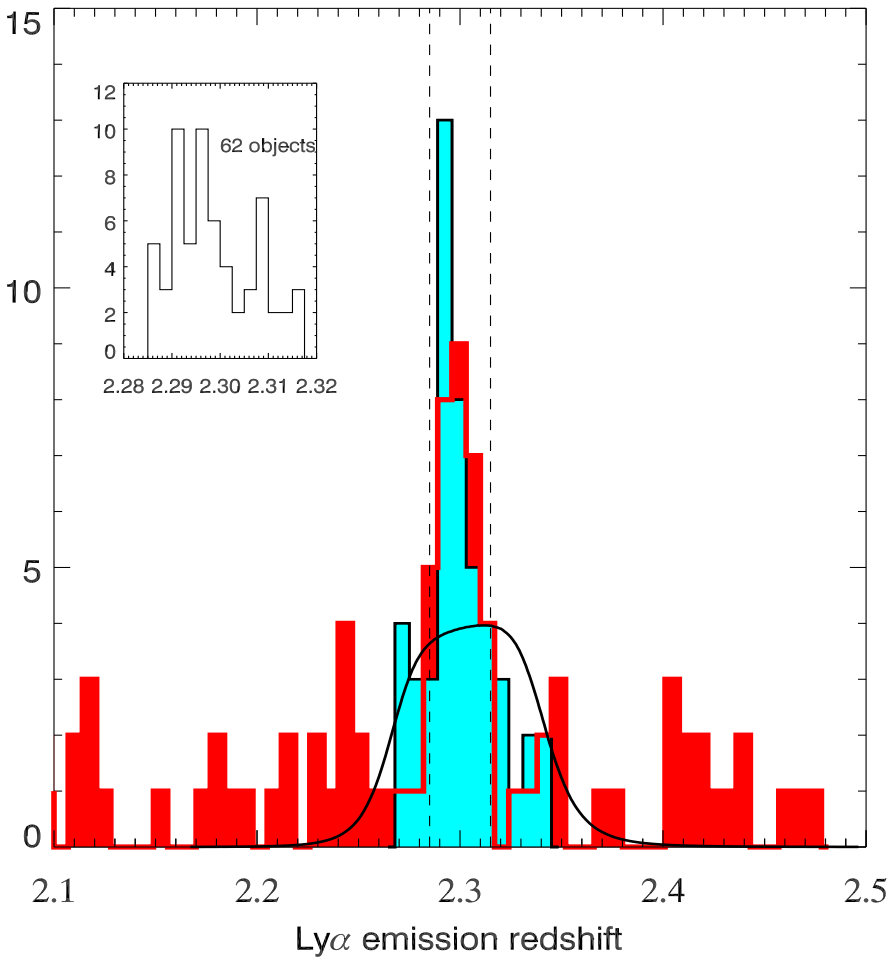

Figure 4.13 Histogram of the redshift distribution in the HS1700+64 proto-cluster field. Blue histogram shows the distribution for Ly α emitters discovered in this work. The red histogram (background) shows redshifts of continuum selected star-forming galaxies that are not selected as Ly α emitters. To accentuate the prominence of the z=2.3 over-density, the black curve shows the width of the filter 4010 Å in redshift space normalized to same total area as the histogram of Ly α emitters. Inset zooms in on the interval $z = 2.300 \pm 0.015$ and shows the distribution for Ly α emitters and continuum selected objects (62 in total). The redshift has been determined by Ly α emission in case of no measurable ISM lines are seen in absorption.

Most of the Ly α emitter sources are much fainter in the $\mathcal{R}$ band than the rest-UV selection limit. Only 25 out of 119 (21%) Ly α excess candidates are found in the broad-band catalog with $\mathcal{R} \leq 25.5$. However, a majority of those bright enough (22 objects, or 88%) are also flagged as $z \sim 2$ or $z \sim 3$ candidates by their $(Un - G)$ and $(G - Rs)$ broad-band colors (Table 4.1). More specifically, 14 are selected as BX $z \sim 2$ galaxy candidates, 1 satisfies the BM selection criteria and 7 are formally classified as $z \sim 3$ LBG candidates. According to matches with rest-UV catalog, we were able to assign redshifts for 9 out of 22 Ly α emitter candidates, and they are all found to be $z \sim 2.3$. As we have shown earlier in Section § 4.5, the follow-up spectroscopy of other Ly α emitter candidates finds the contamination of our 4010 Å excess selection to be very small ($\leq 4\%$).

We can make a crude estimate of the number of Ly α emitters with ($\mathcal{R} \leq 25.5$) expected in the optical survey field. Based on the observed distribution of Ly α equivalent with for Lyman-break galaxies (Steidel et al. 2000; Shapley et al. 2003), only $\sim$ 13% have $EW \geq 30$ Å in rest-frame. Assuming the same distribution is valid for the estimated population of 215 BX galaxies at $z = 2.3$, we would expect to see $\sim$ 28 of them as 4010 Å excess objects. We observe 22 matches between Ly α emitters and continuum selection, which is in very good agreement given our crude calculation. All three narrow-band excess sources which were later identified as galaxies hosting a quasar or an prominent AGN were identified with continuum selection as well (BNB3 (BX116), BNB10 (MD157) and BNB165 (MD94)).

Out of 83 candidate H α emitters we find that 70 objects (84%) can be matched with entries in the R-band selected catalog, and 67 of those are brighter than $R = 25.5$. Therefore a large majority of H α candidates (81%) is within the magnitude limits for rest-UV selection, but we find that only of 29 H α objects (35%) were actually selected as star-forming galaxy candidates through their rest-UV broad band colors (Table 4.2). For 7 sources there were existing spectroscopic observations in the near-infrared, using NIRSPEC (McLean et al. 1998) on the Keck II telescope. Redshifts were determined directly from measurements of the the H α line (Erb et al. 2006b). Combining the results of existing near-infrared and optical spectroscopy, we are able to assign redshifts for 21 H α objects. We find 18 H α objects with $z \sim 2.3$ and three candidates are uncovered as interlopers. The first interloper is a LBG z=3.317, which was most likely selected due to [OIII] 5007 Å emission falling into the Br γ filter band pass. Based on its prominent narrow-band excess $NB_{Br\gamma} - K_s = 2.43$ the estimated [OIII] equivalent width is surprisingly high, $\sim$ 500 Å in the rest-frame, comparable to line strength seen in powerful radio galaxies (Armus et al. 1998). The other two interlopers are identified with a galaxies at z=1.843 and z=2.4213. Based on these three sources we estimate a contamination fraction of $\sim$ 14% for those H α excess sources which are also rest-UV candidates. Unfortunately, at present there are no spectroscopic observations of H α excess sources that do not match rest-UV selection, so the above contamination fraction estimate is formally valid for only 35% of the sample.

Figure 4.14 shows the common near-infrared and optical survey area centered on HS1700+64.

In the central $8' \times 8'$ area, where we selected 83 H α candidates, we find 37 Ly α emitter candidates, more than a factor of 2 less. This is somewhat surprising in view of the fact that H α sources are generally much brighter in the rest-UV continuum than Ly α emitters, and should therefore be less numerous if they follow the same continuum luminosity function. We caution again that the contamination by interlopers might be poorly constrained for the full Brγ excess catalog. However, it should also be taken into account that the volume probed by Brγ filter is about 2 times smaller than for the 4010 Å filter. This increases the estimate of overabundance of H α over Ly α candidates additionally, though probably by less than another factor of two since both samples are likely to be dominated by objects at the proto-cluster redshift $z = 2.300 \pm 0.015$.

Another unexpected result is that there is almost no overlap between candidates obtained from the Ly α and H α narrow-band selections. In Section § 4.7.1 we will investigate this finding in more depth through comparison of spectra of rest-UV selected galaxies that match Ly α or H α excess criteria.

4.7 Ly α Radiation of H α Emitters

4.7.1 Composite Spectrum of H α Emitters

As we have discussed in Section § 4.6, there are a number of objects with 4010 Å or $Br\gamma$ narrow-band excess flux that were also selected as star-forming galaxy candidates based on their $U_n, G, \mathcal{R}$ photometry (Tables 4.1 and 4.2). Objects satisfying both rest-UV and Ly α selection are by and large very faint in the continuum (more than half are fainter than $\mathcal{R} = 25.5$). On the other hand, close to half of H α excess candidates are brighter than $\mathcal{R} = 24.0$. The continuum flux of confirmed H α emitters is usually well detected in the short exposures aimed at redshift identification of continuum selected targets.

We were able to combine the available spectroscopic observations for 16 H α excess galaxies that also satisfy rest-UV selection (part of the list presented in Table 4.2). All of these sources have confirmed redshifts placing then within the proto-cluster $z = 2.300 \pm 0.015$. Figure 4.15 shows the resulting composite spectrum in the rest frame, with the most prominent absorption features labeled. We find that the H α selected sources on average show the Ly α line in absorption, rather than emission, which is consistent with the lack of any overlap between H α and Ly α excess catalogs.

The above observation can be interpreted as an indication of fundamentally different physical conditions in galaxies with strong Ly α and H α emission lines. Though considerable research effort has been invested, the mechanism which creates apparently large equivalent width Ly α emission lines in star-forming galaxies is still not clear. In one of the most recent studies of a well-defined sample of LBG's, Kornei et al. (2009) find that apparent Ly α equivalent width is significantly correlated with the parameters describing the stellar populations. These authors find that galaxies with

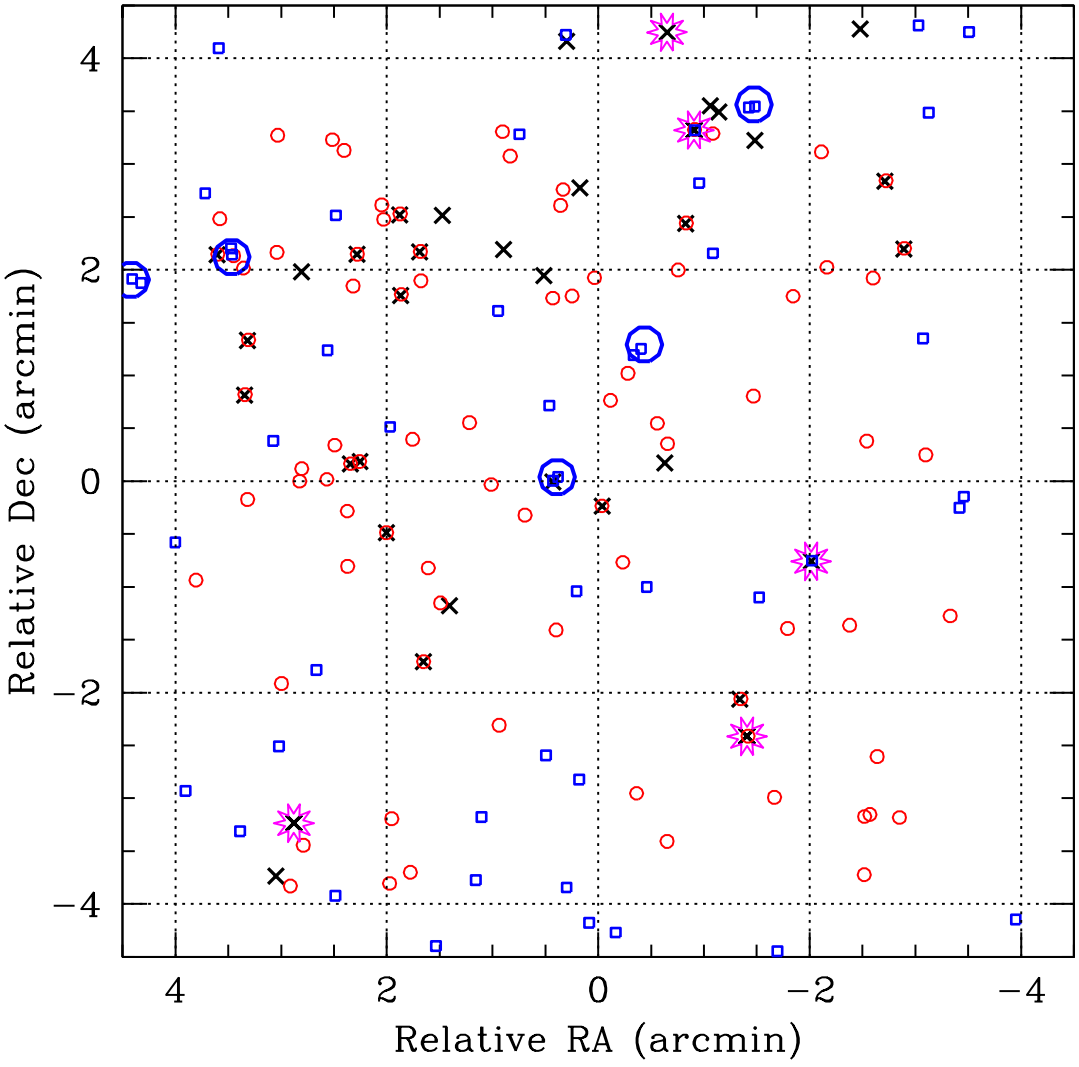

Figure 4.14 Spatial distribution of Lyα and H$\,\alpha$ candidates in a portion of HS1700+64 field with near-infrared imaging coverage. Ly$\,\alpha$ candidates are marked with blue squares, H$\,\alpha$ candidates with red circles. Large blue circles mark the position large Ly$\,\alpha$ blobs (5 out of 6 are seen in this map). Crosses mark rest-UV selected objects which are spectroscopically confirmed to be proto-cluster members. Stars label 5 objects with AGN emission features in the optical or near-infrared spectrum and redshift within $z = 2.30 \pm 0.04$.

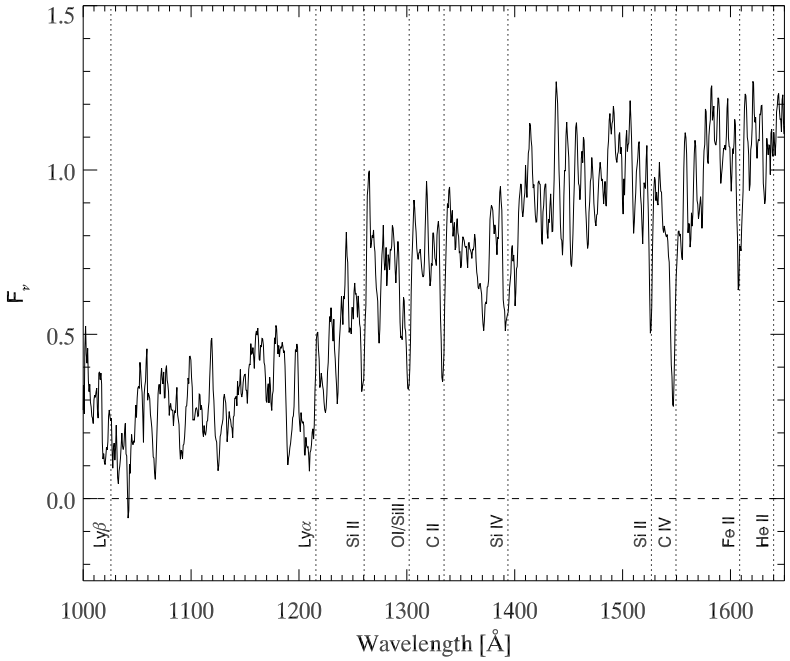

Figure 4.15 The average spectrum of 16 confirmed H α selected galaxies at the proto-cluster redshift $z = 2.300 \pm 0.015$ (Table 4.2). The flux is normalized to unity at 1600Å rest-frame. The average spectrum has Ly α line seen mostly in absorption, not emission. A number of the strongest ISM absorption features are labeled.

older age, lower SFR and lower dust extinction tend to be the ones with prominent Ly α emission. This is in agreement with the expectation that Ly α is easily destroyed by dust grains in the ISM (Pritchet 1994). Additionally, the currently accepted model for explaining the positive velocity offset of Ly α with respect to nebular emission lines (Adelberger et al. 2005) stipulates that large-scale outflows are already established and that we are receiving Ly α photons emitted from the outwardly expanding material on the opposite side of the galaxy (Tenorio-Tagle et al. 1999). A reasonable assumption is that these large-scale outflows should be more prominent in galaxies which now appear to have older stellar population, simply because they have had more time to significantly disturb their ISM.

On the other hand, if Ly α emission is predominantly observed in absorption, this would indicate that scattering by the dust grains in the ISM effectively clears any Lyα photons from our line of sight. One of the causes for this could be that the star-forming episode in the galaxy is still in an early stage and that strong bulk outflow has not yet been established. We know that this is not *necessarily* the case, as demonstrated by detailed studies of cB58, a strongly lensed Lyman-break galaxy at $z = 2.73$, which shows Ly α in absorption but also has a very strong bulk outflow (Pettini et al. 2002).

It has been well established that H α line luminosity is very close to the rate of creation of ionizing photons by the hottest stars, and thus directly related to SFR (Kennicutt 1998). Our near-infrared narrow-band selection requires equivalent width of $EW \geq 90$ Å for H α in rest-frame, which for a representative continuum brightness of $K_s = 21.5$ (Vega) would imply a $SFR \gtrsim 10 M_{\odot} yr^{-}1$. Most star-forming galaxies are indeed observed to have at least as high SFR, as determined from spectroscopic observations of H α in the near-infrared (Erb et al. 2006b) or SED fitting to broad-band observations from optical to mid-infrared (Shapley et al. 2005)). Therefore our H α selection includes objects having even a moderate values of SFR. We conclude that our observation of Ly α in absorption in the average implies that it is either age or dust extinction that are the root cause, and that the value of SFR does not play an equally strong role. However, we show in the following section that the problem may be further complicated when the *spatial* origin of Ly α emission in H α sources is investigated.

4.7.2 Detection of Spatially Extended Ly α Flux from H α Emitters

In this section we will expand our investigation of Ly α flux from confirmed H α emitters at $z = 2.3$.

We have created $10''$ cutouts from the continuum subtracted 4010 Å narrow-band image for the same sample 16 H α emitters that were used in creation of the composite spectrum of Figure 4.15. One object was excluded from the analysis due to bright objects nearby, and the 15 images were averaged. The average radial surface brightness profile is presented in Figure 4.16. In the central $\sim 1''$ (8kpc at $z = 2.3$), comparable to the size of the seeing disk in the image, the flux is formally negative, representing an apparent "deficit" of Ly α emission. This is as expected from the earlier observation that the average optical spectrum of H α emitters shows Ly α line in absorption.

Interestingly, we find a significant detection of extended Ly α flux as far as 50kpc ($6''$). The extended emission would have an total integrated magnitude of $NB \approx 24.9$, more than two magnitudes fainter than what is observed for the large Ly α blobs. Examining the images for the individual $H\alpha$ emitters we find that they do not show such extended emission at high significance above the image noise and it becomes apparent only in the substantially deeper average. The peak flux seen for H α emitters is about $2 \times 10^{-18} ergs^{-1} cm^{-2''-2}$, which is just above 1σ sky noise in a single object measurement. We have verified that this flux seen in the average is not caused by a single or a handful of objects by splitting the sample into several random subsamples and recalculating the radial profile. We find that composite images of all subsamples always show the same overall extent of the Ly α emission.

We compare the radial profile of Ly α from H α emitters with a composite, created in an equivalent way, of 19 objects which are members of the $z = 2.3$ proto-cluster but were not selected as either strong Ly α or H α emitters. These objects were identified during the spectroscopic follow-up of rest-UV continuum selected star-forming galaxy candidates. As seen in Figure 4.16, the observed

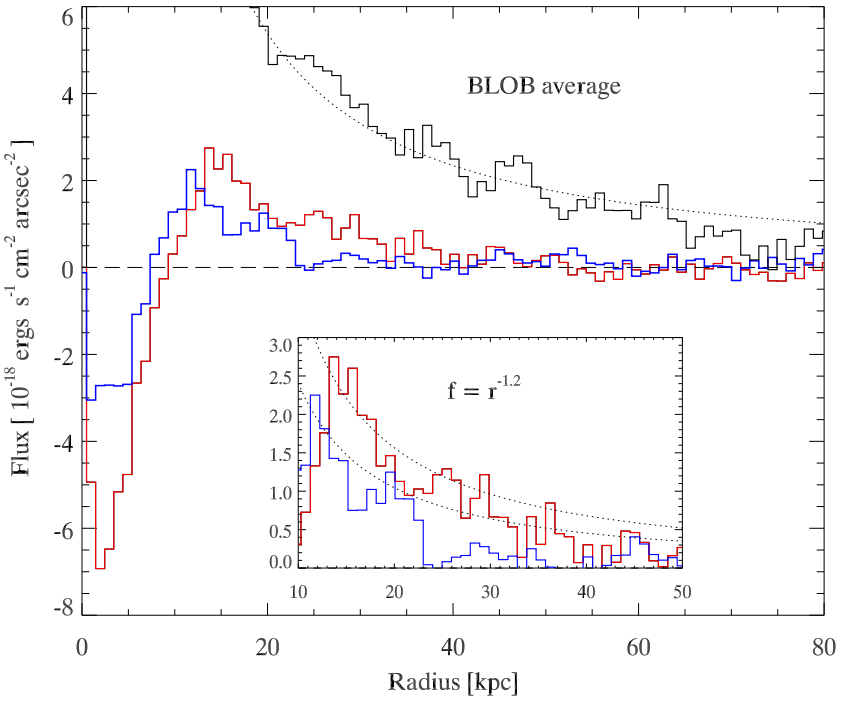

Figure 4.16 Radial profile of Ly α flux from an average of continuum subtracted 4010 Å narrow-band images for six large blobs (black histogram), 16 H α emitters (red histogram), and 19 confirmed $z = 2.3$ proto-cluster members that were not classified as strong Ly α or H α emitters (blue). The inset zooms in on the central 6″ for the latter two samples. The surface brightness of all three seems to be resembles a $f \sim r^{-1.2}$ dependence (dotted).

extended Ly α flux is lower by nearly a factor of two, but the radial profile has a similar overall shape. The surface brightness can be reasonably well approximated with an $r^{-1.2}$ dependence, which has been suggested by recent simulations of Ly α emission from cold gas streams feeding galaxies at high redshift (Goerdt et al. 2009). Figure 4.16 also shows the radial profile obtained in a similar manner from an average of the six Ly α blobs presented in this work. The $r^{-1.2}$ radial dependence fits reasonably well for composites of all three types of objects. However we caution that this agreement is only encouraging, since for the average of the six blobs we find the best fit power-law slope to be closer to $r^{-1.6}$, in the radius $20 - 70$kpc. Furthermore, the spatial dependence could also be represented by an exponential rather than a power-law.

It is not clear whether the higher level of Ly α flux observed for H α emitters is just a consequence of our small sample and flux limit, or a genuine property of H α emitters. The two galaxy samples compared have formally a very similar distribution in broad-band continuum brightness.

In a separate study of a proto-cluster at $z = 3.09$, Hayashino et al. (2004) have found Ly α flux extending out to $\approx$ 40kpc in the composite image of confirmed proto-cluster members not selected as Ly α emitters. Our observations securely establish that this extended emission can appear in

Table 4.4. Properties of the extended Ly α blobs from optical photometry

RA (J2000)	DEC (J2000)	Name	NB[a] (AB)	UG[a] (AB)	$W_{\lambda 0}$[b] (Å)	Area ($''^2$)	F(Lyα) (ergs s^{-1} cm^{-2})	L(Lyα) (ergs s^{-1})
17:01:04.16	+64:12:11.8	BLOB-1	22.15	23.84	129	128	6.6×10^{-16}	2.6×10^{43}
17:00:56.56	+64:13:27.2	BLOB-2	22.83	24.48	125	61	3.5×10^{-16}	1.4×10^{43}
17:00:46.99	+64:15:43.5	BLOB-3	22.54	24.20	126	105	4.6×10^{-16}	1.8×10^{43}
17:01:32.53	+64:14:16.4	BLOB-4	22.38	24.29	158	95	5.6×10^{-16}	2.2×10^{43}
17:01:41.31	+64:14:03.3	BLOB-5	22.69	23.73	71	53	3.2×10^{-16}	1.2×10^{43}
17:01:54.54	+64:13:39.6	BLOB-6	22.81	24.43	121	78	3.5×10^{-16}	1.4×10^{43}

[a] Total flux within the area defined by 1σ above sky contour in the continuum subtracted narrow-band image. This area is given in column 7

[b] Rest-frame equivalent width of Ly α line based on narrow-band filter FHWM = 90 Å and $(NB - UG)$ color.

objects regardless of the shape of Ly α in their spectra. The integrated Ly α flux observed from $1''$ to $6''$ would correspond to a rest-frame equivalent width of $EW \approx 33$ Å, based on the estimate of the underlying continuum flux from U_n and G magnitudes. If ionizing photons produced in star-forming regions are responsible for this Lyman α "glow", as opposed to collisional excitation in the cold flows, then the observed flux represents a significant fraction of total predicted budget of Ly α photons (up to $EW_0 \approx 150$ Å, Charlot & Fall (1993)).

The observation of extended Ly α emission has important consequences for our understanding of the physical mechanism responsible, as it is suggestive that most if not all galaxies show this feature. For example, it would be hard to imagine a scenario where AGN activity or intense starbursts driving superwinds would have a duty cycle long enough to cause extended emission in a majority of galaxies simultaneously.

4.8 Discovery of Six Ly α Blobs

In this section we report on the discovery of 6 large regions with extended Ly α emission in the field of HS 1700+64. Positions, observed flux and other key properties of these Ly α "blobs" are summarized in Table 4.4. The Ly α emission regions were labeled as "blobs" based on an isophotal size greater than 50 arcsec^2.

These 6 Ly α blobs are all located within a region roughly $4'$ in radius, corresponding to ≈ 6.6 Mpc (comoving) at z=2.3. To our surface brightness sensitivity limit in narrow-band ($NB \approx 29$ mag arcsec^{-2} for 1σ detection), these extended Ly α emission regions are seen to extend over a range of areas from 50 to 130 arcsec^2. Their total flux as observed in the 4010 Å narrow-band is in the range NB =22–23, and they show a mean excess of $NB - UG = -1.6$.

Figures 4.18 to 4.27 show the emission regions in the narrow-band image after continuum subtraction and the emission region contours overlaid on the continuum image. We will proceed to describe the properties of each blob individually.

4.8.1 BLOB-1

BLOB-1 is found close to the line of sight to the background quasar HS1700+64 (Figure 4.19). It is the brightest of the 6 new blobs in this field and also the largest, spanning $\approx$ 100kpc). It features a prominent "core," which was designated as the Ly α excess source BNB016. Rest-UV continuum selection has cataloged an object MD109 some $4''$ ($\approx$ 33kpc) away from BNB016, but still well within observed BLOB-1 emission region. The available HST ACS imaging (Figure 4.20) provides us with a high resolution look at what appear to be two similar, faint galaxies located at the positions of BNB016 and MD109. Broad-band near-infrared imaging shows that BNB016 also satisfies the DRG selection criteria, and is cataloged as DRG38 (Table 4.3). On the other hand, MD109 is barely detected in our Br γ and K_s images, so its H α excess could not be securely determined. Fortuitously, MD109 was observed with near-infrared spectroscopy by Erb et al. (2006a) and its nebular emission redshift was measured from H α to be z=2.2942. No other objects are found in optical or near-IR images within the boundaries of detected Ly α emission in BLOB-1.

A "clump" of emission in BLOB-1 has been formally cataloged as the Ly α excess source BNB041, and its centroid is only $\approx 1''$ away from MD109. The follow-up spectroscopy centered on MD109, where BNB041 was just off the edge of the slit, shows that MD109 has a weak Ly α emission at $z = 2.295$ and ISM absorption lines at a redshift $z = 2.297$ (slit position n6, 4.18).

Follow-up optical spectroscopy of BLOB-1 was obtained on two separate occasions, and we sampled the extended emission along two different position angles, PA=76° and PA=140° (Figure 4.18). In both observations we detect a resolved Ly α emission line at the position of BNB016, with $z = 2.290$ and FWHM $\approx$ 20 Å, corresponding to velocity dispersion of $\sigma \approx 1400\mathrm{km\,s^{-1}}$. Faint optical continuum has also been detected at the position of BNB016 (DRG38) enabling identification of ISM absorption lines with a redshift $z = 2.260$. Our spectroscopic follow-up was not sensitive enough to detect emission from other parts of BLOB-1. The spectrum of BNB016 in BLOB-1 is shown in Figure 4.32.

4.8.2 BLOB-2

The second large cloud, BLOB-2, has an apparent elongated shape (Figure 4.21) and is $15''$(120kpc) long. It does not encompass any star-forming galaxy candidates selected by optical or near-infrared imaging.

Two "clumps" in BLOB-2 have been cataloged as separate entries in the Ly α excess catalog : BNB070 and BNB171. In the continuum subtracted image we can clearly see that the blob has a much brighter "core" located about $3\farcs5$ NW of BNB070, but it was not a part of the 4010 Å excess catalog due to blending with a nearby brighter source in the "UG continuum" image. We designate this source as BLOB-2c (for "core"), with estimated brightness $NB \approx 24.8$ and $(NB - UG) \approx -1.2$.

Its properties are included in Table 4.1.

The slit position angle used during follow-up optical spectroscopy includes all three sources, BLOB-2c, BNB070 and BNB171. We detect and identify Ly α emission from all three sources, with redshifts z=2.3082, z=2.3065 and 2.2930 respectively.

The spectra were obtained with LRIS-B in our higher dispersion setup (600/4000 grism), but all three lines are seen to be unresolved, implying intrinsic velocity width less than FWHM= 300km s^{-1} (Figure 4.33). No continuum flux is detected. Of note is that there seems to be a progression in velocity implied by the wavelength of Ly α emission. Going from the emission "core"(BLOB-2c) to BNB171 at the apparent edge of the blob, some 70kpc away, the peak emission is blueshifted by about 1400km s^{-1}.

4.8.3 BLOB-3

BLOB-3 is emission region with a radius of roughly 50kpc. Two separate 4010 Å excess sources are catalog, BNB022 (being the "core" of the blob) and BNB040 (Figure 4.23). It is peculiar that there seem to be no clear identifications at the two positions in the HST ACS image (Figure 4.25) taken with the F814W filter.

BLOB-3 includes another source found about halfway between positions for BNB040 and BNB022 and it is classified as DRG64 from the near-IR photometry. It is a relatively bright object ($K_s \approx 19.2$) and is clearly detected in the ACS image.

With follow-up optical spectroscopy with slit position n1 (PA=76°) we were able to detect the Ly α emission line extending over 4.″0 in length (30 kpc). The width of the line is probably slightly larger than the spectroscopic resolution, having $\sigma \approx 750$km s^{-1}. We determine the redshift to be z=2.2929 and no significant velocity shift over the spatial extent of the detected emission is observed. No continuum flux has been detected in the spectroscopic observation.

Optical spectroscopy has also been successful in detecting the Ly α emission line of BNB040 (z=2.291). We have no spectroscopic information for DRG64, but based on the density of DRG candidates in the field the probability that this is a chance association is negligible.

4.8.4 BLOB-4

BLOB-4 also has been separated into two catalog entries, BNB07 (as the "core") and BNB071 (Figure 4.26). At the position of BNB07 we detect a Ly α emission feature with a redshift $z = 2.296$ which is marginally resolved, with an implied velocity width (after correction for spectroscopic resolution) of 450km s^{-1}.

The emission region contains an rest-UV continuum selected object, BX909, whose spectrum shows a broad Ly α absorption feature and ISM lines at redshift $z = 2.291$ (Figure 4.34). BX909

is also identified as a H α emitter, HaNB45. Another rest-UV continuum candidate, BX912, is found just outside the detected Ly α emission boundary, but at present no spectroscopic redshift is available (Figure 4.27).

4.8.5 BLOB-5

BLOB-5 is the smallest in size of the 6 blobs presented in this paper, spanning just over 6″(50kpc) along its longest axis (Figure 4.28). It contains the rest-UV selected object BX888, which has a confirmed spectroscopic redshift of $z_{em} = 2.270$ and $z_{abs} = 2.263$. Its spectrum shows a weak Lyα emission line which in combination with the Lyα absorption component gives an effective equivalent width close to zero. The "core" of the blob is cataloged as object BNB021, with another clump of emission approximately 6″ (50kpc) to the SW identified as Ly α excess source BNB062. In the spectrum of BNB021 we observed a double-peaked Ly α line at redshifts $z = 2.267$ and $z = 2.272$. We also detect a continuum which enabled identification of ISM absorption features, and possibly a weak C IV 1549 Å emission feature (Figure 4.35). The absorption redshift of BNB021 is found to be $z_{abs} = 2.264$, very close to that observed for BX888. For object BNB062 we have detected a very faint continuum, but we could not confirm a Ly α emission feature at z=2.3, so its redshift is unclear.

The "UG continuum" image shows three additional star-forming galaxy candidates without spectroscopic observations, the closest one being MD139 just 3.″5 from BX888 (Figure 4.29).

4.8.6 BLOB-6

For BLOB-6 we were successful in detecting a spatially extended emission line with two observational configurations (slits n1 and n4, Figure 4.30). In both spatial directions (close to perpendicular cuts along the blob) the emission appears to have no velocity gradient, and we assign a redshift of z=2.299 is assigned to the "core" (cataloged as BNB015) and the blob as a whole. No continuum flux has been detected.

There are three rest-UV continuum selected star-forming galaxy candidates very close to this blob (Figure 4.31). Unfortunately, at this time no spectroscopic observations exist that would suggest if any of them are associated with the Ly α emission.

4.8.7 The structure of the z=2.3 proto-cluster as traced by the Ly α blobs

Figure 4.17 presents the contours of the Ly α emission focusing on the region containing the six blobs. The blob locations extend over 12Mpc (comoving), and it seems that there might be two linear "branches," in the direction from BLOB-1 to BLOB-3 and BLOB-3 to BLOB-6, that each contain three blobs roughly 2Mpc apart and also an apparent overabundance of H α emitters and

rest-UV selected proto-cluster members. The near-IR survey does not cover the area beyond BLOB-4, so at present it is not clear if this trend extends also further across BLOB-5 and BLOB-6. The locations of Ly α emitters appear less significantly correlated with these "branch" directions.

BLOB-6 is found near the edge of our 4010 Å survey coverage, so it is probable that we have not captured the full extent of the proto-cluster region in which blobs appear. Nevertheless, even with our observations we have shown that the $z = 2.3$ proto-cluster is the richest structure identified to date in terms of the number of giant Ly α emission blobs, and is therefore well suited for follow-up observations at other wavelengths.

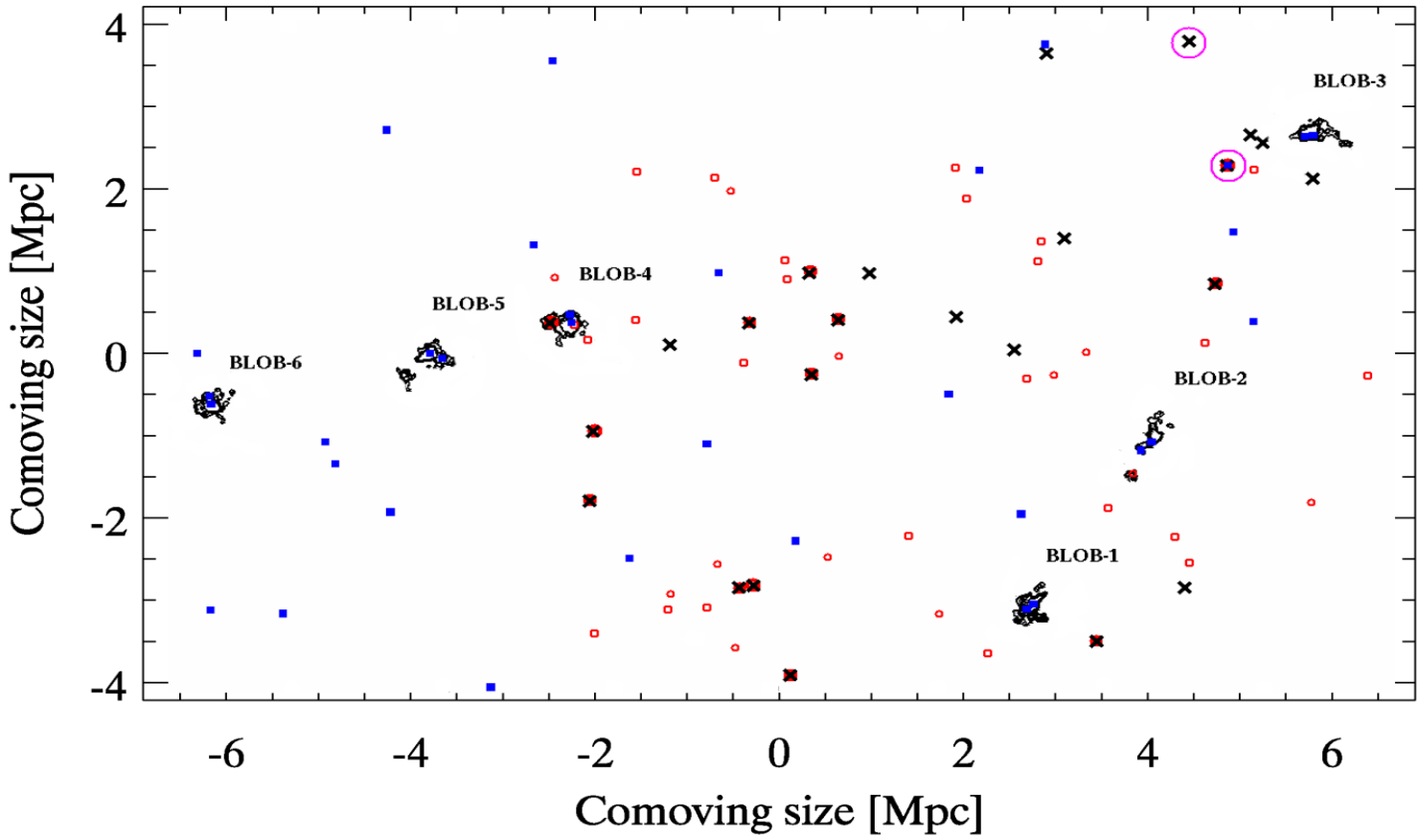

Figure 4.17 Map of Ly α blobs, Ly α and H α emitters presented in comoving coordinates. Blob contours are as presented in Figures 4.18, 4.21 4.23, 4.26, 4.28 and 4.30. Sources from the Ly α and H α excess catalogs are shown with blue squares and red circles. Crosses mark rest-UV selected galaxies with spectroscopic redshifts that places them as members of the z=2.3 proto-cluster. Large magenta circles show the positions of two AGN sources

.

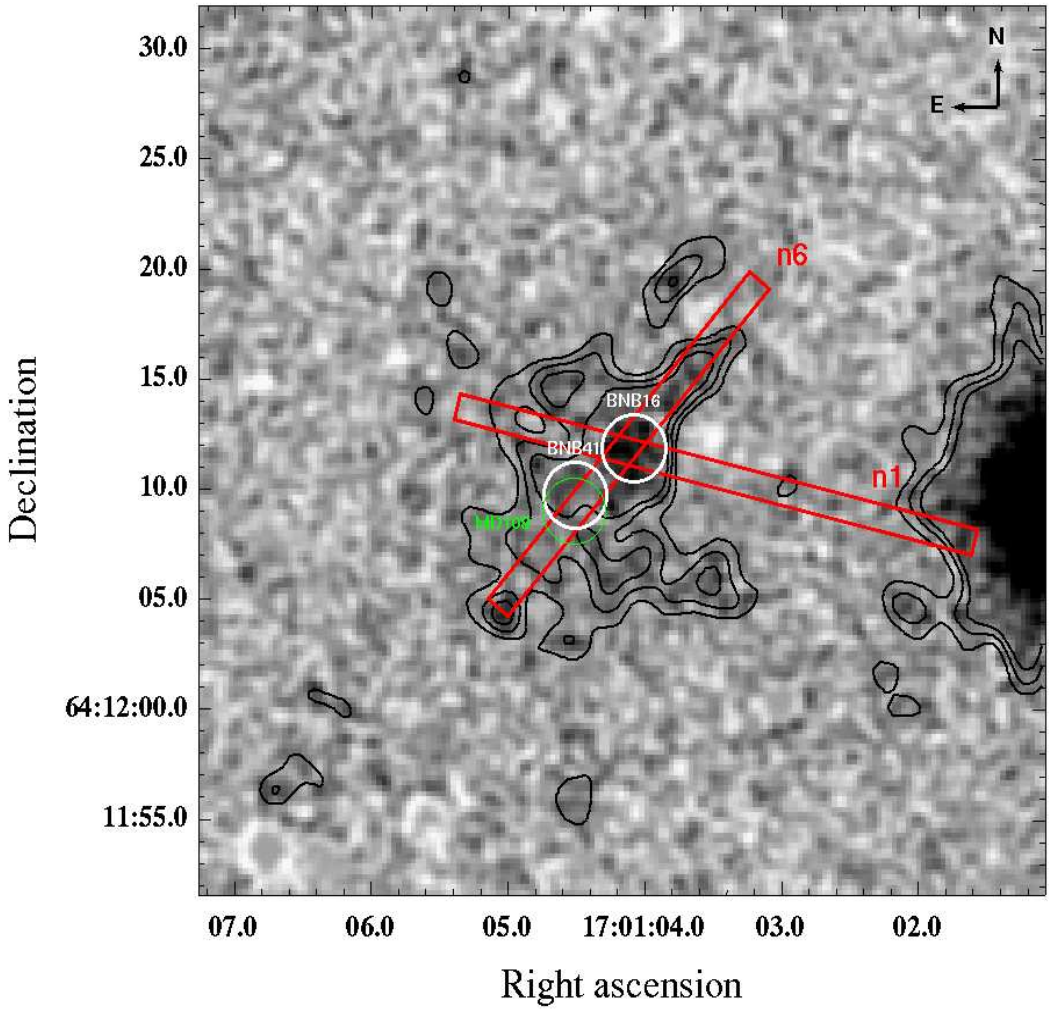

Figure 4.18 A portion of the continuum subtracted narrow-band image (grayscale) centered on BLOB-1. The overlaid contour curves are created after a Gaussian smoothing with FWHM = 7 pixels ($\approx 1\farcs7$) is applied. Contours are marked at surface brightness levels of $1.5, 3$ and 4.5×10^{-18} erg s^{-1} cm^{-2} arcsec^{-2}. Two patches of the blob emission were formally cataloged as narrow-band excess sources BNB016 and BNB041 (circled in white). The latter is coincident with rest-UV continuum selected source MD109 at z=2.294 (green). The slit positions used for optical spectroscopy observations (n1 PA=76° and n6 PA=140°) are shown. The bright object on the right edge of the image is the quasar HS1700+64.

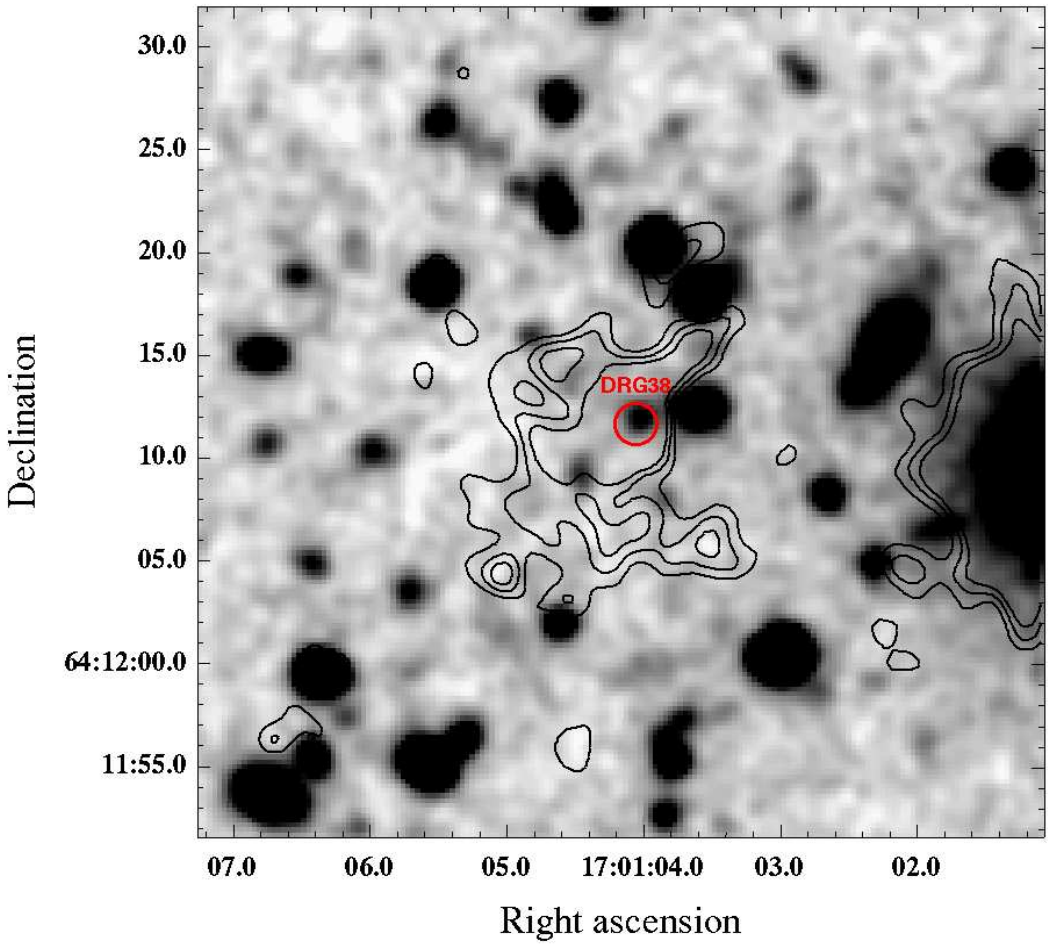

Figure 4.19 Contours of BLOB-1 from Figure 4.18 overlaid on the "UG continuum" image. The core of the emission (narrow-band source BNB016) is also identified as a Distant Red Galaxy object DRG38. Two faint galaxies are seen at the positions of DRG38 and MD109.

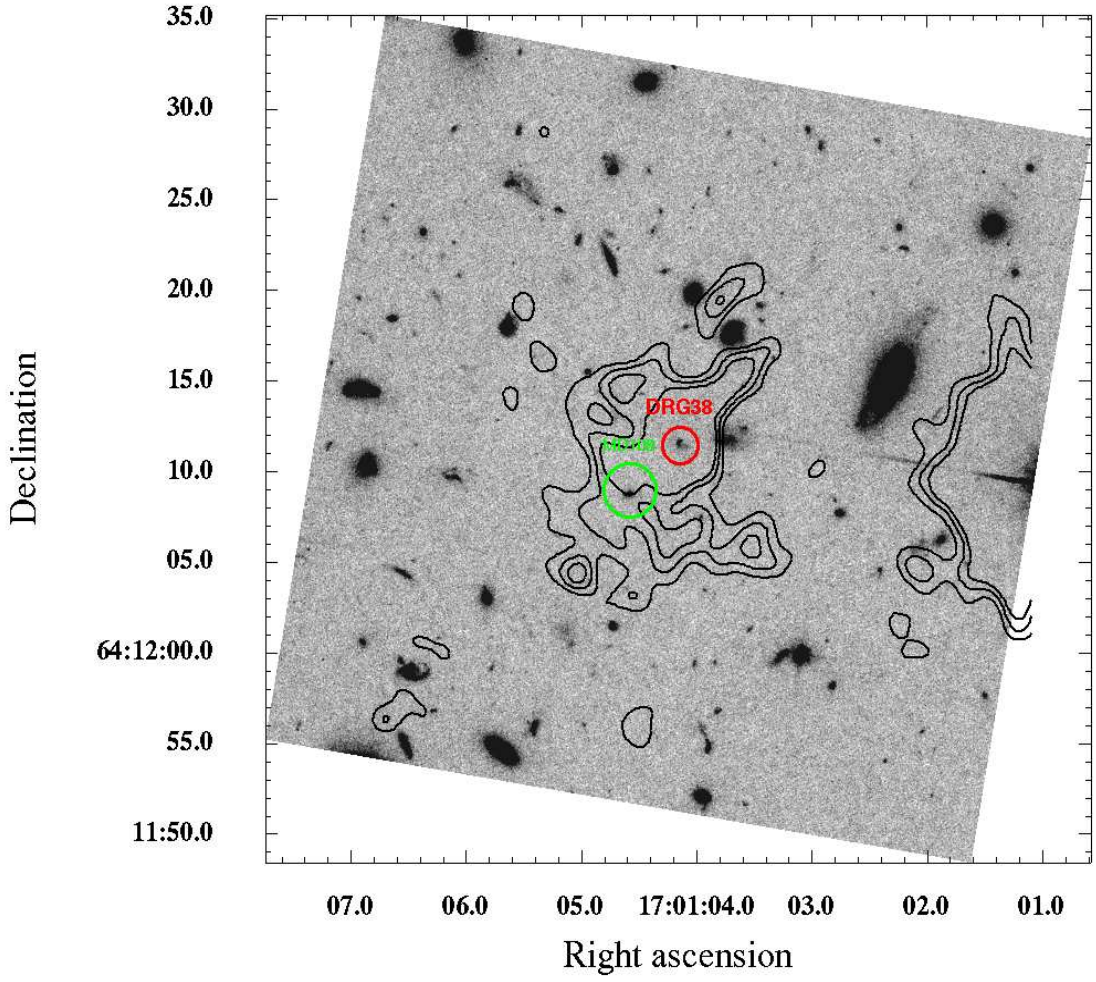

Figure 4.20 Contours of BLOB-1 overlaid on *HST* ACS image centered on BLOB-1. Two faint galaxies are seen at the positions of DRG38 and MD109. No other prominent objects are seen in the region with Ly α emission.

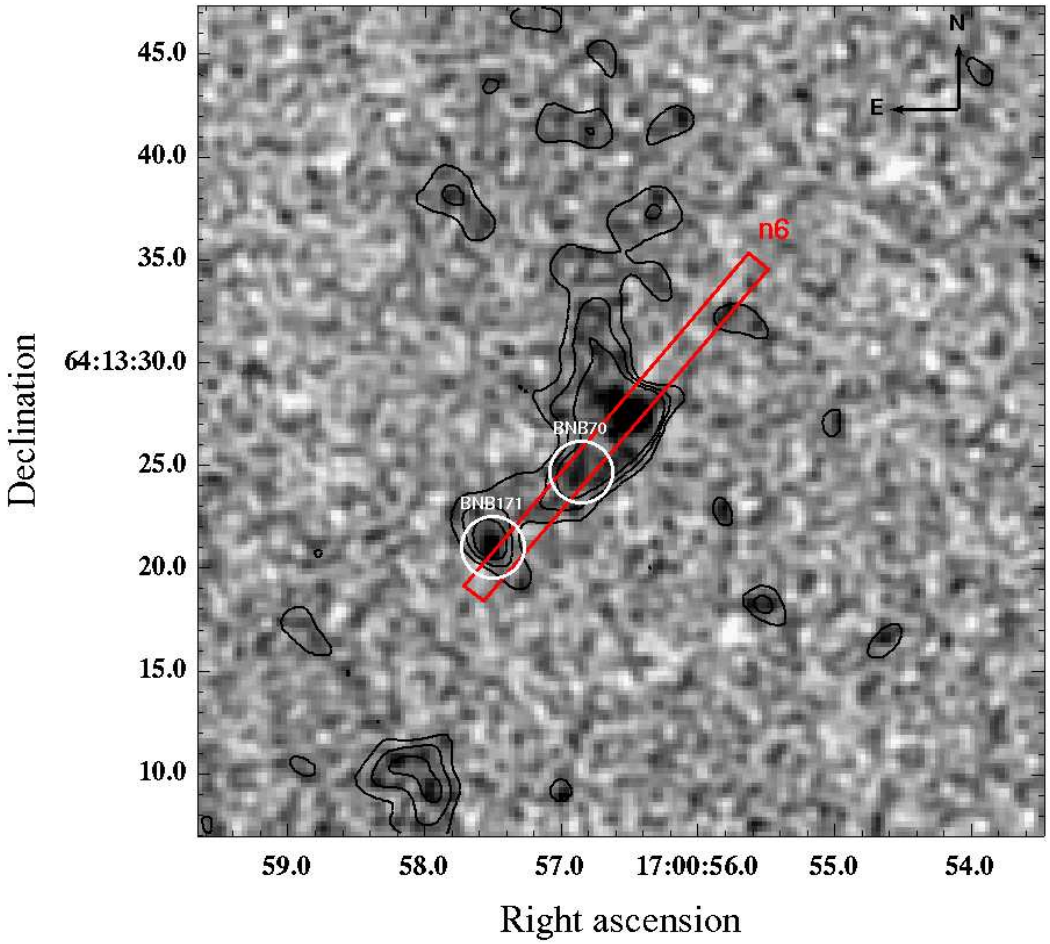

Figure 4.21 A portion of the continuum subtracted narrow-band image (grayscale) centered on BLOB-2. The overlaid contour curves are created after a Gaussian smoothing with FWHM = 7 pixels ($\approx 1\farcs7$) is applied. Contours are marked at surface brightness levels of $1.5, 3$ and 4.5×10^{-18} erg s^{-1} cm^{-2} arcsec^{-2}. Two patches of the blob emission were formally cataloged as narrow-band excess sources BNB070 and BNB171 (circled in white). The slit position n6 (PA=140°) used for follow-up optical spectroscopy is indicated.

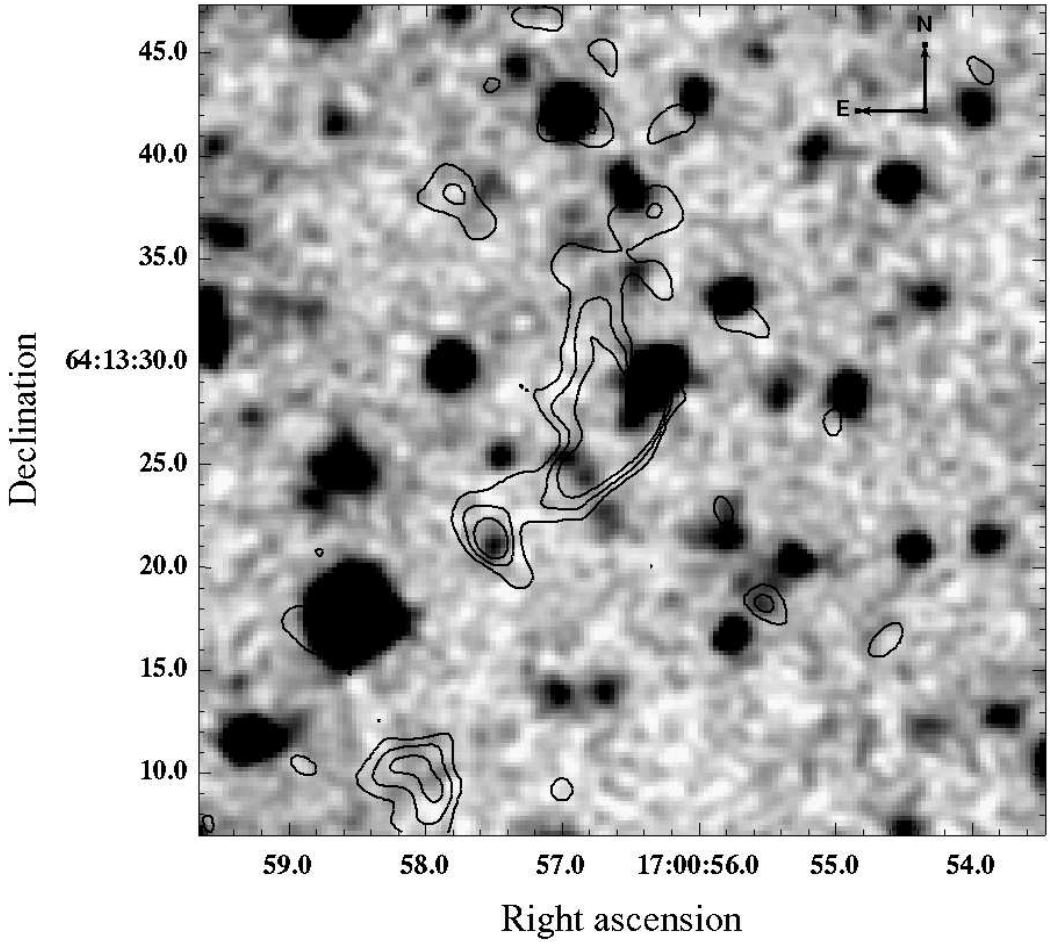

Figure 4.22 Contours of BLOB-2 from Figure 4.21 overlaid on the "UG continuum" image.

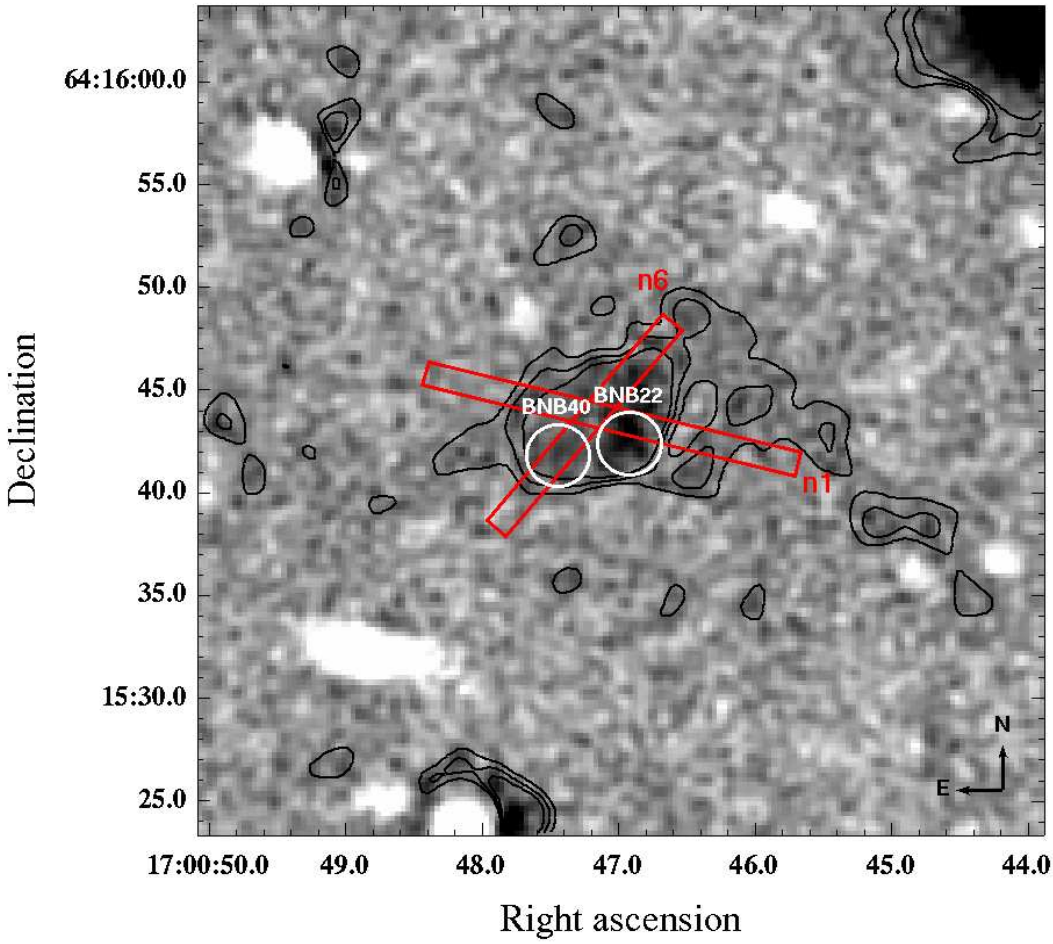

Figure 4.23 A portion of the continuum subtracted narrow-band image (grayscale) centered on BLOB-3. The overlaid contour curves are created after a Gaussian smoothing with FWHM = 7 pixels ($\approx 1\farcs7$) is applied. Contours are marked at surface brightness levels of $1.5, 3$ and 4.5×10^{-18} erg s^{-1} cm^{-2} arcsec^{-2}. Two patches of the blob emission were formally cataloged as narrow-band excess sources BNB040 and BNB022 (circled in white). The slit positions n1 (PA=76°) and n6 (PA=140°) used for follow-up optical spectroscopy are indicated.

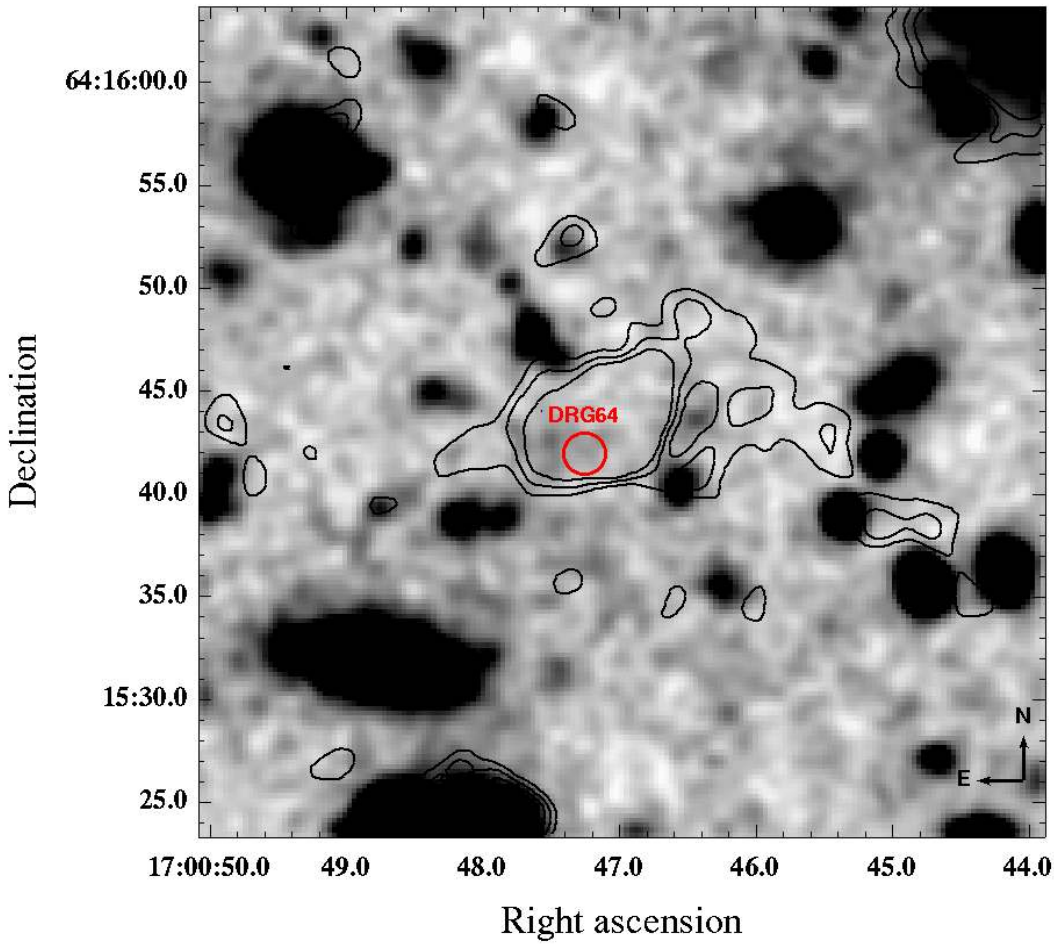

Figure 4.24 Contours of BLOB-3 from Figure 4.23 overlaid on the "UG continuum" image. The position of source DRG64 is marked.

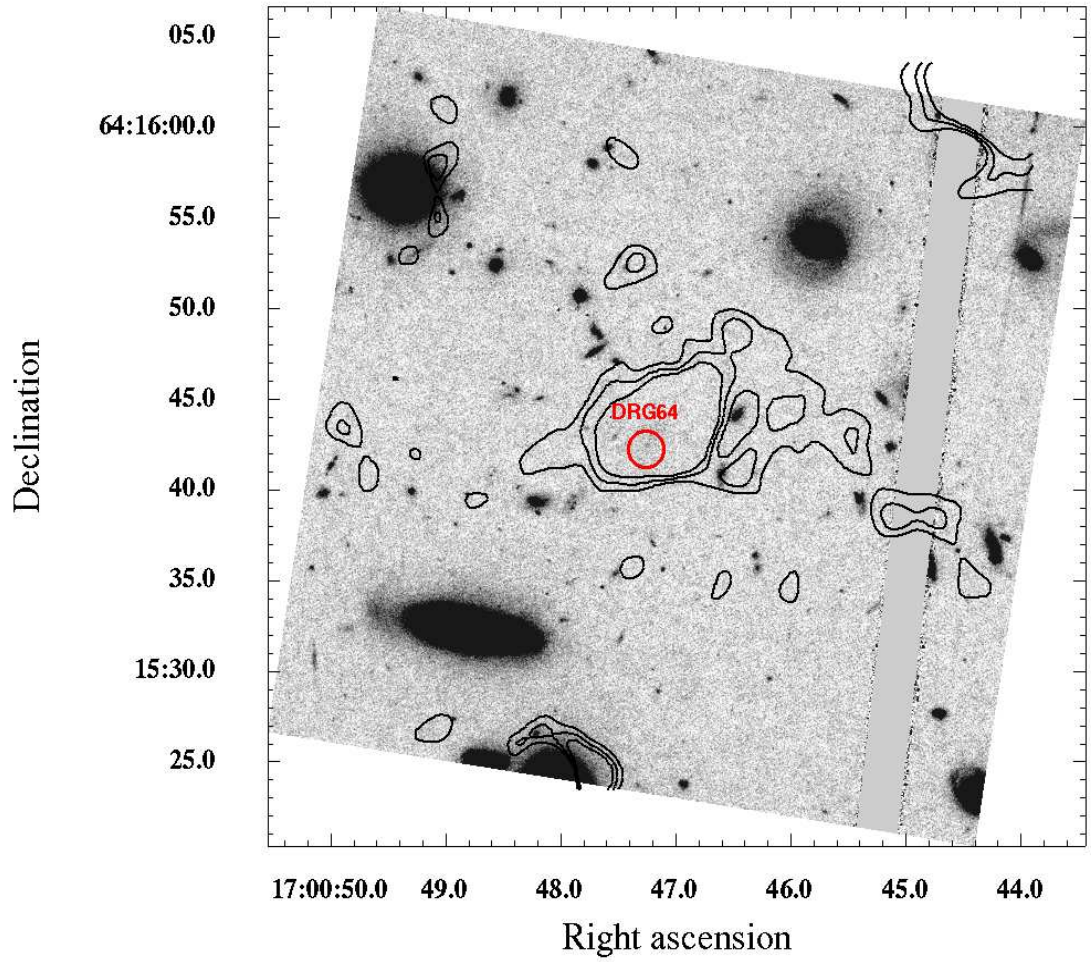

Figure 4.25 Contours of BLOB-3 overlaid on the *HST* ACS image, taken with the F814W filter. The gap in the data on the right side of the image is due to ACS camera geometry.

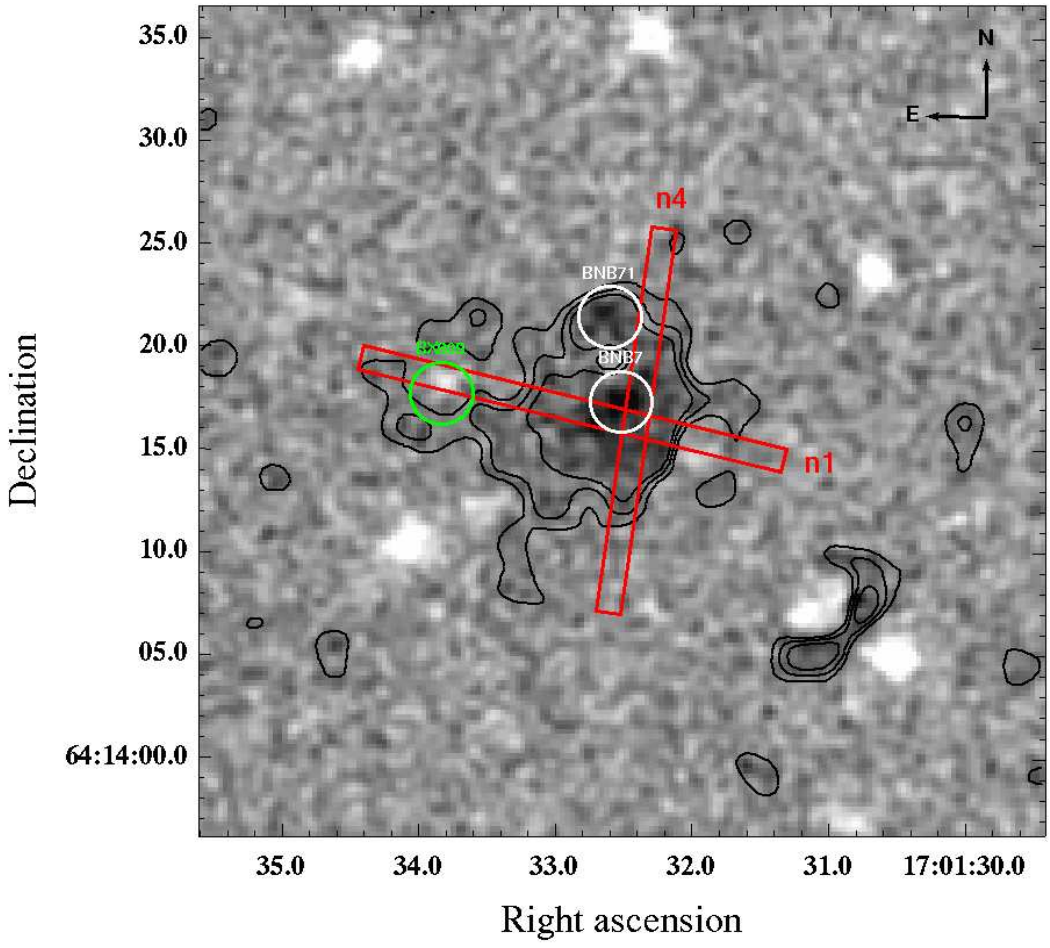

Figure 4.26 A portion of the continuum subtracted narrow-band image (grayscale) centered on BLOB-4. The overlaid contour curves are created after a Gaussian smoothing with FWHM = 7 pixels ($\sim 1''.7$) is applied. Contours are marked at surface brightness levels of $1.5, 3$ and 4.5×10^{-18} erg s^{-1} cm^{-2} arcsec^{-2}. Two patches of the blob emission were formally cataloged as narrow-band excess sources BNB07 (z=2.295) and BNB058 (circled in white). Object BX909 (z=2.291) is marked in green. The slit positions n1 (PA=76°) and n4 (PA=172°) used for follow-up optical spectroscopy are indicated.

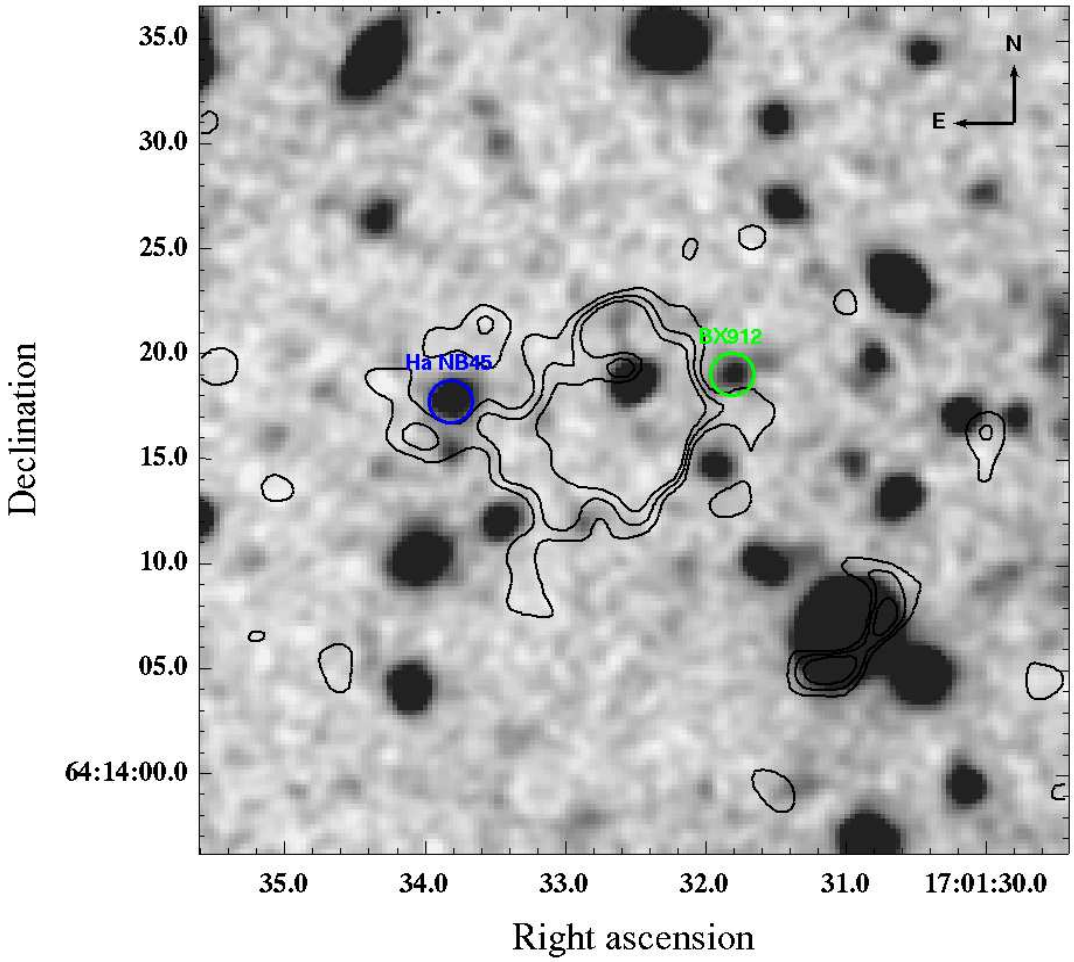

Figure 4.27 Contours of BLOB-4 overlaid on the "UG continuum" image. Object BX912 selected by broad-band rest-UV criteria is marked in green, candidate DRG72 in red. Redshifts are not currently known for these objects. The H α excess candidate HaNB5 is matched with BX909 from the rest-UV selection.

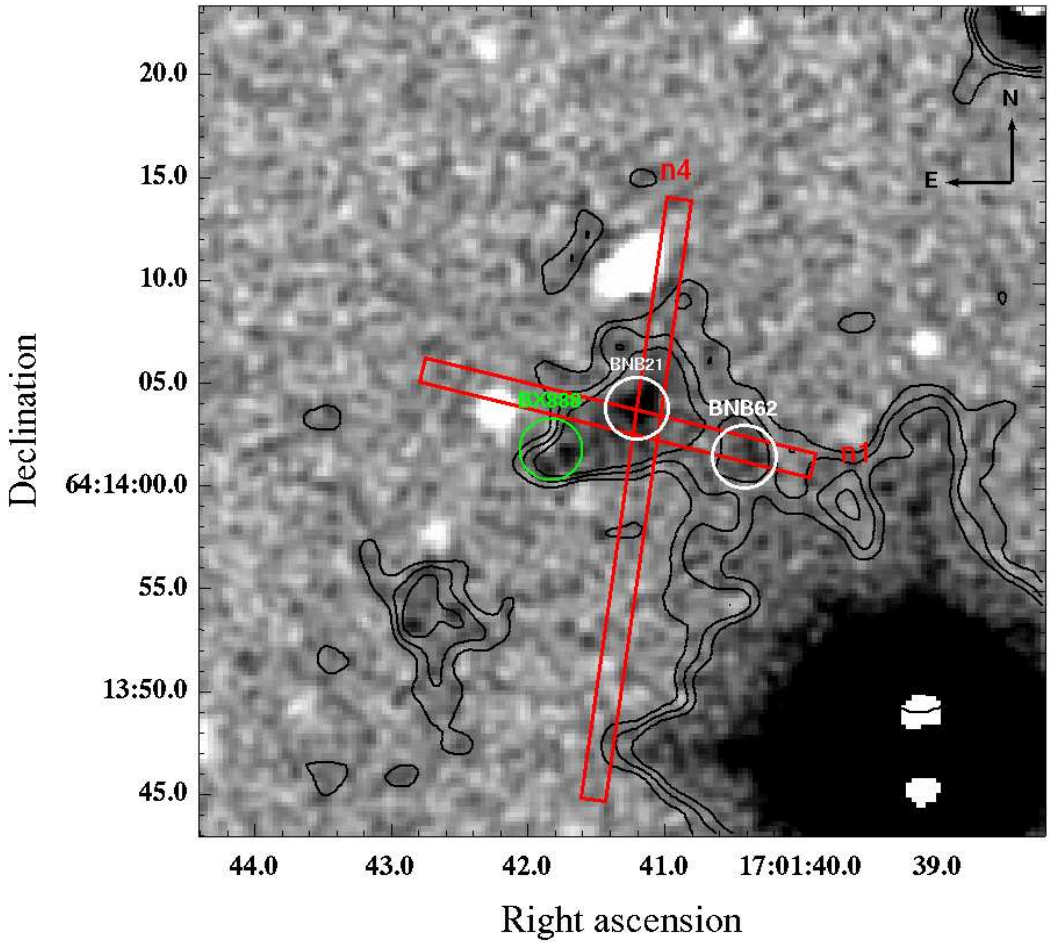

Figure 4.28 A portion of the continuum subtracted narrow-band image (grayscale) centered on BLOB-5. The overlaid contour curves are created after a Gaussian smoothing with FWHM = 7 pixels ($\sim 1''.7$) is applied. Contours are marked at surface brightness levels of $1.5, 3$ and 4.5×10^{-18} erg s^{-1} cm^{-2} arcsec^{-2}. Two patches of the blob emission were formally cataloged as narrow-band excess sources BNB021 (z=2.269) and BNB062 (circled in white). Galaxy BX888 (z=2.270) is very likely related to the blob. The slit positions n1 (PA=76°) and n4 (PA=172°) used for follow-up optical spectroscopy are indicated.

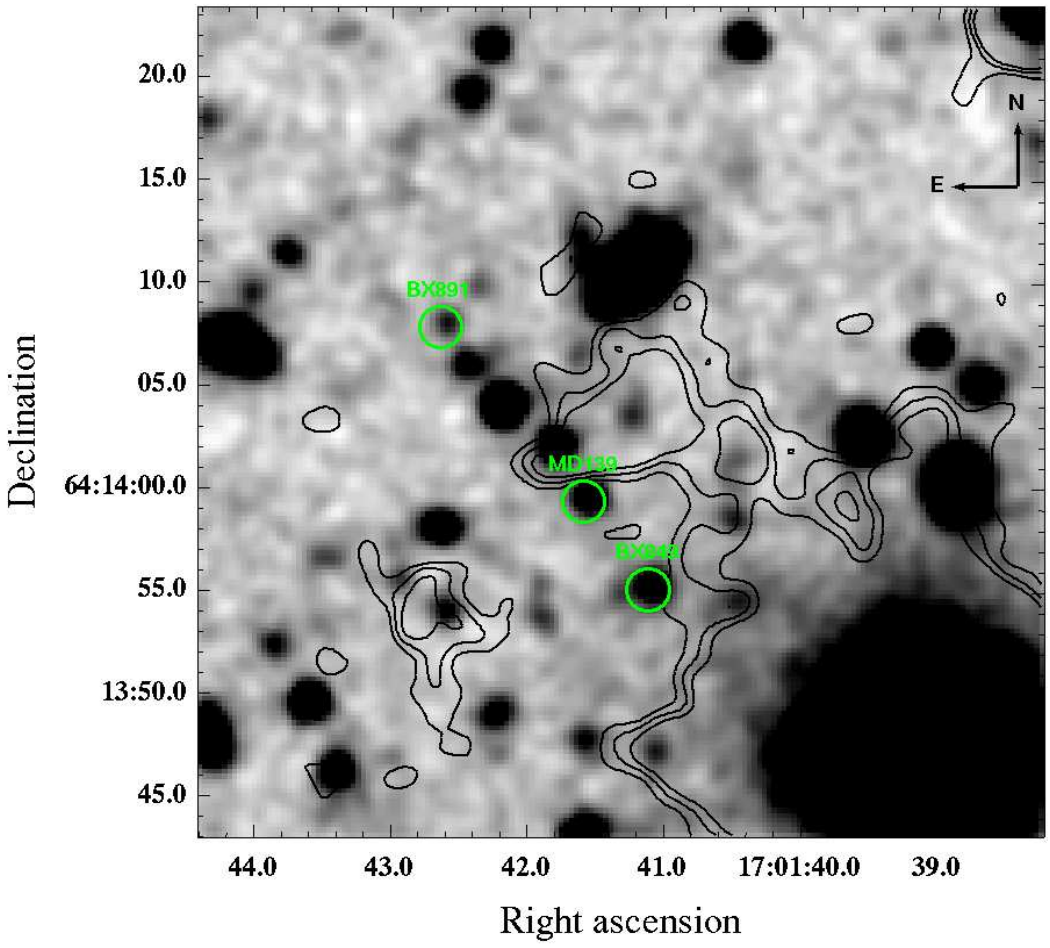

Figure 4.29 Contours of BLOB-5 overlaid on the "UG continuum" image. Three additional sources selected by broad-band rest-UV criteria are indicated (BX891, MD130, BX849). Redshifts are not currently known for these objects.

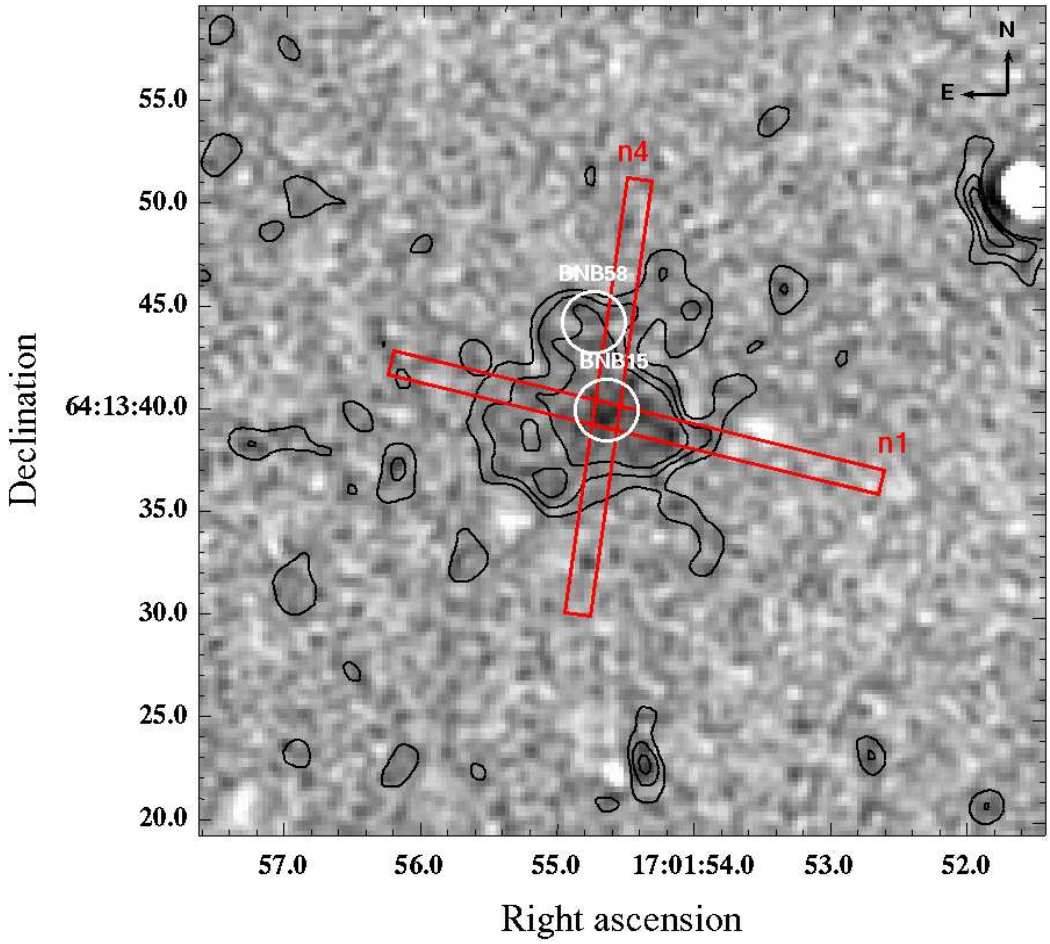

Figure 4.30 A portion of the continuum subtracted narrow-band image (grayscale) centered on BLOB-5. The overlaid contour curves are created after a Gaussian smoothing with FWHM = 7 pixels ($\sim 1\farcs7$) is applied. Contours are marked at surface brightness levels of $1.5, 3$ and 4.5×10^{-18} erg s^{-1} cm^{-2} arcsec^{-2}. Two patches of the blob emission were formally cataloged as narrow-band excess sources BNB015 and BNB058 (circled in white). The slit positions n1 (PA=76°) and n4 (PA=172°) used for follow-up optical spectroscopy are indicated.

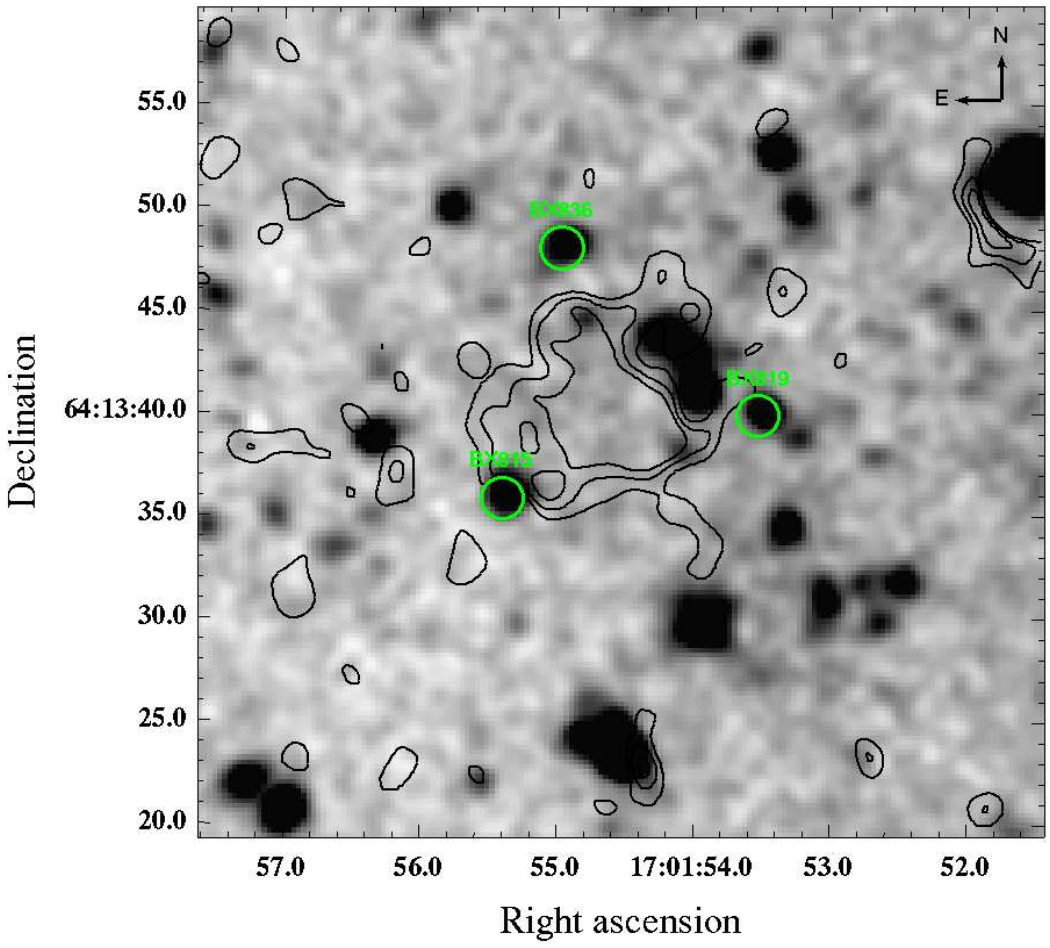

Figure 4.31 Contours of BLOB-6 overlaid on the "UG continuum" image. Three sources selected by broad-band rest-UV criteria are indicated (BX815, BX819, BX836). Redshifts are not currently known for these objects.

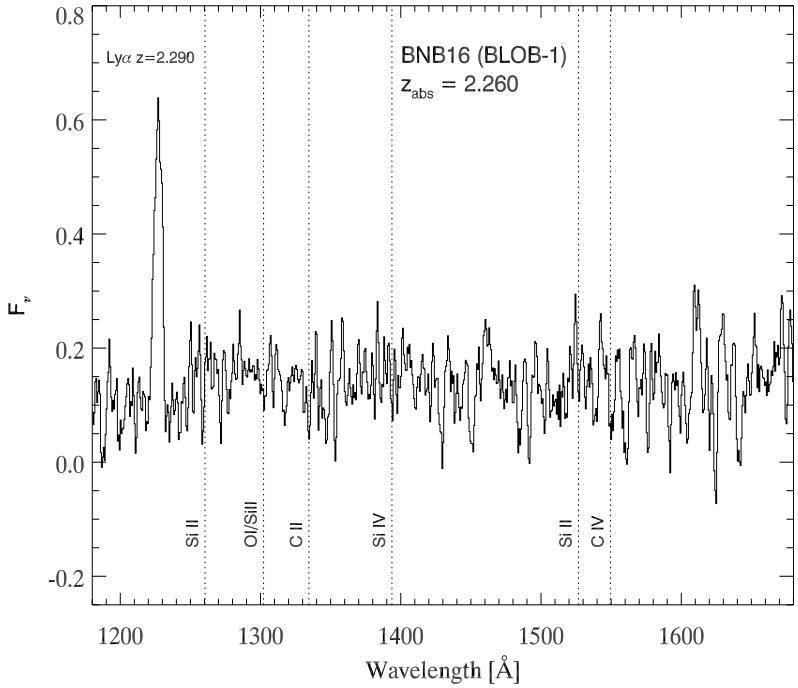

Figure 4.32 Average spectrum from two observations of BNB016 in BLOB-1, shifted to rest-frame according to ISM absorption line redshift.

4.9 Discussion and Conclusions

With the discovery of six large ($\geq$ 50kpc), bright ($L \approx 2 \times 10^{43}\,\mathrm{ergs\,s^{-1}}$) blobs in our survey we can place an estimate of the number density of such objects within the proto-cluster at 6×10^{-5} Mpc^{-3}. From a blind wide-field search at $z = 2.3$ to a comparable Ly α luminosity limit, Yang et al. 2009 estimate the "field" number density of large blobs to be 3×10^{-6} Mpc^{-3}, a factor of 20 times lower. Even after accounting for the $\delta = 7$ increase in redshift-space density of the $z = 2.3$ proto-cluster, we still find an excess of a factor of 3 versus the field observations of Yang et al. 2009. These authors have also reached the same conclusion when comparing to the number of $\geq 50\,\mathrm{kpc}$ blobs found in the SSA22 $z = 3.09$ proto-cluster. Our findings provide further evidence that the over-dense environment plays an important role for the frequency of the blob phenomenon.

At lower redshift, Keel et al. 2009 do not find any extended emission sources at $z = 0.8$ down to $\approx 10^{43}\,\mathrm{ergs\,s^{-1}}$ limit in luminosity of Ly α. These authors conclude that there must be a very strong redshift evolution of the comoving volume density from redshifts beyond $z \approx$3–4 to $z = 0.8$. We might be viewing the progression of this evolution with our finding that the brightest of our six blobs (BNB-1) is still about four times less luminous than the brightest two blobs discovered in the SSA22 field. Only a few blobs reaching $10^{44}\,\mathrm{ergs\,s^{-1}}$ at redshifts lower than $z = 3.0$ have

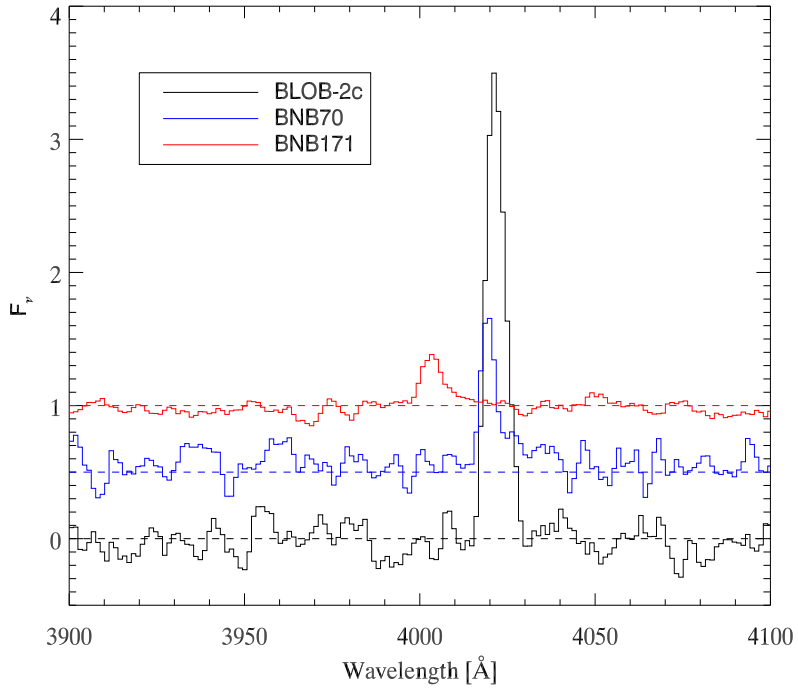

Figure 4.33 Spectra of sources BLOB-2c, BNB070 and BNB171. All three emission lines are unresolved. The spectra have been shifted in the y-axis for clarity.

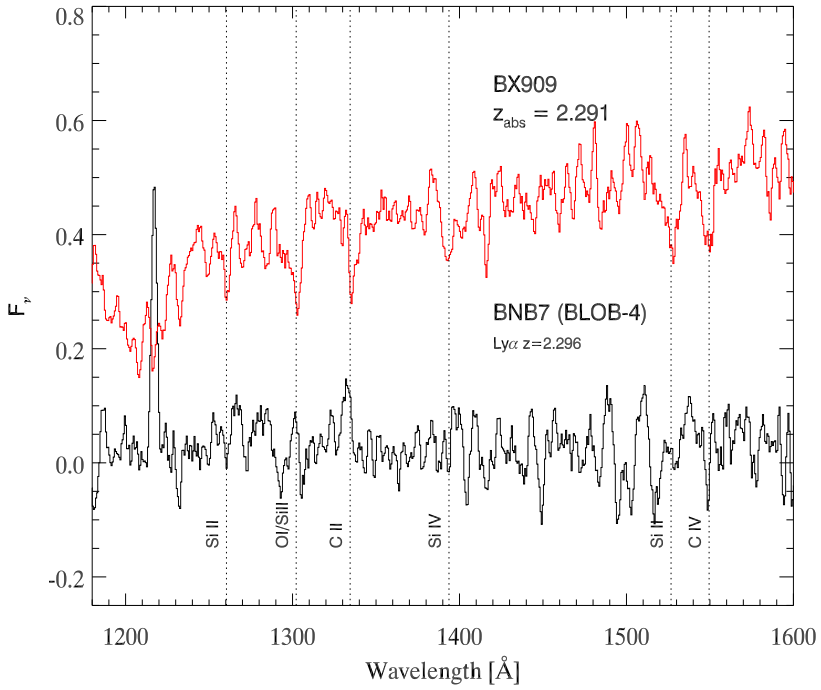

Figure 4.34 Spectra of BX909 and BNB07 ("core" of BLOB-4), both shifted to the rest-frame according to ISM absorption line redshift of BX909.

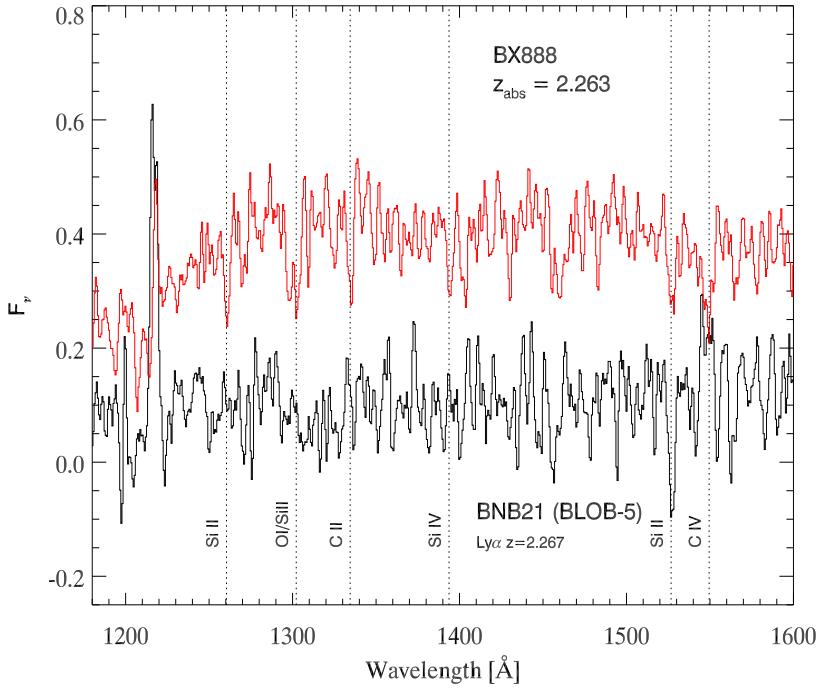

Figure 4.35 Spectra of BX888 and BNB021 ("core" of BLOB-5), shifted to the rest-frame according to ISM absorption line redshift.

been found to date (Francis et al. 2001; Dey et al. 2005; Smith et al. 2008; Palunas et al. 2004). However, as observed in most Ly α narrow-band searches, blobs can exhibit a broad range in size and luminosity. Hayashino et al. 2004 have demonstrated that objects not classified as Ly α emitters can show extended emission if the sensitivity of the observation is increased. Deep Lymanα narrow-band imaging of H α emitters showed that this extended emission region is definitely not a characteristic of objects initially selected as Ly α emitters. In fact, similar extended emission is observed for sources that are not initially classified as either Ly α or H α emitters. In study by Rauch et al. 2008, a stack of low surface brightness Ly α emitters with redshifts $2.67 < z < 3.75$ shows extended emission out to $4''$ (30kpc). Thus this might likely be a feature of *most* if not all galaxies at these redshifts, whether they are located in a proto-cluster or a more typical local environment.

The combination of optical and near-infrared broad band and narrow-band imaging has allowed for significant new insight into the population of the $z = 2.3$ proto-cluster region. For the first time we were in a position to investigate the relation of H α emitters with Ly α emitters and giant (50–100 kpc) blobs. To our sensitivity limit in $NB_{Br\gamma} = 20.5$ we find one blob (BLOB-4) to be related with a confirmed H α emitter.

Most, but not all, large blobs discovered so far were observed to incorporate a continuum selected star-forming galaxy. This holds true in our sample as well, we find one blob (BLOB-2) that does not

appear to have any objects selected by the optical or near-infrared broad-band criteria. However, for 4 out of 6 of our blobs we were able to confirm the relation with continuum selected (BX,MD or DRG) galaxies, with another one (BLOB-5) likely being related to at least one of the three BX candidate in close proximity.

The importance of near-infrared observations is stressed by the discovery of object DRG64 close to the center of BLOB-3, without the presence of other optically selected objects. Interestingly, none of the optical continuum selected objects found in the blobs are located at the "core" of the emission, the only such object being the near-infrared selected galaxy DRG38 in BLOB-1.

None of these objects found in blobs appear to harbor an unobscured AGN, according to the results of out follow-up spectroscopy (though note the possible CIV 1549 Å feature in the spectrum of BNB021 in BLOB-5, Figure 4.35). A deep *Chandra*/ACIS-I observation of this field (≈ 200 ks, Digby-North et al., 2010, in preparation) finds no X-ray sources related to any of these six blobs. Their findings give further support to claims that blob emission is not related to an ongoing AGN activity, even though some blobs have been reported to harbor them (Keel et al. 1999; White et al. 2004; Yang et al. 2009).

We were successful in detecting continuum flux at the "cores" of two out of six blobs (BLOB-1 and BLOB-5). This allowed us to measure a redshift from strong ISM absorption lines, and their values are similar ($z = 2.260$ and $z = 2.264$, respectively). Of note is the large difference between the offset of Ly α from the absorption redshift in these two blobs, from $\delta z = 0.030$ to $\delta z = 0.005$, suggesting that there may exist a very broad range of outflow velocities in the blobs.

The cooling flow interpretation of the relation of proto-clusters and Ly α blobs (Steidel et al. 2000; Goerdt et al. 2009) suggests that the over-dense environment is directly boosting the appearance of the blob phenomenon. However, we can see from the span in blob redshifts that whatever conditions in the IGM (if any) are among the primary causes of the extended emission, their influence reaches beyond the formally designated boundaries $z = 2.300 \pm 0.015$ as initially outlined by the most significant redshift-space over-density of continuum selected star-forming galaxies.

Similarly as in previous studies, we also observe a broad range of Ly α width in blobs and Ly α emitters, from unresolved (FWHM $\leq 300\mathrm{km\,s^{-1}}$) to FWHM $\geq 1400\mathrm{km\,s^{-1}}$. We find a striking anti-correlation of the strength of Ly α and H α in our survey, as the average spectrum of H α emitters shows strong absorption in Ly α line. Though H α candidates are comparatively bright in the continuum, they have a larger surface density than Ly α emitters. We also find that only about a half of H α candidates satisfy the optical broad-band selection criteria. Additional spectroscopic observations are necessary to properly examine if this would imply that any strong contamination is present in the current H α sample. An alternative explanation could be that H α emitter selection uncovers galaxies missed by broad band rest-UV continuum criteria.

Appendix A

Spectra of the DLCS Sample

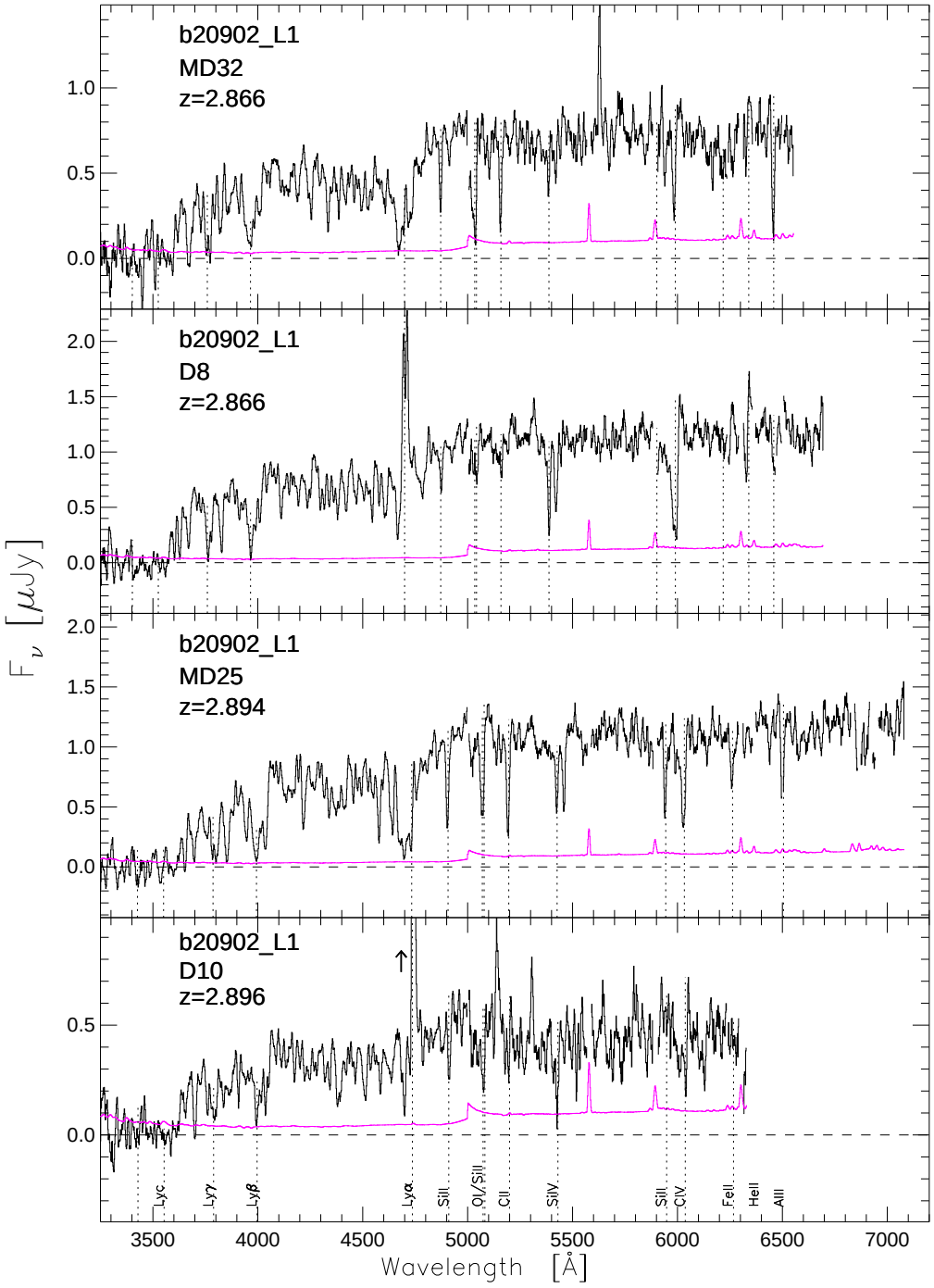

Figure A.1 Spectra of 121 galaxies from the Deep Lyman Continuum Survey. Wavelengths are in observed frame. The y-axis is flux in units of μJy. Note that the flux range varies among panels. The magenta line shows the 1σ statistical error spectrum based on considerations of sky brightness and detector read noise. A jump in the error spectrum at 5000 Å is due to a switch between spectrograph arms. Below 5000 Å the spectra are observed with LRIS-B and reduced with the improved data reduction algorithm as presented in Section 2.3. Spectra above 5000 Å are observed with the red side spectrograph, LRIS-R, and data reduced with the standard algorithm. Objects are presented per field in order of increasing redshift.

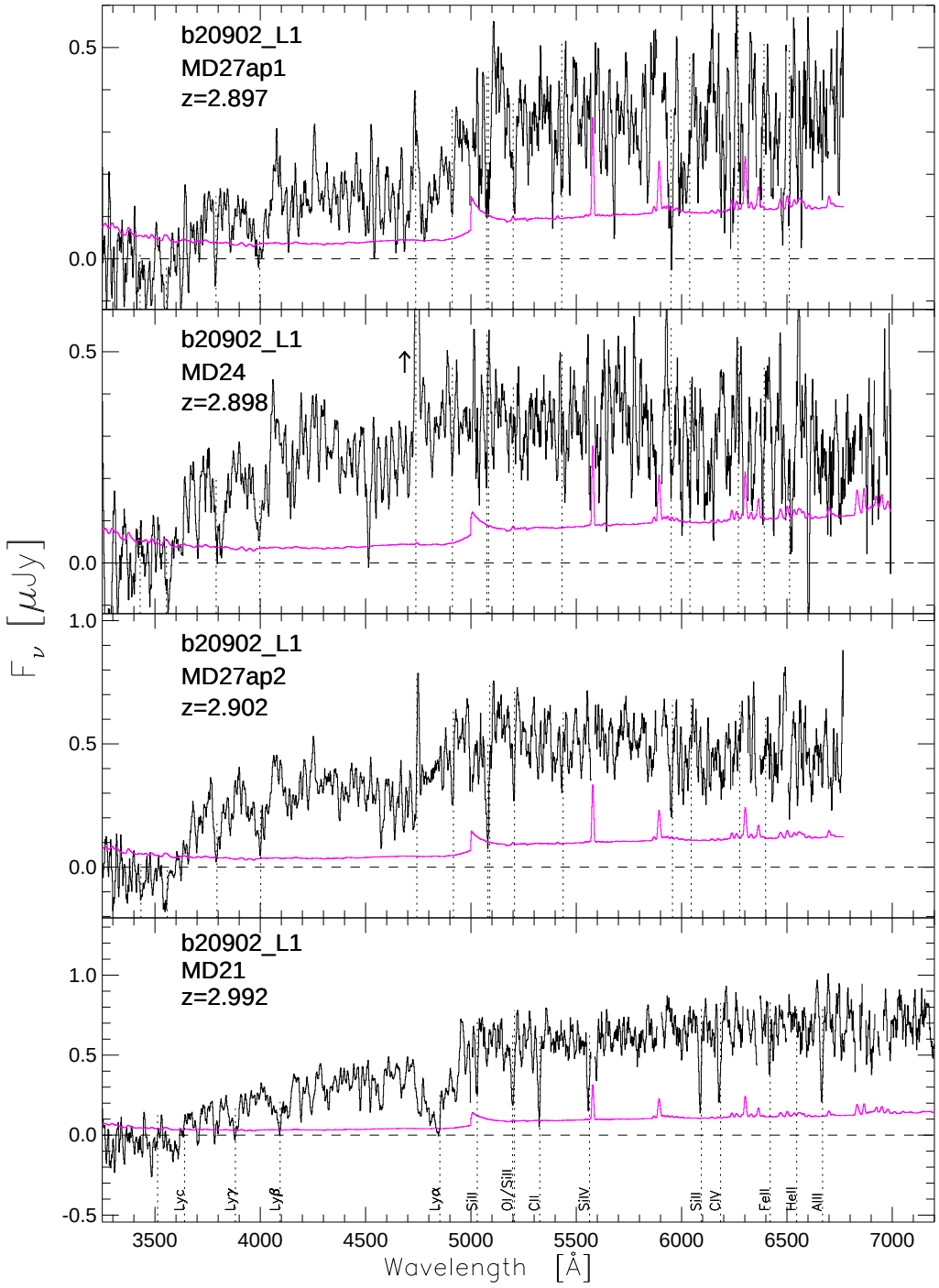

Figure A.2 Continued from Figure A.1

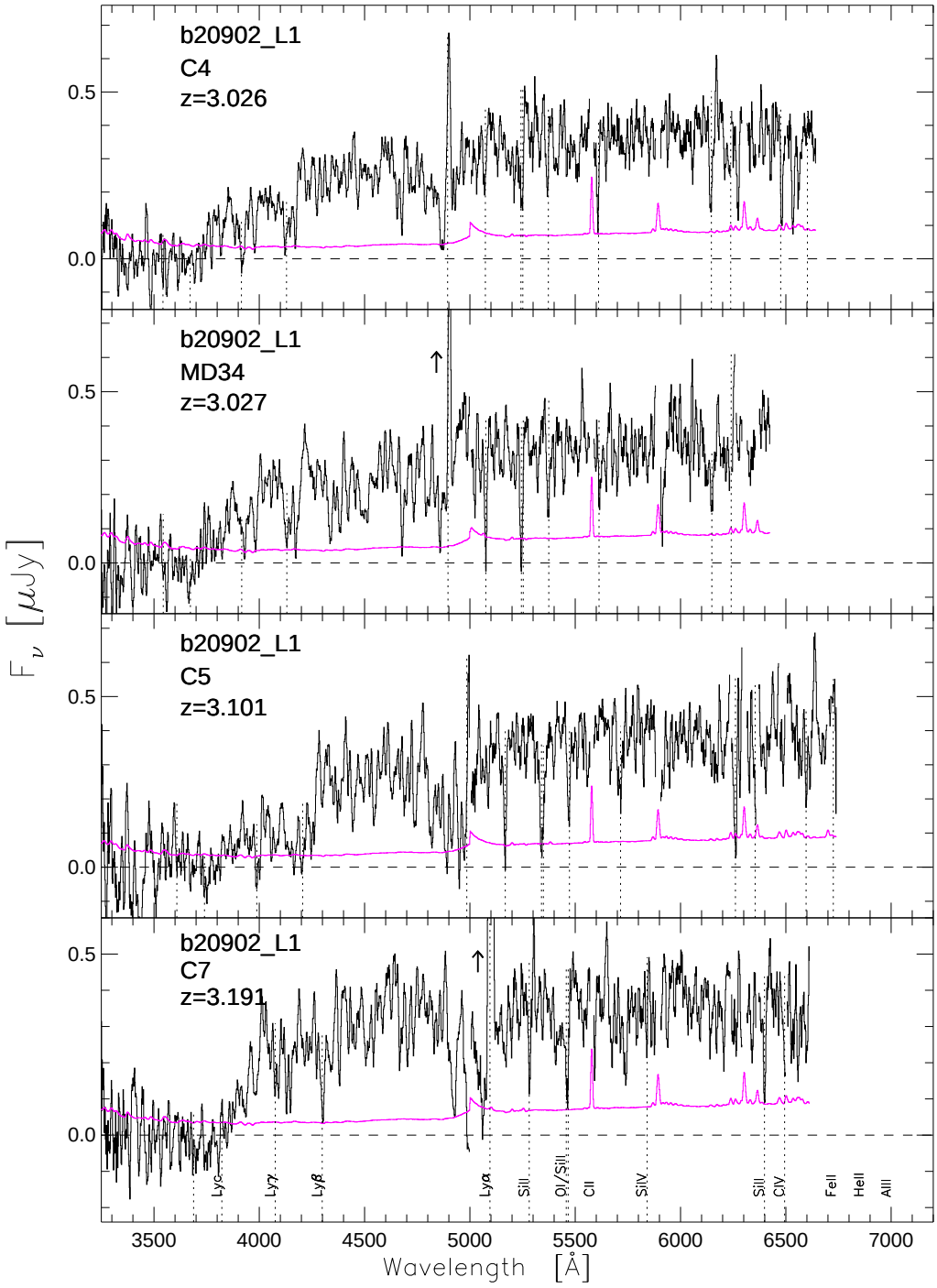

Figure A.3 Continued from Figure A.1

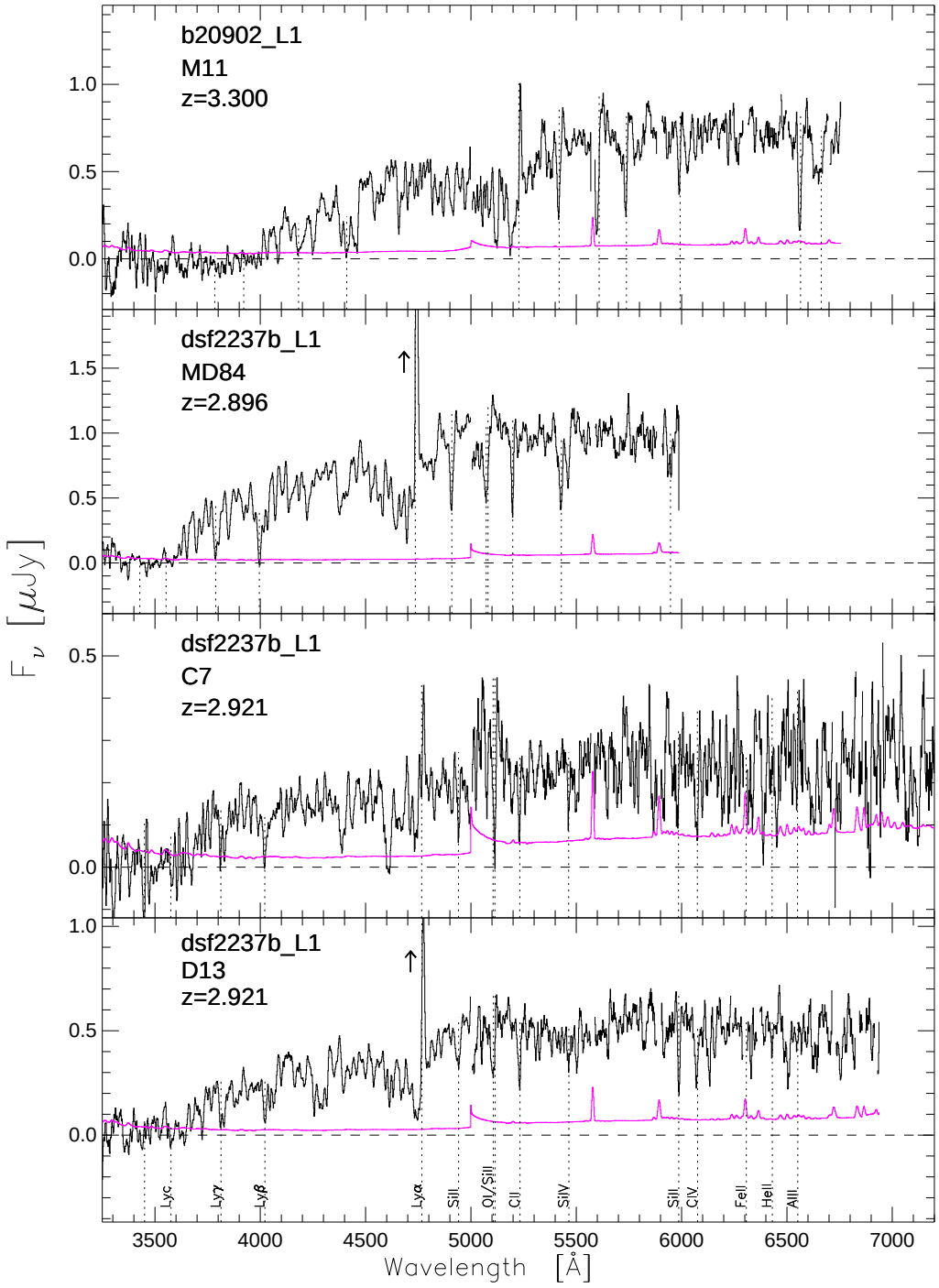

Figure A.4 Continued from Figure A.1

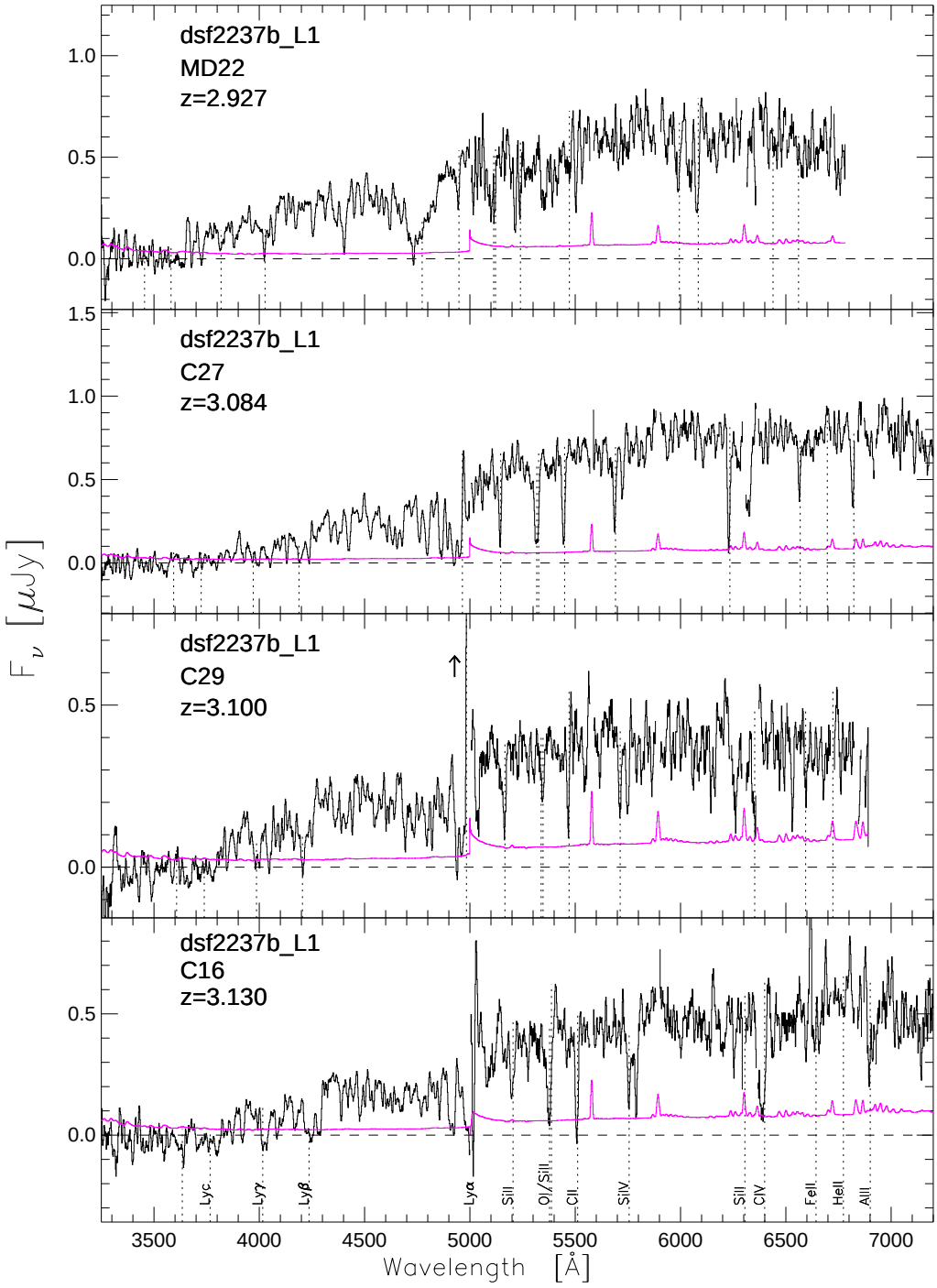

Figure A.5 Continued from Figure A.1

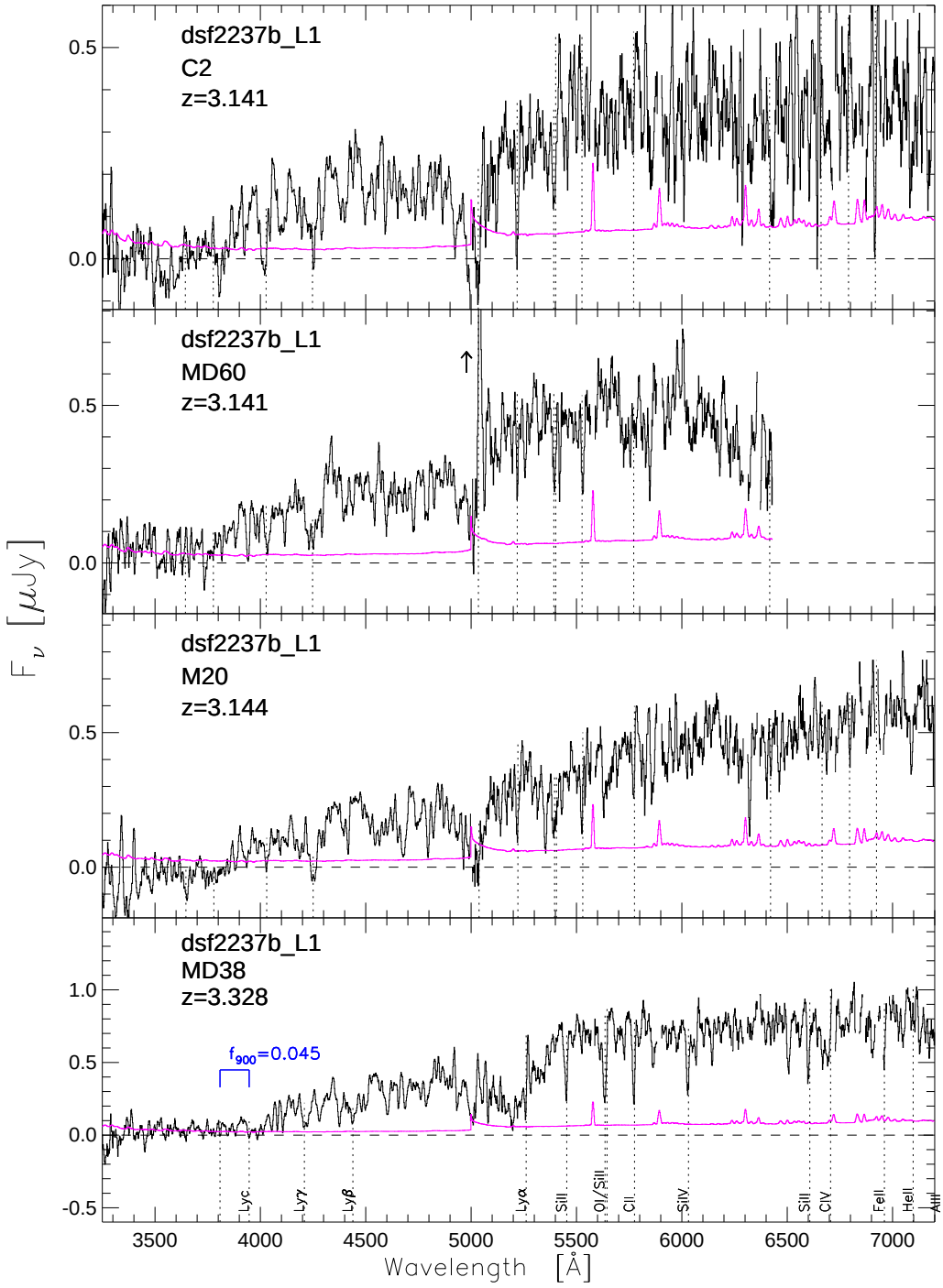

Figure A.6 Continued from Figure A.1

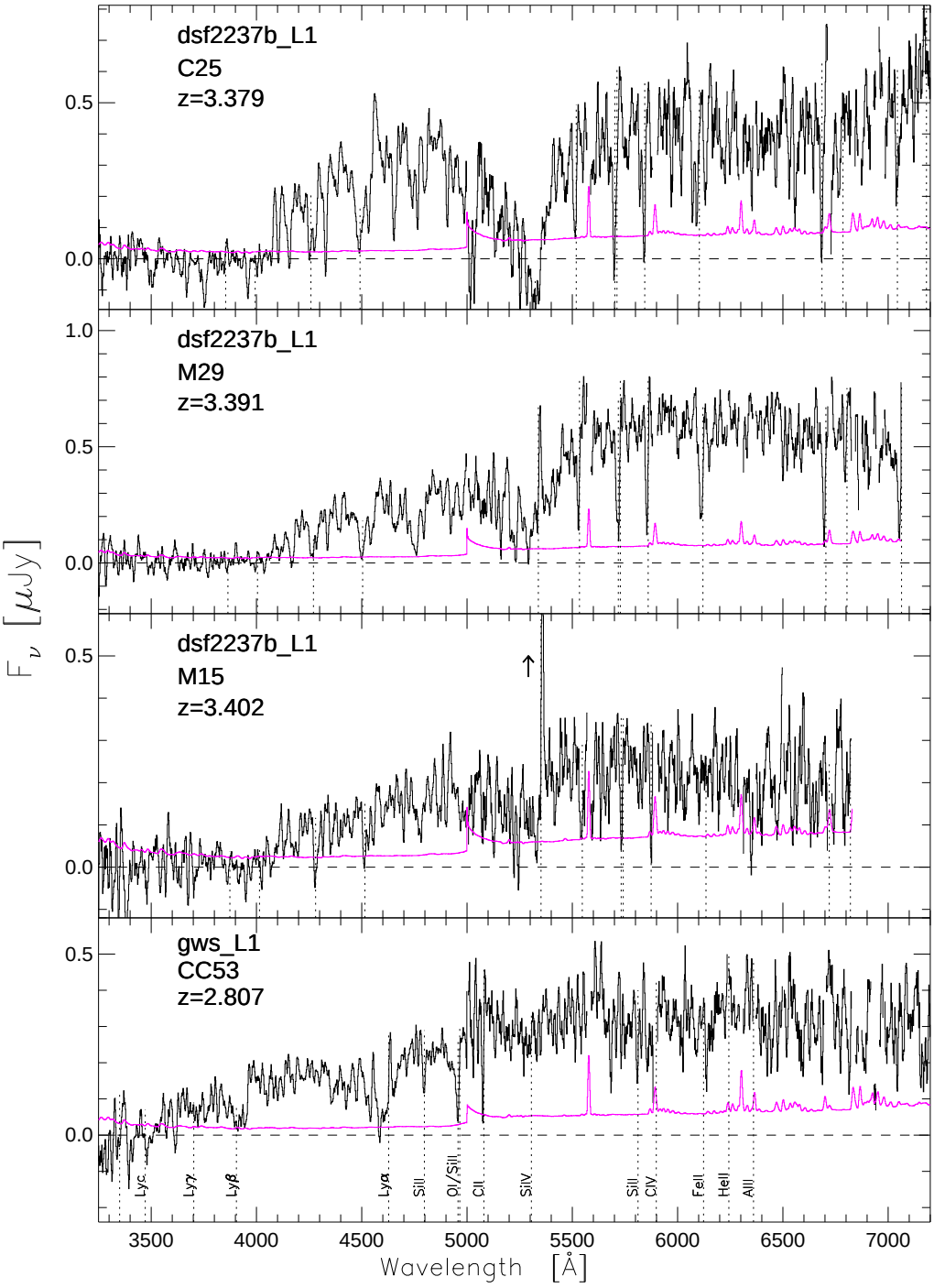

Figure A.7 Continued from Figure A.1

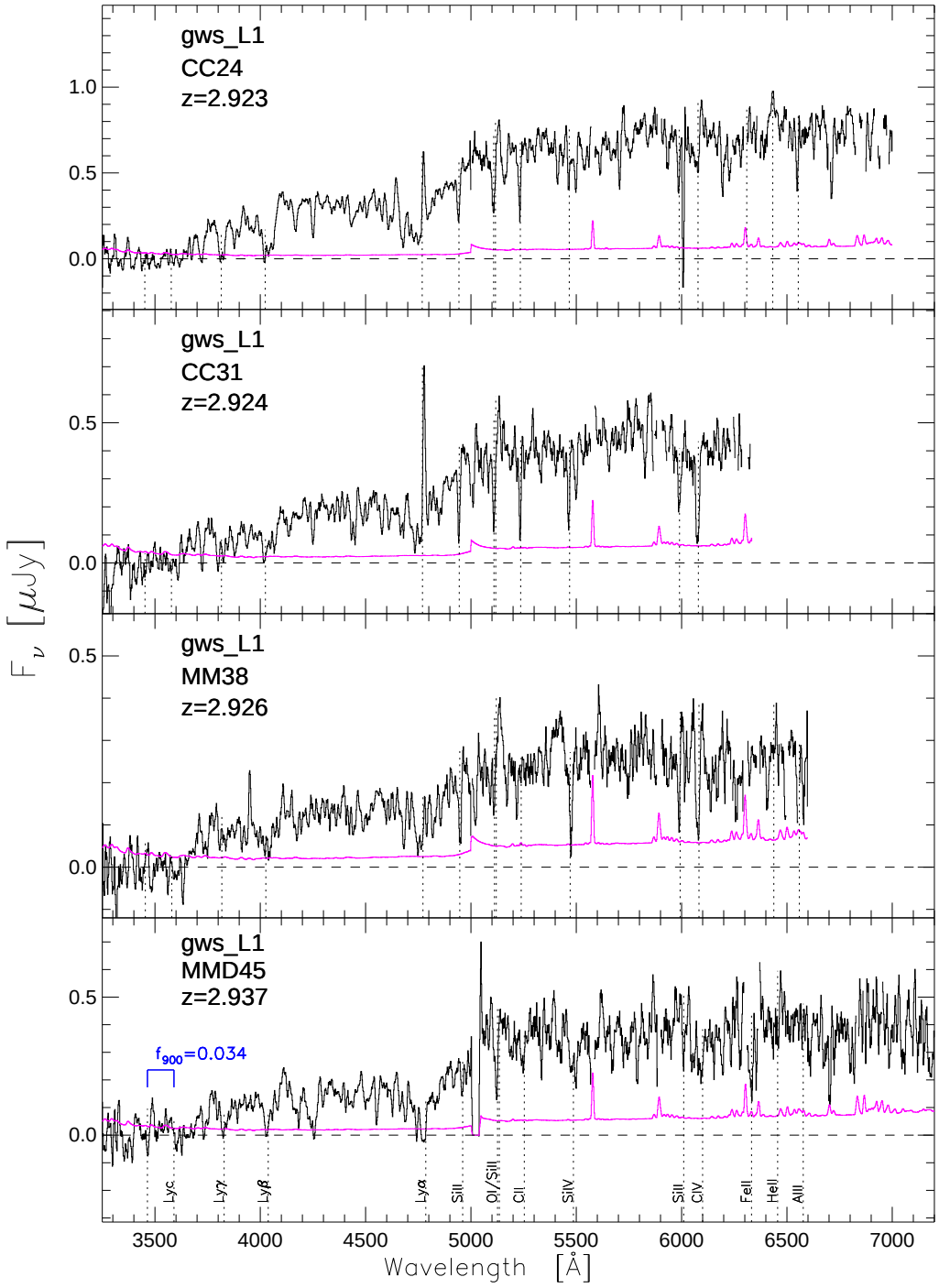

Figure A.8 Continued from Figure A.1

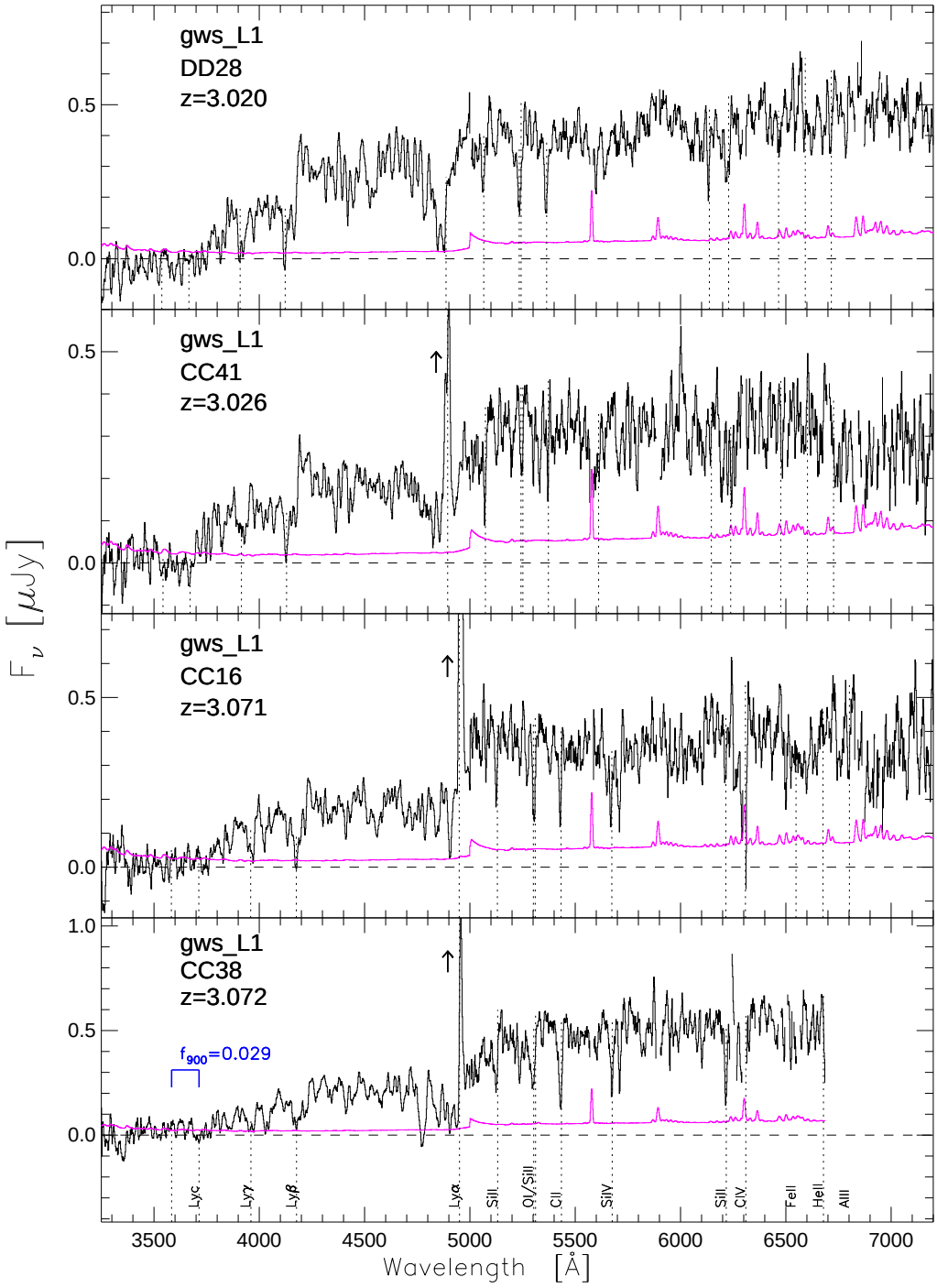

Figure A.9 Continued from Figure A.1

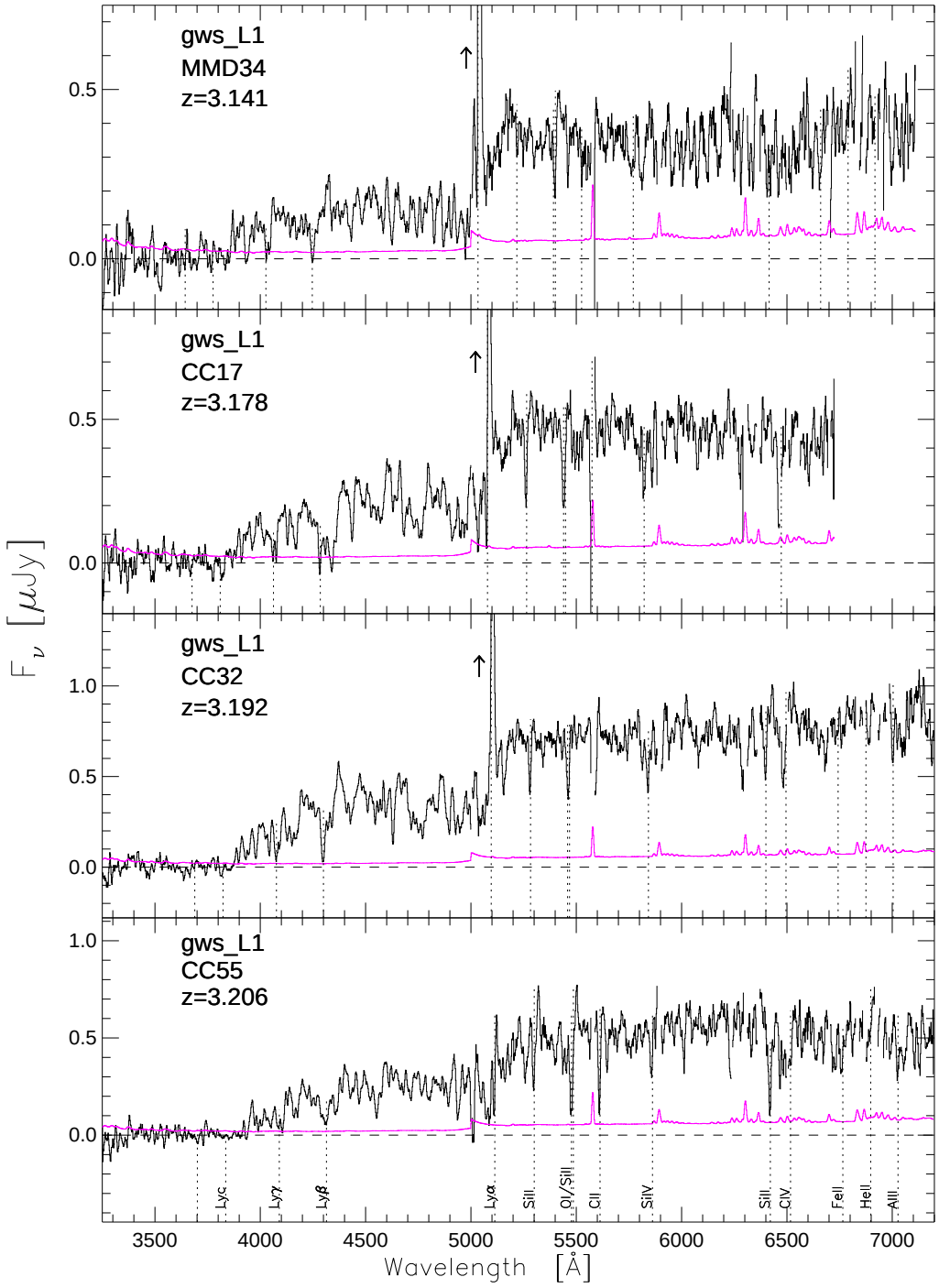

Figure A.10 Continued from Figure A.1

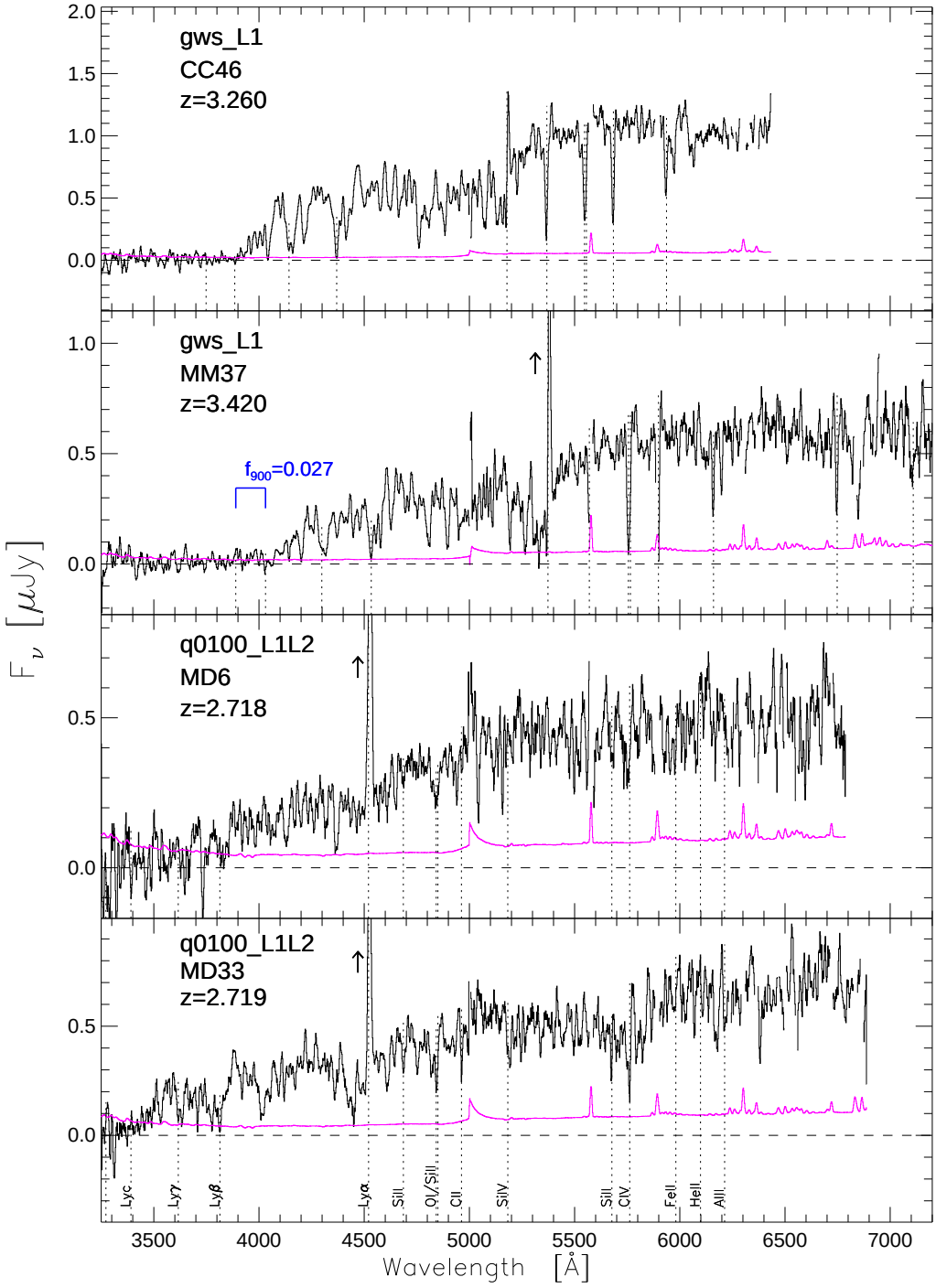

Figure A.11 Continued from Figure A.1

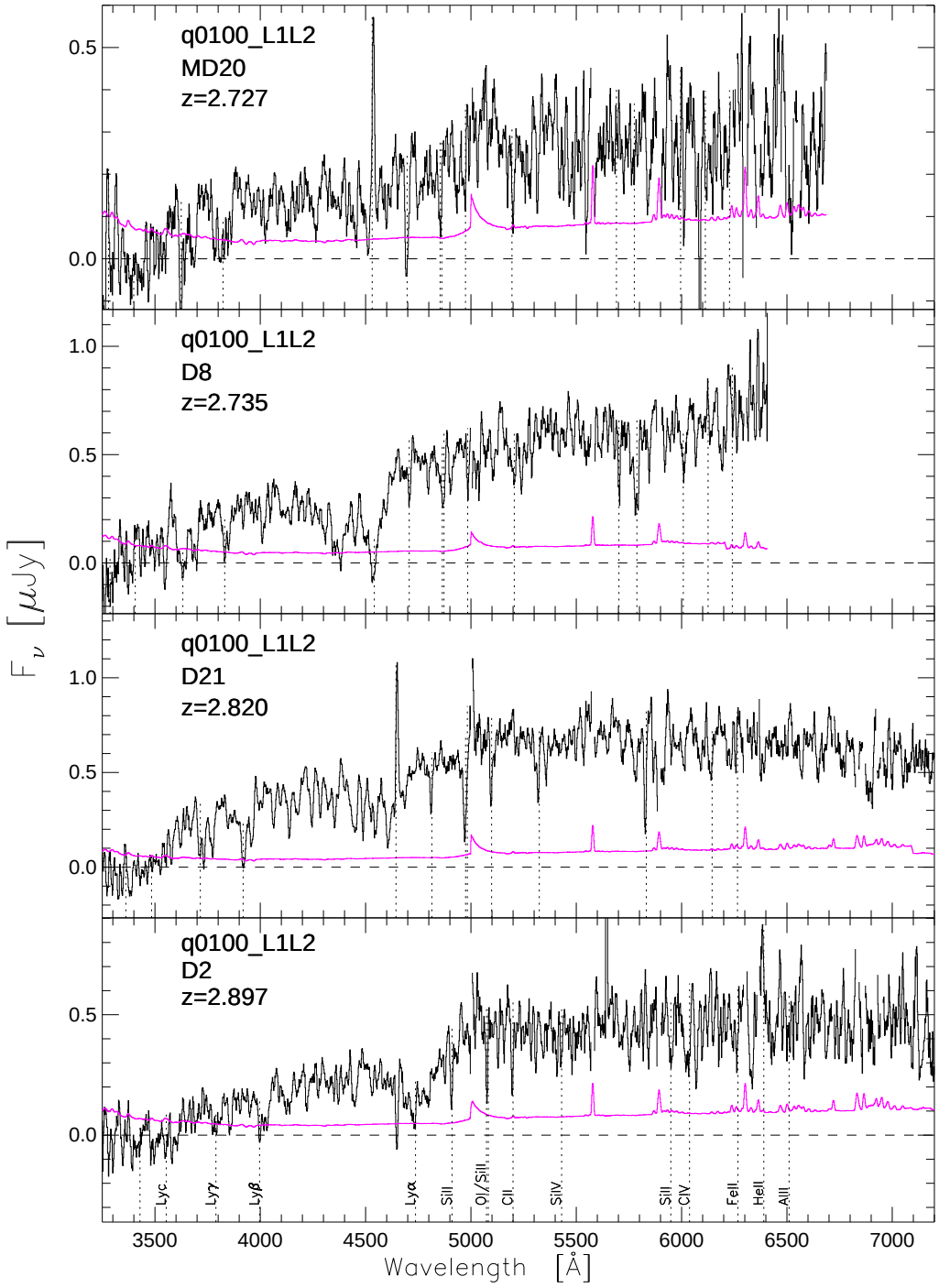

Figure A.12 Continued from Figure A.1

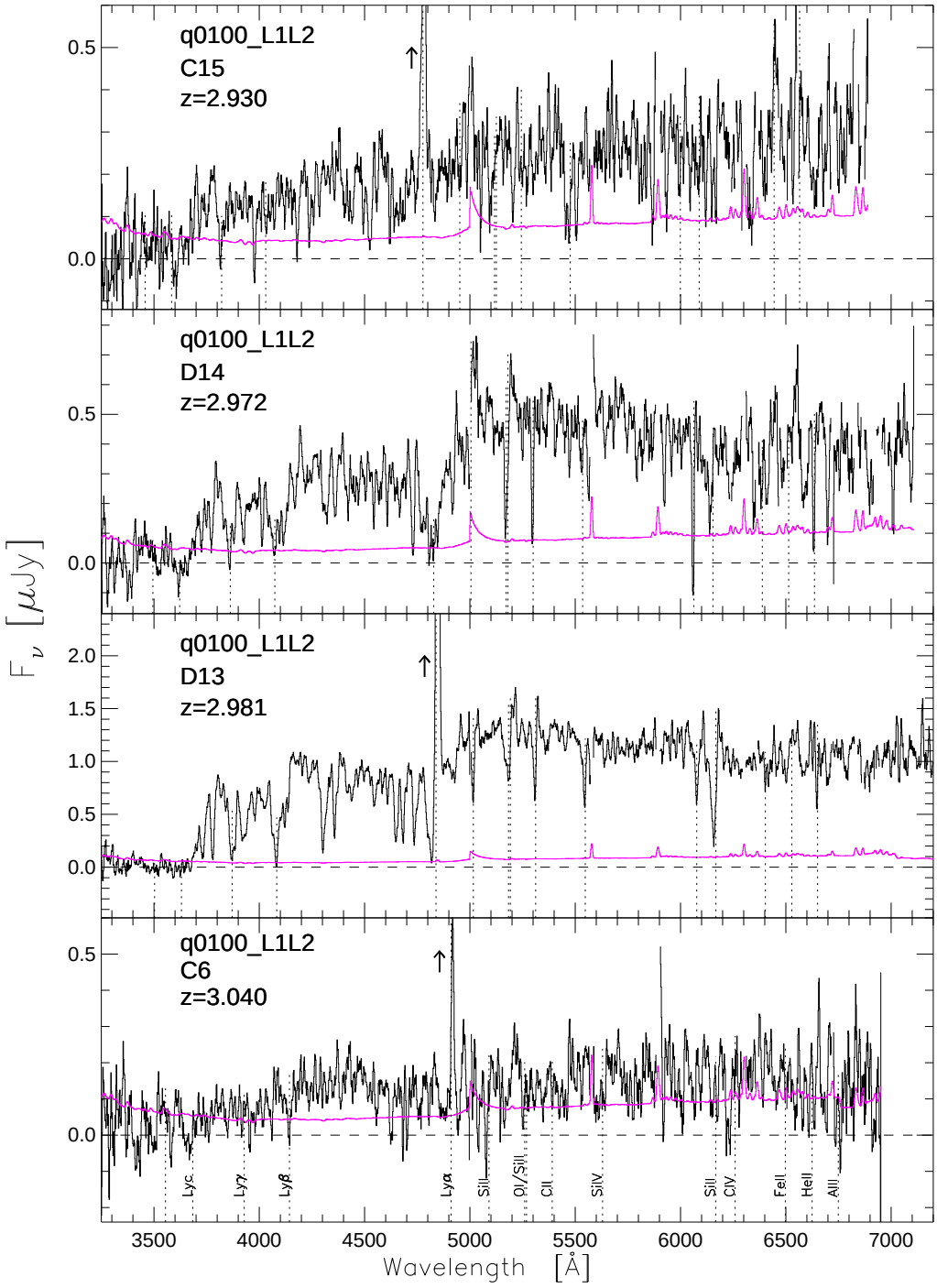

Figure A.13 Continued from Figure A.1

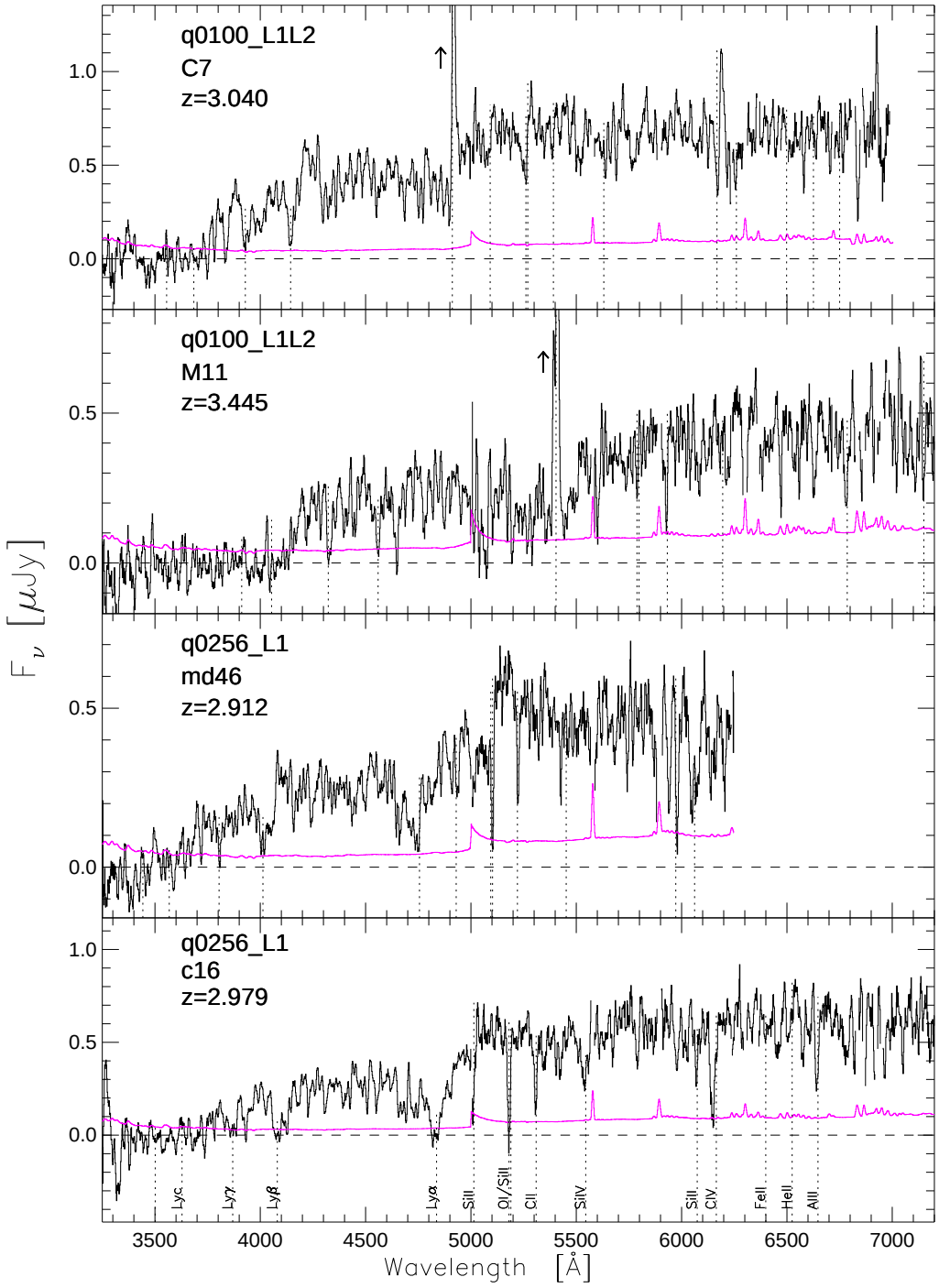

Figure A.14 Continued from Figure A.1

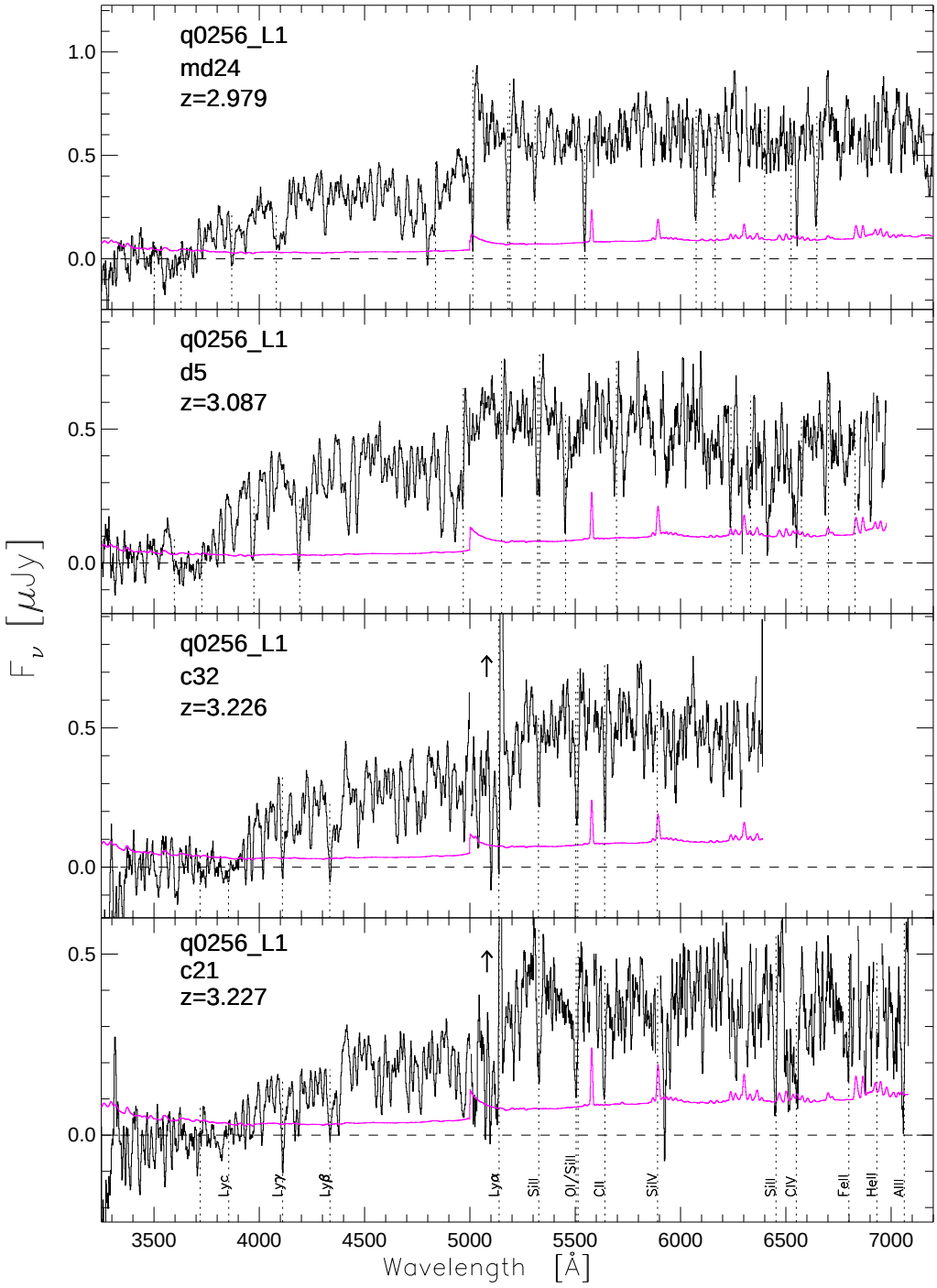

Figure A.15 Continued from Figure A.1

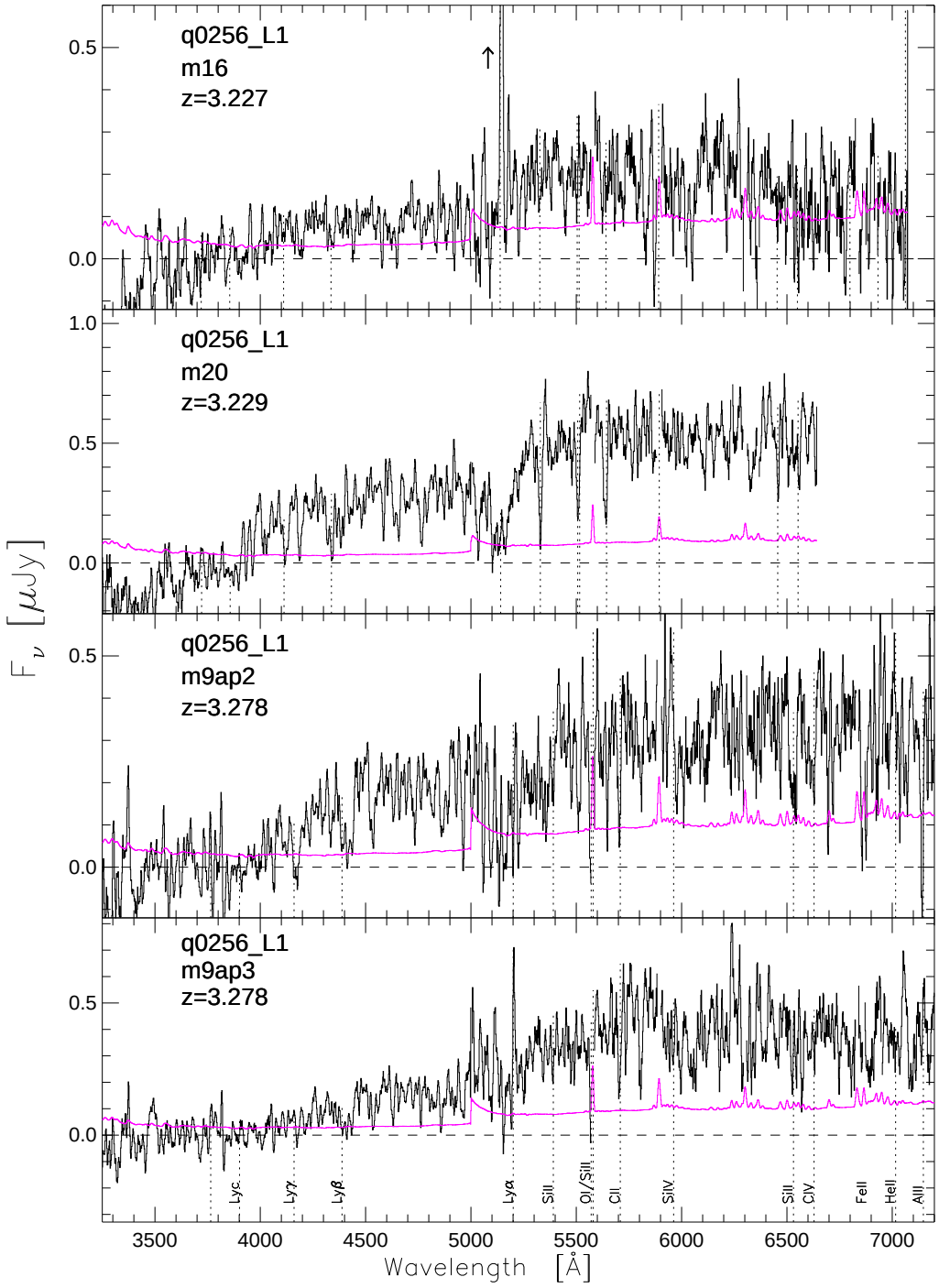

Figure A.16 Continued from Figure A.1

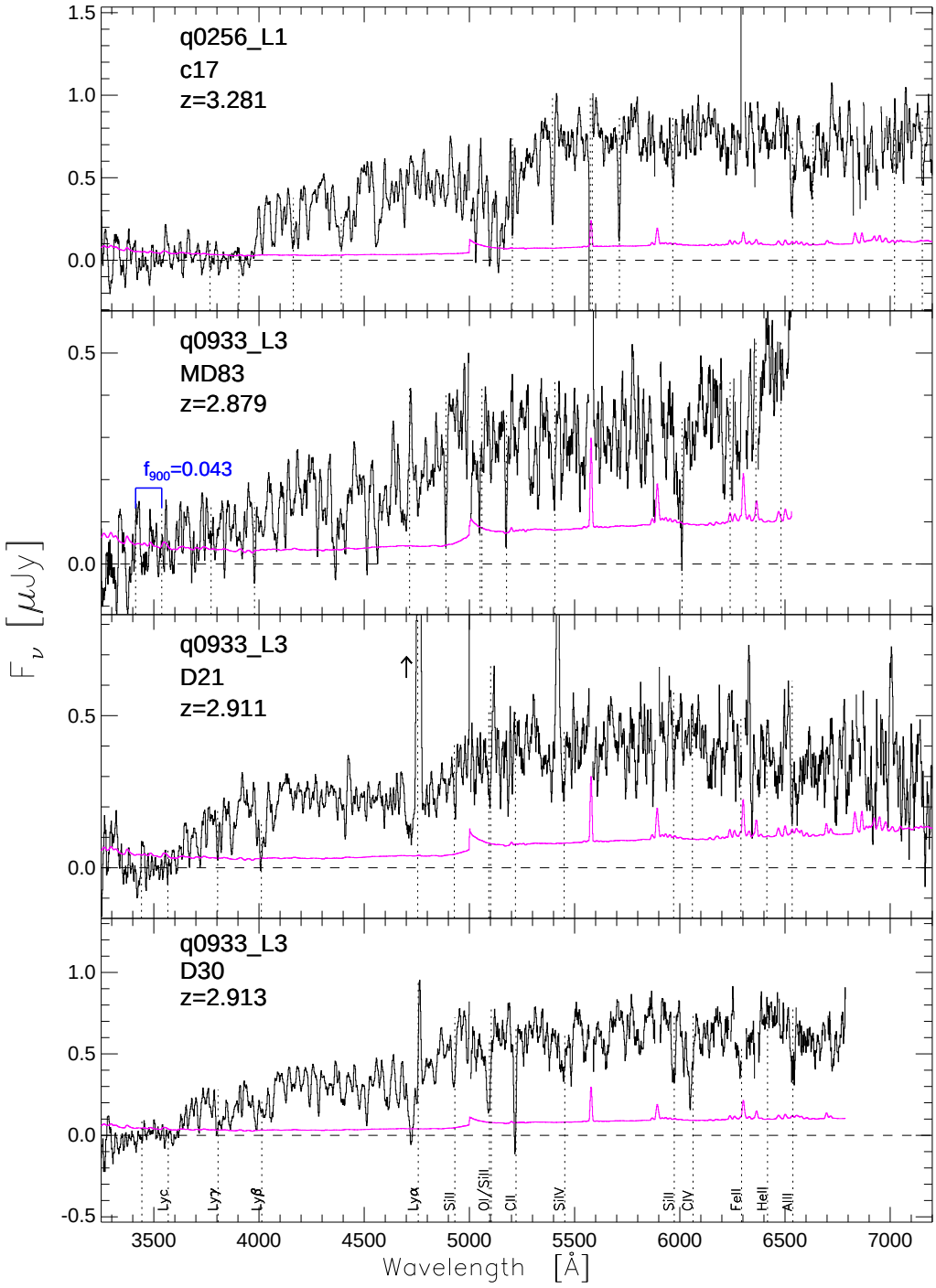

Figure A.17 Continued from Figure A.1

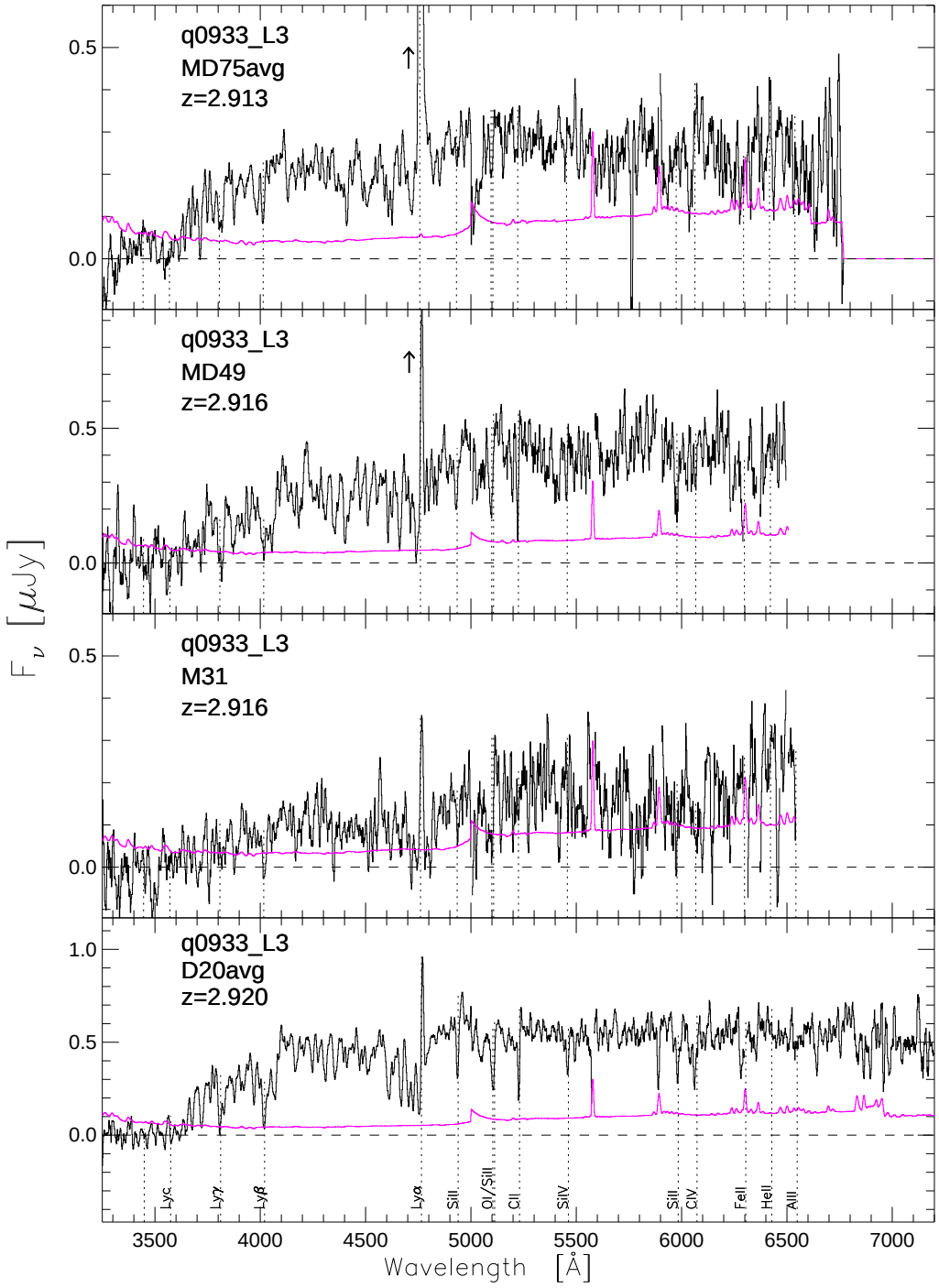

Figure A.18 Continued from Figure A.1

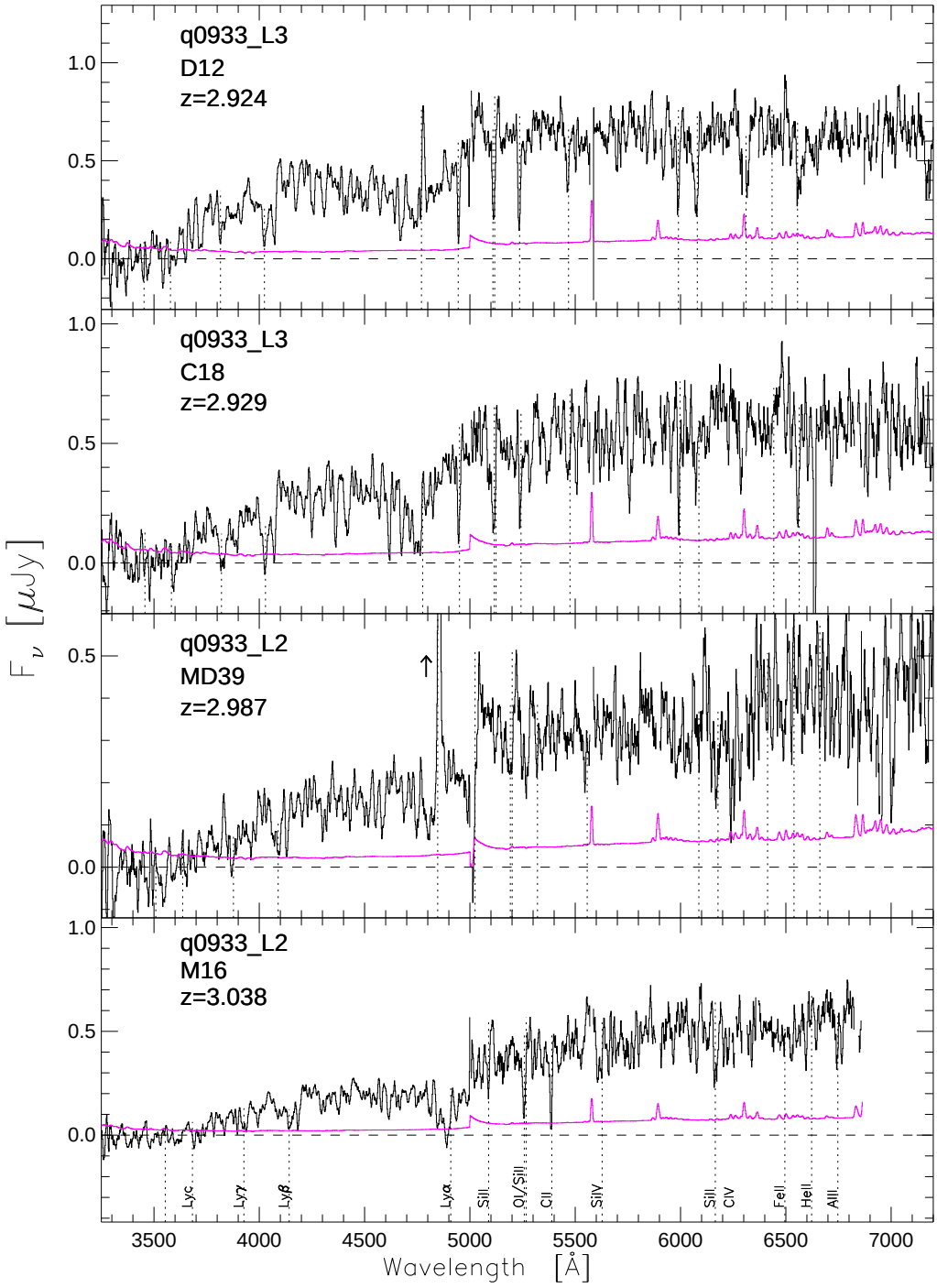

Figure A.19 Continued from Figure A.1

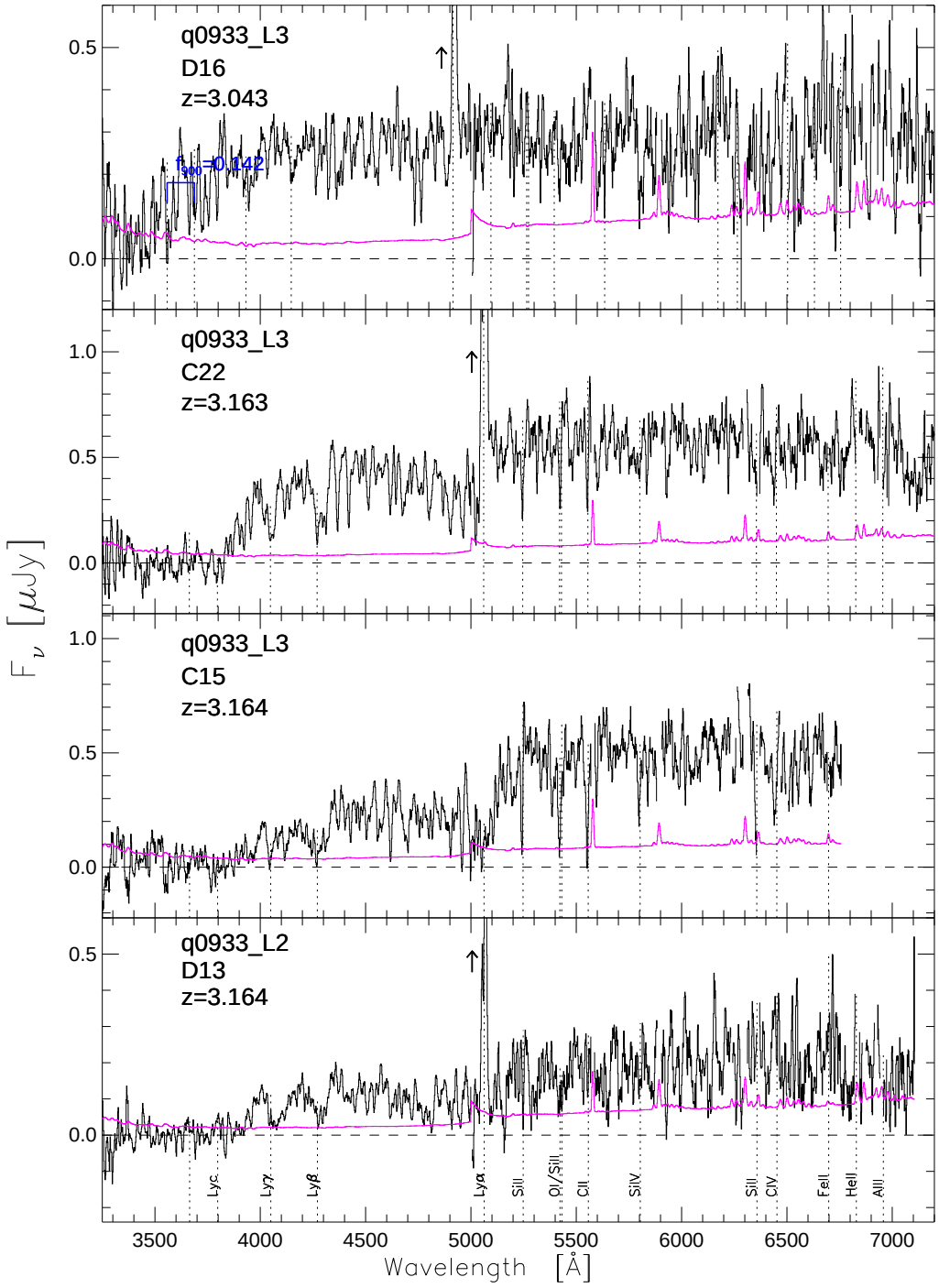

Figure A.20 Continued from Figure A.1

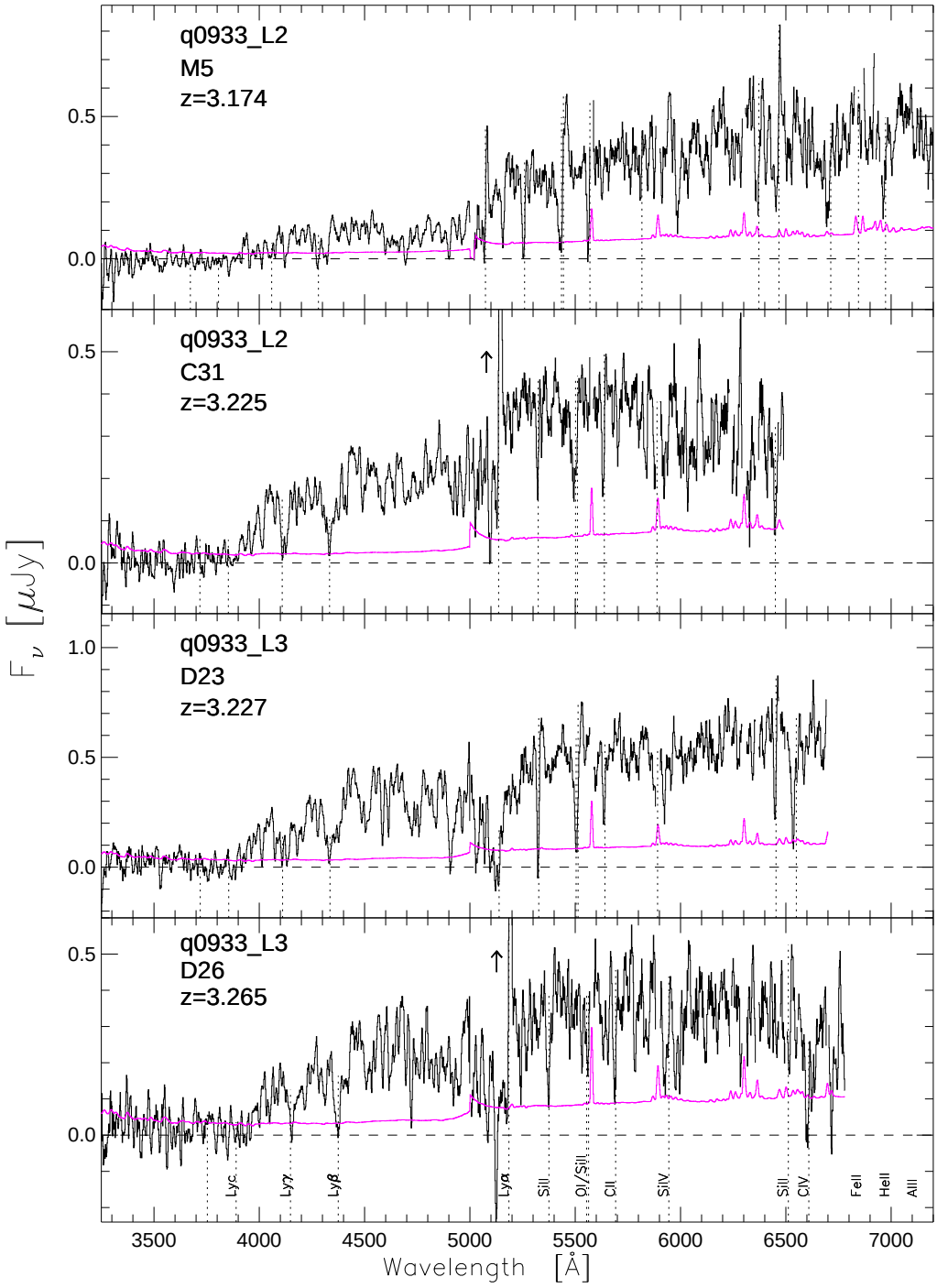

Figure A.21 Continued from Figure A.1

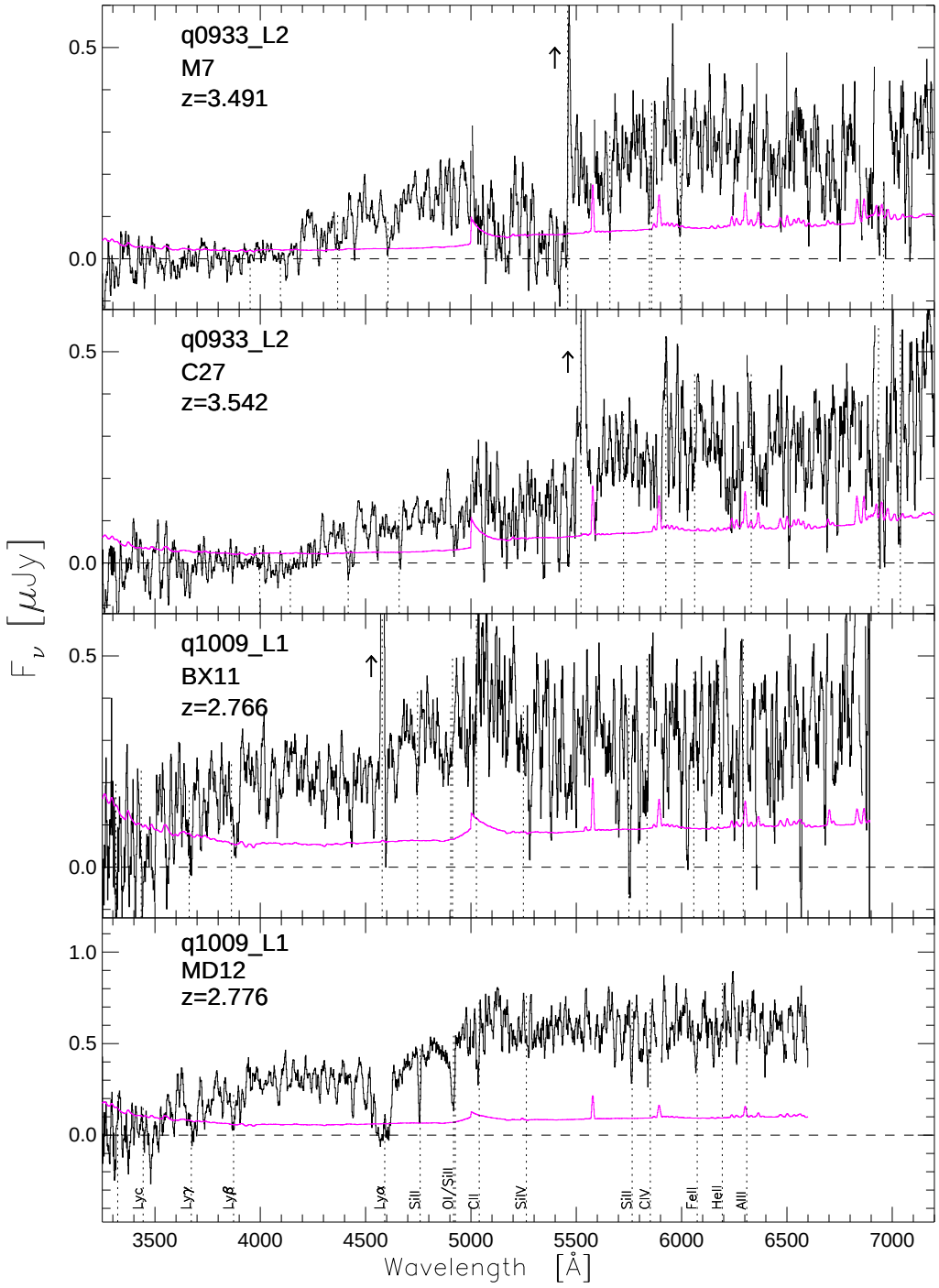

Figure A.22 Continued from Figure A.1

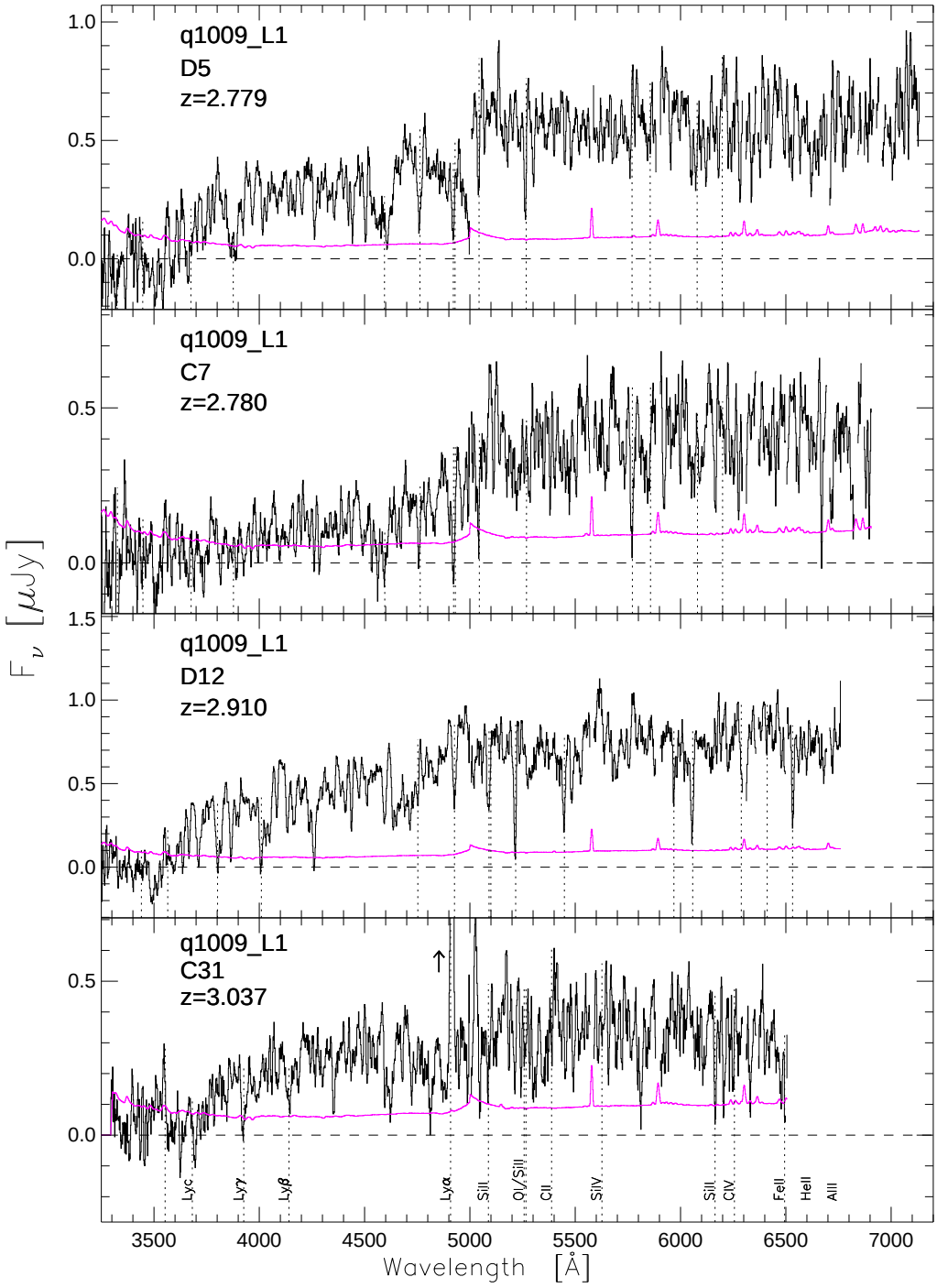

Figure A.23 Continued from Figure A.1

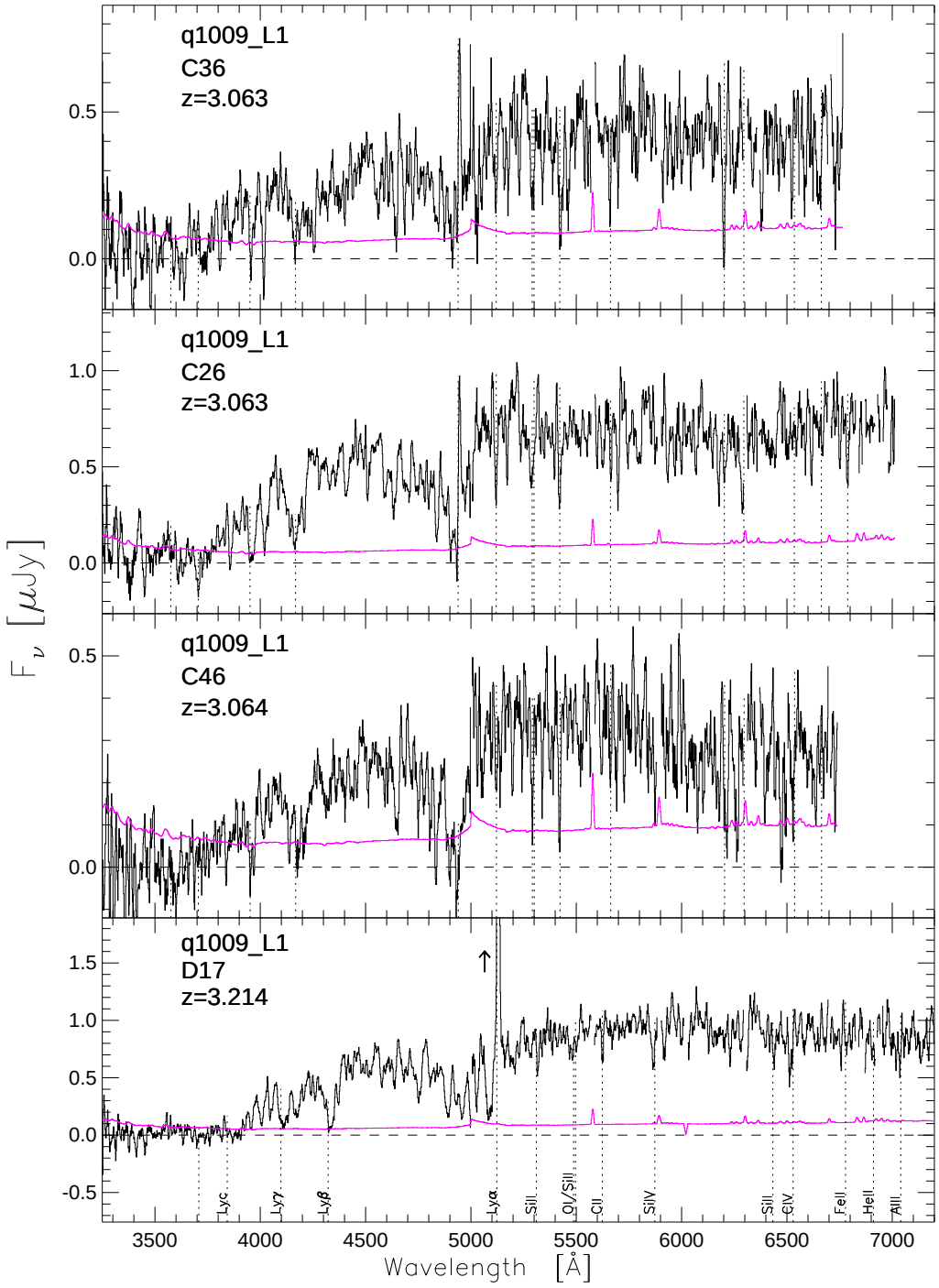

Figure A.24 Continued from Figure A.1

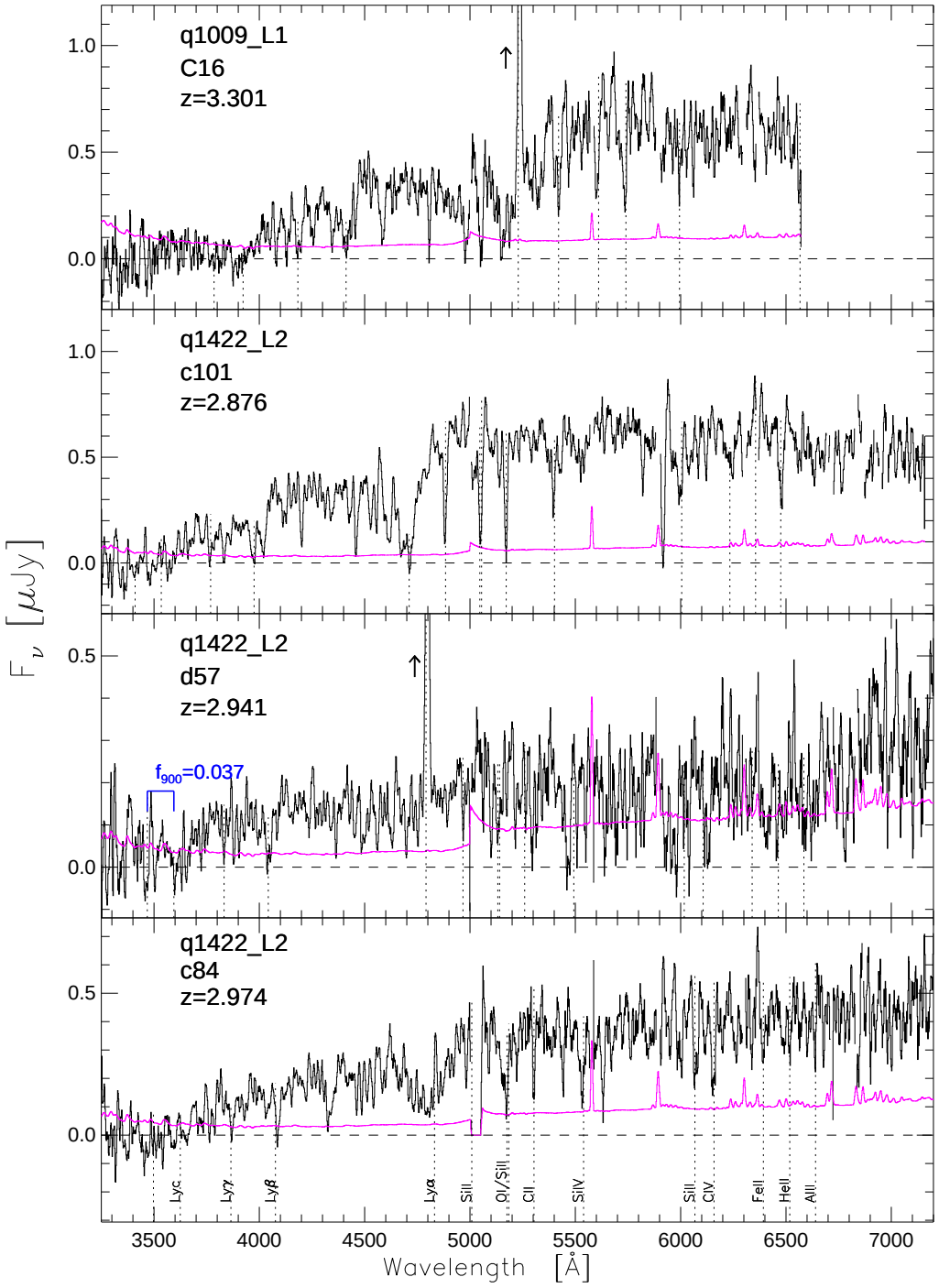

Figure A.25 Continued from Figure A.1

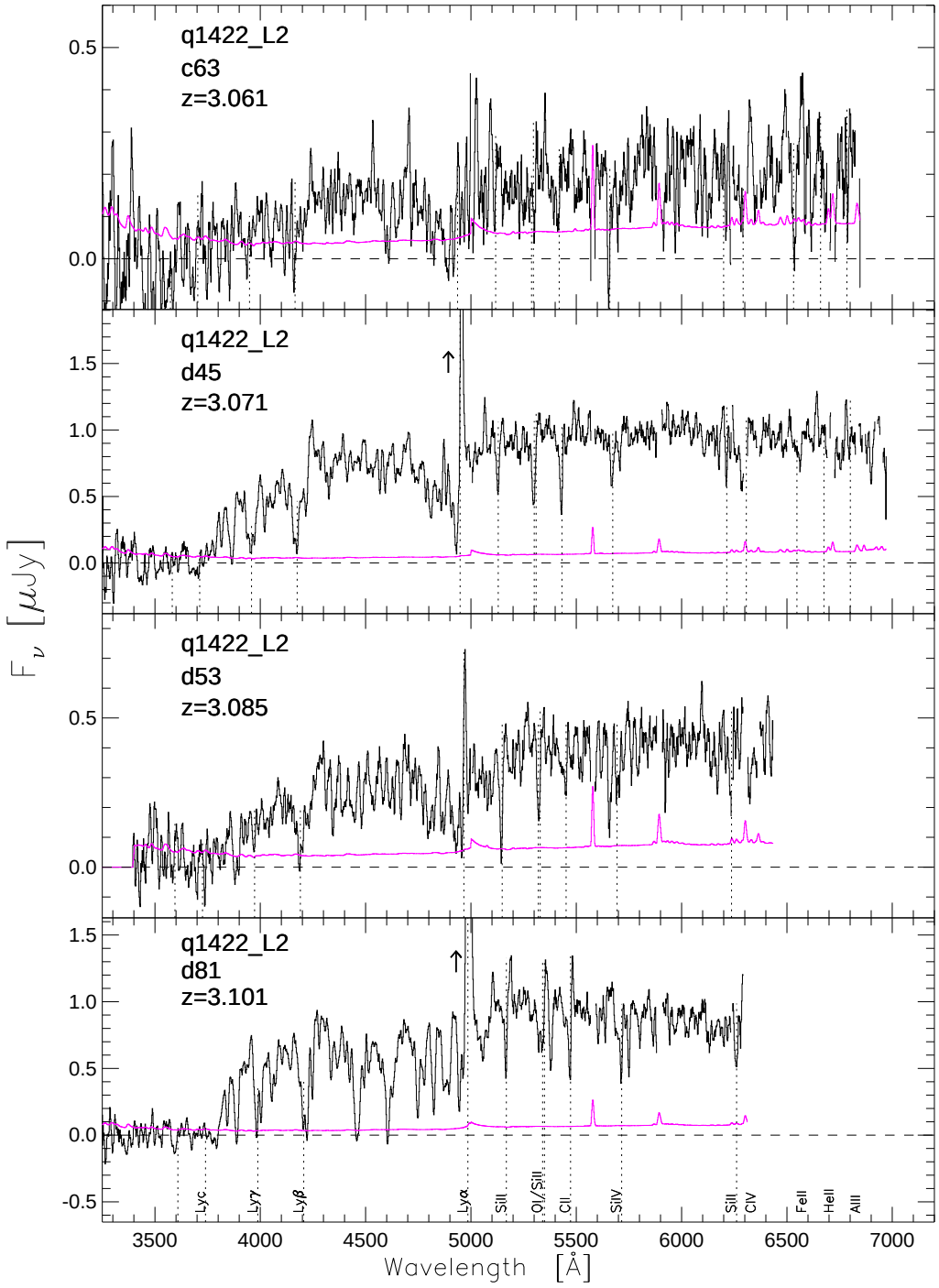

Figure A.26 Continued from Figure A.1

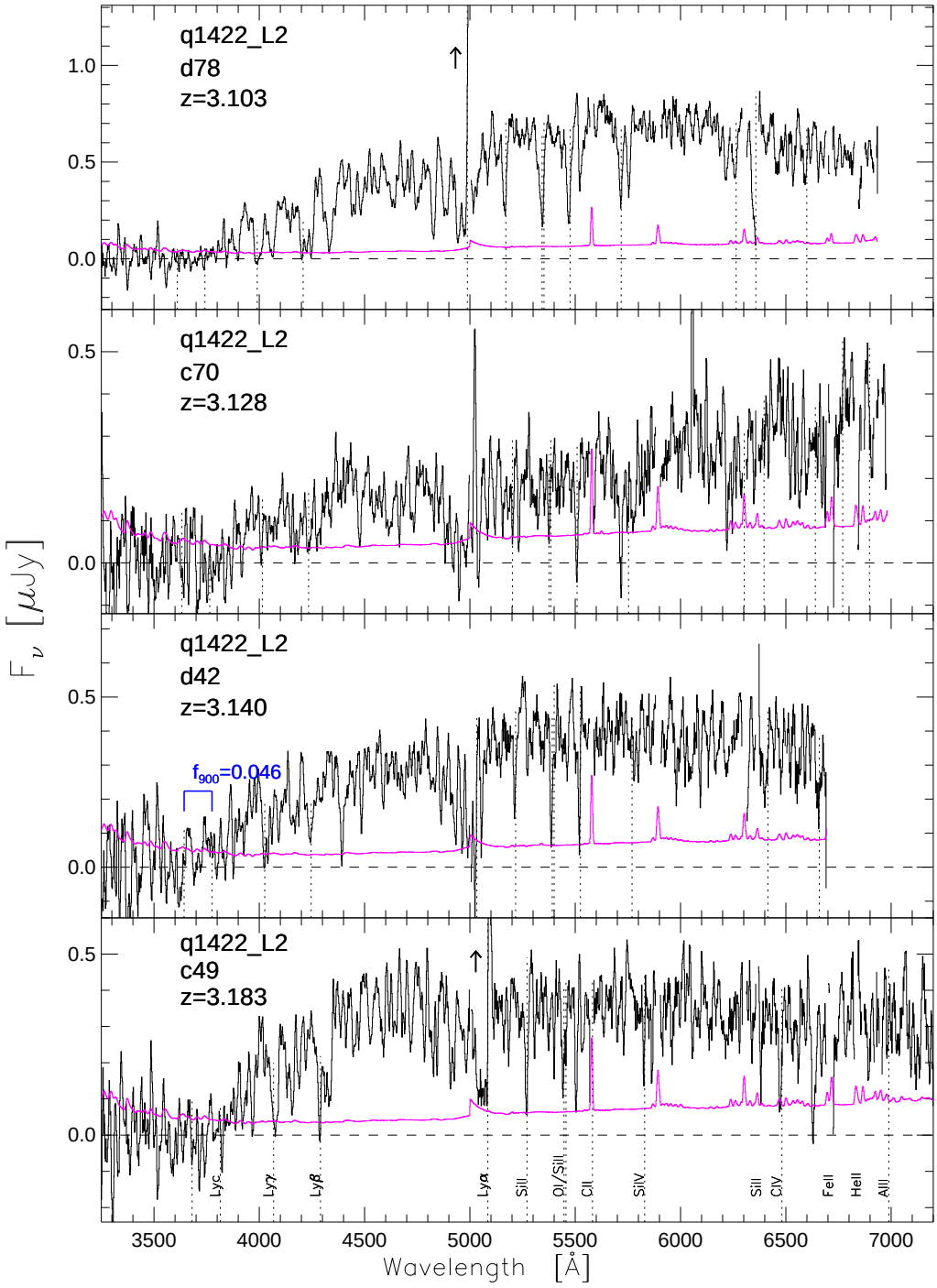

Figure A.27 Continued from Figure A.1

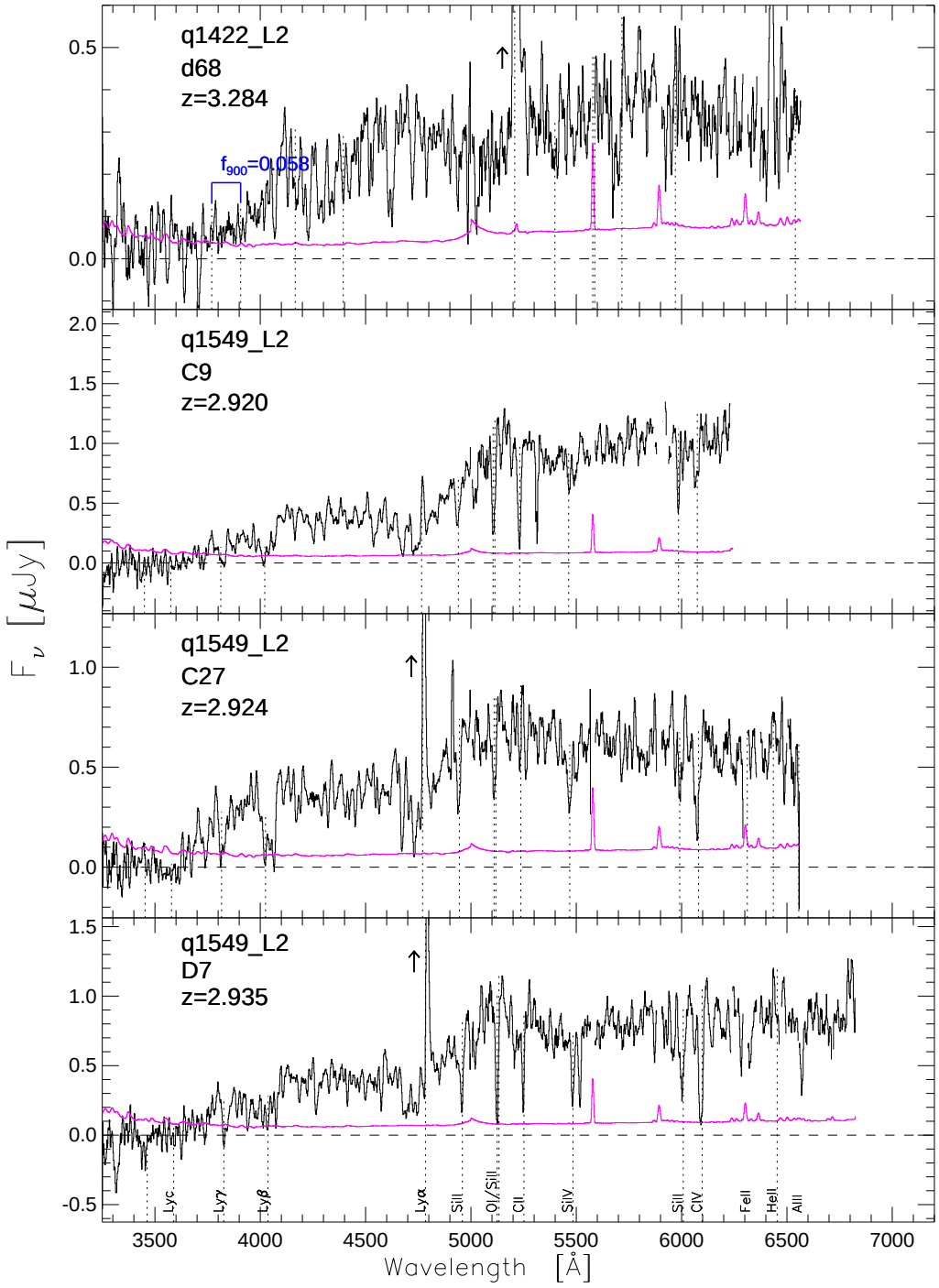

Figure A.28 Continued from Figure A.1

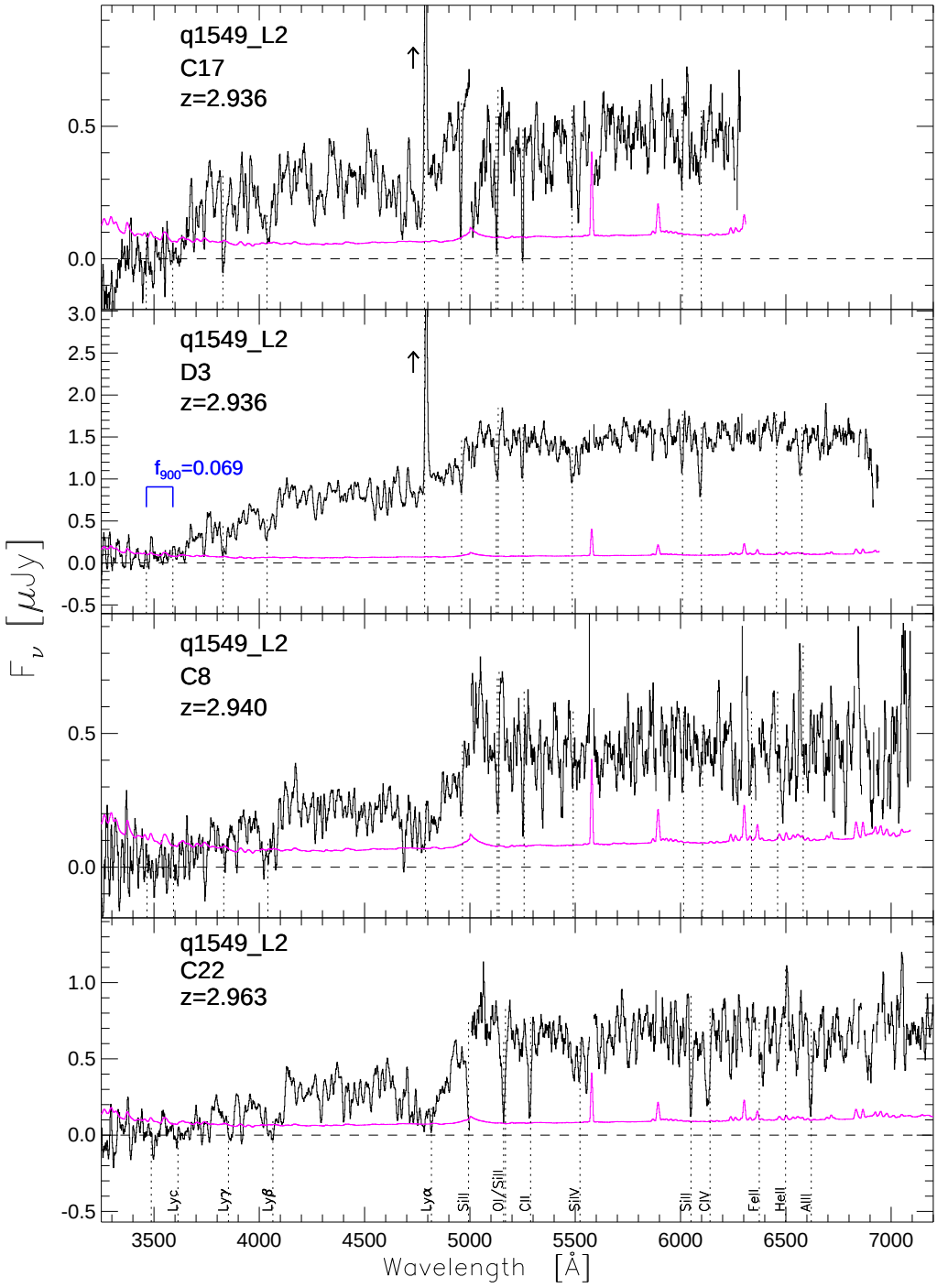

Figure A.29 Continued from Figure A.1

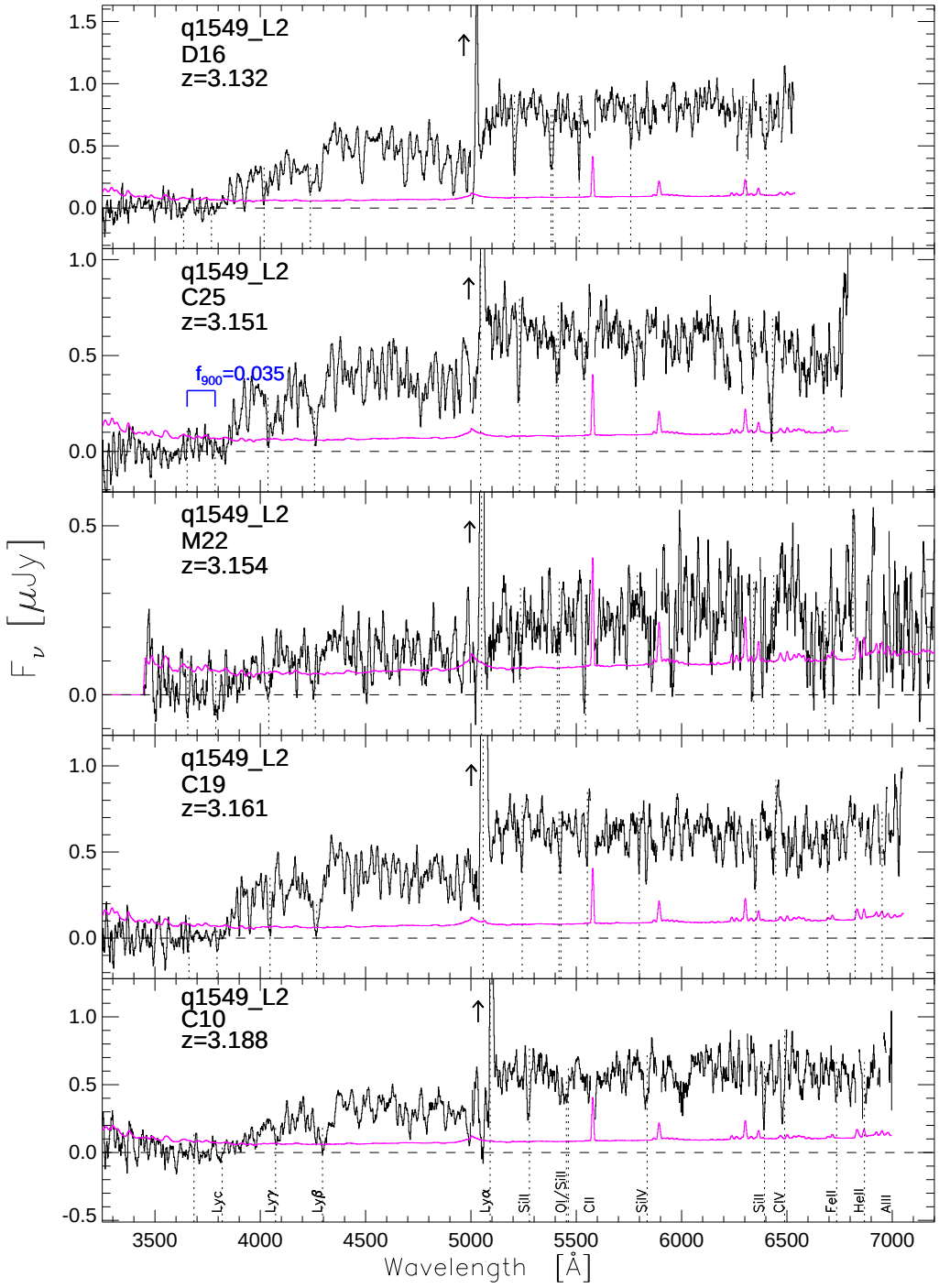

Figure A.30 Continued from Figure A.1

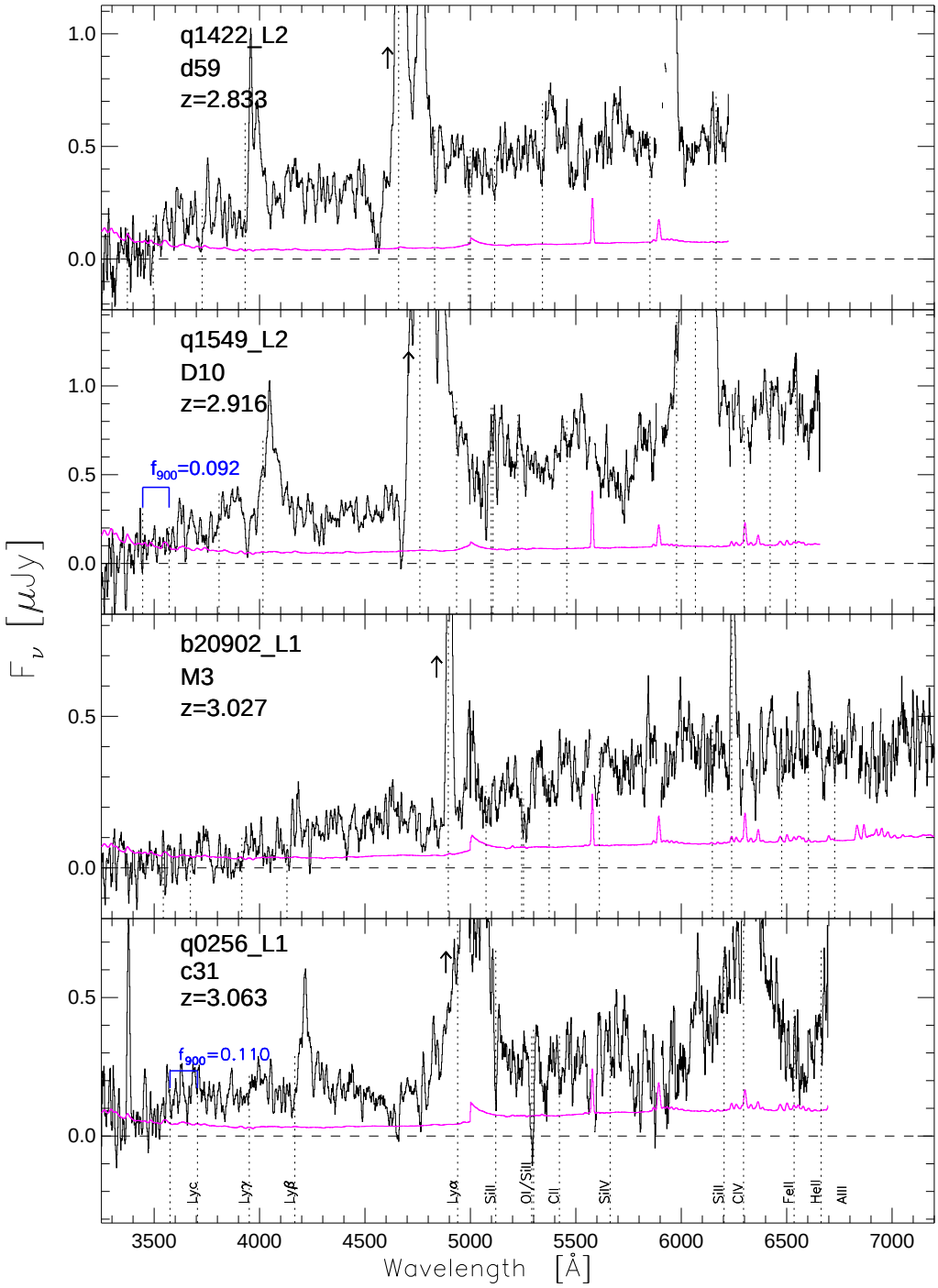

Figure A.31 Deep spectra for 2 objects classified as broad-lined QSO (Q1549-D10 and Q0256-c31) and 2 objects with prominent narrowlined AGN features (Q1422-d59 and B20902-M3). Note that one QSO and one AGN have a significant detection of Lyman continuum flux.

Bibliography

Adelberger, K. L., &Steidel, C. C. 2000, ApJ, 544, 218

Adelberger, K. L., Steidel, C. C., Shapley, A. E., & Pettini, M. 2003, ApJ, 584, 45

Adelberger, K. L., Steidel, C. C., Shapley, A. E., Hunt, M. P., Erb, D. K., Reddy, N. A., & Pettini, M. 2004, ApJ, 607, 226

Adelberger, K. L., Shapley,A. E., Steidel, C. C., Pettini, M., Erb, D. K., & Reddy, N. A. 2005,ApJ, 629, 636

Adelberger, K. L., Steidel, C. C., Kollmeier, J. A., & Reddy, N. A. 2006, ApJ, 637, 74

Armus, L., Soifer, B. T.,Murphy, T. W., Jr., Neugebauer, G., Evans, A. S., & Matthews, K. 1998, ApJ, 495, 276

Barkana, R., & Loeb, A. 2003, Nature, 421, 341

Bauer, A., et al. 2003, Bulletin of the American Astronomical Society, 35, 1262

Bechtold, J., Weymann, R. J., Lin, Z., & Malkan, M. A. 1987, ApJ, 315, 180

Bergvall, N.,Zackrisson,E., Andersson, B.-G., Arnberg, D., Masegosa, J.,Östlin, G., 2006, A&A, 448, 513

Bershady, M. A., Charlton,J. C., & Geoffroy, J. M. 1999, ApJ, 518, 103

Bertin, E., & Arnouts,S. 1996, A&AS, 117, 393

Bland-Hawthorn,J., & Maloney, P. R. 1999, ApJ, 510, L33

Bogosavljevic, M., Djorgovski, S. G., Castro, S. M., Mahabal, A. A., & Lopes, P. 2002, Bulletin of the American Astronomical Society, 34, 1234

Bogosavljevic, M., Mahabal, A., & Djorgovski, S. G. 2003, GRB Coordinates Network, 2275, 1

Bogosavljevic, M., Djorgovski, S. G., Mahabal, A., Thompson, D., & Castro, S. 2005, Bulletin of the American Astronomical Society, 37, 1186

Bouwens, R. J., Illingworth, G. D., Franx, M., & Ford, H. 2007, ApJ, 670, 928

Browning, M. K., Tumlinson, J., & Shull, J. M. 2003, ApJ, 582, 810

Bruzual, G., & Charlot, S. 2003, MNRAS, 344, 1000

Calzetti, D. 1997, AJ, 113, 162

Carilli, C. L., et al. 2008, ApJ, 689, 883

Chapman, S. C., Scott, D., Windhorst, R. A., Frayer, D. T., Borys, C., Lewis, G. F., & Ivison, R. J. 2004, ApJ, 606, 85

Charlot, S., & Fall,S. M. 1993, ApJ, 415, 580

Cowie, L. L., & Hu, E. M. 1998,AJ, 115, 1319

Cowie, L. L., Barger, A. J., & Trouille, L. 2009, ApJ, 692, 1476

Cui, J., Bechtold, J., Ge, J., & Meyer, D. M. 2005, ApJ, 633, 649

Deharveng, J.-M., Buat,V., Le Brun, V., Milliard, B., Kunth, D., Shull, J. M., & Gry, C. 2001, A&A, 375, 805

Dessauges-Zavadsky, M., D'Odorico, S., Schaerer, D., Modigliani, A., Tapken, C., & Vernet, J. 2009, arXiv:0912.4384

Dey, A., et al. 2005, ApJ, 629,654

Djorgovski, S. G., Bogosavljevic, M., Mahabal, A. A., Lopes, P., & Castro, S. M. 2002, Bulletin of the American Astronomical Society, 34, 1325

Djorgovski, S. G., et al. 2003, Bulletin of the American Astronomical Society, 35, 1315

Djorgovski, S. G., et al. 2004, Bulletin of the American Astronomical Society, 36, 1487

Djorgovski, S. G., et al. 2004, Bulletin of the American Astronomical Society, 36, 805

Djorgovski, S. G., et al. 2005, Bulletin of the American Astronomical Society, 37, 1201

Djorgovski, S. G., Bogosavljevic, M., & Mahabal, A. 2006, New Astronomy Review, 50, 140

Erb, D. K., Steidel, C. C.,Shapley, A. E., Pettini, M., Reddy, N. A., & Adelberger, K. L. 2006,ApJ, 646, 107

Erb, D. K., Steidel, C. C.,Shapley, A. E., Pettini, M., Reddy, N. A., & Adelberger, K. L. 2006,ApJ, 647, 128

Fan, X., Carilli, C. L., & Keating,B. 2006, ARA&A, 44, 415

Faucher-Giguère, C.-A., Lidz, A., Hernquist, L., & Zaldarriaga, M. 2008, ApJ, 682, L9

Faucher-Giguère, C.-A., Lidz, A., Zaldarriaga, M., & Hernquist, L. 2009, ApJ, 703, 1416

Fernández-Soto, A., Lanzetta, K. M., & Chen, H.-W. 2003, MNRAS, 342, 1215

Filippenko, A. V. 1982, PASP, 94, 715

Francis, P. J., et al. 2001, ApJ, 554, 1001

Franx, M., et al. 2003, ApJ,587, L79

Ge, J., Bechtold, J., & Kulkarni, V. P. 2001, ApJ, 547, L1

Giallongo, E., Cristiani, S., D'Odorico, S., & Fontana, A. 2002, ApJ, 568, L9

Giavalisco, M. 2002,ARA&A, 40, 579

Glikman, E., Djorgovski,S. G., Stern, D., Bogosavljević, M., & Mahabal, A. 2007, ApJ,663, L73

Glikman, E., Bogosavljevic, M., Djorgovski, S. G., Stern, D., Dey, A., Jannuzi, B. T., & Mahabal, A. 2009, arXiv:0912.2799

Goerdt, T., Dekel, A.,Sternberg, A., Ceverino, D., Teyssier, R., & Primack, J. R. 2009,arXiv:0911.5566

Grimes, J. P., et al. 2007, ApJ, 668, 891

Gunn, J. E., & Peterson,B. A. 1965, ApJ, 142, 1633

Haardt, F., & Madau, P. 1996, ApJ, 461, 20

Hashimoto, Y., Barcons,X., Böhringer, H., Fabian, A. C., Hasinger, G., Mainieri, V., &Brunner, H. 2004, A&A, 417, 819

Hayashino, T., et al. 2004, AJ, 128, 2073

Hogg, D. W., Baldry, I. K.,Blanton, M. R., & Eisenstein, D. J. 2002, arXiv:astro-ph/0210394

Hunt, M. P., Steidel, C. C., Adelberger, K. L., & Shapley, A. E. 2004, ApJ, 605, 625

Hurwitz, M., Jelinsky, P., & Dixon, W. V. D. 1997, ApJ, 481, L31

Inoue, A. K., & Iwata, I. 2008, MNRAS, 387, 1681

Inoue, A. K., Iwata, I.,Deharveng, J.-M., Buat, V., & Burgarella, D. 2005, A&A, 435, 471

Ivezić, Ž., etal. 2004, Astronomische Nachrichten, 325, 583

Iwata, I., et al. 2009, ApJ,692, 1287, IW09

Jannuzi, B. T., & Dey, A. 1999, Photometric Redshifts and the Detection of High Redshift Galaxies, 191, 111

Jannuzi, B. T., & Dey, A. 1999, The Hy-Redshift Universe: Galaxy Formation and Evolution at HighRedshift, 193, 258

Jiang, L., Fan, X., & Vestergaard, M. 2008, ApJ, 679, 962

Keel, W. C., Cohen,S. H., Windhorst, R. A., & Waddington, I. 1999, AJ, 118, 2547

Keel, W. C., White, R. E.,Chapman, S., & Windhorst, R. A. 2009, AJ, 138, 986

Kennicutt, R. C., Jr. 1998,ARA&A, 36, 189

Kereš, D., Katz, N., Weinberg, D. H., & Davé, R. 2005, MNRAS, 363, 2

Kornei, K. A., Shapley, A. E.,Erb, D. K., Steidel, C. C., Reddy, N. A., Pettini, M., & Bogosavljević, M. 2009, arXiv:0911.2000

Kriek, M., et al. 2006, ApJ,649, L71

Laird, E. S., Nandra, K., Hobbs, A., & Steidel, C. C. 2006, MNRAS, 373, 217

Law, D. R., Steidel, C. C., Erb,D. K., Larkin, J. E., Pettini, M., Shapley, A. E., & Wright, S. A. 2007, ApJ, 669, 929

Law, D. R., Steidel, C. C., Erb,D. K., Pettini, M., Reddy, N. A., Shapley, A. E., Adelberger, K. L.,& Simenc, D. J. 2007, ApJ, 656, 1

Leitherer, C., Ferguson, H. C., Heckman, T. M., & Lowenthal, J. D. 1995, ApJ, 454, L19

Leitherer, C., et al. 1999,ApJS, 123, 3

Lilly, S. J. 1988, ApJ, 333, 161

López-Cruz, O., et al. 2005, Revista Mexicana de Astronomia y Astrofisica Conference Series, 24, 164

Madau, P., Ferguson, H. C., Dickinson, M. E., Giavalisco, M., Steidel, C. C., & Fruchter, A. 1996, MNRAS, 283, 1388

Madau, P., Pozzetti, L., &Dickinson, M. 1998, ApJ, 498, 106

Madau, P., Haardt, F., & Rees, M. J. 1999, ApJ, 514, 648

Madau, P. 1995, ApJ, 441, 18

Mahabal, A., et al. 2003, Bulletin of the American Astronomical Society, 35, 1262

Mahabal, A., et al. 2004, arXiv:astro-ph/0408035

Mahabal, A., et al. 2005, Bulletin of the American Astronomical Society, 37, 1211

Mahabal, A., Stern, D., Bogosavljević, M., Djorgovski, S. G., & Thompson, D. 2005, ApJ, 634, L9

Malkan, M., Webb, W., & Konopacky, Q. 2003, ApJ, 598, 878

Massey, P., Strobel, K.,Barnes, J. V., & Anderson, E. 1988, ApJ, 328, 315

Matsuda, Y., et al. 2004,AJ, 128, 569

Maughan, B. J., Jones,L. R., Ebeling, H., & Scharf, C. 2004, MNRAS, 351, 1193

McLean, I. S., et al. 1998,ProcSPIE, 3354, 566

Meier, D. L. 1976, ApJ, 207, 343

Mesinger, A., &Haiman, Z. 2007, ApJ, 660, 923

Mesinger, A. 2009, arXiv:0910.4161

Miralda-Escude, J., & Ostriker, J. P. 1990, ApJ, 350, 1

Nilsson, K. K., Fynbo,J. P. U., Møller, P., Sommer-Larsen, J., & Ledoux, C. 2006, A&A,452, L23

Noterdaeme, P., Ledoux, C., Petitjean, P., & Srianand, R. 2008, A&A, 481, 327

Oke, J. B., et al. 1995, PASP,107, 375

Ouchi, M., et al. 2009, ApJ,706, 1136

Overzier, R. A., et al. 2009, ApJ, 704, 548

Palunas, P., Teplitz, H. I.,Francis, P. J., Williger, G. M., & Woodgate, B. E. 2004, ApJ, 602,545

Partridge, R. B., &Peebles, P. J. E. 1967, ApJ, 147, 868

Peter, A. H. G., Shapley, A. E.,Law, D. R., Steidel, C. C., Erb, D. K., Reddy, N. A., & Pettini, M. 2007, ApJ, 668, 23

Petitjean, P., Srianand, R., & Ledoux, C. 2000, A&A, 364, L26

Pettini, M., Rix, S. A.,Steidel, C. C., Hunt, M. P., Shapley, A. E., & Adelberger, K. L. 2002, Ap&SS, 281, 461

Pettini, M., Rix, S. A., Steidel, C. C., Adelberger, K. L., Hunt, M. P., & Shapley, A. E. 2002, ApJ, 569, 742

Prescott, M. K. M. 2009, Ph.D. Thesis

Pritchet, C. J. 1994, PASP,106, 1052

Prochaska, J. X., et al. 2009, ApJ, 691, L27

Putman, M. E., Bland-Hawthorn, J., Veilleux, S., Gibson, B. K., Freeman, K. C., & Maloney, P. R. 2003, ApJ, 597, 948

Quider, A. M., Shapley, A. E., Pettini, M., Steidel, C. C., & Stark, D. P. 2009, arXiv:0910.0840

Rabinowitz, D., et al. 2003, Bulletin of the American Astronomical Society, 35, 1262

Raiter, A., Fosbury, R. A. E., & Teimoorinia, H. 2009, arXiv:0912.4305

Rauch, M., et al. 2008, ApJ, 681, 856

Reddy, N. A., & Steidel, C. C. 2009, ApJ, 692, 778

Reddy, N. A., Steidel, C. C.,Pettini, M., Adelberger, K. L., Shapley, A. E., Erb, D. K., &Dickinson, M. 2008, ApJS, 175, 48

Richards, G. T., et al. 2006, AJ, 131, 2766

Robert, C., Pellerin, A., Aloisi, A., Leitherer, C., Hoopes, C., & Heckman, T. M. 2003, ApJS, 144, 21

Rutledge, R. E., Fox, D. W., Bogosavljevic, M., & Mahabal, A. 2003, ApJ, 598, 458

Saito, T., Shimasaku, K.,Okamura, S., Ouchi, M., Akiyama, M., & Yoshida, M. 2006, ApJ, 648,54

Shapley, A. E., Steidel,C. C., Adelberger, K. L., Dickinson, M., Giavalisco, M., & Pettini,M. 2001, ApJ, 562, 95

Shapley, A. E., Steidel, C. C., Pettini, M., & Adelberger, K. L. 2003, ApJ, 588, 65

Shapley, A. E., Steidel,C. C., Erb, D. K., Reddy, N. A., Adelberger, K. L., Pettini, M.,Barmby, P., & Huang, J. 2005, ApJ, 626, 698

Shapley, A. E., Steidel,C. C., Pettini, M., Adelberger, K. L., & Erb, D. K. 2006, ApJ, 651,688

Sheffer, Y., Prochaska, J. X., Draine, B. T., Perley, D. A., & Bloom, J. S. 2009, ApJ, 701, L63

Shimasaku, K., et al. 2003, ApJ, 586, L111

Siana, B., et al. 2007, ApJ,668, 62

Siana, B., et al. 2008, ApJ, 675, 49

Smith, D. J. B., Jarvis, M. J.,Lacy, M., & Martínez-Sansigre, A. 2008, MNRAS, 389, 799

Springel, V., et al. 2005,Nature, 435, 629

Steidel, C. C., &Hamilton, D. 1993, AJ, 105, 2017

Steidel, C. C., Adelberger,K. L., Dickinson, M., Giavalisco, M., Pettini, M., & Kellogg, M. 1998, ApJ, 492, 428

Steidel, C. C., Adelberger,K. L., Giavalisco, M., Dickinson, M., & Pettini, M. 1999, ApJ, 519,1

Steidel, C. C., Adelberger,K. L., Shapley, A. E., Pettini, M., Dickinson, M., & Giavalisco, M. 2000, ApJ, 532, 170

Steidel, C. C., Pettini, M.,& Adelberger, K. L. 2001, ApJ, 546, 665

Steidel, C. C., Adelberger,K. L., Shapley, A. E., Pettini, M., Dickinson, M., & Giavalisco, M. 2003, ApJ, 592, 728

Steidel, C. C., Shapley,A. E., Pettini, M., Adelberger, K. L., Erb, D. K., Reddy, N. A., &Hunt, M. P. 2004, ApJ, 604, 534

Steidel, C. C., Adelberger,K. L., Shapley, A. E., Erb, D. K., Reddy, N. A., & Pettini, M. 2005,ApJ, 626, 44

Telfer, R. C., Zheng, W., Kriss,G. A., & Davidsen, A. F. 2002, ApJ, 565, 773

Tenorio-Tagle, G.,Silich, S. A., Kunth, D., Terlevich, E., & Terlevich, R. 1999,MNRAS, 309, 332

Vanden Berk, D. E., et al. 2001, AJ, 122, 549

Vanzella, E., et al. 2009, arXiv:0912.3007

Walborn, N. R., Fullerton, A. W., Crowther, P. A., Bianchi, L., Hutchings, J. B., Pellerin, A., Sonneborn, G., & Willis, A. J. 2002, ApJS, 141, 443

White, R. E., III, Keel,W. C.,& Windhorst, R. A. 2004, BAAS, 36, 961

Wilkes, B. J. 1986, MNRAS, 218, 331

Wilson, J. C., et al. 2003,ProcSPIE, 4841, 451

Wise, J. H., & Cen, R. 2009,ApJ, 693, 984

Wittman, D. M., et al. 2002, Proc. SPIE, 4836, 73

Wittman, D. M., et al. 2002,ProcSPIE, 4836, 73

Womble, D. S., Sargent, W. L. W., & Lyons, R. S. 1996, Cold Gas at High Redshift, 206, 249

Wuyts, S., van Dokkum, P. G.,Franx, M., Förster Schreiber, N. M., Illingworth, G. D.,Labbé, I., & Rudnick, G. 2009, ApJ, 706, 885

Wyithe, J. S. B., & Cen, R. 2007, ApJ, 659, 890

Yang, Y., Zabludoff, A., Tremonti,C., Eisenstein, D., & Davé, R. 2009, ApJ, 693, 1579